Role of MICOS-dependent cristae membrane dynamics within mitochondria

Inaugural-Dissertation

zur Erlangung des Doktorgrades

der Mathematisch-Naturwissenschaftlichen Fakultät

der Heinrich-Heine-Universität Düsseldorf

vorgelegt von

Mathias Golombek

aus Soest

Düsseldorf, März 2024

aus dem Institut für Biochemie und Molekularbiologie I

der Heinrich-Heine-Universität Düsseldorf

Gedruckt mit der Genehmigung der

Mathematisch-Naturwissenschaftlichen Fakultät der

Heinrich-Heine-Universität Düsseldorf

Berichterstatter:

1. Prof. Dr. Andreas Reichert

2. Prof. Dr. Andreas Weber

Tag der mündlichen Prüfung: 11.06.2024

Everything we hear is an opinion, not a fact.

Everything we see is a perspective, not the truth.

Marcus Aurelius

Table of contents

1. Introduction 1

1.1. Mitochondrial origin and function 1

1.2. Physiological role of mitochondrial dynamics and quality control 3

1.3. Mitochondrial ultrastructure 5

1.4. Maintenance, expression and role of mitochondrial genome 6

1.5. Electron transport chain (ETC) and ATP production 9

1.6. MICOS (mitochondrial contact site and cristae organizing system) 12

1.7. Super resolution nanoscopy and cristae membrane dynamics 17

1.8. Cristae membrane remodelling 21

1.9. Relevance of SLC25 carries for mitochondrial function and morphology 23

2. Aims of the doctoral thesis 27

3. Results 28

3.1. Cristae dynamics is modulated in bioenergetically compromised mitochondria 28

3.2. MIC26 and MIC27 cooperate to regulate cardiolipin levels and the landscape of OXPHOS complexes 53

3.3. Involvement of necroptosis in the selective toxicity of the natural compound (±) gossypol on squamous skin cancer cells in vitro 71

4. Discussion 90

4.1. Bioenergetic and "chemical" requirements for cristae remodelling 92

4.2. Molecular players involved in cristae remodelling 95

4.3. Possible roles of cristae remodelling 98

4.4. Conclusions 102

5. Summary 104

6. References 106

7. Publications 117

8. Acknowledgments 118

Eidesstattliche Erklärung 120

1. Introduction

1.1. Mitochondrial origin and function

Mitochondria are cellular organelles that are found in virtually all eukaryotic cells and tissues where they display vital functions for cell survival and development [1]. From an evolutionary point of view, mitochondria and their precursors developed about two billion years ago by endosymbiosis, retaining several of characteristics which are evident to date [2]. They inherited parts of their genome from alpha-proteobacteria [3, 4]. Mitochondria are involved in numerous cellular functions. While receiving a lot of attention for housing several critical metabolic pathways, such as oxidative phosphorylation (OXHOS) or the tricarboxylic acid cycle (TCA-cycle), they play vital roles in regulation of apoptosis, biosynthesis of iron–sulfur clusters (Fe-S-clusters), redox and calcium signalling, and regulation of immune responses [5-7]. Mitochondria possess their own genome and their own replication, transcription and expression machinery [8-10]. They have interaction sites with numerous other organelles such as the endoplasmic reticulum (ER) or peroxisomes [11]. Mitochondria have a complex import machinery for proteins and are rich in cannels and carriers for exchange of ions and metabolites [12-14]. Furthermore, mitochondria are organized in different subcompartments, this organization is established via protein complexes in the inner mitochondrial membrane (IMM) and are essential for mitochondrial function (**Figure 1**) [15, 16].

Mitochondria were discovered over 150 years ago. Albert von Koelliker was the first scientist to describe mitochondria, without using this term, in 1857, as he described granules that he observed in muscle cells of insects [17]. Richard Altman is another pioneer in the field of mitochondrial research. He observed specific forms of granules in several different cell types, assuming that they are elementary entities with a distinct metabolic and genetic independency. He introduced the term “bioblasts” for these granules in 1894 [18, 19]. About four years later Carl Bender used the term “mitochondria” for the first time, as a combination of the two Greek words μίτος, *mitos*, "thread", and χονδρίον, *chondrion*, "granule” to describe his observations [20].

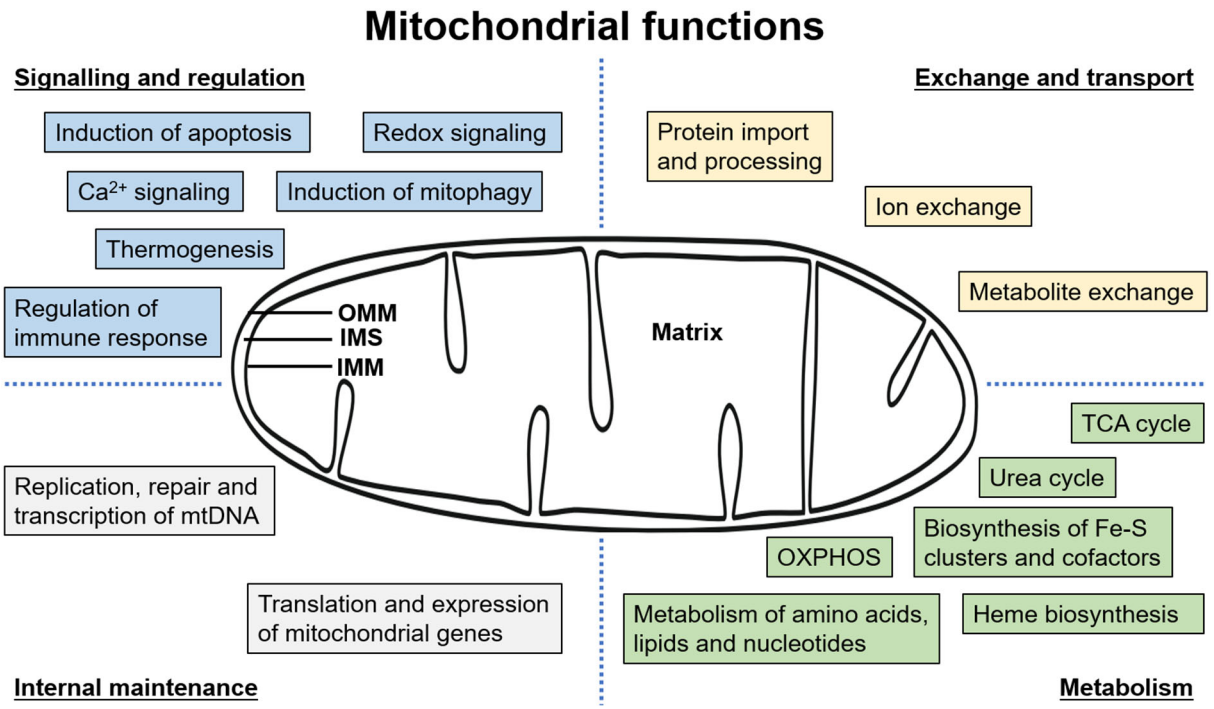

Figure 1. Overview of mitochondrial functions. Mitochondria can be separated into four main structural sections, outer mitochondrial membrane (OMM), intermembrane space (IMS), inner mitochondrial membrane (IMM) and matrix. This schematic depiction illustrates the broad variety of functions, mitochondria are involved in, grouped into four main categories: signalling and regulatory processes like induction of apoptosis, redox signalling, Ca^{2+} signalling, induction of mitophagy, thermogenesis and regulation of immune response; exchange and transport like protein import and processing, ion exchange and metabolite exchange; metabolism like TCA cycle, urea cycle, OXPHOS, biosynthesis of Fe-S clusters and cofactors, metabolism of amino acids, lipids and nucleotides and heme biosynthesis; internal maintenance mechanisms like replication, repair and transcription of mtDNA and translation and expression of mitochondrial genes [12].

Mitochondria are vital organelles essential for survival and development of eukaryotic cells and organisms. Due to their involvement in various cellular functions, they are associated with a large number of diseases, often being associated with neurodegenerative diseases, muscular atrophies and many metabolic disorders [21-26]. Examples being Alzheimer´s disease, Parkinson´s disease, Leigh-syndrome, Barth-syndrome, MELAS, diabetes and even mental diseases like depression were connected to mitochondrial dysfunction [25, 27-30]. Furthermore, mitochondria are gaining relevance as regulator of immune response and induction of inflammation as result of mtDNA release [31, 32]. Over the past 20 years mitochondrial dysfunction has been discussed to play a relevant role tumor growth and cancer development. As cancer therapies try to reduce tumor growth without damaging healthy tissues, drug repurposing and combinational treatments of established drugs in combination with

natural compounds are promising tools [33]. Additionally, mitochondria were identified as promising targets for cancer therapy as modulation of metabolism in cancer cells was shown to reduce tumor growth [23, 34-36]. Overall, mitochondrial diseases occur with a prevalence of about 1:5000 in adults, although many case studies report that patients suffering from mitochondrial diseases die at young age [37, 38].

1.2. Physiological role of mitochondrial dynamics and quality control

Mitochondria were initially discovered using brightfield microscopes. These microscopes, allowed an initial description of mitochondria but were not suited for advanced studies on their functions or physiological relevance. The development of fluorescent dyes and laser scanning microscopes (LSM) was a breakthrough for mitochondrial research. Although the first fluorescence microscopes were already developed in the 1910s, they were mostly used for visualization of autofluorescence, emitted by bacteria or animal and plant tissue. The development of fluorescent probes was essential for establishing fluorescence microscopy as a tool for cell biological applications. The green fluorescence protein (GFP) is certainly one of the world's most well-known proteins, discovered in 1961 by Shimomura, it was the first fluorescent label and led to development of new state-of-the-art LSMs. By understanding the concept of naturally occurring bioluminescence, Shimomura developed numerous fluorescent probes [39, 40]. Today fluorescent probes covering the whole spectra of visible light from about 380 nm to 700 nm including ultraviolet to near-infrared are available by numerous manufacturers.

Using these probes on its own and in combination helped to understand the dynamic behaviour of the mitochondrial network and its numerous interaction partners within the cell [41]. Mitochondria form a highly dynamic tubular network throughout the cell, they undergo fusion and fission and form contact sites with several other organelles like the ER [42, 43]. Mitochondrial dynamics are essential for exchange of membrane and matrix proteins as well as quality control. Depending on cellular demands or cell-cycle phase, mitochondria can fuse to increase mitochondrial mass. Fission on the other hand increases the overall number of individual mitochondria and can help to sort out dysfunctional mitochondria that then can potentially undergo mitophagy. Mitochondrial dynamics is closely tied to quality control via mitophagy [44]. The underlying processes for mitochondrial fusion and fission are well studied and

characterized [42, 45]. Mutations or deficiencies in crucial proteins for these processes have been associated with several diseases like heritable juvenile parkinsonism, Charcot-Marie-Tooth disease 2A, autosomal dominate optic atrophy, lung cancer and other cardiometabolic diseases [46].

To fuse two mitochondria with one another their outer membranes need to fuse first. This step is performed with help of two dynamin-related GTPases, mitofusin (MFN) 1 and 2 [47]. MFNs can form homo- and heterodimers between the two mitochondria that are about to fuse and thereby tether them together [48]. Although the two proteins have a highly similar sequence, they are not redundant in their specific functions [49]. As MFN2 for example has been reported to take part in regulation of mitochondrial metabolism and was shown to form tethers between mitochondria and ER at contact sites [50, 51]. After fusion of the OMM, the IMM needs to be fused in a coordinated manner. This process is regulated by the dynamin-like GTPase OPA1 located in the IMM. Due to proteolytic cleavage, OPA1 is present as a short form (S-OPA1) and membrane-bound long form (L-OPA1) [52]. Lack of mitochondrial fusion can reduce stability of mtDNA as it increases chances for mutation, while mutations and deficiencies of key proteins are found in various severe diseases like Charcot-Marie-Tooth disease 2A (MFN2) or optic atrophy type I [53-55].

Mitochondrial fission is initiated by dynamin-1-like protein (DRP1), a dynamin-like GTPase. It is recruited to the OMM from the cytosol by other OMM proteins like mitochondrial fission factor (MFF), mitochondrial dynamics proteins of 49 and 51 kDa (MiD49/51) and mitochondrial fission protein 1 (Fis1). They can accumulate at the OMM and recruit DRP1 to the OMM, too, to form a ring-like oligomer around the mitochondrion to initiate fission [56]. Although DRP1 is the driving force for mitochondrial fission, other proteins like dynamin 2 (Dyn2) and even other organelles, in this case the ER are suggested to be involved in promoting fission [57, 58]. Mitochondrial fission is essential for mitochondrial quality control, as it allows degradation of mitochondria via mitophagy. Two types of mitochondrial fission, both regulated by DRP1, were identified. Midzone fission events lead to proliferation of mitochondria and is additionally regulated by ER contact sides and MFF, while peripheral fission events create small mitochondria that are designated for mitophagy [59].

Mitophagy is a mitochondrial quality control mechanism, that allows selective degradation of damaged mitochondria via autophagy [60, 61]. Mitophagy is most commonly activated either via the Pink1/Parkin-mediated pathway or the receptor mediated pathway [62]. For activation of mitophagy via Pink1/Parkin, initially Pink1 accumulates on the OMM and forms dimers that autophosphorylate each other and thereby activates itself. In a next step the activated Pink1 continues and phosphorylates ubiquitin and Parkin. Upon binding of phospho-ubiquitin to the phosphorylated Parkin it gets fully activated and promotes ubiquitination of OMM proteins that are involved in induction of mitophagy. Ubiquitin are again phosphorylated by the Pink1 dimers and thereby create a feedforward loop that ultimately induces mitophagy [63]. Alternatively, mitophagy can be receptor-mediated, for example via BCL2/adenovirus E1B 19-kDa-interacting protein 3-like (BNIP3L/NIX) [64, 65]. These receptors accumulate at the OMM and interact with members of the ATG8 family, like GABARAP or LC3 via a short-linear motive termed ATG8-interactig motive (AIM) or LC3-interacting region (LIR), both of which form a connection between mitochondria and autophagosome for degradation of the malfunctioning mitochondria [66].

1.3. Mitochondrial ultrastructure

When mitochondria were discovered, they were initially descried as small grain-like structures that appear to be aligned in a string-like fashion. This view changed drastically with the development of the electron microscopy (EM) by Ernst Ruska. Palade and colleagues were among the first ones to apply this new technique to investigate mitochondria with high resolution that was impossible to achieve with conventional light microscopy for the following decades. In the 1950s the fine mitochondrial ultrastructure was first resolved and described [67]. Although this was over 70 years ago it still holds true today. Mitochondria have two membranes. The outer mitochondrial membrane (OMM) itself is not very characteristic from a structural point of view. Whereas the inner mitochondrial membrane (IMM) is highly unique. It can be separated in two sub compartments. The membrane regions running in parallel to the OMM are referred to as the inner boundary membrane (IBM). Essential for any distinct ultrastructure are the cristae membranes (CM). This characteristic infolds into the mitochondrial matrix increase the surface area allowing dense packing of OXPHOS complexes and other proteins like ADT/ATP translocases (ANTs) from the SLC25

carrier family [68-70]. Overtime, several models for organization of the IMM were proposed [16]. The earliest being the “Baffle- model”, proposed by Palade in 1952 [67]. It describes crista as broad openings into the mitochondrial matrix. Another model was proposed by Fritiof Sjöstrand a few years later to Palade´s “Baffle-model”. Sjöstrand´s “Septa-model” suggested a separation of the mitochondrial matrix into compartments via entire membrane sheets that span perpendicular along the length of the mitochondrion [71]. The model that stood the test of time and was proven to be correct is the “Crista junction model”, developed by Daems and Wisse in 1966 [72]. This model names crista junctions (CJ) as pore-like structures, from which cristae membranes are formed. Several studies confirmed this model that is established today [73, 74]. CJs have a width of about 12 to 40 nm and act as a diffusion barrier for proteins and electrons [75].

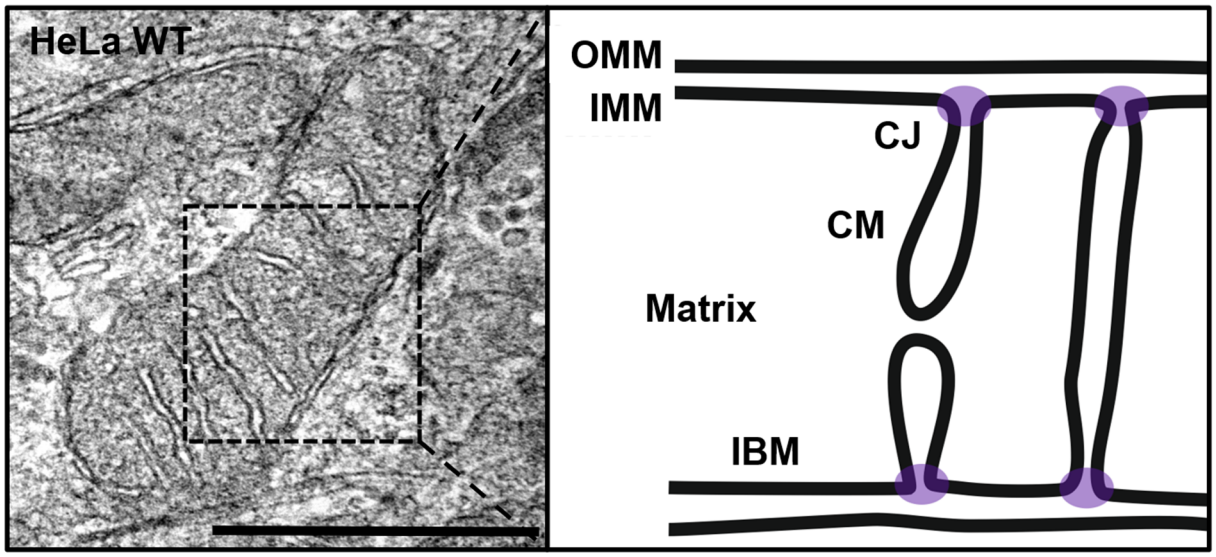

Figure 2. Detailed description of mitochondrial subcompartmentalization. Electron microscopy image of mitochondrial section in a HeLa WT cell, taken by Andrea Borchardt (Institute of biochemistry and molecular biology I of university clinic Düsseldorf) (left). Scale bar represent 500 nm. Schematic depiction of mitochondrial ultrastructure with outer mitochondrial membrane (OMM), inner mitochondrial membrane (IMM), divided into inner boundary membrane (IBM) and cristae membrane (CM), including crista junction (CJ) in blue and the mitochondrial matrix (right) [76].

1.4. Maintenance, expression and role of mitochondrial genome

Mitochondria have their own genome and not only encode a separate set of genes, but also have their own specialized gene replication and expression machinery.

It is organized in the mitochondrial nucleoids and mitochondrial RNA granules (MRGs) with their own mitochondrial ribosomes (**Figure 3**) [10, 77].

Mitochondrial nucleoids were already described in the 1960s by Nass and colleagues [78-81]. Over a decade later the mitochondrial genome was fist characterized in detail by Anderson in 1981. It was shown that the human mitochondrial genome is indeed quite small, as it only codes for 13 messenger RNAs (mRNA), 22 transfer-RNAs (tRNA) and two ribosomal RNAs (rRNA) with a total size of about 16.6 kb. The mitochondrial DNA (mtDNA) is organized in one light and only heavy chain, that also features a noncoding reading termed the displacement loop or D-loop, where the promotors of transcription are located [82]. It is stored in form of nucleoids together with some proteins of the mitochondrial transcription machinery such as transcription factor A, mitochondrial (TFAM). TFAM binds mtDNA and helps with their condensation. It was reported that the ratio of TFAM to mtDNA affects the nucleoid population and transcription activity. If the ratio is higher on the side of TFAM the nucleoids are more condensed, smaller in size and less transcribed. Low levels of TFAM result on larger and more actively transcribing nucleoids [83-87]. The replication and transcription of mtDNA is regulated by a variety of proteins. Some essential proteins are the mitochondrial DNA polymerase subunit gamma (POLG), the mtDNA helicase twinkle and the single stranded DNA binding protein 1 (mtSSB) [9, 88-93]. Upon analysis of isolated nucleoids, many proteins involved in mtDNA replication, repair, maintenance and expression were found. Interestingly mitofilin (today known as MIC60), that essential for formation of crista junctions was found as well [94]. Further studies revealed close proximity between mitochondrial nucleoids and the IMM, indicating possible interaction between both [95, 96]. Today CJs are speculated to be hubs of mitochondrial gene expression [97].

The mitochondrial genome features a distinctive arrangement, as the encoded mRNAs and rRNAs are flanked by tRNAs. This characteristic arrangement is known as the tRNA punctuation model [98]. After transcription, these tRNAs need to be cleaved of from the respective mRNAs. This process is regulated by several RNA processing enzymes. Especially, RNase-P and -Z play an important role in tRNA and mRNA maturation [99]. Mitochondrial RNA granules are the place for posttranscriptional processing and translation of mtDNA. MRG are found in close proximity to the transcribing nucleoids and are organized in a layered manner, with the

RNA at the centre with respective RNA binding proteins like the guanine-rich RNA sequence binding factor 1 (GRSF1) or Fas-activated serine/threonine kinase domains 2 (FASTKD2) [100]. MRGs are the places where the mitochondrial ribosomes are assembled and the mitochondrial genome is expressed. In yeast as well as in mammalian cells, the mitochondrial 55S ribosomes consists out of a large ribosomal subunit (39S) and a small ribosomal subunit (28S) [101, 102]. The formation of mitochondrial ribosomes is guided by several proteins for example FASTKD2 or Mitochondrial DEAD Box Protein 28 (DDX28) [103, 104].

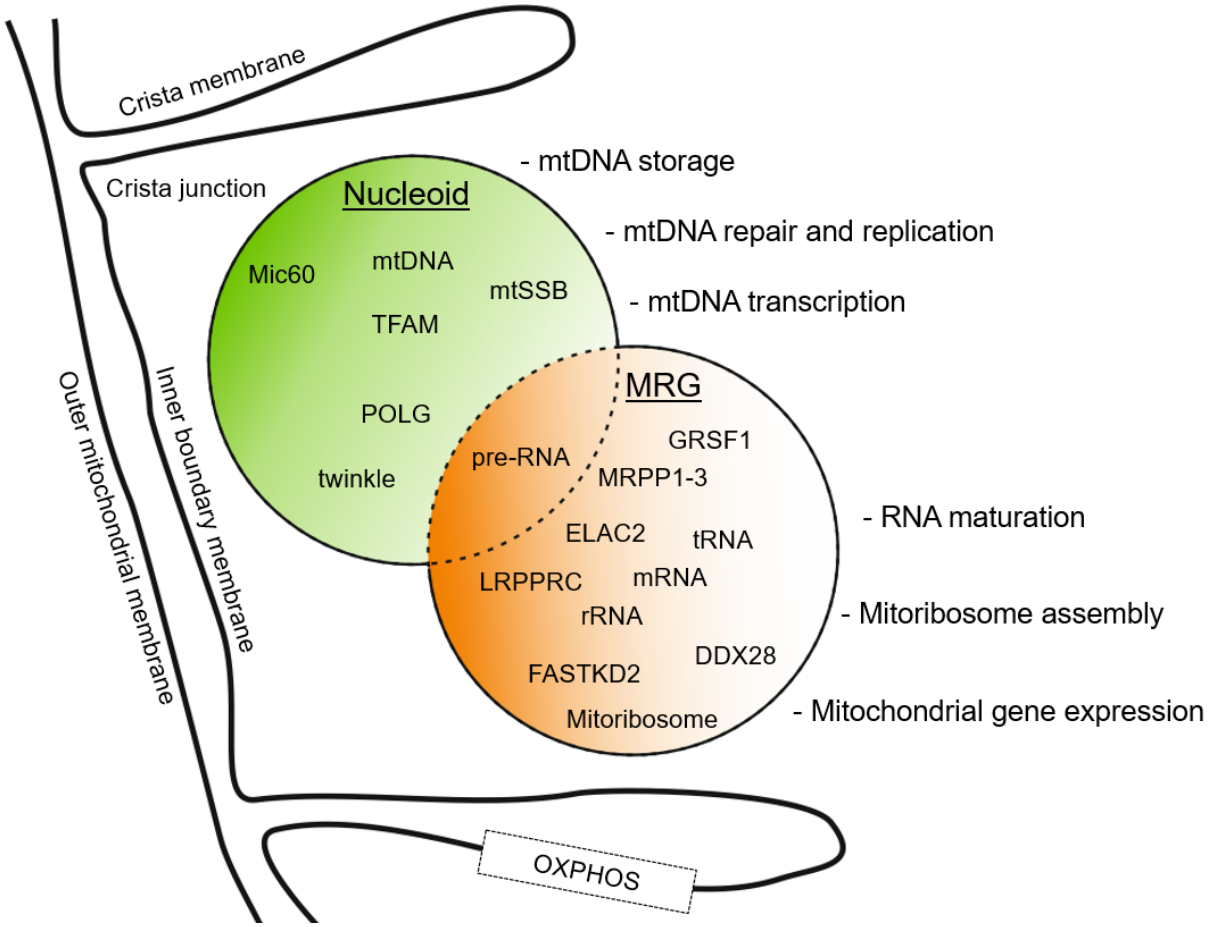

Figure 3. Mitochondrial gene replication and expression takes place at nucleoids and MRGs respectively. Mitochondrial nucleoids (green) replicate, transcribe and repair mtDNA, as they do not only contain it but additionally house the required proteins. MRGs (red) are the centres of post-transcriptional RNA processing and maturation, translation and mitochondrial ribosome formation. Actively transcribing nucleoids and MRGs often overlay each other to a certain degree, this overlay can vary between cell types and conditioning (indicated by dotted lines) [105].

Although the mitochondrial genome is very limited in size, defects in its maintenance or expression can cause severe problem for cells and organisms as they encode for proteins needed in the proper assembly and function of several OXPHOS

complexes. Alterations in mtDNA can have severe consequences as single point mutations can cause a drastic disease phenotype. Mitochondrial encephalomyopathy, lactic acidosis and stroke-like episodes (MELAS) is caused by the MT-TL1 m.3243A> G mutation [106]. This mutation is carried by about 80% of all MELAS patients [107]. As mitochondria are virtually present in all tissues in higher organisms, including humans, mitochondrial diseases have a multi systematic character with often overlapping symptoms. An example for this is a specific mutation on the *FASTKD2* gene (p.R205X and p.L255P) that has been reported to cause a MELAS-like syndrome, with a patient suffering from seizure, stroke-like episode and optic atrophy [108]. Similar to MELAS, Leigh- syndrome or subacute necrotizing encephalomyopathy is associated with mutations of the mitochondrial genome, causing a drastic reduction in mitochondrial function and energy production, especially in OXHOS [109]. But even when mtDNA is intact, Leigh- syndrome can occur due to issues in mitochondrial gene expression. Mutations in the RNA binding protein leucine-rich pentatricopeptide repeat containing (LRPPRC) of MRGs are associated with Leigh-syndrome and were shown to cause the French-Canadian type of Leigh-syndrome [110, 111]. Furthermore, Leigh-syndrome patients were shown to have mitochondria with aberrant crista structures [27].

1.5. Electron transport chain (ETC) and ATP production

Mitochondria are essential hubs for numerous metabolic pathways and reactions. One of their key functions is the production of the cellular energy currency Adenosine triphosphate (ATP) [112]. ATP is synthesized from adenosine diphosphate (ADP) and free phosphate (P) at the F_1F_O-ATP-synthase (Complex V/ CV). For efficient synthesis of ATP several coupled reactions take place in an array of protein complexes in the IMM. This array of protein complexes is called electron transport chain (ETC) and is essential for the generation of a proton gradient across the IMM, the mitochondrial membrane potential ($\Delta\Psi_m$) (**Figure 4**) [113]. The ETC requires the coenzymes nicotinamide adenine dinucleotide (NAD) and flavin adenine dinucleotide (FAD), that are produced in the tricarboxylic acid cycle (TCA cycle) and act as redox equivalents [114].

The ETC consist of four major protein complexes, NADH:ubiquinone oxidoreductase (Complex I/ CI), succinate dehydrogenase (SDH) (Complex II/ CII),

cytochrome *bc₁* oxidoreductase (Complex III/ CII) and cytochrome *c* oxidase (Complex IV/ CIV), together with two addition mobile electron carriers, that are able to bind electrons and transfer them from one complex to another, namely the membrane-embedded hydrophobic ubiquinone and the soluble cytochrome *c* [115]. In context of ATP synthesis this whole series of reactions including the phosphorylation of ADP to ATP is referred to as oxidative phosphorylation (OXPHOS). Except for Complex II, which is purely nuclear encoded, all other OXPHOS complexes are assembled from mitochondrial encoded proteins and nuclear encoded ones. Complex II stands out from the other ETC complexes, as it is not involved in direct proton pumping across the IMM. The proton pumping is performed by Complexes I, III, and IV. This continues pumping establishes a potential across the IMM with charge difference of about -180 to -200 mV [116].

Complex I is the largest OXPHOS complex and is composed of 14 core subunits and 31 supernumerary subunits. It can be structurally divided into the hydrophilic or matrix arm, where the oxidation of NADH to NAD^+ takes place and the membrane arm. The hydrophilic arm features the initial electron acceptor flavin mononucleotide and eight Fe-S clusters. Complex I has a total of seven mitochondrial encoded subunits, most of all OXPHOS complexes, that are all essential for formation of the membrane arm. Upon oxidization of NADH, Complex I pumps a total of four protons across the IMM into the intermembrane space and transfers two electrons to ubiquinone [117-119]. A common inhibitor of Complex I is the natural compound rotenone, it binds a specific rotenone-binding site and thereby inhibits the transfer of electrons to ubiquinone [120]. Complex II (SDH) only consist of four subunits, that are all nuclear encoded. It couples the oxidation of succinate to fumarate, while reducing ubiquinone to ubiquinol. For the initial reduction of succinate the two soluble units SDHA and SDHB are required as they contain covalently bond FAD that is required as an initial electron acceptor, followed by three Fe-S clusters [121]. Third in line is Complex III, it usually forms homodimers that support its function as it is transferring electrons from quinone to the soluble electron carrier cytochrome *c* via cytochrome *b*. In doing so Complex III pumps a total for four additional protons across the IMM [122]. The function of Complex III can be effectively inhibited by treatment with antimycin A, a compound isolated from *Streptomyces*, as it binds the cytochrome *bc₁* complex and thereby inhibits the transfer of electrons [123]. Complex IV is the last complex of the ETC. It consists of 13 subunits and accepts electrons from cytochrome *c*. These electrons are

used to reduce oxygen to water while pumping four further electrons (two for each water molecule) across the IMM into the IMS [124]. Assembly of individual ETC complexes is a stepwise process. The early assembly steps take place in the IBM while late of ETC complexes takes place in the cristae membrane, where the mature complexes are located [125, 126]. The complexes of the ETC are reported to form assemblies of higher-order or supercomplexes (SCs) [127]. SCs can feature different combinations of ETC complexes, usually in combinations of $CICIII_2CIV$, $CICIII_2$ and $CIII_2CIV$ and are assembled exclusively in the cristae membranes [128-131]. Supercomplex assembly is dependent on cardiolipin levels. This has been demonstrated as mammalian cells lacking both apolipoproteins of MICOS, MIC26 and MIC27, displayed alterations in cardiolipin levels and reduced OXPHOS complex assembly. As prove of principle OXPHOS assembly could be rescued by stable expression of cardiolipin synthase (CRLS1) into the cells lacking both apolipoproteins [132].

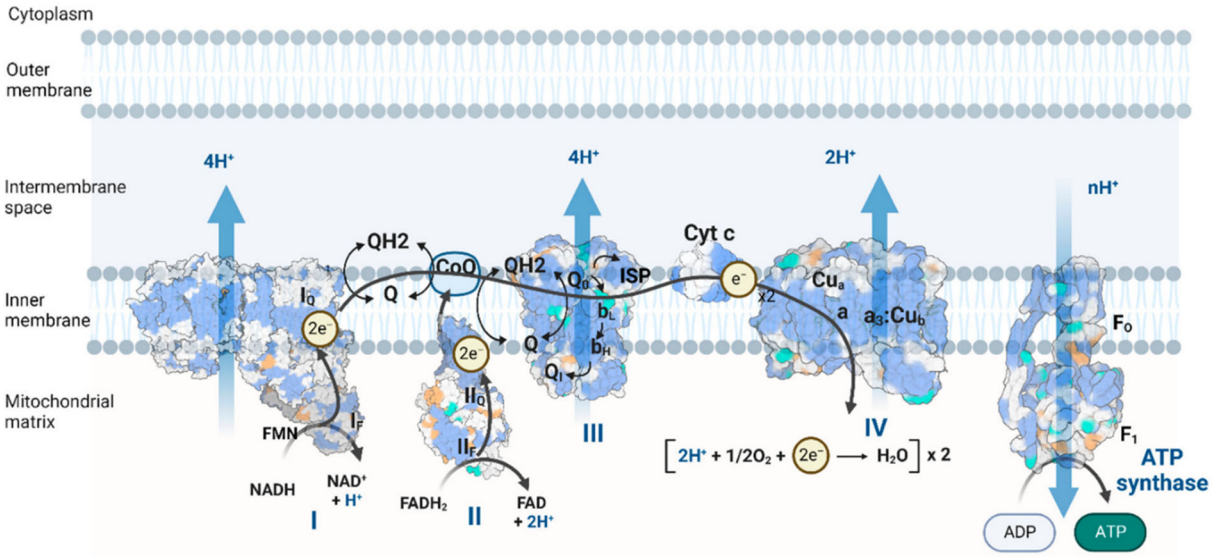

Figure 4. Overview of functions and localization of individual OXPHOS complexes. The electron transport chain (ETC) is located in the IMM and consist of four complexes (CI-CIV) that transport electrons, released from redox reactions from one complex to another while (except for CII) pumping protons across the IMM into the IMS generation a constant proton gradient, the mitochondrial membrane potential ($\Delta\Psi_m$). This is utilized by the ATP-synthase (CV) to generate ATP from ADP + P_i. ETC complexes can form assemblies of higher-order, termed supercomplexes after maturation in the cristae membranes, adapted from Tseng et al., 2022 [113].

The final steps of OXPHOS take place at Complex V and are dependent on the formation of a proton gradient across the IMM by the ETC [133]. In mitochondria F-type ATP synthases utilize the proton gradient, generated by the ETC, to

phosphorylate ADP and generate ATP [134]. The consist of two domains, the F_O and F_1 domain. The F_O domain is located at the membrane and is responsible for proton translocation and dimerization. ATP synthase dimers are especially found at cristae tips and rims of crista junctions, where they are crucial for induction of positive membrane curvature [15, 135]. ATP synthases were shown to be form higher oligomers in different species [136]. The soluble F_1 domain consist of three α- and β-subunits each that form the catalytic head that is required for synthesis of ATP. Both domains are connected by a central stalk and a peripheral stalk. The central stalk consists of several γ, δ and ε subunits and transmits a rotary movement of the c-ring to the F_1 domain. The rotation utilizes the established membrane potential and transports protons across the IMM back into the mitochondrial matrix during ATP production. The peripheral stalk stabilizes the F_1 domain by preventing rotation of the αβ subunits [137]. ATP synthases are often associated with production of ATP, but were lately also shown to be able to hydrolyse ATP in a reverse mode of action, to generate proton motive force under certain cellular stresses [138, 139]. Complex V can be specifically inhibited by oligomycin A, by blocking the proton channel of the F_O domain and thereby inhibit the production of ATP. Oligomycin A is naturally occurring compound, that can be isolated from *Streptomyces* [140].

1.6. MICOS (mitochondrial contact site and cristae organizing system)

MICOS is a hetero oligomeric protein complex that is known to consist of 7 known subunits, all termed “MIC” with the respective protein size in kDa [141]. Proteins of the MICOS complex are highly conserved among species [142-144]. As the name implies, MICOS is essential for formation of mitochondrial contact sites between OMM and IMM and establishing the formation of crista junctions [15, 145-147]. MICOS is key in forming the mitochondrial intermembrane space bridging complex (MIB) together with the sorting and assembly machinery (SAM) (**Figure 5**) [148, 149]. Recent studies also connected MICOS so play a vital role in further cellular processes like heme biosynthesis [150]. Loss or wrong assembly of MICOS was shown to drastically effect mitochondrial morphology and function, as crista junctions and thereby crista are lost while other mitochondrial functions like respiration are drastically reduced.

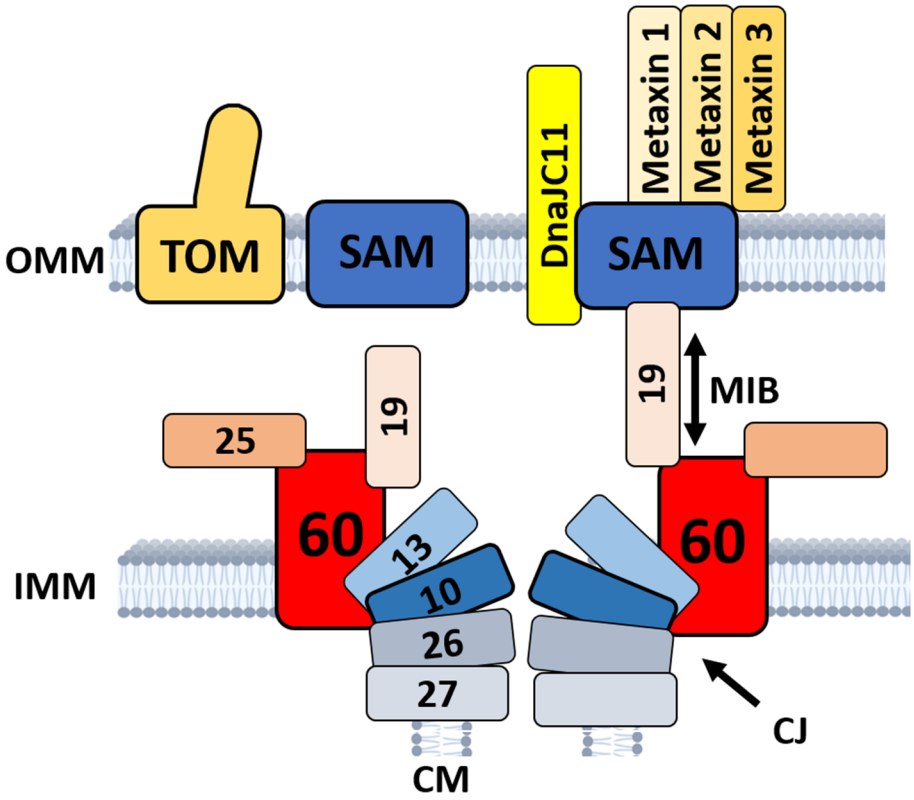

Figure 5. Scheme of MICOS localisation at the IMM and its interaction partners at the OMM. The MICOS complex and its seven proteins are located at the crista junction (CJ) and separate the inner mitochondrial membrane (IMM) from the cristae membrane (CM). The organization of the MICOS into its two subcomplexes and there for the genetic and functional classification is indicated by the colouring, MIC60 subcomplex toned in red, with MIC60 red and MIC19/25 in shades of orange, while MIC10 subcomplex toned in blue, with MIC10 and MIC13 in shades of blue and the two apolipoproteins MIC26 and MIC27 in shades of bluegray. The formation of the mitochondrial intermembrane space bridging (MIB) complex between MIC19 and SAM is indicated by a black arrow [11, 69, 148].

MICOS consists of two main subunits and migrates at a size of about 700 kDa in blue native gels [151]. The largest protein of the MICOS complex is MIC60. MIC60 was early on identified as a master regulator of cristae formation in mammals and yeast [15, 152]. Depletion of MIC60 caused drastic changes in cristae morphology as CJs are lost, resulting in an onion or stack like phenotype (depending on the cell line, either yeast or mammalian cells). In addition, overexpression of MIC60 was shown to cause extensive cristae branching in baker´s yeast [15]. MIC60 was shown to distribute evenly throughout mammalian mitochondria in a helical fashion [153]. It is discussed that MIC60 initially establishes the MICOS complex at the IMM, with the other proteins being added one after another. Addition of MIC60 could induce tube formation to giant unilamellar vesicles (GUVs) in *in vitro* experiments, proving its ability to reshape double membranes on its own [154]. The lipid-binding site of MIC60 consist of two alpha-

helices between the coild-coil (CHCH) domain and its mitofilin domain, that allow interactions with liposomes. Essential for a functional MIC60 is its C-terminal domain, as it is required for formation of CJs and important for interaction with SAM [155]. MIC60 is highly conserved among different species and often associated with lipid trafficking, e.g., in plants [156]. Further MIC60 interacts with mitochondrial nucleoids as co-immunoprecipitation of mitochondrial nucleoids featured MIC60 (Mitofilin) as one interaction partner [94]. Recent studies suggested CJs as hubs of active mtDNA transcription [97]. A proposed model of a balanced cristae architecture established by MIC60 at the cristae junctions and ATP-Synthase dimers along the rims and especially the tips of cristae was proposed upon finding of MIC60 as key player of CJ organization [15].

Within the MICOS complex the closest interaction partners of MIC60 are MIC19 and MIC25, with MIC25 being the homolog of MIC19 [26]. Together they form the MIC60 subcomplex and are not only essential for prime positions of MICOS at the IMM but especially for the establishment of the contact sites. In that regard MIC19 plays a crucial role for interaction with SAM50 to form the mitochondrial inner membrane bridging complex (MIB) together with metaxins 1 and 2 (**Figure 5**) [148, 157, 158]. Recent *in vivo* studies proposed a possible crystal structure of a complex between MIC60 and MIC19 and how these two proteins are able to span and establish a CJ. In this model MIC19 supports the tetramerization of MIC60 as the CHCH domain of MIC19 binds to the mitofilin domain of MIC60 via a conserved interface and thereby tightens the CJ [159].

Besides the MIC60/MIC19/MIC25 subcomplex another subcomplex with the remaining MICOS proteins is found. The MIC10/MIC13/MIC26/MIC27 subcomplex is essential for a fully stable and functional MICOS complex. Similar to the MIC60 subcomplex, the components of the MIC10 subcomplex have different functions in this model. MIC10 is the smallest protein of the MICOS-complex. Depletion of MIC10 is known to cause drastic destabilization of the mitochondrial ultrastructure, as CJs majorly are lost and the remaining cristae membranes form onion or stack-like shapes. MIC10 features an GXGXGXG motive that allows for formation of oligomers at the cristae junctions [160]. These oligomers stabilize the negative membrane curvature established with MIC60 in wild type conditions and can help to tighten the crista junction [161, 162]. Further these oligomers were shown to interact with dimeric F_1F_O-

ATP Synthase [163]. MIC13 was considered to bridge between the MIC60 and MIC10 subcomplex, as previous studies showed a drastic reduction in protein levels of other MIC10 subcomplex proteins and changes in cristae morphology [164]. It features conserved GxxxG and WN motifs that are essential for its function in cristae junction formation [151, 165]. MIC13 is the first protein that has been identified as a regulator of cristae dynamics, as HeLa cells depleted of MIC13 displayed a drastic reduction in observed cristae fission and fusion [166]. MIC26 and MIC27 belong to the family of apolipoproteins. They both take part in the regulation of cardiolipin levels in mitochondria with MIC27 being able to directly bind CL [167]. It was shown that both proteins regulate their expression in a reciprocal manner, as knockout of one results in higher protein levels of the other one. This effect might be the reason for a very mild change in cristae morphology upon loss of only one of these proteins. Studies featuring a combinational knockout of both apolipoproteins revealed a more drastic phenotype in HAP1 cells, comparable to loss of core subunits like MIC10 or MIC60 [132].

Overall destabilization or loss of MICOS as a whole has drastic effects on cristae morphology and their dynamic behaviour. Cell culture experiments allow maintenance of MICOS deficient cell lines, lacking single or multiple subunits [132, 166]. This drastically changes once we step into animal studies as whole-body knockouts of MIC60 for example are embryonic lethal an can often only be achieved in single tissues [168]. A specific mutation (c.895A>G (p. Lys299Glu)) of the *IMMT* gene was recently shown to cause developmental encephalopathy and bilateral optic neuropathy [169]. Mitochondria from patients, suffering from this mutation, displayed drastic changes in crista ultra-structure including swollen and onion-like crista [169]. Furthermore, mutations of MIC60 and altered levels of MICOS proteins were found in Parkinson's disease patients [170]. Mitochondrial hepato-encephalopathy was shown to be caused by a deficiency of MIC13 and being accompanied by tissue specific alterations in mitochondrial morphology, reduction in respiration and changes in metabolism that cause impaired liver function and acute liver failure, while being associated with impaired heart development and function, such as sudden cardiac death or ventricular arrhythmias in other mammals. [151, 171-175]. Recently, MIC26 received more clinical attention, as X-linked mutations were shown to cause lactic acidosis combined with neurological problems and muscle weakness [176]. A specific mutation in the APOO/MIC26 gene (NM_024122.5): c.532G>T (p.E178*) results in a nonsense mutation. It causes a depletion of about 20 amino acids at the C-terminal region,

resulting in progeria-like phenotypes and impaired development causing death within 12 to 18 months [177]. As some MICOS proteins are either directly or indirectly interacting with lipids, especially MIC27 that directly interact with cardiolipin, it is noteworthy that certain mitochondrial diseases are related to problems in lipid thesis and mutations in involved genes. Barth-syndrome is caused by mutations in the *tafazin* gene, that is crucial for maturation of cardiolipin [178]. These mutations and lack of mature cardiolipin lead to aberrant crista morphology and reduced efficiency of the organelle itself [179, 180]. MICOS related diseases are gaining greater attention in the field of mitochondrial diseases but are often associated with other causes [11, 70, 181].

MICOS interacts with SAM to form the MIB complex (**Figure 5**) [142]. SAM is located at the OMM and is one of several mitochondrial protein complexes involved in protein import and assembly. These import complexes are found in the OMM and in the IMM. Similar to SAM, the translocase of the outer mitochondrial membrane (TOM) is also located at the OMM and has a counter part in the IMM, the translocase of the inner membrane (TIM). Especially for TIM23 a dynamic localization between IBM and CM was described [182]. This complex import machinery is required as the small mitochondrial genome, requires import of the vast majority of the mitochondrial proteome. Only 13 mRNAs are encoded on the mtDNA, whereas the rest of the 1136 mitochondrial proteins in humans are trafficked from cytosol (according to MitoCarta3.0) [183]. Nuclear encoded mitochondrial proteins feature a mitochondrial targeting sequence (MTS) which is essential to ensure the proteins correct destination. The translocase of the outer mitochondrial membrane (TOM) is one of two large protein complexes found at the OMM and forms supercomplexes with SAM cross the OMM [184]. The TOM complex consists of two major subunits with Tom70, Tom22 and Tom20 being the cytosolic facing part and Tom40 acting as the pore forming component [185-188]. Also located in the OMM is the SAM. The main function of the SAM protein complex is the insertion of β-barrel proteins into the OMM [189].

Once nuclear-encoded proteins cross the OMM and reach the IMS, they can take different transport routes across the IMM. The proteins can either translocate via the mitochondrial intermembrane space import and assembly (MIA), or via one of the two TIM complexes [190, 191]. Beta barrel proteins are inserted into the OMM by Sam50 and while carrier proteins designated for the IMM are inserted by Tim22, as Tim22 is able to insert no cleavable multi spanning precursor proteins into the

membrane. This separation and insertion of carrier proteins and beta barrel proteins is mediated by small TIM chaperones Tim9 and Tim10 at the IMS [192-195]. In case of protein presequences, they are transported across the IMM by Tim23, Tim50 and the mitochondrial chaperon mtHsp70 at the mitochondrial matrix, that binds the newly imported polypeptides and acts as the motor for protein import and ensures their correct folding to prevent malfunction, aggregation or degradation of the protein precursors [196, 197].

1.7. Super resolution nanoscopy and cristae membrane dynamics

The ongoing pursuit for higher resolution has been a driving force of innovation of imaging devices, resulting in new microscope systems with extremely powerful lasers, fast cameras and sensitive doctors. The addition of a confocal pinhole to LSMs allowed a dramatic increase in image quality. The confocal pinhole blocked scattered light emitted from the illuminated sample as only light from the confocal plane could reach the microscopes detector or camera respectively. Further innovations in light amplification by stimulation of radiation (LASER) technology, cameras and detectors improved LSM more and more. However, according to Ernst Abbe´s law of the diffraction limit of light, resolution obtained through light is limited. According to his formula the highest possible resolution is about 250 to 300 nm as it takes the numerical aperture of the used objective and wave length of used light into account.

For decades Abbe´s law was not broken, but in the 2010s this law was more than just challenged by pioneers in the field of physics and optics. One of the first techniques to overcome this barrier was Airyscan microscopy. In addition to conventional confocal imaging, where the confocal pinhole usually is kept as small as possible to reduce scattered light, Airyscan utilized a fully open pinhole. With this open pinhole more emitted light reaches the detector. But more light does not directly translate to a higher resolution as with more light more noise is produced, overall lowering the signal to noise ratio. Airyscan bypassed this issue, as the signal does not hit a common camera or detector but a whole honeycomb shaped array of detectors. Airyscan utilizes a 32-channel gallium arsenide phosphide photomultiplier tube (GaAsP-PMT) area detector in which each channel functions as an individual pinhole. Combined with post imaging processing, based on robust deconvolution reconstruction and pixel rearrangement strategies, Airyscan allows imaging at resolutions of about

140 nm in x and y [198]. Another techniques that overcomes the diffraction limit of light is structured illumination microscopy (SIM) [199]. For this technique a grid with a defined space grid pattern is imaged in front of the sample in several angles causing an interference that can be calculated and applied for image processing to enhance resolution. As imaging itself and post imaging processing are time consuming this method offers a decent increase in resolution with the trade for frame rate. Latest improvements and development of enhanced speed structured illumination microscopy (Fast-SIM) was able to resolve individual crista and their dynamic behaviour [200].

Airyscan and SIM overcame Abbe´s of optical resolution. Ongoing developments in the field of super resolution imaging techniques redefined this law once again. Two independently developed methods pushed resolution even further STED and PALM/STORM [201-203]. Both, based on confocal LSMs, they drastically differ in use and fundamental construction. Both techniques require a very different set of fluorophores. For PALM/STORM special blinking fluorophores are required. As these fluorophores are never all active at the same time, they cannot be excited at the same time. Taking a single image of a cell of organelle stained with these fluorophores will show a very scattered pattern of single dots. The advantage though is that each dot represents one fluorophore whereas scanning a sample with a LASER excited not only one fluorophore but also the ones surrounding it. PALM/STORM takes advantage of the single fluorophores, requiring hundreds or thousands of pictures of the same specimen to be taken, though. In later image processing steps an overlay of these images is created, reconstructing the desired specimen. Image quality can be further improved by statistically calculating the centre of each and every fluorophore which is ultimately taken into account for the final image. Once all these measures are considered into the final image, it is possible to obtain a resolution as low as 20 nm [203]. Although this resolution is revolutionary in the field of imaging, the method comes with several drawbacks. Sample preparation is complicated, reconstruction is time consuming and it is impossible to perform this method on living cells, as the samples have to be fixed.

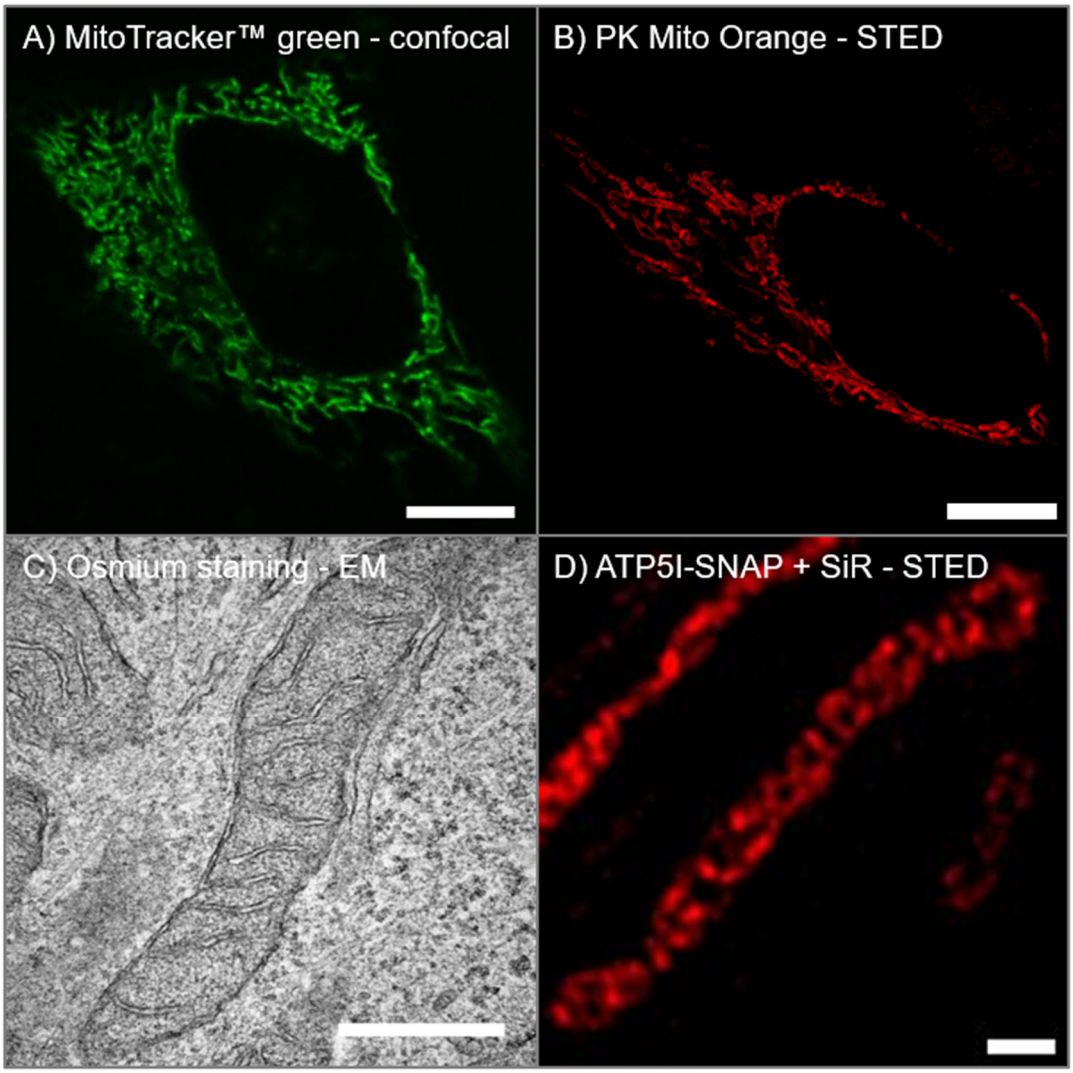

Figure 6. Comparison of different mitochondrial imaging techniques. Today a vast variety of imaging techniques are established for mitochondrial imaging. Each technique of choice has its own applications and advantages. All images display mitochondria of HeLa WT cells. A) an overview image of a MitoTracker™ green staining imaged with a confocal microscope. B) an overview image of a cell stained with PK Mito Orange utilizing a microscope equipped with a STED module, that allows super resolution imaging and resolving individual crista. C) an EM image of a mitochondrial section stained with osmium (again by Andrea Borchardt) and D) a mitochondrion of a cell that transiently expresses an ATP5I-Snap Tag and was stained with silicone rhodamine (SiR). The last image was taken with a microscope equipped with a STED module in a live cell imaging setup and shows individual crista with a resolution of about 60 nm. Scale bar in A) and B) represents 10 µm and 500nm in C) and D).

Stimulated emission depletion microscopy (STED) takes a different approach to overcome the diffraction barrier of light described in Abbe´s law as well as the sample preparation. In contrast to many conventional LSMs, STED utilizes two LASERs. The first one, the excitation LASER, is a conventional LASER with the respective wave length to excite the used fluorophore. Interestingly, the second LASER which is called

as depletion LASER, a very power full LASER where its beam is reshaped by a phase plate within the beam path into a doughnut like shape [202]. The two LASERs need to be aligned in a way that the intensity maximum of the excitation LASER is right in the centre, or at the intensity minimum of the depletion LASER. An alignment like this increases the resolution in XY drastically as the depletion LASER depletes the fluorescence signal in the surroundings of the excited fluorophore. Resolution in Z can be improved, too, if a second LASER doughnut is projected perpendicular on the specimen. This method is called 3D STED and can help to increase resolution. STED microscope often utilize hybrid detectors, these detectors combine the working principles of photon multiplier tubes (PMT) and avalanche detectors and can detect individual photons. STED microscopy requires fluorophores that are very photo stable and can withstand the high energy transmitted by the depletion LASER. STED can be used for conventional fixed antibody staining as well as for live cell imaging. For later one STED capable dyes for a direct labelling approach can be used or expression systems for tags like Halo- or SNAP- [204, 205]. In live cell imaging with STED resolutions of 50 to 60 nm can be achieved. This is not high enough to look into cristae junctions, but is allows detections cristae and tracking of their movement (**Figure 6**) [70, 166, 206].

Although STED is already a very advanced imaging technique, Dr. Stefan Hell and colleagues were able to push the limits of resolution further. The development of MINSTED and later MINFLUX allows light-based imaging with a resolution in the range of few nm, by localizing fluorescently labelled molecules with very high precision, which results a smaller demand for photons [207, 208]. MINFLUX was able to resolve MICOS proteins with a special resolution of 5 nm [209]. Other techniques like 4Pi STORM, that use a combination of two objectives, are able to resolve single molecules in the sub-10 nm range in a three-dimensional manner [210].

Today many dyes are known that can help to track basic information about mitochondrial calcium levels, ROS formation, or membrane potential that do not require a genetic manipulation of the respective cells of interest. There is no need for a transient or stable overexpression as many dyes are cell permeable and can be observed via fluorescence microscopy, plate reader or fluorescence activated cell sorting (FACS) [211]. Other dyes offer a high resistance against photobleaching allowing their usage even in microscopy system like STED that use high laser powers

[212]. These dyes might play a crucial role in reduction of genetically induced artefacts and observation of cellular processes in a more natural environment.

1.8. Cristae membrane remodelling

The earliest high-resolution representations of mitochondria were generated using EM [67]. These images were suitable to characterize the basic ultra-structure for mitochondria. Several decades later the first three dimensional high-resolution images were generated using electron tomography (ET). Using this technique, the existence of crista junctions was shown to be pore- or slit- like structures to act as a diffusion barrier for proteins, metabolites and electrons [75, 213]. Although EM and ET allow imaging of biological samples with high resolution, the necessary fixation of the samples is a limitation of these methods. As the majority of data about cristae morphology originated from these techniques, cristae were considered to be static entities for long. This paradigm has been challenged and changed in recent years. In the past several experiments gave hints to an altered IMM structure under specific conditions. One of the earliest experiments by Hackenbrock and colleagues investigated the effects of ADP addition to isolated mitochondria from rat liver samples. He found that addition of ADP caused a matrix swelling in the mitochondria and thereby changes in the IMM structure [214]. About 40 years later these observations were confirmed using ET [73]. Other instances for alterations of the IMM can be observed during apoptosis. Upon induction of apoptosis, EM images indicated a cytochrome *c* release from the crista into the IMS through the widening of CJs [215]. Yet, these studies did not change the dogma of static crista. They provided an insight into alterations in crista morphology and crista junction formation, yet as the presented results and findings originated from static imaging techniques like EM or ET they contributed to the static notion of crista.

As previously discussed, innovative developments in the field of light microscopy led to a revolution in resolution of imaging techniques that could be applied to broad variety of biological samples, including mitochondria. These new techniques allowed live cell imaging with high resolution and precision. Expression of fluorescent tags followed by a staining with highly photostable dyes was proven to be a very successful approach for the imaging of mitochondrial crista [166, 216]. It was not only shown that crista are highly dynamic but also that they undergo continuous cycles of

membrane fusion and fission in the time scale of seconds. Furthermore, MICOS was established as a key player in cristae remodelling [166]. Various types of crista fission and fusion were described in detail. In general, these events can be dived into remodelling events that are dependent or independent of CJ movement. In the case of CJ-independent remodelling it was observed that crista undergo fission around the middle of a matrix spanning cristae to form two separate crista or fusion as the tips of two opposing crista reach each other. Upon movement of CJs, it has been observed, that crista form the letters “X” or “Y”. An X-type fission or fusion event represent loss or generation of a connection between two matrix spanning crista in close proximity to each other, while a Y-type event describes fusion or fission at the tip of one cristae that does not span the matrix entirely to (or from respectively) a cristae that stretches the matrix entirely (**Figure 7**) [11, 69, 70, 166, 206].

These studies were ground breaking as they did not only prove the overall dynamics of crista but elegantly showcased cristae membrane fission and fusion events. Further is could be shown that individual cristae undergo full fission and fusion events including mixing of both cristae membranes respectively and content mixing utilizing polyethylene glycol (PEG)-based cellular fusion assays [166]. Other studies used Airyscan in combination with tetramethylrhodamine ethyl ester perchlorate (TMRE) to stain the membrane potential of individual crista live and showcasing altering potentials between them and the exchange of high and low potentials. These observations challenge the long lasting cable theory, by which the membrane potential is uniform across one mitochondrion and demonstrate that crista can be view as individual biogenetic units functioning independently from one another [217]. Besides MICOS other molecular players like OPA1 or Yme1L have been brought up to influence cristae dynamics [218]. Furthermore, the distinct role of calcium regulation and transport was associated with changes in crista junction morphology and cristae dynamics. Loss of MICU1 has been reported to alter CJ morphology in a similar way as loss of OPA1 does. It forms the mitochondrial Ca^{2+} uniporter complex together with MCU, EMRE and anchors it to the IBM [219]. Furthermore, intracellular release of Ca^{2+} was shown to reduce IMM remodelling. The close spatial proximity of the mitochondrial Ca^{2+} uniporter complex and the fact that its assembly effects CJ morphology hinds to a regulatory role of the mitochondrial Ca^{2+} homeostasis via the CJs in cristae remodelling [220, 221]. Yet many open questions about the regulation, metabolic requirements and overall purpose of cristae remodelling remain unanswered.

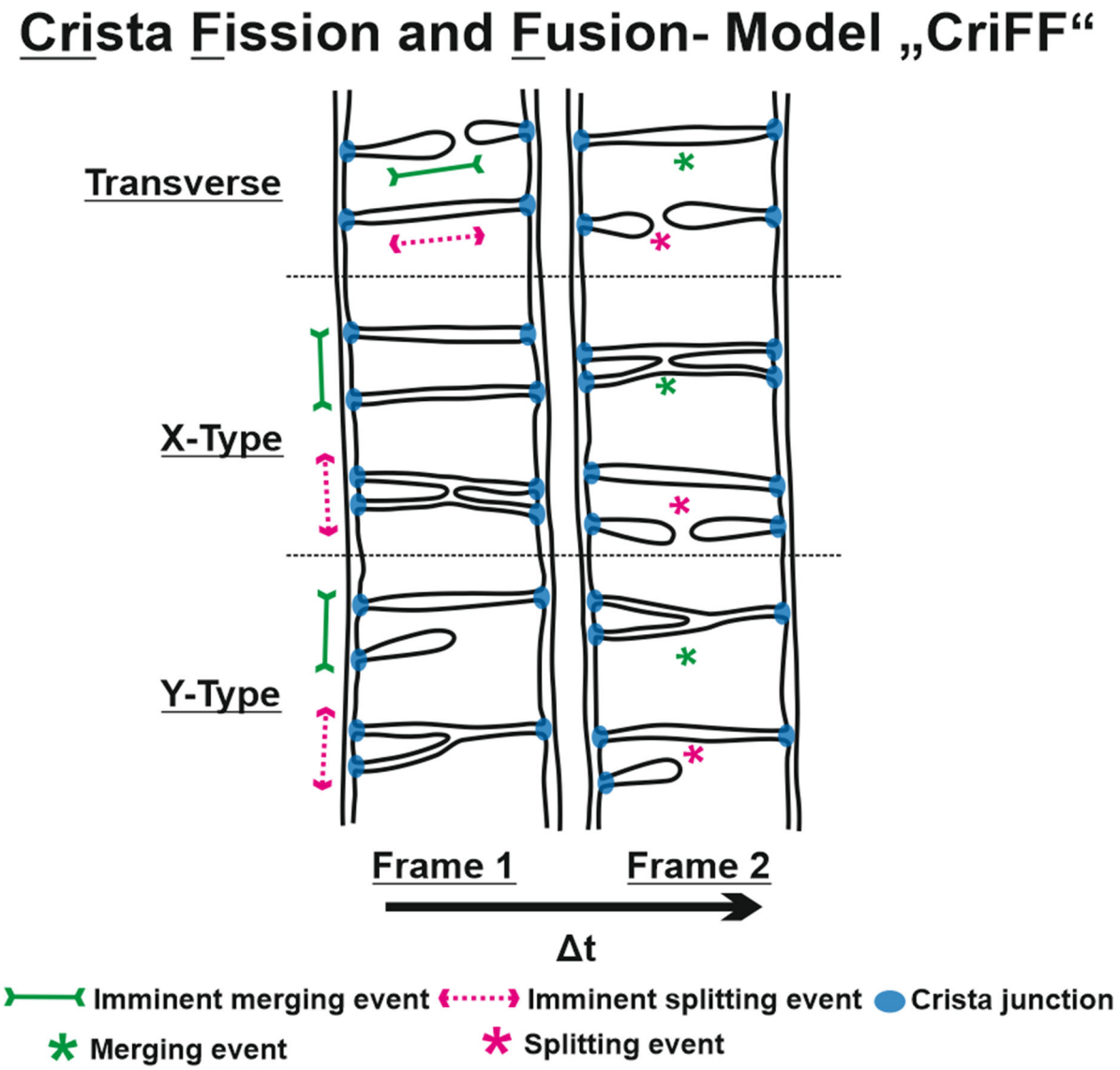

Figure 7. Overview of different types of merging and splitting events according to CriFF model. Different types of cristae merging and splitting events were observed and described using live cell STED super-resolution nanoscopy. IMM merging or splitting can occur with or without movement of the crista junctions (CJ, indicated in blue). If the CJ do not move, the most common form of merging and splitting are transverse evets, where crista merge or split as they cross the mitochondrial matrix. Upon movement of the CJs X- and Y- shaped crista formations and respective merging and splitting events were observed, too. The scheme indicates an imminent merging event by a green arrow facing inwards with a green asterisk in the next frame indicating the respective merging event, likewise a red dotted arrow facing outwards indicates an imminent splitting event that is marked by a red asterisk in the next frame [11, 70, 166].

1.9. Relevance of SLC25 carries for mitochondrial function and morphology

The IMM is highly enriched in membrane proteins and protein complexes. Many of which belong to OXPHOS but another large group of proteins is involved in

exchange of amino acids, nucleotides, cofactors, inorganic ions, protons, fatty acids and di- or tri-carboxylates across IMM and OMM belonging to the SLC25 carrier family [222]. Some members of the SLC25 carrier family are not only involved in regulatory processes inside the mitochondrial but can be involved in processes outside the mitochondrion, too. An example is SLC25A46 as it is found in the OMM and plays a role in mitochondrial dynamics by establishing ER-mitochondria contact sites and import of lipids, required for membrane biogenesis. In the case of this carrier it was also shown, that SLC25A46 deficiency causes an aberrant crista morphology and hyperfused mitochondria [223]. Recently the adenine nucleotide translocators (ANTs) or ADP/ATP translocases have been closely linked to crista morphology and dynamics. ANTs are found as four isoforms named ANT1-4 and are the most abundant proteins in the IMM, making up for about ten percent of IMM protein content [224-226]. For the exchange of ADP and ATP the ANTs switch between two states, the membrane opened state (m-state) and the intermembrane space opened state (c-state), bringing ATP into the IMS and ADP into the matrix. By undergoing a conformational change during this process, positive charges at the substrate binding site of the carrier are exposed and attract the cargo for transport. The constant domains of the carrier remain in their position, while an opening or closing of the matrix gate or cytoplasmic gate (cytoplasmic gate open during c-state and matrix gate open during m-state) takes place.

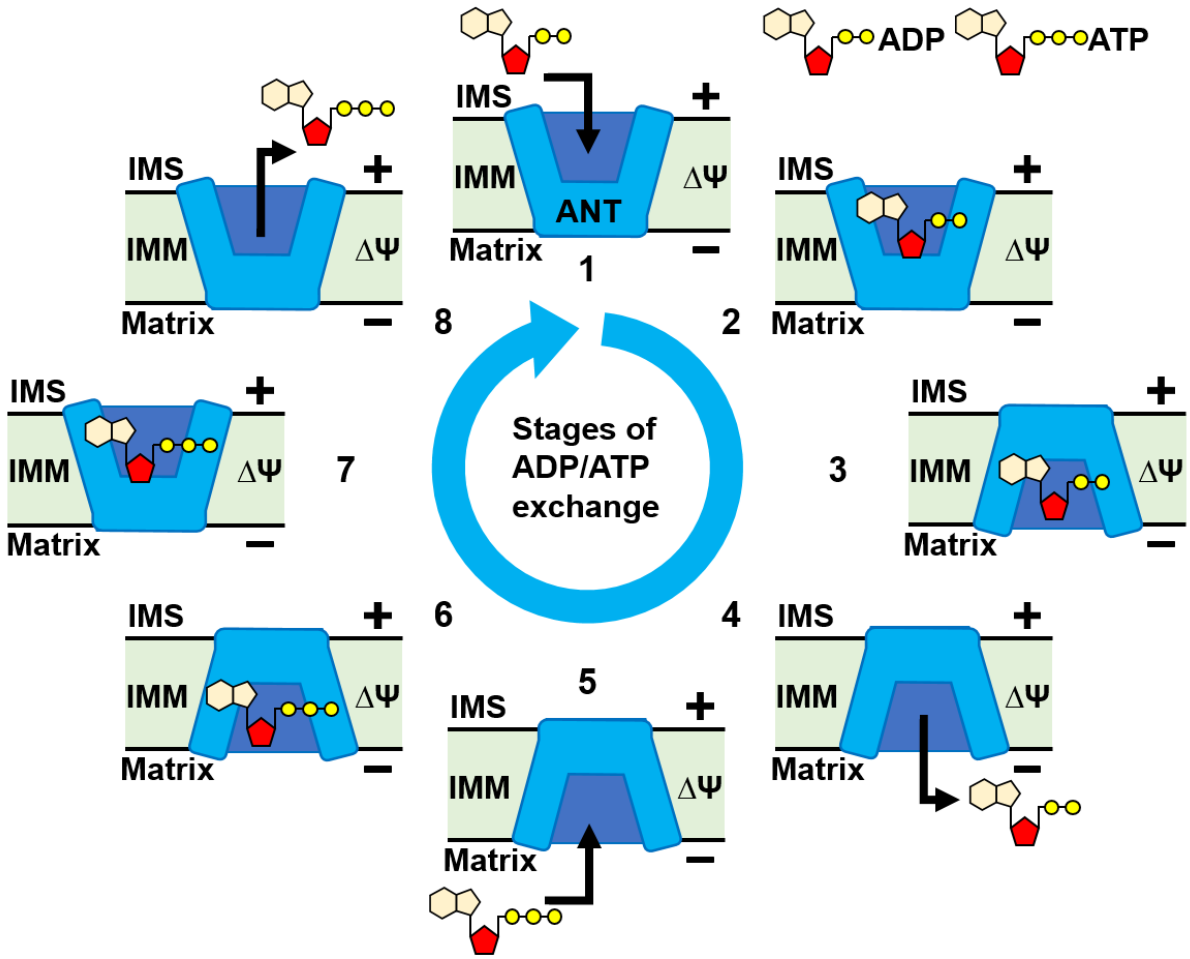

Figure 8. Different stages of ADP/ATP exchange. Adenine nucleotide translocases (ANT) are highly abundant in the inner mitochondrial membrane (IMM). The four known isoforms of ANTs work in a similar manner and undergo different stages to transport ADP into the mitochondrial matrix and ATP into the intermembrane space (IMS). Stage 1: empty c-state; Stage 2: ADP-bound c-state, Stage 3: ADP bound m-state, Stage 4: ADP leaving m-state, Stage 5: empty m-state, Stage 6: ATP-bound m-state, Stage 7: ATP-bound c-state, Stage 8: ATP leaving c-state [227, 228].

Starting with an ATP leaving c-state, the carrier is open to the IMS allowing ATP to leave the carrier creating an empty c-state with three free positive charges at the centre of the carrier. In this state an ADP molecule can bind (ADP bound c-state) before the charge difference from ATP to ADP indices the conformational change to the ADP bound m-state. Once the carrier has opened up towards the matrix, ADP is released into the less proton dense mitochondrial matrix (ADP leaving m-state). As the carrier reaches the empty m-state, one ATP molecule can bind to the free positive charge of the carrier (ATP-bound m-state) to induce again a conformational change to the ATP-bound c-state before release of the ATP molecule into the intermembrane space, allowing the cycle to start once again [68, 229]. ANTs can be trapped in either the m-state of the c-state, by treating cells with certain compounds like bongkrekic acid

(BKA) for blockade in the m-state or carboxyatractyloside (CATR) for the c-state, respectively [227, 230, 231]. In case of BKA the ANTs are not able to transition between m- and c-state any more as BKA occupies the substrate binding sites of the transporter and is kept in place due to formation of several hydrogen bonds, salt bridges and van der Waals interactions [229]. Although the mechanism of action of ANT inhibition with BKA was studied in detail the question how such an inhibition of ANTs effects the dynamic behaviour of the IMM remained unanswered. Within the scope of this thesis, this question was addressed. Using state of the art super-resolution techniques we provide evidence that blockade of ANTs with BKA does not only drastically reduces the mitochondrial membrane potential ($\Delta\Psi_m$) but in addition causes dramatic aberrancies in crista morphology and reduced frequencies of crista merging and splitting events [206].

As members of the SLC25 carrier family are found in the IMM in high abundancies and are involved in many essential mitochondrial functions, they are also found to be affected in several severe diseases including Parkinson´s disease, optic atrophy, myopathies, cardiomyopathies and reduced metabolic capacities [232-235]. ANTs are found to cause several diseases where deficiencies of ANT1 causes autosomal dominant progressive external ophthalmoplegia with mitochondrial DNA deletions 2 (AdPEO2) and mitochondrial DNA depletion syndrome (MTDPS) 12A and B (cardiomyopathic type) [38, 236, 237]. These diseases are characterized by reduced respiration and OXPHOS capacity, deletions in mtDNA and reduced mtDNA copy number, resulting in cardiomyopathy and myopathy [228, 238-240].

2. Aims of the doctoral thesis

In the last years, live-cell super-resolution imaging techniques allowed observation of intraorganellar membrane dynamics. Although the fluorescent labelling of organelles had shown that mitochondria form a highly dynamic network in mammalian cells with numerous contact sites to other organelles, the IMM was considered a static entity. Early hints for a dynamic reshaping of the IMM were known, but it was not until recent years that the first live-cell images with suitable resolution off the IMM were published. Furthermore, an organized remodelling of the IMM was proposed as several types of membrane fission and fusion events. It was concluded that the rapid rate of fission and fusion occur on a time scale of seconds.

These discoveries can be summarized in the proposed cristae fission and fusion or CriFF model (**Figure 7**). The CriFF model did not only characterize different types of IMM fission and fusion but in doing so established the mitochondrial contact side and cristae organizing system (MICOS) a key element of IMM remodelling, too. Without full assembly of the MICOS complex the number crista junctions (CJs) and membrane remodelling events are drastically reduced. In summary, it is known that IMM remodelling occurs in a MICOS-dependent manner in the time scale of seconds. Further questions about this process remain unanswered at the beginning of this doctoral thesis. This study aims to elucidate the role of MICOS-depended cristae remodelling by addressing the following objectives:

1. Finding out which metabolic and bioenergetic requirements are necessary to maintain the high IMM remodelling rates in mammalian mitochondria. Especially determine the effects of altering mitochondrial ATP levels and $\Delta\Psi_m$ by inhibition of OXHOPS and depletion of $\Delta\Psi_m$ with classical mitochondrial toxins.

2. Decipher the role of ADP/ATP exchange on IMM remodelling, by locking the adenine nucleotide translocases (ANTs) in the matrix-opened state (m-state) with bongkrekic acid (BKA).

3. Determining the role of MICOS in OXPHOS complex assembly and membrane remodelling.

The results of the studies are presented in form of three peer reviewed and published manuscripts (3.1., 3.2. and 3.3.) followed by the discussion that highlights the relevance of the results in the context of cristae dynamics.

3. Results

3.1. Cristae dynamics is modulated in bioenergetically compromised mitochondria

Research Article

TRANSPARENT PROCESS OPEN ACCESS Life Science Alliance

Cristae dynamics is modulated in bioenergetically compromised mitochondria

Mathias Golombek[1], Thanos Tsigaras[1], Yulia Schaumkessel[1], Sebastian Hänsch[2], Stefanie Weidtkamp-Peters[2], Ruchika Anand[1], Andreas S Reichert[1], Arun Kumar Kondadi[1]

Cristae membranes have been recently shown to undergo intramitochondrial merging and splitting events. Yet, the metabolic and bioenergetic factors regulating them are unclear. Here, we investigated whether and how cristae morphology and dynamics are dependent on oxidative phosphorylation (OXPHOS) complexes, the mitochondrial membrane potential ($\Delta\Psi_m$), and the ADP/ATP nucleotide translocator. Advanced live-cell STED nanoscopy combined with in-depth quantification were employed to analyse cristae morphology and dynamics after treatment of mammalian cells with rotenone, antimycin A, oligomycin A, and CCCP. This led to formation of enlarged mitochondria along with reduced cristae density but did not impair cristae dynamics. CCCP treatment leading to $\Delta\Psi_m$ abrogation even enhanced cristae dynamics showing its $\Delta\Psi_m$-independent nature. Inhibition of OXPHOS complexes was accompanied by reduced ATP levels but did not affect cristae dynamics. However, inhibition of ADP/ATP exchange led to aberrant cristae morphology and impaired cristae dynamics in a mitochondrial subset. In sum, we provide quantitative data of cristae membrane remodelling under different conditions supporting an important interplay between OXPHOS, metabolite exchange, and cristae membrane dynamics.

DOI 10.26508/lsa.202302386 | Received 20 September 2023 | Revised 3 November 2023 | Accepted 6 November 2023 | Published online 13 November 2023

Introduction

Mitochondria are highly dynamic organelles playing vital roles in various cellular functions involving energy conversion, calcium buffering, iron–sulfur cluster biogenesis, immune responses, apoptosis, and various metabolic reactions. Mitochondria consist of a smooth outer membrane (OM) and a heterogenous inner membrane (IM). Furthermore, the IM is spatially divided into the inner boundary membrane (IBM) and cristae membrane (CM). IBM runs parallel to the OM, whereas CM invaginates towards the mitochondrial matrix. Crista junctions (CJs) are located at the interface between IBM and CM. CJs are slot- or pore-like structures typically having a diameter in the range of 25 nm (Frey & Mannella, 2000) which separates the intracristal space and intermembrane space adjacent to the IBM. CJs act as a diffusion barrier for proteins (Gilkerson et al, 2003; Vogel et al, 2006; Wurm & Jakobs, 2006; Davies et al, 2011). In addition, CJs are proposed to play a role in the metabolite diffusion such as ATP, Ca^{2+}, cytochrome *c* (Frey et al, 2002; Mannella et al, 2013). In fact, it has been shown that CJs establish electrochemical boundaries that allow differential membrane potential between the cristae and IBM (Wolf et al, 2019). In addition, individual cristae within a mitochondrion possess disparate membrane potentials demonstrating their functional independency. CJ formation was shown to depend on the high-molecular weight "Mitochondrial Contact Site and Cristae Organizing System" (MICOS) complex consisting of at least seven proteins located at CJs (Rabl et al, 2009; Harner et al, 2011; Hoppins et al, 2011; von der Malsburg et al, 2011). A uniform nomenclature of MICOS subunits was established subsequently (Pfanner et al, 2014). MIC10, MIC13, MIC19, MIC25, MIC26, MIC27, and MIC60 constitute the proteins of the MICOS complex. The loss of CJs is observed upon depletion of most MICOS proteins leading to separation of IBM and CM (Harner et al, 2011; Hoppins et al, 2011; von der Malsburg et al, 2011; Stephan et al, 2020). MIC13 bridges the two subcomplexes: MIC60/19/25 and MIC10/26/27 (Guarani et al, 2015; Anand et al, 2016) via conserved WN and GxxxG MIC13 motifs (Urbach et al, 2021). Some subunits of the MICOS complex are evolutionarily conserved and have an endosymbiotic origin in α-proteobacteria (Munoz-Gomez et al, 2015; Eramo et al, 2020; Munoz-Gomez et al, 2023). The MICOS complex proteins are involved in mitochondrial protein import (von der Malsburg et al, 2011), lipid trafficking (Michaud et al, 2016), bending, and remodeling the membranes (Hessenberger et al, 2017; Tarasenko et al, 2017) in addition to their role in the formation of CJs. Mutations of MICOS subunits have been associated with Parkinson's disease, mitochondrial encephalopathy with liver disease and bilateral optic neuropathy, myopathy, and lactic acidosis (Guarani et al, 2016; Tsai et al, 2018; Beninca et al, 2021; Marco-Hernández et al, 2022). Apart from the MICOS complex, F_1F_O ATP synthase and OPA1 (Optic Atrophy Type I) play important roles in cristae remodelling as interplay of

[1]Institute of Biochemistry and Molecular Biology I, Medical Faculty and University Hospital Düsseldorf, Heinrich-Heine-University Düsseldorf, Düsseldorf, Germany
[2]Center for Advanced Imaging, Faculty of Mathematics and Natural Sciences, Heinrich Heine University Düsseldorf, Düsseldorf, Germany

Correspondence: reichert@hhu.de; kondadi@hhu.de

these complexes and cardiolipin is required for formation and maintenance of cristae and CJs (Kondadi et al, 2019, 2020b; Anand et al, 2021).

Cristae exist in various shapes and sizes depending on the cells, tissues, and bioenergetic requirements (Zick et al, 2009). Moreover, alterations in cristae structure have been associated with neurodegeneration, diabetes, obesity, cardiomyopathy, and myopathies (Zick et al, 2009; Eramo et al, 2020). For several decades, a static view of cristae prevailed based on the early existing electron microscopy (EM) data despite several indications of cristae remodeling. Cells undergoing apoptosis showed a massive reorganization of the mitochondrial IM where it reorganized and interconnected within a short span of few minutes (Scorrano et al, 2002). EM and electron tomography (ET) revealed that when isolated mitochondria were exposed to ADP, the IM confirmation changed to a highly interconnected network accompanied by matrix condensation termed State III respiration (Hackenbrock, 1966; Mannella et al, 1994; Perkins et al, 1997). Reduction in ADP levels resulted in a drastic decrease of the interconnected cristae network accompanied by matrix expansion or state IV respiration. The application of SR techniques to resolve mitochondrial membranes has conclusively shown that cristae membranes are highly dynamic (Huang et al, 2018; Wang et al, 2019; Kondadi et al, 2020a; Kondadi et al, 2020b; Liu et al, 2022). Recently, we showed using live-cell–stimulated emission depletion (STED) super-resolution (SR) nanoscopy that cristae membranes are dynamic and undergo continuous cycles of membrane remodeling dependent on the MICOS complex (Kondadi et al, 2020a). The cristae merging and splitting events are balanced, reversible, and depend on the presence of the MICOS subunit MIC13. Fluctuation of membrane potential within individual cristae and photoactivation experiments at cristae-resolving resolution support the notion that cristae can exist transiently as isolated vesicles which are able to fuse and split with other cristae or the IBM (Kondadi et al, 2020a). It was recently shown that OPA1 and YME1L also affect cristae dynamics (Hu et al, 2020). However, it is unclear which metabolic factors are required to ensure cristae membrane dynamics, a process likely to consume considerably amounts of energy, for example, from ATP hydrolysis.

We asked for the bioenergetic parameters which modulate the rates of cristae merging and splitting events: whether ATP levels or the mitochondrial membrane potential ($\Delta\Psi_m$) influence cristae membrane dynamics and to which extent. In this endeavor, we performed advanced live-cell STED SR nanoscopy on mitochondria after inhibition of the electron transport chain (ETC) or the F_1F_O ATP synthase using classical oxidative phosphorylation (OXPHOS) inhibitors. Furthermore, we used an OXPHOS uncoupler dissipating the $\Delta\Psi_m$. Consistent with earlier studies using EM, we observed ~50% mitochondria to be enlarged, which showed decreased cristae density when compared with mitochondria which were not enlarged. We could further dissect and show that enlarged mitochondria in particular showed a moderate nonsignificant trend of increased cristae membrane dynamics. We conclude that the rate of cristae membrane dynamics is not negatively affected by inhibiting OXPHOS including dissipation of the $\Delta\Psi_m$, reducing mitochondrial ATP levels but is rather moderately enhanced in enlarged mitochondria with reduced cristae density. Thus, cristae dynamic events are ongoing despite reduced cristae density. This would be consistent with the view that cristae dynamics is either limited by structural constraints such as densely packed cristae or that reduction in cristae density is followed by an increased cristae fusion and fission rate as kind of a compensatory mechanism. Furthermore, inhibition of adenine nucleotide translocator (ANT) by applying bongkrekic acid (BKA) to HeLa cells led to aberrant cristae morphology. Contrary to our observations using other OXPHOS inhibitors, we observed a clear reduction in cristae membrane dynamics in a subset of mitochondria, namely those showing aberrant cristae morphology. Overall, our results indicate that cristae membrane dynamics is linked to the bioenergetic state of mitochondria and point to a prominent role of the ADP/ATP metabolite exchange in this process.

Results

Cristae membrane dynamics is not impaired in mammalian cells treated with OXPHOS inhibitors

Recent application of novel SR techniques has revealed MICOS-dependent intramitochondrial cristae membrane dynamics in living cells (Kondadi et al, 2020a). However, the bioenergetic requirements which define such highly dynamic membrane remodeling processes are unknown. Cristae membrane remodeling has been used to describe cristae dynamic events (i.e., cristae merging and splitting) and overall changes in cristae morphology within a single mitochondrion in this article. Here, we used live-cell STED SR nanoscopy and determined dynamic alterations in cristae structure upon inhibition of ETC complexes, the F_1F_O ATP synthase or the $\Delta\Psi_m$. For this, we treated HeLa cells with the following classical drugs: rotenone, antimycin A, oligomycin A inhibiting Complex I, Complex III, Complex V (F_1F_O ATP synthase), respectively, and CCCP, a protonophore dissipating the $\Delta\Psi_m$. We refer to these drugs collectively as mitochondrial toxins throughout the article. We performed respirometry experiments using HeLa cells to validate the function of various mitochondrial toxins we used while imaging (Fig S1). Using respirometry experiments, the basal, maximal respiratory, and spare respiratory capacities were similar to another set of standard mitochondrial toxins commercially available confirming that the mitochondrial toxins we used are functioning as expected (Fig S1A and B). Previously, we employed ATP5I-SNAP, marking F_1F_O ATP synthase, to visualize cristae using live-cell STED SR nanoscopy in living cells (Kondadi et al, 2020a). Therefore, HeLa cells expressing ATP5I-SNAP were treated with silicon–rhodamine (SiR) dye, which binds covalently to the SNAP-tag, followed by addition of mitochondrial toxins. SiR is suitable for SR imaging owing to its photostability and minimal fluorophore bleaching (Lukinavicius et al, 2013). We decided to follow cristae structure and cristae dynamics at very early time points, within 30 min, after addition of the respective toxins because of the following reasons: (1) to determine the immediate effect of acute bioenergetic alterations induced by different mitochondrial toxins on cristae remodeling; (2) to minimize secondary effects occurring later such as mitochondrial fragmentation which imposes methodological limitations for subsequent analyses; and (3) cells do not develop any obvious signs of cell death or undergo apoptosis for at least 1 h after the

addition of these mitochondrial toxins according to earlier reports (Minamikawa et al, 1999; Duvezin-Caubet et al, 2006). The concentrations of mitochondrial toxins used in this article are broadly in the range used for real-time respirometry measurements where oxygen consumption has been shown to either increase or decrease depending on the mode of action of mitochondrial toxins used (Kondadi et al, 2020a; Stephan et al, 2020).

Using live-cell STED SR imaging, we followed cristae dynamics of cells treated with or without various mitochondrial toxins (Fig 1A). We achieved an image acquisition time of 0.94 s/frame which is improved compared with 1.2–2.5 s/frame achieved earlier (Kondadi et al, 2020a) using this technique. In all cases, we observed that cristae showed robust dynamic events at a timescale of seconds independent of the presence of any mitochondrial toxin (Figs 1A and S2 and Video 1, Video 2, Video 3, Video 4, and Video 5). Within the time span of each movie, we observed that cristae dynamics constantly revealed the formation and reshaping of X- and Y-like structures observed in our previous study (Kondadi et al, 2020a). There was no apparent difference in the way cristae appeared or remodeled between the different toxins. Yet to analyze this in more detail and to test whether we missed subtle changes, we performed a blind quantification of cristae merging and splitting events within individual mitochondria. In our previous study, we obtained a spatial resolution of 50–60 nm using live-cell STED nanoscopy (Kondadi et al, 2020a) meaning that cristae with a distance more than 60 nm between them can be distinguished. We found that treatment of cells with mitochondrial toxins did not lead to any significant changes in the frequency of merging or splitting events (simplified depiction shown in Fig 1B) in mitochondria (Fig 1C). We conclude that inhibition of mitochondrial OXPHOS complexes by these toxins does not impair cristae dynamics or cause an imbalance of merging and splitting events.

Cristae structure is altered in a subset of mammalian cells treated with mitochondrial toxins

To further analyze whether alterations in cristae dynamics is eventually linked only to a subset of mitochondria, we performed a detailed characterization of cristae architecture upon treatment with various toxins. We noted that the treatments of HeLa cells with various mitochondrial toxins led to the formation of mitochondria with increased width in a fraction of cells (Fig 2A, bottom panel), whereas another fraction did not show a change in mitochondrial width (Fig 2A, top panel) and resembled control cells. We categorized the percentage of mitochondria possessing corresponding mitochondrial widths under each condition (Fig 2B–F). Frequency distribution curves revealed that control cells displayed a Gaussian-like distribution of mitochondrial width with the highest percentage of mitochondria present in 400–500 nm range, whereas a maximum mitochondrial width of 600 nm was observed (Fig 2B). On the contrary, treatment of cells with mitochondrial toxins led to substantially increased mitochondrial width (Fig 2A, bottom panel and Fig 2C–F) as shown by a shift towards the right in percentage mitochondria. We found that irrespective of the toxin used, around 50% of the mitochondria (maximum two mitochondria considered per cell) were enlarged (width ≥ 650 nm), and that no mitochondria under control conditions had an average width larger than or equal to 650 nm (Fig 2B–F). Hence, mitochondrial dysfunction induced by rotenone, antimycin A, oligomycin A, and CCCP uniformly led to enlarged mitochondria within 30 min. Based on these results, we used 650 nm mitochondrial width as the cut-off for defining mitochondria as "enlarged" (from here on) as this excluded all the mitochondria from the control group (referred to as "normal" mitochondria here on). We next quantified cristae structure-related parameters for all mitochondria including distributing them into subsets of normal and enlarged mitochondria. We characterized the cristae number per μm^2 of mitochondrial area defined as cristae density, average distance between cristae in a mitochondrion defined as intercristae distance and the percentage area occupied by cristae within a mitochondrion. We did not find major differences in different cristae parameters described above when we compared the entire population of mitochondria in cells treated with or without various mitochondrial toxins (Figs 2G and S3A and C). Still, we observed an apparent trend indicating that cristae density is negatively correlated with mitochondrial width when mitochondrial toxins were applied (Fig S3E–I). Control HeLa cells exhibited a median cristae density of around 7 cristae/μm^2 which was similar to cells treated with mitochondrial toxins (Fig 2G). When we distributed the mitochondria as having normal or enlarged width, we found that mitochondria with normal mitochondrial width showed similar cristae density compared with untreated mitochondria (Fig 2H). Enlarged mitochondria exposed to mitochondrial toxins had a median cristae density of 4 cristae/μm^2 compared with 7 cristae/μm^2 in control cells. Only mitochondria showing enlarged width showed a statistically significant decrease of the cristae density for all toxins when compared with control mitochondria (Fig 2H). Thus, these results indicate that reduced cristae density is an effect of mitochondrial enlargement upon application of mitochondrial toxins. These findings are well recapitulated by the observed increased trend in the average intercristae distance which is altered again for enlarged mitochondria (Fig S3A and B). We next checked whether applying mitochondrial toxins led to a change in the percentage cristae area occupied per mitochondrion. We observed that the percentage cristae area per mitochondrion was unchanged upon addition of mitochondrial toxins within the time window of imaging (Fig S3C) which was independent of the mitochondrial width (Fig S3D). Taken together, STED SR nanoscopy revealed that bioenergetically compromised mammalian cells within a short time span result in structural changes where ~50% of mitochondria are characterized by decreased cristae density, increased average distances between adjacent cristae with no gross changes in the relative cristae area occupied by mitochondria. These observations are reflected in the negative correlation of cristae density and mitochondrial width (Fig S3E–I). We next aimed to check ultrastructural changes under these conditions using EM. Consistent with results obtained using STED nanoscopy (Figs 2A–F and S3), electron micrographs revealed enlarged mitochondria and increased distance between the cristae (shown using white arrows) upon treatment of HeLa cells with all mitochondrial toxins (Fig 2I). Increased distances between the cristae contributed to a visible decrease in the cristae density compared with control mitochondria which was in line with previous observations that

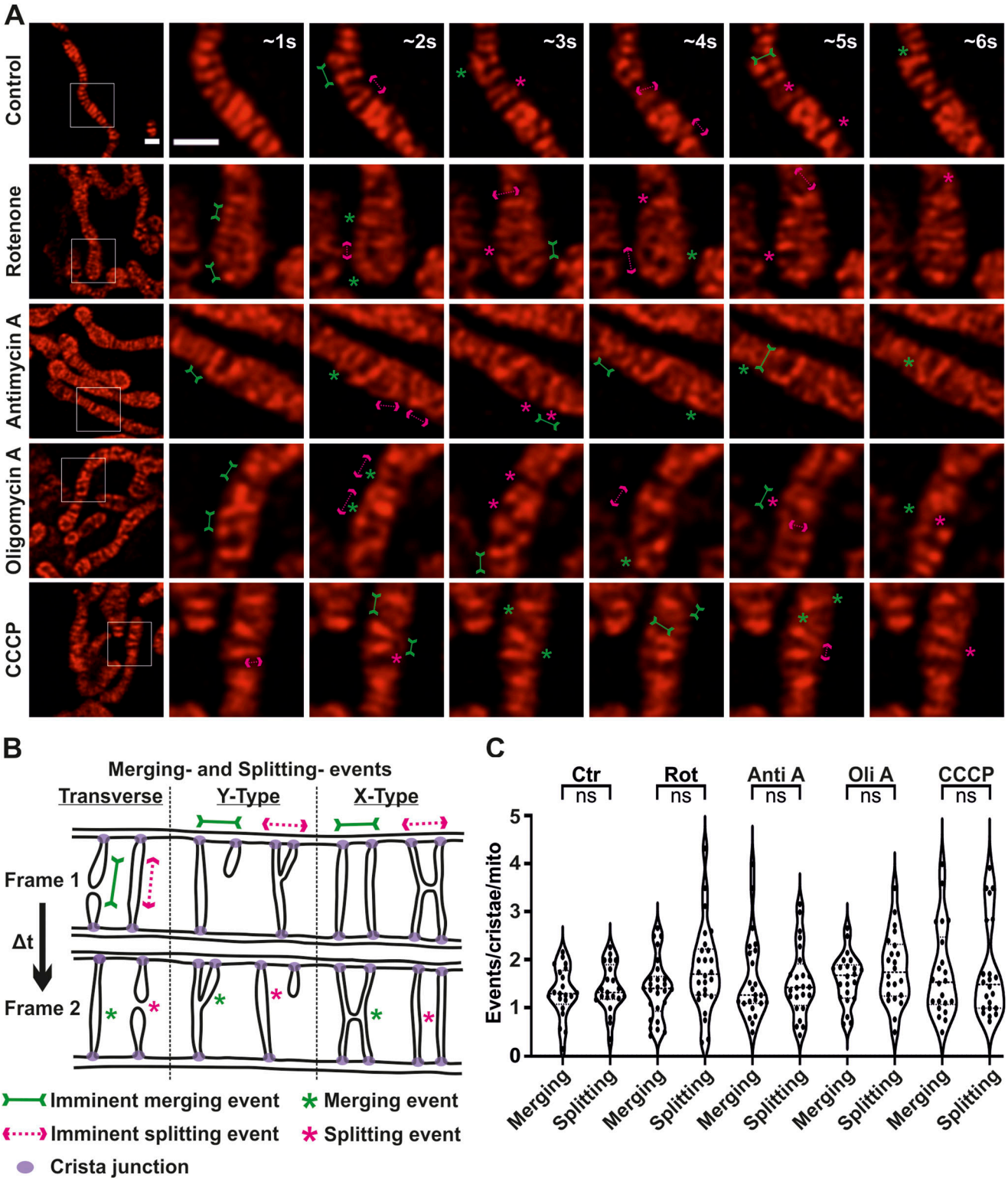

Figure 1. Crista merging and splitting events occur in a balanced manner upon inhibition of OXPHOS complexes and ΔΨm dissipation.
(A) Representative live-cell STED SR images of HeLa cells, expressing ATP5I-SNAP and stained with silicon–rhodamine, untreated or treated with rotenone, antimycin A, oligomycin A, and CCCP. Images at the extreme left show whole mitochondria along with white inset boxes. Other images on the right-side display time-lapse series (0.94 s/frame) of zoom of mitochondrial portion in the white inset at ~1, 2, 3, 4, 5, and 6 s. Green and magenta asterisks show corresponding merging and splitting events, whereas solid green arrows pointing inward and dotted magenta arrows pointing outward show imminent merging and splitting events, respectively. Scale bar represents 500 nm. **(B)** A scheme illustrating cristae merging and splitting events is shown. **(A, C)** Blind quantification of cristae merging and splitting events per mitochondrion in

cells treated with different mitochondrial toxins resulted in enlarged mitochondria accompanied by decreased cristae density (Gottlieb et al, 2003; Hytti et al, 2019). Overall, using a combination of STED SR nanoscopy and EM, we show that treatment of HeLa cells with various mitochondrial toxins, which disrupt the ETC function and $\Delta\Psi_m$, resulted in enlarged mitochondria accompanied by increased intercristae distance and reduced cristae density.

Cristae membrane dynamics is unchanged in enlarged mitochondria treated with various mitochondrial toxins

Given the structural alterations in a subset of mitochondria and the finding that cristae dynamics is overall robustly occurring in bioenergetically compromised mitochondria (Fig 1), we wondered whether cristae dynamics is specifically altered in mitochondria that have been structurally altered and the overall effect was masked. Upon treatment with mitochondrial toxins, in enlarged mitochondria, the frequencies of merging and splitting events remained balanced and we observed X- and Y-like structures appearing and disappearing at a timescale of seconds (Figs 3A and S4A–C and Video 6, Video 7, Video 8, and Video 9). Overall, when we revisited normal and enlarged mitochondria separately, we observed an apparent, yet no significant increase in the frequency of both merging and splitting events in enlarged mitochondria after cells were treated with antimycin A and oligomycin A but not in normal mitochondria after the same treatments (Fig 3A–E). However, in enlarged mitochondria, a significant increase of splitting events was observed after rotenone treatment and of merging and splitting events when the $\Delta\Psi_m$ was dissipated by CCCP (Fig 3C and E). Also, we rule out that cristae membrane dynamics is reduced upon inhibition of OXPHOS in the subset of enlarged mitochondria. In contrast, cristae membrane dynamics is moderately increased after dissipating the $\Delta\Psi_m$. Although all the imaging experiments involving mitochondrial toxins were performed within 30 min, we were interested to understand what happens to cristae morphology when they are treated with respective mitochondrial toxins for longer periods of time. We performed STED SR imaging of mitochondria to visualize the cristae around 4 h after treatment with mitochondrial toxins and found that, in general, there was clear mitochondrial fragmentation. Cristae were clearly interconnected in swollen mitochondria. Thus, imaging mitochondria after longer exposure to mitochondrial toxins is not optimal for studying cristae dynamics which was severely stunted (Fig S5).

To check how the mitochondrial ATP levels were influenced by various mitochondrial toxins and whether there was a correlation between cristae membrane dynamics and ATP levels, we checked the mitochondrial ATP levels after the respective treatments within the time span of 30 min similar to STED nanoscopy. For determining mitochondrial ATP levels, we took advantage of the mitGO-Ateam2 probe (Nakano et al, 2011). mitGO-ATeam2 is a ratiometric intramolecular FRET probe which binds ATP to bring the GFP, acting as FRET donor, close to orange fluorescent protein, the FRET acceptor, leading to an increased acceptor emission. Hence, reduction of ATP levels leads to decrease in the ratio of emission maximum at 580 nm (orange fluorescent protein)/520 (GFP) nm. mitGO-ATeam2 and mitoAT1.03 probes have been used to study spatiotemporal modulations of mitochondrial ATP levels (Imamura et al, 2009; Nakano et al, 2011). Pseudocolor ratiometric rainbow LUT images clearly showed that emission of 580/520 nm significantly decreased in mitochondria of cells treated with rotenone, antimycin A, and oligomycin A when compared with control HeLa cells (Fig 4A, bottommost panel). Accordingly, quantification of the ratio of emission maximum at 580/520 nm showed that all cells treated with rotenone, antimycin A, and oligomycin A displayed a significant reduction of ATP levels (Fig 4B). Surprisingly, treatment of HeLa cells with CCCP did not show any change in the ATP levels within the short time span of 30 min. Furthermore, we checked whether the reduction of ATP levels was affected by mitochondrial width. For this, we compared the ATP levels of cellular population treated with OXPHOS inhibitors. Cells were binned as having either normal or enlarged mitochondria. However, we did not find any differences in ATP levels of cells which predominantly contained either normal or enlarged mitochondria (Fig 4C). This suggests that the observed reduction in mitochondrial ATP levels in cells treated with mitochondrial toxins precedes formation of enlarged mitochondria. Overall, we conclude that unaltered cristae dynamics in enlarged mitochondria is not because of delayed or inefficient action of mitochondrial toxins demonstrating that cristae dynamics is robustly maintained at reduced ATP levels.

Next, we addressed how $\Delta\Psi_m$ is influenced after applying the respective mitochondrial toxins in the time window which was used for STED SR nanoscopy and ratiometric FRET-based ATP level detection. Antimycin A and CCCP strongly decreased $\Delta\Psi_m$ (Fig S6A). Accordingly, detailed quantification revealed a significant decrease of $\Delta\Psi_m$ when cells were treated either with antimycin A or CCCP when compared with untreated mitochondria (Fig S6B). There was a modest but significant decrease of $\Delta\Psi_m$ with rotenone treatment, whereas cells treated with oligomycin showed no change in the $\Delta\Psi_m$. When we put the rate of cristae dynamics (Fig 3) in the context of $\Delta\Psi_m$ measurements (Fig S6), we find that there was no reduction in the rate of cristae merging and splitting events in enlarged mitochondria upon introduction of rotenone, antimycin A, and CCCP compared with control mitochondria despite a significant decrease of $\Delta\Psi_m$. On the contrary, cells treated with F_1F_O ATP synthase inhibitor, oligomycin A, exhibited no significant change in the number of merging and splitting events compared with control mitochondria and did not show a decrease of $\Delta\Psi_m$ despite a significant reduction in ATP levels. Overall, we conclude that the merging and splitting events occur in enlarged mitochondria independent of $\Delta\Psi_m$. Thus, cristae dynamics appears to operate independent of the $\Delta\Psi_m$ and is maintained even at reduced ATP levels. Furthermore, we also checked if there is any correlation between OPA1 forms and cristae dynamics. It is well known that, at steady state, the long

different conditions as described in (A). Pooled data from three individual experiments with 21–26 mitochondria are shown as violin plots with individual data points. Each symbol represents one mitochondrion. (ns = nonsignificant *P*-value > 0.05). To increase the number of cells considered for quantification, a maximum of two mitochondria were randomly considered from a single cell, throughout the article, where STED nanoscopy was performed. One-way ANOVA was used for statistical analysis.

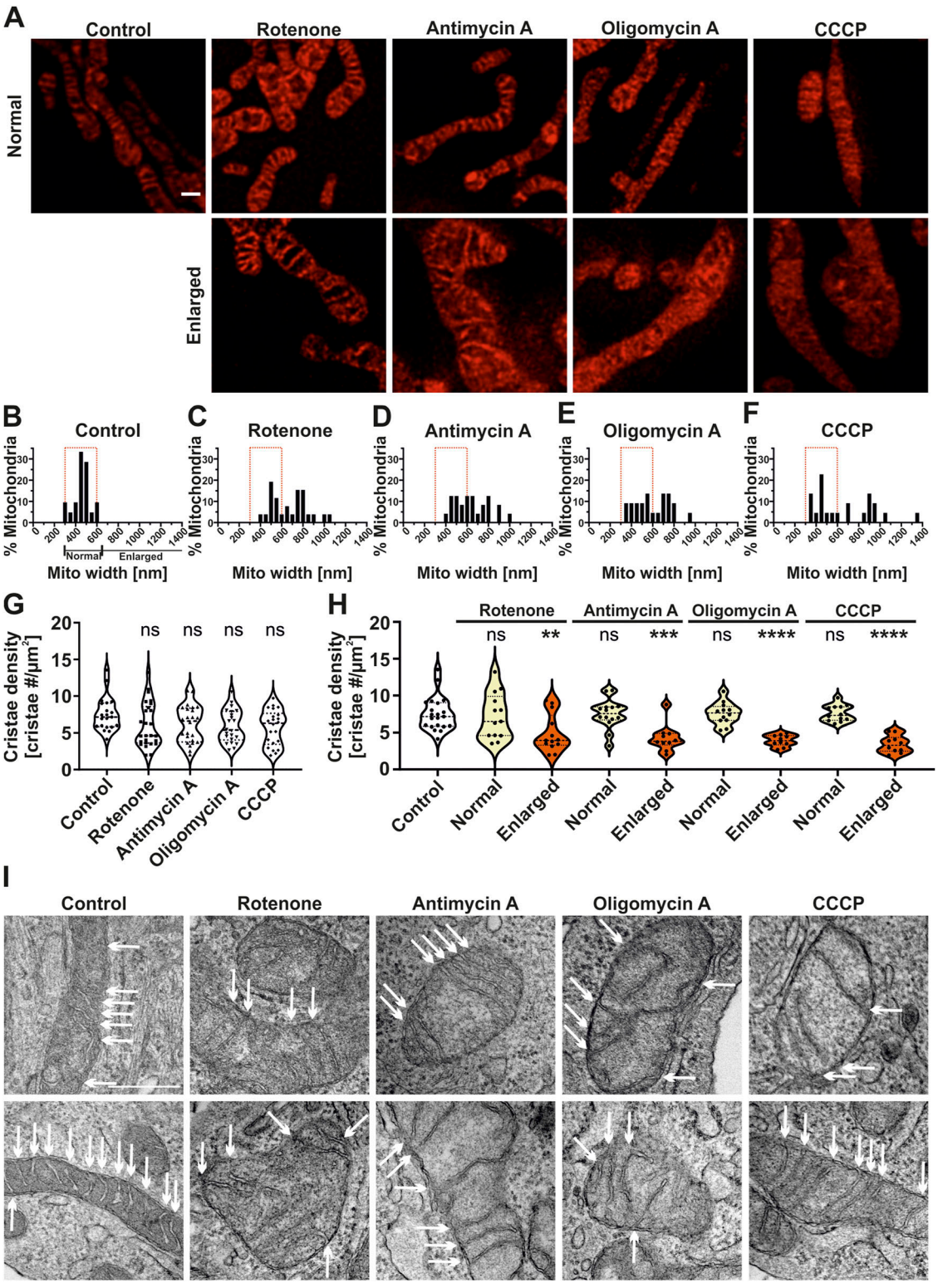

Figure 2. Mitochondrial toxins alter the morphology of cristae and mitochondria.
(A) Representative STED SR images of HeLa cells expressing ATP5I-SNAP, stained with silicon–rhodamine, displaying normal (<650 nm) or enlarged (≥650 nm) mitochondrial width upon rotenone, antimycin A, oligomycin A, and CCCP treatment. Top and bottom rows show mitochondria with normal and enlarged width, respectively. Scale bar represents 500 nm. **(B, C, D, E, F)** Frequency distribution (50 nm bins) of percentage mitochondria having particular mitochondrial width in control cells (B) and cells treated with rotenone (C), antimycin A (D), oligomycin A (E), and CCCP (F) obtained from three independent experiments (21–26 mitochondria). Red rectangle indicates width distribution of untreated control group which was superimposed in toxin-treated conditions. **(G, H)** Quantification of cristae density (cristae

forms of OPA1 (L-OPA1) are proteolytically cleaved into short forms (S-OPA1) in a balanced manner (Deshwal et al, 2020). Depolarisation of mitochondria leads to conversion of L-OPA1 to S-OPA1 (Duvezin-Caubet et al, 2006; Baker et al, 2014). However, this conversion depends on the concentration of mitochondrial toxins used and treatment time. Thus, we checked if there is any difference in the pattern of L-OPA1 and S-OPA1 in our conditions at 30 min. We found that CCCP treatment leads to enhanced cleavage of L-OPA1 to S-OPA1. There was no difference in patterns of OPA1 forms upon treating with other mitochondrial toxins. Therefore, enhanced merging and splitting events upon CCCP treatment (Fig 3C and E) correlated to accumulation of S-OPA1 (Fig S6C).

Cristae morphology is perturbed when HeLa cells are treated with an inhibitor of the ANT

We next asked whether ADP/ATP exchange of mitochondria, mediated by the ANT, is regulating the dynamics of cristae membranes. In this context, we used various concentrations of BKA, an ANT inhibitor, at 10, 25, and 50 μM along with a combination of various mitochondrial toxins, employed while imaging, on HeLa cells (Fig 5A and B). A clear dose-dependent decrease of oxygen consumption was observed with increasing concentration of BKA within the time window (30 min) used for imaging cristae membrane dynamics and ATP levels throughout this article (Fig 5A and B). We used the highest concentration (50 μM) of BKA for imaging cristae morphology and dynamics as it showed the strongest decrease in mitochondrial oxygen consumption termed BKA response. The maximal respiration was also significantly reduced after addition of different concentrations of BKA when compared with untreated condition. We noted that cristae morphology was clearly aberrant upon BKA treatment compared with untreated controls (Fig 5C and D). STED nanoscopy revealed numerous mitochondria with huge spaces devoid of cristae and highly interconnected cristae upon BKA treatment (Fig 5C and D, top panel, E and Fig S7A and B) and also other abnormal cristae organization where cristae were either clumped or accumulated in the central region of swollen mitochondria (Fig S7C). Overall, the alterations in cristae morphology observed by STED imaging were validated when EM was employed (Fig 5C and D, bottom panel). Therefore, we characterized the percentage of mitochondria having normal and abnormal cristae morphologies. There was a clear increase of mitochondria which had abnormal cristae morphology in BKA-treated condition when compared with untreated cells when the data from all five experiments were pooled as ~33% mitochondria had abnormal cristae morphology when compared with ~13% mitochondria in untreated conditions (Fig S7A and B). There were instances where live-cell STED movies of BKA-treated mitochondria showed highly interconnected cristae where the cristae dynamics was apparently highly reduced or static (Fig 5E and Video 10). We quantified the cristae dynamics in control and BKA-treated mitochondria and found no change in the overall merging and splitting events (Fig S7D). However, BKA-treated mitochondria with abnormal cristae morphology showed significantly reduced cristae dynamics compared with all mitochondria with BKA treatment or untreated mitochondria (Fig 5F and G). The cristae merging and splitting events were still balanced in control cells and BKA-treated cells (Fig S7D). The $\Delta\Psi_m$ was significantly decreased in BKA-treated cells (Fig S7E and F). Thus, despite the overall decrease in $\Delta\Psi_m$, a reduction in cristae dynamics was observed only in those mitochondria where the cristae morphology was aberrant. Overall, we conclude that inhibition of the ANT by BKA results in alteration of cristae morphology and a partial reduction of cristae membrane dynamics suggesting that ADP/ATP exchange across the inner membrane is critical to maintain cristae membrane dynamics independent of the membrane potential.

Discussion

The development of SR and high-resolution techniques which overcame the diffraction barrier of light, and their recent application to biological structures like mitochondria in fixed and living cells, has opened up exciting prospects to decipher mechanistic insights (Kondadi et al, 2020b; Jakobs et al, 2020). Whereas EM could provide valuable insights into cristae morphology by providing static data at different time-points, one could apply live-cell SR techniques like STED nanoscopy to understand the role of various proteins and metabolic factors regulating mitochondrial cristae dynamics. Here, we asked a basic question, namely whether modulation of OXPHOS, $\Delta\Psi_m$, ATP levels or ADP/ATP exchange in mitochondria determines cristae membrane dynamics, and if so, to which extent. In this study, we used advanced live-cell STED nanoscopy combined with newly developed and optimized quantification methods to study cristae morphology and dynamics when we inhibited the functioning of OXPHOS complexes I, III, V, and dissipated the $\Delta\Psi_m$. Application of a set of well-characterized mitochondrial toxins led to the formation of enlarged mitochondria, yet, contrary to our expectations, none of these toxins blocked cristae membrane dynamics. Before we discuss the details of the latter aspect, it is worth discussing the morphological alterations. Mitochondrial swelling is a phenomenon where there is an increase in the volume of the matrix caused because of osmotic imbalance between the matrix and cytosol (Kaasik et al, 2007). The osmotic balance is regulated by various channels and ion exchangers. Therefore, dysregulation of specific channels and exchangers in mitochondria could result in mitochondrial swelling. In addition, opening of the mitochondrial permeability transition pore causes mitochondrial swelling as the IM becomes permeable to

number per mitochondrial area in μm^2) per mitochondria, (G) Pooled data from three individual experiments are shown as violin plots with individual data points (21–26 mitochondria). Each symbol represents one mitochondrion. One-way ANOVA was used for statistical analysis. **(H)** Data were separated into normal and enlarged based on mitochondrial width with each condition having 10–21 mitochondria. Conditions were compared with untreated control group. (ns = nonsignificant *P*-value > 0.05, ** *P*-value ≤ 0.01, *** *P*-value ≤ 0.001, **** *P*-value ≤ 0.0001). One-way ANOVA was used for statistical analysis. **(I)** Representative transmission electron micrographs of mitochondria of cells treated without or with rotenone, antimycin A, oligomycin A, and CCCP. Individual cristae within a mitochondrion are marked using white arrows. A higher number of arrows in control mitochondria show increased number of cristae per mitochondrial section when compared with mitochondria where the cells were treated with various mitochondrial toxins. Two mitochondria are shown per condition. Scale bar represents 500 nm.

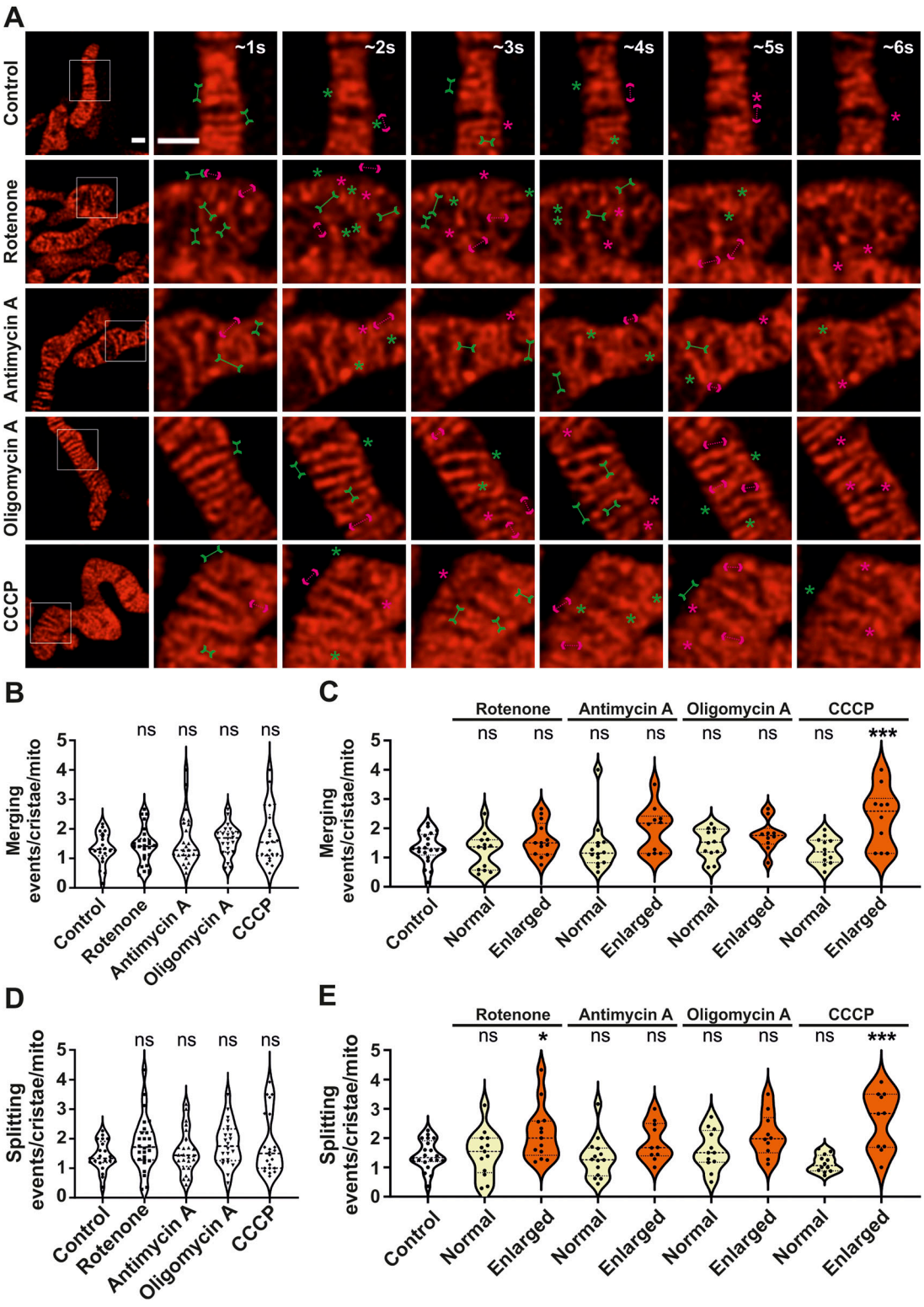

Figure 3. Crista merging and splitting events are maintained in enlarged mitochondria.
(A) Representative live-cell STED SR images of HeLa cells, expressing ATP5I-SNAP and stained with silicon–rhodamine, showing control and enlarged mitochondria obtained after treatment without or with various mitochondrial toxins respectively. Images at the extreme left show whole mitochondria along with white inset boxes. Other images on the right side display time-lapse series (0.94 s/frame) of zoom of the mitochondrial portion at ~1, 2, 3, 4, 5, and 6 s. Green and magenta asterisks show corresponding merging and splitting events, whereas solid green arrows pointing inward and dotted magenta arrows pointing outward show imminent merging and splitting events, respectively. Scale bar represents 500 nm. **(A, B, C, D, E)** Blind quantification of cristae merging and splitting events per mitochondrion in different

solutes with a molecular weight less than 1.5 kD (Lemasters et al, 2009). Mitochondrial swelling was proposed as mild reversible and excessive irreversible with the former regulating mitochondrial metabolism and the latter leading to mitochondrial dysfunction (Bernardi, 1999; Khmelinskii & Makarov, 2021a, 2021b). The treatment of cells with mitochondrial toxins and imaging within a time window of 30 min using live-cell STED nanoscopy suggests that the mitochondrial enlargement is in reversible mode with no loss of the outer membrane which is consistent with our EM images. EM data from previous studies (Gottlieb et al, 2003; Hytti et al, 2019) are consistent with our live-cell STED nanoscopy and EM observations where the application of the described mitochondrial toxins led to structural alterations in enlarged mitochondria characterized by decreased cristae density. Consistent with our observations, it was shown that dissipation of $\Delta\Psi_m$ by CCCP treatment led to decreased cristae density (Segawa et al, 2020). Concurrent to decreased cristae density, there was a trend of increased intercristae distance which was significantly higher in enlarged mitochondria after treatment with rotenone and CCCP. Overall, the cristae area was not changed when enlarged mitochondria were compared with normal mitochondria treated with mitochondrial toxins or not. Therefore, cristae density was reduced because of an overall increase in the mitochondrial area but not because of changes in the cristae area.

Using live-cell respirometry and consistent with textbooks, it has been shown that mammalian cells instantaneously display decreased oxygen consumption upon inhibition of OXPHOS complexes I, III, and V and increased oxygen consumption upon dissipation of $\Delta\Psi_m$ using CCCP (Kondadi et al, 2020a; Stephan et al, 2020). Thus, addition of various mitochondrial toxins leads to opposing trends of oxygen consumption with CCCP displaying increased mitochondrial consumption as opposed to other three toxins. It is noteworthy to mention that only upon CCCP treatment in enlarged mitochondria, a cleavage of L-OPA1 to S-OPA1 was observed making it tempting to speculate that regulation of cristae merging and splitting events is influenced by accumulation of S-OPA1. It has been shown that a balance of L-OPA1 and S-OPA1 keep CJs tight (Frezza et al, 2006). Furthermore, it was demonstrated that S-Mgm1 (homolog of human OPA1) has the ability to form helical lattice both on the inside and outside of lipid tubes (Faelber et al, 2019). In addition, it could be either a left- or right-handed helix. Both these properties contribute to exert constricting and pulling forces which were proposed to play important roles not only in inner membrane fusion and fission but also in cristae stabilization. At the level of cristae morphology, it is known that depletion of OPA1 leads to reduced number of cristae and CJs (Kushnareva et al, 2013) and disorganized cristae (Olichon et al, 2003). Accordingly, it has been shown that cristae dynamics is reduced in OPA1 KO cells (Hu et al, 2020). Unexpectedly, when the mitochondrial oxygen consumption was reduced after addition of rotenone, antimycin A, and oligomycin A, we did not observe any change in the number of merging and splitting events in enlarged mitochondria when compared with normal mitochondria (depicted in Fig 6). On the contrary, increased oxygen consumption during CCCP exposure is connected to increased number of cristae merging and splitting events. In addition, we demonstrated that the maintenance of the $\Delta\Psi_m$ is not essential for cristae dynamics. Moreover, despite varying differences in cells treated with mitochondrial toxins w.r.t $\Delta\Psi_m$, it can be concluded that largely no changes in the frequency of cristae dynamics were observed when the effects of different toxins are compared (depicted in Fig 6). Our data not only demonstrate that cristae membrane dynamics is not hampered upon loss of the membrane potential, it even shows an increase in merging and splitting events under these conditions. It should be noted that loss of $\Delta\Psi_m$ is not a requirement for mitochondrial enlargement as cells treated with oligomycin A showed enlarged mitochondria but did not lose $\Delta\Psi_m$. Overall, mitochondrial enlargement was necessary but not sufficient to display enhanced cristae membrane dynamics and these data point to the possibility that conditions of high oxygen consumption, which is equivalent to high electron flow from NADH to oxygen in the respiratory chain, may be one criterion to promote cristae merging and splitting events. Another criterion which has already been introduced is that the cristae dynamics might be regulated by OPA1 cleavage which was only observed in CCCP treatment and not in treatments with other mitochondrial toxins within 30 min. Thus, OPA1 cleavage could be a possible mechanism for regulating cristae dynamics.

What is the functional interplay between ATP levels and cristae dynamics? To decipher the ATP levels at the level of mitochondria, we used mitGO-ATeam2 probe which is a genetically encoded sensor based on FRET for detecting differences in ATP levels (Nakano et al, 2011). The ATP levels are based on ratiometric FRET imaging meaning that the expression levels of the construct do not influence the ATP measurements. Furthermore, it was shown that removal of glucose from the culture media results in a decrease of FRET ratio of mitochondrial ATP levels from 1.0 to ~0.7–0.9 in various cell types (Depaoli et al, 2018). Consistent with this previous study, we found a decrease in ATP levels of mitochondria. Whereas we found a consistent decrease of mitochondrial ATP levels in all cells exposed to mitochondrial toxins (except CCCP), cells containing normal mitochondria already showed decreased ATP levels. Interestingly, there was no further decrease in mitochondrial ATP levels in cells containing enlarged mitochondria indicating that the increased cristae dynamics served to maintain the already reduced ATP levels. It is interesting to note that the cristae merging and splitting was increased in enlarged mitochondria which coincided with maintenance of mitochondrial ATP levels upon CCCP treatment. Next, inhibition of the ANT translocator by BKA treatment led to increased percentage of mitochondria with abnormal cristae morphology (depicted in Fig 6). Overall, when analyzing all mitochondria at first,

conditions described in (A). **(B)** Quantification of cristae merging events per mitochondrion from three individual experiments (21–26 mitochondria) is shown as violin plots with individual data points. Each symbol represents one mitochondrion. **(C)** The number of cristae merging events were classified into normal (<650 nm) or enlarged (≥650 nm) mitochondria, with each condition having 10–21 mitochondria. Mitochondrial toxin treatment conditions were compared with untreated control group. **(D)** Quantification of cristae splitting events per mitochondrion from three individual experiments (21–26 mitochondria) is shown as violin plots with individual data points. Each symbol represents one mitochondrion. **(E)** The number of cristae splitting events were classified into normal (<650 nm) or enlarged (≥650 nm) mitochondria, with each condition having 10–21 mitochondria. Different conditions were compared with the untreated control group. (ns = nonsignificant P-value > 0.05, *P-value ≤ 0.05, ***P-value ≤ 0.001). One-way ANOVA was used for statistical analysis.

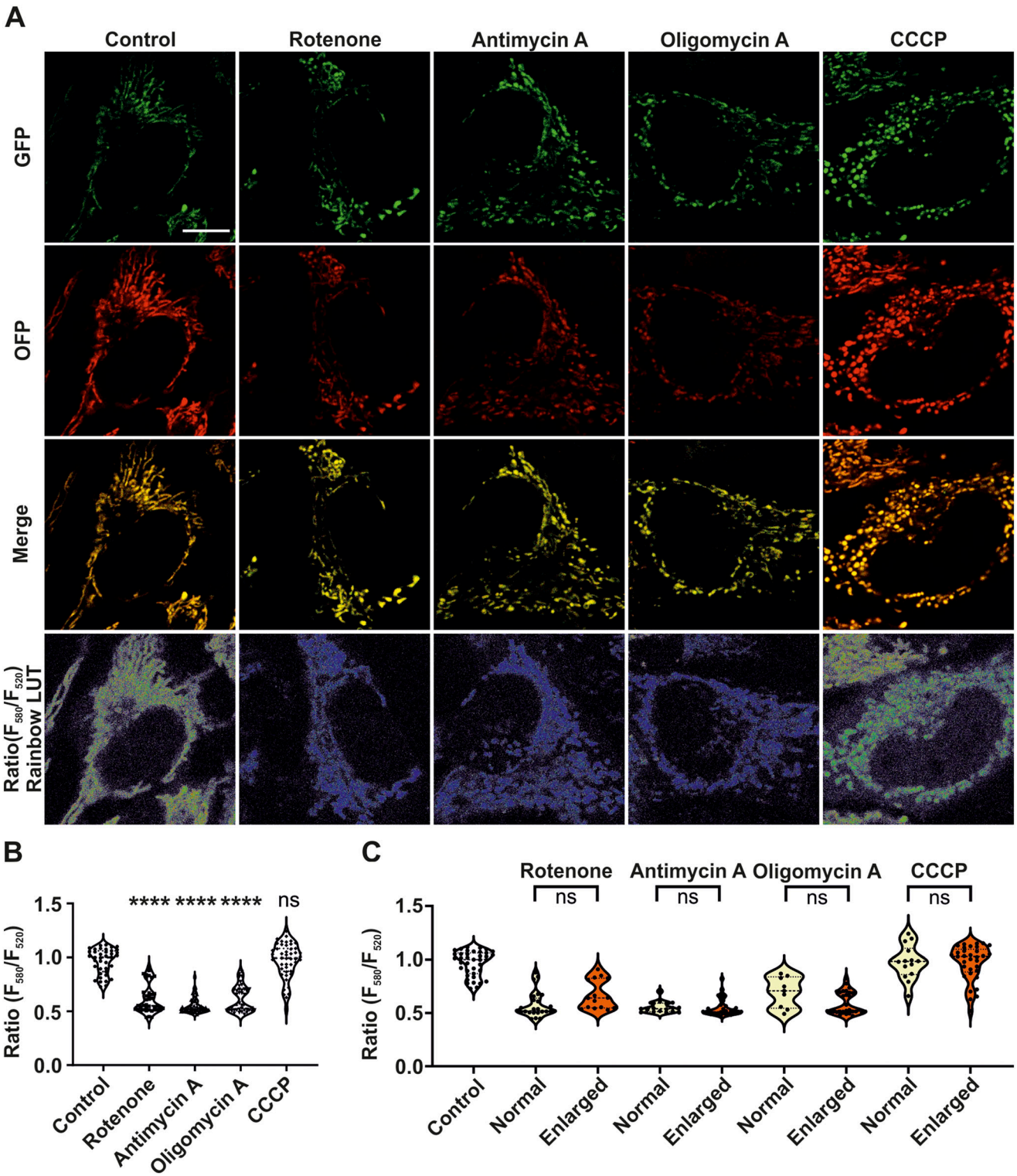

Figure 4. Mitochondrial ATP levels are significantly reduced upon inhibition of ETC complexes I, III, and V.
(A) Representative images of HeLa cells expressing mitGO-ATeam2, a ratiometric FRET-based genetically-encoded sensor determining the ATP levels, in cells treated without or with rotenone, antimycin A, oligomycin A, and CCCP. The images in first row show the FRET donor emission (GFP), whereas the images in second row display the FRET acceptor emission (OFP). The third row represents a merge of FRET donor and acceptor emission channels. The bottommost row represents ratiometric 32-bit float images, shown using pseudocolour rainbow LUT intensities, used as a basis for quantifying mitochondrial ATP levels. Rainbow LUT intensities reveal low-intensity blue pixels in cells exposed to mitochondrial toxins compared with high-intensity green and red pixels in untreated control cells. Scale bar represents 10 μm.
(B, C) Quantification of cellular mitochondrial ATP levels obtained by dividing the intensities of FRET acceptor emission (580 nm) by FRET donor emission (520 nm) in

we did not observe significant changes in cristae membrane dynamics, yet we detected the subpopulations of mitochondria with apparent different cristae membrane dynamics. When we considered this and divided our population in mitochondria where cristae morphology was abnormal versus normal, the cristae merging and splitting were significantly decreased compared with untreated mitochondria (depicted in Fig 6). This agrees with previous data which showed cristae dynamics was reduced in *MIC13* KO (Kondadi et al, 2020a). Mitochondrial ultrastructure was aberrant in *MIC13* KO because of loss of CJs. Therefore, we propose that cristae morphology and dynamics is interlinked. Given that enlarged mitochondria upon CCCP treatment show enhanced cristae dynamics, we propose that cristae dynamics is possibly determined by structural constraints. In such a scenario, highly, densely packed cristae would impose a constraint limiting cristae dynamics. It may also be that a reduction in cristae density is followed by an increased cristae fusion and fission rate serving as kind of a compensatory mechanism. Another aspect that appears to be important with respect to regulation of cristae membrane dynamics is the possible link to metabolic flux across the inner membrane. As discussed, we observe enhanced cristae membrane dynamics when the $\Delta\Psi_m$ is dissipated resulting in increased oxygen consumption, a condition characterized by high electron and proton flux. We further observe ongoing cristae dynamics even when various OXPHOS inhibitors were applied. It should be emphasized that under these conditions, cellular ATP demand is partially compensated by enhanced glycolysis and that ADP/ATP exchange across the inner membrane is still possible and maintained. This exchange is known to restore $\Delta\Psi_m$ partially by two mechanisms, namely by the electrogenic exchange of cytosolic ATP^{4-} with matrix-located ADP^{3-} and by the reverse F_1F_O-ATPase–driven proton-pumping activity requiring the constant import of ATP from the cytosol. Importantly, we observed that under conditions that hamper ADP/ATP exchange cristae membrane dynamics is partially blocked whereas, neither isolated inhibition of OXPHOS complexes I, III, V, nor mild reduction in ATP levels hampered cristae membrane dynamics grossly. We propose that next to structural constraints, in particular, the extent of ADP/ATP flux across the inner membrane is regulating cristae dynamics. Future studies will have to dissect which metabolite fluxes are of particular importance and how they are interconnected. Yet, our study reveals important and partly unexpected insights into the interlink between different modes of OXPHOS modulation and cristae membrane dynamics.

Materials and Methods

Cell culture, transfection, and mitochondrial toxin treatment

HeLa cells were maintained in DMEM cell culture media with 1 g/liter glucose (PAN-Biotech), 1 mM sodium pyruvate (Gibco), 2 mM glutaMAX (Gibco), Pen-Strep (PAN-Biotech, penicillin 100 U/ml and streptomycin 100 μg/ml) and 10% FBS (PAN Biotech) at 37°C and 5% CO_2. The cells were transfected with 1 μg of ATP5I-SNAP (Kondadi et al, 2020a) or 1 μg of mitGO-ATeam2 plasmid DNA using GeneJuice (Novagen) reagent for 48 h according to the manufacturer's protocol. For live-cell SR imaging, HeLa cells expressing ATP5I-SNAP were stained with 3 μM SNAP-cell 647-SiR (silicon–rhodamine) (NEB) for 30 min, in FluoroBrite DMEM media (Gibco) without phenol red containing 10% FBS (PAN Biotech), 1 mM sodium pyruvate (Gibco), 2 mM glutaMAX (Gibco) and Pen-Strep (penicillin 100 U/ml and streptomycin 100 μg/ml; Sigma-Aldrich). After silicon–rhodamine staining, cells were washed twice with FluoroBrite media. The third wash was done 10 min after the second wash after which mitochondrial toxins were added. Live-cell STED imaging was done in a time window of 10–30 min after addition of toxins at 37°C and 5% CO_2. The following concentrations of mitochondrial toxins (Merck) were used: rotenone (5 μM), antimycin A (10 μM), oligomycin A (5 μM), CCCP (10 μM), and BKA (10, 25 or 50 μM). A later time-point involving STED imaging was done in the last 15 min of 4 h.

Live-cell STED super-resolution nanoscopy and quantification of cristae dynamics

Live-cell STED SR imaging was performed on Leica SP8 laser scanning microscope equipped with a 93X glycerol objective (N.A = 1.3) and a STED module. The samples were excited using a white light laser at 633 nm and the images were collected at emission wavelength from 640 to 730 nm using a hybrid detector (HyD) while using a pulse STED depletion laser beam at a wavelength of 775 nm. To increase the specificity of the signal, gating STED was used from 0.8 ns onwards. An optimised pixel size of 22 nm was used and images were obtained at a rate of 0.94 s/frame. Before every imaging session, the alignment of the excitation and depletion laser beams was optimised using 80-nm colloidal gold particles (BBI Solutions) to ensure the maximum possible resolution. Huygens Deconvolution software (21.10.0p0) was used to process the acquired images. The raw data images are provided. The STED videos were carefully analysed frame-wise and manually quantified in a blind manner to account for the average number of merging and splitting events per cristae within a mitochondrion using ImageJ software (Fiji). The average number of merging and splitting events per mitochondrion was determined and the whole mitochondrial population belonging to a particular condition was represented using violin plots.

Quantification of various parameters related to cristae morphology

As cellular bioenergetic status influences mitochondrial ultrastructure, the cristae morphology of various mitochondria is fairly

HeLa cells treated with or without the mentioned mitochondrial toxins. **(B)** Quantification of mitochondrial ATP levels (ratiometric data) is shown as violin plots from three individual experiments (39–50 cells). Each symbol represents mitochondrial ATP levels of an individual cell. Conditions are compared with untreated control group. **(C)** Ratiometric data were separated into cells with either prevalent normal or enlarged mitochondria (described in methods). Cells with mixed mitochondrial morphology were excluded from this evaluation resulting in 9–39 cells for each group. Statistical analysis was performed between the two classified groups for each treatment condition, with untreated control group as reference. (ns = nonsignificant *P*-value > 0.05, ****P-value ≤ 0.0001). One-way ANOVA was used for statistical analysis.

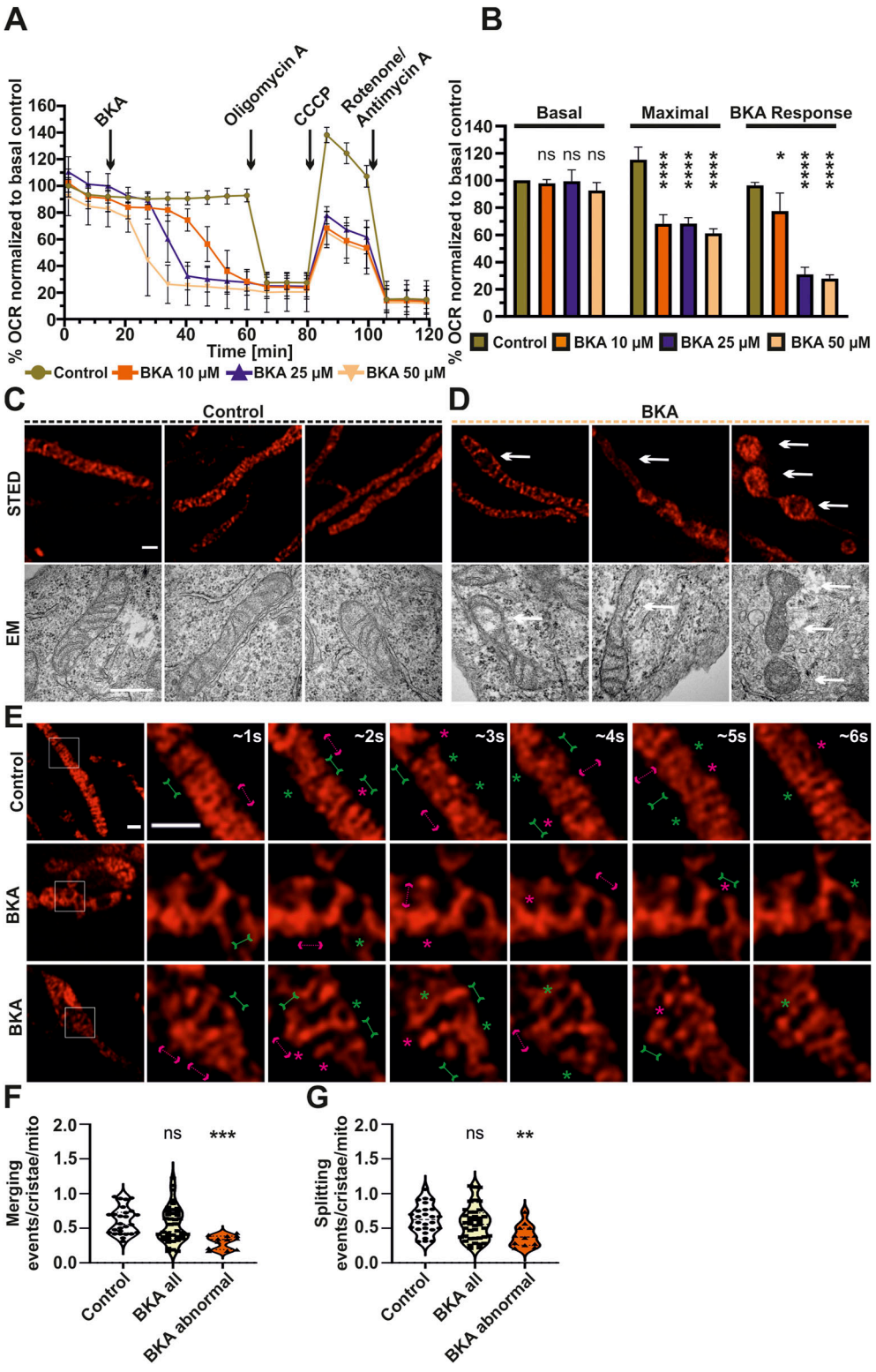

Figure 5. Inhibition of ANT causes perturbations in cristae morphology and dynamics.
(A) Representative experiment showing percentage oxygen consumption rates, normalized to basal respiration of control HeLa cells, treated without or with various BKA concentrations (10, 25 or 50 μM BKA, as indicated in the color code) are shown. ~45 min after BKA injection, routine Seahorse Mito Stress Test was performed. Respective compound injection time-points are indicated by black arrows. Error bars represent SD. **(B)** Comparison of basal respiration, maximal respiration, and BKA response (calculated ~32 min after BKA injection) of HeLa WT cells treated without or with various concentrations of BKA (10, 25 or 50 μM BKA) as indicated using a color code. Error bars represent SD from three independent biological replicates. **(C, D)** Representative STED SR images (top row) of HeLa cells expressing ATP5I-SNAP, stained with silicon–rhodamine treated without (C) or with (D) 50 μM BKA and corresponding electron micrographs of mitochondria (bottom row) displaying a similar mitochondrial ultrastructure are shown. Three columns (C) display untreated mitochondria with normal morphology (D) Abnormal cristae morphology of BKA-treated mitochondria showing regions of sparse cristae. Similar perturbations in cristae morphology visualized by STED and EM images are indicated by arrows. Scale bars represent 500 nm. **(E)** Additional live-cell STED SR images of HeLa cells, from same conditions as (C, D) are shown. Images at the extreme left show whole mitochondria along with white inset boxes. Other images on the right-side display time-lapse series (0.94 s/frame) of zoom of mitochondrial portion at ~1, 2, 3, 4, 5, and 6 s. Green and magenta asterisks show corresponding merging and splitting events, whereas solid green arrows pointing inward and dotted magenta arrows pointing outward show imminent merging and splitting events, respectively. Scale bar represents 500 nm. **(F, G)** Blind quantification of cristae merging (F) and splitting (G) events per mitochondrion in HeLa cells treated without or with BKA. Mitochondria from BKA-treated cells were further separated into all mitochondria or those with exclusively abnormal cristae morphology and the individual groups compared with the untreated control (ns = nonsignificant P-value > 0.05, **P-value ≤ 0.01, ***P-value ≤ 0.001). One-way ANOVA was used for statistical analysis.

uniform in individual cells. Thus, we maximised the number of cells used for STED nanoscopy by considering only a maximum of two mitochondria from each cell when they were treated with or without toxins, where we quantified various cristae parameters including merging and splitting events. We determined mitochondrial width, cristae density, average intercristae distance, and

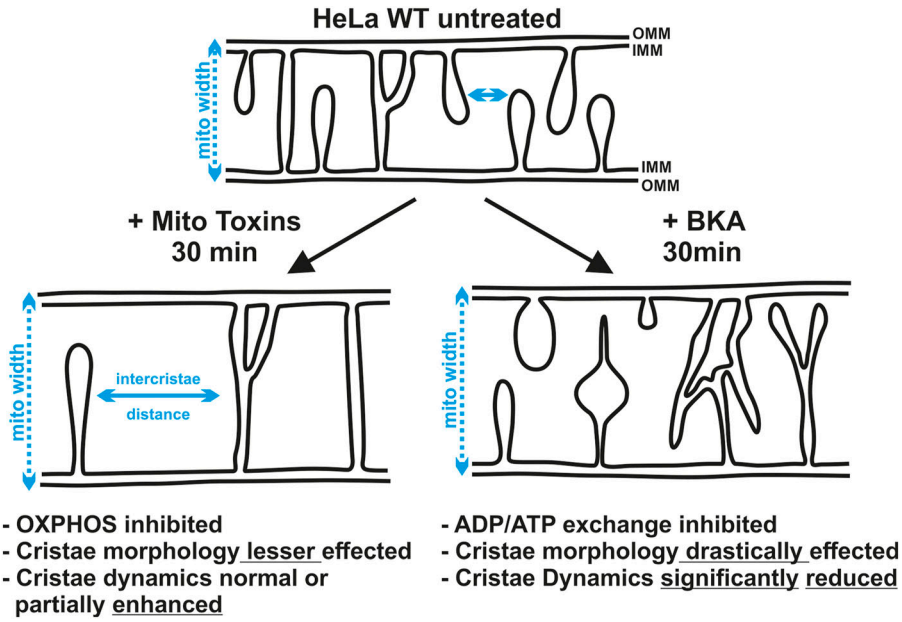

Figure 6. A model showing the influence of mitochondrial toxins on cristae morphology and dynamics.
On one hand, treatment of HeLa cells with various mitochondrial toxins (rotenone, antimycin A, oligomycin A, and CCCP) leads to inhibition of ETC or the F_1F_O ATP synthase along with enlargement of mitochondria. The distance between the cristae (intercristae distance) increases because of mitochondrial enlargement, whereas the cristae dynamics is either unchanged or increased (CCCP treatment). On the other hand, BKA treatment, inhibiting ATP/ADP exchange, also leads to mitochondrial enlargement. However, cristae morphology and the number of merging and splitting events are severely reduced in a subset of mitochondria.

percentage cristae area occupied by mitochondria using custom-made macros in Fiji. To determine the width of an individual mitochondrion in images obtained using STED nanoscopy, we used the average of three separate line scans covering the maximum diameter at both ends and the centre of mitochondria which were roughly drawn equidistant from each other. Furthermore, to determine the cristae density, a segmented line was manually drawn across the length of each mitochondrion and an intensity profile of the pixels across the length of the line was created. The algorithm detected the number of cristae by using the number of maximum intensity points of the graph along the length of mitochondrial plot profiles. The obtained cristae number was divided by the previously determined area of the respective mitochondrion to calculate the cristae number per μm^2 which we termed cristae density.

To measure the average distance between cristae defined as intercristae distance (in nm), we used the previously acquired intensity profiles of mitochondria to determine the exact coordinates of each crista in the image. Euclidean distances between cristae were calculated using a custom-made macro. Because of the drastic variations in mitochondrial and cristae morphology upon BKA treatment, the above-described macro for determination of cristae number was not used. For these datasets, the number of cristae per mitochondrion was counted manually and used for normalization of merging and splitting events. Next, for calculation of the percentage cristae area occupied by mitochondria, we used a semiautomated batch-processing custom-made macro. Cristae structures were manually selected by applying appropriate threshold on the images and the total mitochondrial area was selected by drawing the outline of the whole mitochondrion. The "Analyze Particles" function of Fiji was used to calculate the cristae area where structures less than five pixels were excluded. The macro divided the sum of all cristae area by the whole mitochondrial area and multiplied the result by 100 to acquire the percentage cristae area occupied by that particular mitochondrion.

Electron microscopy

HeLa cells were grown in 15-cm petri dishes at 37°C with 5% CO_2 and treated with respective mitochondrial toxins for 30 min which were then fixed with 3% glutaraldehyde, 0.1 M sodium cacodylate buffer at pH 7.2. Cell pellets were washed in fresh 0.1 M sodium cacodylate buffer at pH 7.2, before embedding in 3% low melting agarose. They were stained by incubating in 1% osmium tetroxide for 50 min followed by two washes for 10 min with 0.1 M sodium cacodylate buffer and one wash with 70% ethanol for 10 min. Samples are stained using 1% uranyl acetate/1% phosphotungstic acid mixture in 70% ethanol for 60 min. Graded ethanol series was used to dehydrate the specimen. The samples were embedded in spur epoxy resin for polymerization at 70°C for 24 h. Ultrathin sections obtained using a microtome were imaged with a transmission electron microscope (H600; Hitachi) at 75 V which had a Bioscan 792 camera (Gatan).

FRET-based microscopy to measure ATP levels

Cells expressing the genetically-encoded mitGO-ATeam2 were used to determine the ATP levels, kindly provided by Hiromi Imamura, Kyoto, Japan (Nakano et al, 2011). Single optical sections were obtained with a 93X glycerol objective (N.A = 1.3) using Leica SP8 confocal microscope maintained at 37°C and 5% CO_2. The samples were excited at 471 nm and the green and orange emission channels were simultaneously obtained from 502 to 538 nm (termed 520 nm) and 568–592 nm (termed 580 nm), respectively, as described (Nakano et al, 2011) in the photon counting mode. To quantify the ratiometric images obtained, a semiautomated custom-made macro was designed using Fiji software to analyse the acquired images in a batch processing mode. The cells of interest were manually selected by drawing a region of interest. The obtained orange emission channel images

(580 nm) were divided by respective green emission channel images (520 nm) by using the "Image Calculator" function of Fiji. A threshold was manually applied on the resulting ratiometric 32-bit float image to exclude background pixels using the "Clear Outside" command. To categorise cell population as containing either swollen or normal mitochondria, the cut off for swollen mitochondria was set to 650 nm in congruence with STED SR nanoscopy. If 85% of the mitochondrial population featured enlarged mitochondria, the cells were designated as swollen. Similarly, if 85% of the mitochondrial population featured mitochondria whose width was less than 650 nm, the cell was considered as having normal mitochondria. We measured the diameter of whole mitochondrial population in the respective cells using Leica Application Suite X software (version 3.7.1.21655).

Determination of mitochondrial membrane potential ($\Delta\Psi_m$)

HeLa cells were incubated with 20 nM TMRM (Invitrogen) and 50 nM MitoTracker Green (Invitrogen) in DMEM cell culture media along with other supplements (mentioned above) for 30 min at 37°C followed by three washes. 10 min after the addition of respective toxins, cells were imaged for 20 min in DMEM media containing 10 mM HEPES buffer (Gibco) and other supplements. Mitochondrial toxins were present in the media during imaging sessions. Imaging was done on spinning disc confocal microscope (PerkinElmer) using a 60x oil-immersion objective (N.A = 1.49). Single optical sections were obtained using excitation wavelengths of 488 nm (MitoTracker Green) and 561 nm (TMRM). The microscope was equipped with a Hamamatsu C9100 camera. Image analysis including background subtraction and measurement of mean fluorescence intensity were performed using Fiji software after drawing a region of interest around individual cells.

Live-cell respirometry

All the respiration measurements were performed using Seahorse XFe96 Analyzer (Agilent). HeLa cells were seeded in Seahorse XF96 cell culture plate (Agilent) at a density of 3.5×10^4 cells per well overnight. Next day, cells were washed and incubated in basic DMEM media (103575-100; Agilent) supplemented with 10 mM glucose (Sigma-Aldrich), 2 mM glutamine (Thermo Fisher Scientific), and 1 mM pyruvate (Gibco) at 37°C, with no CO_2 incubation 1 h before the assay. For testing the functionality of mitochondrial toxins we used, they were compared with commercially available Seahorse compounds. Thus, mitochondrial respiration was measured using Seahorse XF Cell Mito Stress Test kit (Agilent) according to the manufacturer's instructions by using rotenone (0.5 μM), antimycin A (0.5 μM), oligomycin A (1 μM), FCCP (0.5 μM) or using corresponding concentration of mitochondrial toxins used for microscopy experiments described in the mitochondrial toxin treatment methods section.

For the BKA experiment, three concentrations of BKA (Sigma-Aldrich) were tested at 10, 25, and 50 μM. The dilutions of BKA and all corresponding mitochondrial toxins used throughout the article were prepared in Seahorse medium. The duration between any two measurements is ~6 min. BKA response was calculated ~32 min after BKA injection (fifth measurement after BKA addition). The measurements after BKA injection were followed by subsequent injections of oligomycin A, CCCP, and a mixture of rotenone and antimycin A as routinely performed to assess mitochondrial oxygen consumption in Seahorse live-cell respirometry experiments. Cell number was normalized after the run using Hoechst staining. Data were analysed using wave software (Agilent). Further calculations were done in Microsoft Excel and figure preparation in GraphPad Prism.

SDS gel electrophoresis and Western blotting

Cells were treated for 30 min with the respective toxins using same concentrations as in the imaging experiments. Cells were washed thrice with cold DPBS (PAN-biotech) and harvested by scrapping and pelleting at 1,000*g*, 4°C for 10 min. Cell pellets were resuspended in an appropriate volume of RIPA buffer 150 mM NaCl, 0.1% SDS, 0.05% sodium deoxycholate, 1% Triton-X-100, 1 mM EDTA, 1 mM Tris, pH 7.4, 1x protease inhibitor (Sigma-Aldrich). Protein concentration was determined using Lowry assay with the DCTM protein assay kit (BIO-RAD). SDS samples were prepared using Laemmli buffer and subsequent heating at 95°C for 5 min 20 μg protein were loaded on 10% SDS–PAGE gels. After SDS–PAGE, the proteins were transferred onto a nitrocellulose membrane. To assess loading and transfer quality, the membrane was stained using Ponceau S (Sigma-Aldrich) after the transfer. After 1 h of blocking the membrane with 5% milk in TBS-T at room temperature, it was decorated against OPA1 (Pineda, custom-made) over night at 4°C. Goat IgG anti-rabbit IgG (Dianova) HRP-conjugate was used for detection. The chemiluminescent signals were obtained using Signal Fire ECL reagent (Cell Signaling Technology) and VILBER LOURMAT Fusion SL equipment (Peqlab).

Statistics and data representation

Statistical significance was tested by one-way ANOVA followed by Dunnett´s test for multiple comparisons against single control group or Šídák's test for multiple comparisons of selected pairs with ns = nonsignificant P-value > 0.05, *P-value ≤ 0.05, **P-value ≤ 0.01, ***P-value ≤ 0.001, ****P-value ≤ 0.0001. For statistical analysis and data representation, GraphPad Prism (version 9.5.1) was used.

Supplementary Information

Supplementary Information is available at https://doi.org/10.26508/lsa.202302386.

Acknowledgements

We thank Andrea Borchardt and Tanja Portugall for excellent technical assistance in performing electron microscopy and molecular biological experiments. The STED SR and FRET-based ATP experiments were performed at the Centre for Advanced Imaging (CAi), HHU, Düsseldorf. We are grateful to Hiromi Imamura from Kyoto University, Japan, for providing us with the mitGO-ATeam2 plasmid used for detecting ATP levels. Funding: this work was funded by the Deutsche Forschungsgemeinschaft (DFG) SFB 1208, project B12

(ID 267205415), to AS Reichert and by the DFG grant KO 6519/1-1 to AK Kondadi.

Author Contributions

M Golombek: data curation, software, formal analysis, validation, investigation, visualization, methodology, and writing—review and editing.
T Tsigaras: software, formal analysis, investigation, and visualization.
Y Schaumkessel: formal analysis and investigation.
S Hänsch: resources, software, validation, and methodology.
S Weidtkamp-Peters: resources and methodology.
R Anand: supervision, validation, investigation, visualization, and writing—review and editing.
AS Reichert: conceptualization, supervision, funding acquisition, project administration, and writing—review and editing.
AK Kondadi: conceptualization, supervision, funding acquisition, investigation, project administration, and writing—original draft, review, and editing.

Conflict of Interest Statement

The authors declare that they have no conflict of interest.

References

Anand R, Strecker V, Urbach J, Wittig I, Reichert AS (2016) Mic13 is essential for formation of crista junctions in mammalian cells. *PLoS one* 11: e0160258. doi:10.1371/journal.pone.0160258

Anand R, Reichert AS, Kondadi AK (2021) Emerging roles of the micos complex in cristae dynamics and biogenesis. *Biology (Basel)* 10: 600. doi:10.3390/biology10070600

Baker MJ, Lampe PA, Stojanovski D, Korwitz A, Anand R, Tatsuta T, Langer T (2014) Stress-induced oma1 activation and autocatalytic turnover regulate opa1-dependent mitochondrial dynamics. *EMBO J* 33: 578–593. doi:10.1002/embj.201386474

Benincá C, Zanette V, Brischigliaro M, Johnson M, Reyes A, Valle DAD, J Robinson A, Degiorgi A, Yeates A, Telles BA, et al (2021) Mutation in the micos subunit gene apoo (mic26) associated with an x-linked recessive mitochondrial myopathy, lactic acidosis, cognitive impairment and autistic features. *J Med Genet* 58: 155–167. doi:10.1136/jmedgenet-2020-106861

Bernardi P (1999) Mitochondrial transport of cations: Channels, exchangers, and permeability transition. *Physiol Rev* 79: 1127–1155. doi:10.1152/physrev.1999.79.4.1127

Davies KM, Strauss M, Daum B, Kief JH, Osiewacz HD, Rycovska A, Zickermann V, Kühlbrandt W (2011) Macromolecular organization of atp synthase and complex i in whole mitochondria. *Proc Natl Acad Sci U S A* 108: 14121–14126. doi:10.1073/pnas.1103621108

Depaoli MR, Karsten F, Madreiter-Sokolowski CT, Klec C, Gottschalk B, Bischof H, Eroglu E, Waldeck-Weiermair M, Simmen T, Graier WF, et al (2018) Real-time imaging of mitochondrial atp dynamics reveals the metabolic setting of single cells. *Cell Rep* 25: 501–512.e3. doi:10.1016/j.celrep.2018.09.027

Deshwal S, Fiedler KU, Langer T (2020) Mitochondrial proteases: Multifaceted regulators of mitochondrial plasticity. *Annu Rev Biochem* 89: 501–528. doi:10.1146/annurev-biochem-062917-012739

Duvezin-Caubet S, Jagasia R, Wagener J, Hofmann S, Trifunovic A, Hansson A, Chomyn A, Bauer MF, Attardi G, Larsson NG, et al (2006) Proteolytic processing of opa1 links mitochondrial dysfunction to alterations in mitochondrial morphology. *J Biol Chem* 281: 37972–37979. doi:10.1074/jbc.M606059200

Eramo MJ, Lisnyak V, Formosa LE, Ryan MT (2020) The "mitochondrial contact site and cristae organising system" (micos) in health and human disease. *J Biochem* 167: 243–255. doi:10.1093/jb/mvz111

Faelber K, Dietrich L, Noel JK, Wollweber F, Pfitzner AK, Mühleip A, Sánchez R, Kudryashev M, Chiaruttini N, Lilie H, et al (2019) Structure and assembly of the mitochondrial membrane remodelling gtpase mgm1. *Nature* 571: 429–433. doi:10.1038/s41586-019-1372-3

Frey TG, Mannella CA (2000) The internal structure of mitochondria. *Trends Biochem Sci* 25: 319–324. doi:10.1016/s0968-0004(00)01609-1

Frey TG, Renken CW, Perkins GA (2002) Insight into mitochondrial structure and function from electron tomography. *Biochim Biophys Acta* 1555: 196–203. doi:10.1016/s0005-2728(02)00278-5

Frezza C, Cipolat S, Martins de Brito O, Micaroni M, Beznoussenko GV, Rudka T, Bartoli D, Polishuck RS, Danial NN, De Strooper B, et al (2006) Opa1 controls apoptotic cristae remodeling independently from mitochondrial fusion. *Cell* 126: 177–189. doi:10.1016/j.cell.2006.06.025

Gilkerson RW, Selker JM, Capaldi RA (2003) The cristal membrane of mitochondria is the principal site of oxidative phosphorylation. *FEBS Lett* 546: 355–358. doi:10.1016/s0014-5793(03)00633-1

Gottlieb E, Armour SM, Harris MH, Thompson CB (2003) Mitochondrial membrane potential regulates matrix configuration and cytochrome c release during apoptosis. *Cell Death Differ* 10: 709–717. doi:10.1038/sj.cdd.4401231

Guarani V, McNeill EM, Paulo JA, Huttlin EL, Fröhlich F, Gygi SP, Van Vactor D, Harper JW (2015) Qil1 is a novel mitochondrial protein required for micos complex stability and cristae morphology. *Elife* 4: e06265. doi:10.7554/eLife.06265

Guarani V, Jardel C, Chrétien D, Lombès A, Bénit P, Labasse C, Lacène E, Bourillon A, Imbard A, Benoist JF, et al (2016) Qil1 mutation causes micos disassembly and early onset fatal mitochondrial encephalopathy with liver disease. *Elife* 5: e17163. doi:10.7554/eLife.17163

Hackenbrock CR (1966) Ultrastructural bases for metabolically linked mechanical activity in mitochondria. I. Reversible ultrastructural changes with change in metabolic steady state in isolated liver mitochondria. *J Cell Biol* 30: 269–297. doi:10.1083/jcb.30.2.269

Harner M, Körner C, Walther D, Mokranjac D, Kaesmacher J, Welsch U, Griffith J, Mann M, Reggiori F, Neupert W (2011) The mitochondrial contact site complex, a determinant of mitochondrial architecture. *EMBO J* 30: 4356–4370. doi:10.1038/emboj.2011.379

Hessenberger M, Zerbes RM, Rampelt H, Kunz S, Xavier AH, Purfürst B, Lilie H, Pfanner N, van der Laan M, Daumke O (2017) Regulated membrane remodeling by mic60 controls formation of mitochondrial crista junctions. *Nat Commun* 8: 15258. doi:10.1038/ncomms15258

Hoppins S, Collins SR, Cassidy-Stone A, Hummel E, Devay RM, Lackner LL, Westermann B, Schuldiner M, Weissman JS, Nunnari J (2011) A mitochondrial-focused genetic interaction map reveals a scaffold-like complex required for inner membrane organization in mitochondria. *J Cell Biol* 195: 323–340. doi:10.1083/jcb.201107053

Hu C, Shu L, Huang X, Yu J, Li L, Gong L, Yang M, Wu Z, Gao Z, Zhao Y, et al (2020) Opa1 and micos regulate mitochondrial crista dynamics and formation. *Cell Death Dis* 11: 940. doi:10.1038/s41419-020-03152-y

Huang X, Fan J, Li L, Liu H, Wu R, Wu Y, Wei L, Mao H, Lal A, Xi P, et al (2018) Fast, long-term, super-resolution imaging with hessian structured illumination microscopy. *Nat Biotechnol* 36: 451–459. doi:10.1038/nbt.4115

Hytti M, Korhonen E, Hyttinen JMT, Roehrich H, Kaarniranta K, Ferrington DA, Kauppinen A (2019) Antimycin a-induced mitochondrial damage

causes human rpe cell death despite activation of autophagy. *Oxid Med Cell longev* 2019: 1583656. doi:10.1155/2019/1583656

Imamura H, Nhat KP, Togawa H, Saito K, Iino R, Kato-Yamada Y, Nagai T, Noji H (2009) Visualization of atp levels inside single living cells with fluorescence resonance energy transfer-based genetically encoded indicators. *Proc Natl Acad Sci U S A* 106: 15651–15656. doi:10.1073/pnas.0904764106

Jakobs S, Stephan T, Ilgen P, Brüser C (2020) Light microscopy of mitochondria at the nanoscale. *Annu Rev Biophys* 49: 289–308. doi:10.1146/annurev-biophys-121219-081550

Kaasik A, Safiulina D, Zharkovsky A, Veksler V (2007) Regulation of mitochondrial matrix volume. *Am J Physiol Cell Physiol* 292: C157–C163. doi:10.1152/ajpcell.00272.2006

Khmelinskii I, Makarov V (2021a) Reversible and irreversible mitochondrial swelling in vitro. *Biophys Chem* 278: 106668. doi:10.1016/j.bpc.2021.106668

Khmelinskii I, Makarov V (2021b) Reversible and irreversible mitochondrial swelling: Effects of variable mitochondrial activity. *Biosystems* 210: 104559. doi:10.1016/j.biosystems.2021.104559

Kondadi AK, Anand R, Reichert AS (2019) Functional interplay between cristae biogenesis, mitochondrial dynamics and mitochondrial DNA integrity. *Int J Mol Sci* 20: 4311. doi:10.3390/ijms20174311

Kondadi AK, Anand R, Hänsch S, Urbach J, Zobel T, Wolf DM, Segawa M, Liesa M, Shirihai OS, Weidtkamp-Peters S, et al (2020a) Cristae undergo continuous cycles of membrane remodelling in a micos-dependent manner. *EMBO Rep* 21: e49776. doi:10.15252/embr.201949776

Kondadi AK, Anand R, Reichert AS (2020b) Cristae membrane dynamics - a paradigm change. *Trends Cell Biology* 30: 923–936. doi:10.1016/j.tcb.2020.08.008

Kushnareva YE, Gerencser AA, Bossy B, Ju WK, White AD, Waggoner J, Ellisman MH, Perkins G, Bossy-Wetzel E (2013) Loss of opa1 disturbs cellular calcium homeostasis and sensitizes for excitotoxicity. *Cell Death Differ* 20: 353–365. doi:10.1038/cdd.2012.128

Lemasters JJ, Theruvath TP, Zhong Z, Nieminen AL (2009) Mitochondrial calcium and the permeability transition in cell death. *Biochim Biophys Acta* 1787: 1395–1401. doi:10.1016/j.bbabio.2009.06.009

Liu T, Stephan T, Chen P, Keller-Findeisen J, Chen J, Riedel D, Yang Z, Jakobs S, Chen Z (2022) Multi-color live-cell sted nanoscopy of mitochondria with a gentle inner membrane stain. *Proc Natl Acad Sci U S A* 119: e2215799119. doi:10.1073/pnas.2215799119

Lukinavicius G, Umezawa K, Olivier N, Honigmann A, Yang G, Plass T, Mueller V, Reymond L, Corrêa IR, Jr, Luo ZG, et al (2013) A near-infrared fluorophore for live-cell super-resolution microscopy of cellular proteins. *Nat Chem* 5: 132–139. doi:10.1038/nchem.1546

Mannella CA, Marko M, Penczek P, Barnard D, Frank J (1994) The internal compartmentation of rat-liver mitochondria: Tomographic study using the high-voltage transmission electron microscope. *Microsc Res Tech* 27: 278–283. doi:10.1002/jemt.1070270403

Mannella CA, Lederer WJ, Jafri MS (2013) The connection between inner membrane topology and mitochondrial function. *J Mol Cell Cardiol* 62: 51–57. doi:10.1016/j.yjmcc.2013.05.001

Marco-Hernández AV, Tomás-Vila M, Montoya-Filardi A, Barranco-González H, Vilchez Padilla JJ, Azorín I, Smeyers Dura P, Monfort-Membrado S, Pitarch-Castellano I, Martínez-Castellano F (2022) Mitochondrial developmental encephalopathy with bilateral optic neuropathy related to homozygous variants in immt gene. *Clin Genet* 101: 233–241. doi:10.1111/cge.14093

Michaud M, Gros V, Tardif M, Brugière S, Ferro M, Prinz WA, Toulmay A, Mathur J, Wozny M, Falconet D, et al (2016) Atmic60 is involved in plant mitochondria lipid trafficking and is part of a large complex. *Curr Biol* 26: 627–639. doi:10.1016/j.cub.2016.01.011

Minamikawa T, Williams DA, Bowser DN, Nagley P (1999) Mitochondrial permeability transition and swelling can occur reversibly without inducing cell death in intact human cells. *Exp cell Res* 246: 26–37. doi:10.1006/excr.1998.4290

Muñoz-Gómez SA, Slamovits CH, Dacks JB, Baier KA, Spencer KD, Wideman JG (2015) Ancient homology of the mitochondrial contact site and cristae organizing system points to an endosymbiotic origin of mitochondrial cristae. *Curr Biol* 25: 1489–1495. doi:10.1016/j.cub.2015.04.006

Munoz-Gomez SA, Cadena LR, Gardiner AT, Leger MM, Sheikh S, Connell LB, Bily T, Kopejtka K, Beatty JT, Koblížek M, et al (2023) Intracytoplasmic-membrane development in alphaproteobacteria involves the homolog of the mitochondrial crista-developing protein mic60. *Curr Biol* 33: 1099–1111.e6. doi:10.1016/j.cub.2023.02.059

Nakano M, Imamura H, Nagai T, Noji H (2011) Ca^{2+} regulation of mitochondrial atp synthesis visualized at the single cell level. *ACS Chem Biol* 6: 709–715. doi:10.1021/cb100313n

Olichon A, Baricault L, Gas N, Guillou E, Valette A, Belenguer P, Lenaers G (2003) Loss of opa1 perturbates the mitochondrial inner membrane structure and integrity, leading to cytochrome c release and apoptosis. *J Biol Chem* 278: 7743–7746. doi:10.1074/jbc.C200677200

Perkins G, Renken C, Martone ME, Young SJ, Ellisman M, Frey T (1997) Electron tomography of neuronal mitochondria: Three-dimensional structure and organization of cristae and membrane contacts. *J Struct Biol* 119: 260–272. doi:10.1006/jsbi.1997.3885

Pfanner N, van der Laan M, Amati P, Capaldi RA, Caudy AA, Chacinska A, Darshi M, Deckers M, Hoppins S, Icho T, et al (2014) Uniform nomenclature for the mitochondrial contact site and cristae organizing system. *J Cell Biol* 204: 1083–1086. doi:10.1083/jcb.201401006

Rabl R, Soubannier V, Scholz R, Vogel F, Mendl N, Vasiljev-Neumeyer A, Körner C, Jagasia R, Keil T, Baumeister W, et al (2009) Formation of cristae and crista junctions in mitochondria depends on antagonism between fcj1 and su e/g. *J Cell Biol* 185: 1047–1063. doi:10.1083/jcb.200811099

Scorrano L, Ashiya M, Buttle K, Weiler S, Oakes SA, Mannella CA, Korsmeyer SJ (2002) A distinct pathway remodels mitochondrial cristae and mobilizes cytochrome c during apoptosis. *Dev Cell* 2: 55–67. doi:10.1016/s1534-5807(01)00116-2

Segawa M, Wolf DM, Hultgren NW, Williams DS, van der Bliek AM, Shackelford DB, Liesa M, Shirihai OS (2020) Quantification of cristae architecture reveals time-dependent characteristics of individual mitochondria. *Life Sci Alliance* 3: e201900620. doi:10.26508/lsa.201900620

Stephan T, Brüser C, Deckers M, Steyer AM, Balzarotti F, Barbot M, Behr TS, Heim G, Hübner W, Ilgen P, et al (2020) Micos assembly controls mitochondrial inner membrane remodeling and crista junction redistribution to mediate cristae formation. *EMBO J* 39: e104105. doi:10.15252/embj.2019104105

Tarasenko D, Barbot M, Jans DC, Kroppen B, Sadowski B, Heim G, Möbius W, Jakobs S, Meinecke M (2017) The micos component mic60 displays a conserved membrane-bending activity that is necessary for normal cristae morphology. *J Cell Biol* 216: 889–899. doi:10.1083/jcb.201609046

Tsai PI, Lin CH, Hsieh CH, Papakyrikos AM, Kim MJ, Napolioni V, Schoor C, Couthouis J, Wu RM, Wszolek ZK, et al (2018) Pink1 phosphorylates mic60/mitofilin to control structural plasticity of mitochondrial crista junctions. *Mol cell* 69: 744–756.e6. doi:10.1016/j.molcel.2018.01.026

Urbach J, Kondadi AK, David C, Naha R, Deinert K, Reichert AS, Anand R (2021) Conserved gxxxg and wn motifs of mic13 are essential for bridging two micos subcomplexes. *Biochim Biophys Acta Biomembr* 1863: 183683. doi:10.1016/j.bbamem.2021.183683

Vogel F, Bornhövd C, Neupert W, Reichert AS (2006) Dynamic subcompartmentalization of the mitochondrial inner membrane. *J Cell Biol* 175: 237–247. doi:10.1083/jcb.200605138

von der Malsburg K, Müller JM, Bohnert M, Oeljeklaus S, Kwiatkowska P, Becker T, Loniewska-Lwowska A, Wiese S, Rao S, Milenkovic D, et al (2011) Dual role of mitofilin in mitochondrial membrane organization

and protein biogenesis. *Dev Cell* 21: 694–707. doi:10.1016/j.devcel.2011.08.026

Wang C, Taki M, Sato Y, Tamura Y, Yaginuma H, Okada Y, Yamaguchi S (2019) A photostable fluorescent marker for the superresolution live imaging of the dynamic structure of the mitochondrial cristae. *Proc Natl Acad Sci U S A* 116: 15817–15822. doi:10.1073/pnas.1905924116

Wolf DM, Segawa M, Kondadi AK, Anand R, Bailey ST, Reichert AS, van der Bliek AM, Shackelford DB, Liesa M, Shirihai OS (2019) Individual cristae within the same mitochondrion display different membrane potentials and are functionally independent. *EMBO J* 38: e101056. doi:10.15252/embj.2018101056

Wurm CA, Jakobs S (2006) Differential protein distributions define two sub-compartments of the mitochondrial inner membrane in yeast. *FEBS Lett* 580: 5628–5634. doi:10.1016/j.febslet.2006.09.012

Zick M, Rabl R, Reichert AS (2009) Cristae formation-linking ultrastructure and function of mitochondria. *Biochim Biophys Acta* 1793: 5–19. doi:10.1016/j.bbamcr.2008.06.013

Supplementary material - Cristae dynamics is modulated in bioenergetically compromised mitochondria. Life Sci Alliance. 2023 Nov 13. doi: 10.26508/lsa.202302386

Mathias Golombek, Thanos Tsigaras, Yulia Schaumkessel, Sebastian Hänsch, Stefanie Weidtkamp-Peters, Ruchika Anand, Andreas S. Reichert, Arun Kumar Kondadi

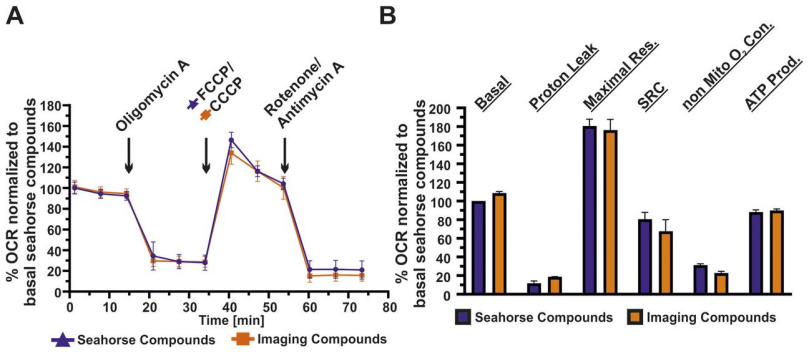

Figure S1. The mitochondrial toxins used in this study respond as expected. (A) Representative experiment showing percentage oxygen consumption rates normalized to basal respiration of the control group (commercially available Seahorse kit). The data were obtained with commercially available Seahorse Mito Stress Test kit compounds and mitochondrial toxins used throughout the article at corresponding concentration. FCCP was used in a commercially available Seahorse test kit, whereas CCCP was used otherwise including microscopy experiments throughout the article. **(B)** Comparison of various bioenergetic parameters shows no change in oxygen consumption of HeLa cells including basal, maximal, and spare respiratory capacity. Error bars represent SD of three independent experiments.

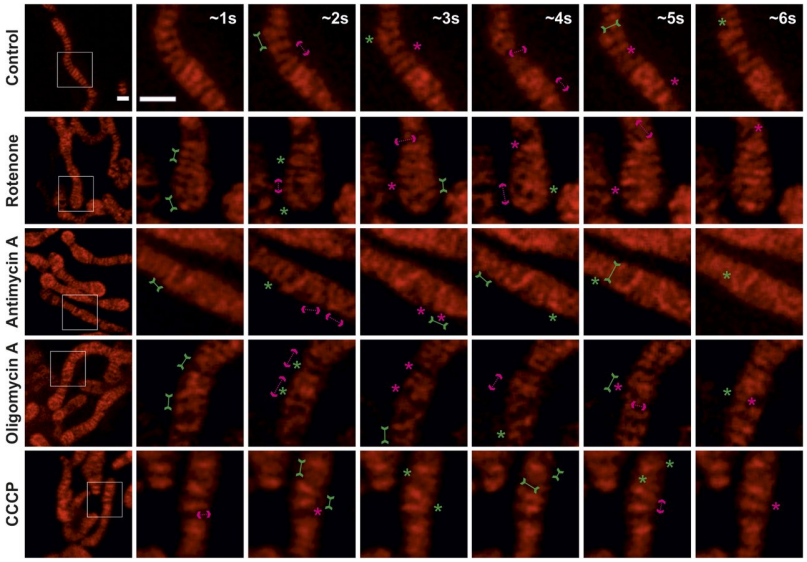

Figure S2. Crista merging and splitting events can be resolved in live-cell STED SR images even without deconvolution. Respective raw data of live-cell STED SR images, shown in Fig 1A, of HeLa cells expressing ATP5I-SNAP and stained with silicon–rhodamine, untreated or treated with the rotenone, antimycin A, oligomycin A, and CCCP. Images at the extreme left show whole mitochondria along with white inset boxes. Other images on the right-side display time-lapse series (0.94 s/frame) of zoom of mitochondrial portion at ~1, 2, 3, 4, 5, and 6 s. Green and magenta asterisks show corresponding merging and splitting events, whereas solid green arrows pointing inward and dotted magenta arrows pointing outward show imminent merging and splitting events, respectively. Scale bar represents 500 nm.

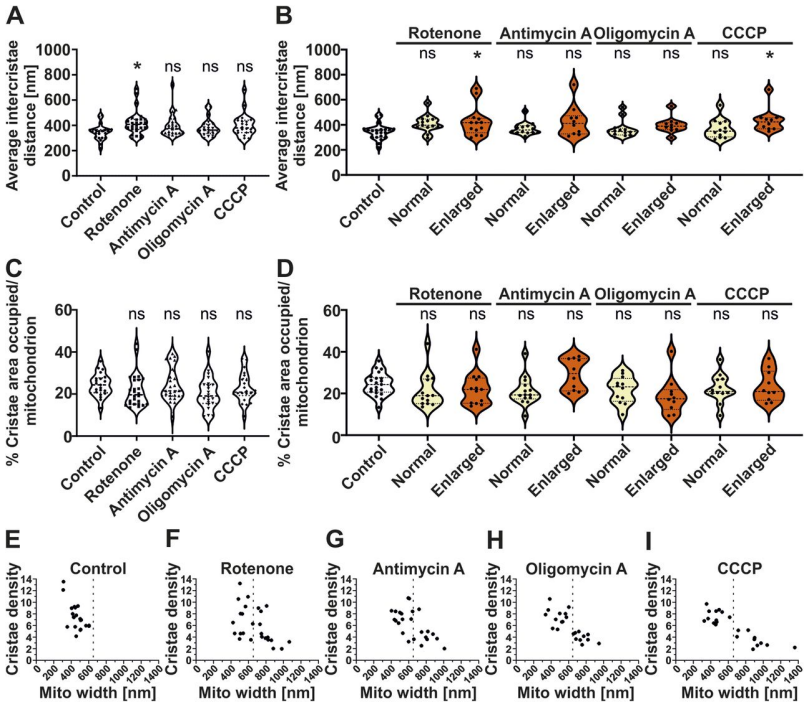

Figure S3. Mitochondrial enlargement correlates with reduced cristae density with no change in the cristae area. (A, B) Quantification of average intercristae distance (nm) per mitochondria; (A) pooled data from three individual experiments are shown as violin plots with individual data points (21–26 mitochondria). Each symbol represents one mitochondrion. **(B)** Data were separated into normal (<650 nm) or enlarged (≥650 nm) mitochondria with each condition having 10–21 mitochondria. Conditions are compared with the untreated control group. **(C, D)** Quantification of percentage crista area occupied per total mitochondrial area shown as violin plots with individual data points. Each symbol represents one mitochondrion. **(D)** Data were separated into normal and enlarged mitochondria (10–21 mitochondria). Conditions are compared with untreated control group. **(E, F, G, H, I)** Correlation of cristae density and mitochondrial width in control and toxin-treated conditions. **(E, F, G, H, I)** Dotted line at 650 nm separates normal and enlarged mitochondria distributed in control cells (E) and cells treated with rotenone (F), antimycin A (G), oligomycin A (H), and CCCP (I) from three independent experiments with each condition including 21–26 mitochondria. (ns = nonsignificant *P*-value > 0.05, **P*-value ≤ 0.05). One-way ANOVA was used for statistical analysis.

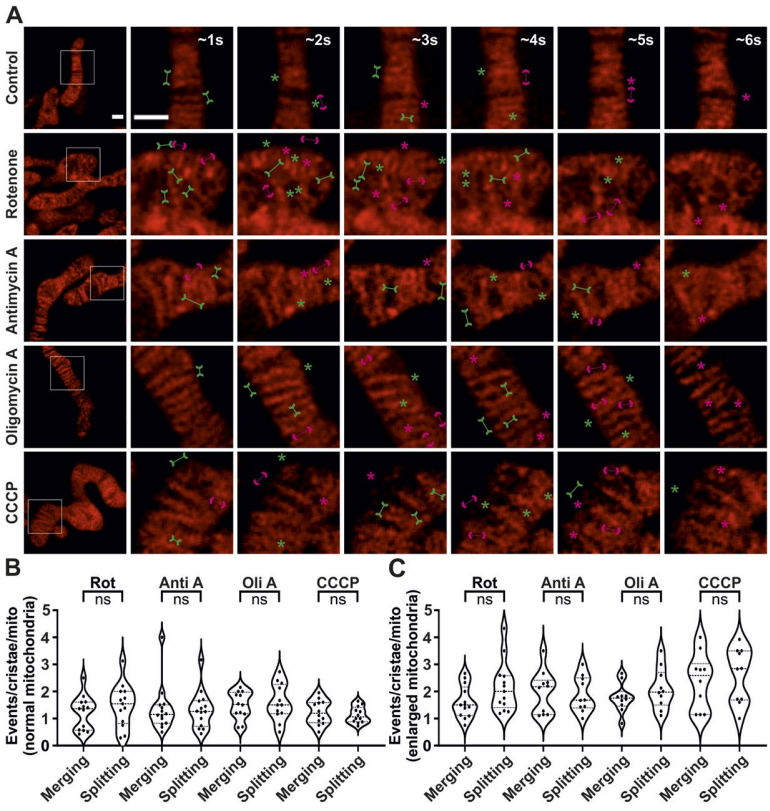

Figure S4. Crista merging and splitting events are present in a balanced manner in enlarged mitochondria. (A) Respective raw data of live-cell STED SR images shown in Fig 3A of HeLa cells, expressing ATP5I-SNAP and stained with silicon–rhodamine, untreated (containing normal mitochondria) or treated (containing enlarged mitochondria) with the various mitochondrial toxins. Images at the extreme left show whole mitochondria along with white inset boxes. Other images on the right-side display time-lapse series (0.94 s/frame) of zoom of mitochondrial portion in the white inset at ~1, 2, 3, 4, 5, and 6 s. Green and magenta asterisks show corresponding merging and splitting events, whereas green arrows pointing inward and dotted magenta arrows pointing outward show imminent merging and splitting events, respectively. Scale bar represents 500 nm. **(A, B, C)** Blind quantification of merging and splitting events of cristae per mitochondrion in different conditions described in (A) and further separated into normal (B) and enlarged (C) mitochondria. Statistical analysis was performed within the individual treatment conditions using one-way ANOVA. (ns = nonsignificant *P*-value > 0.05).

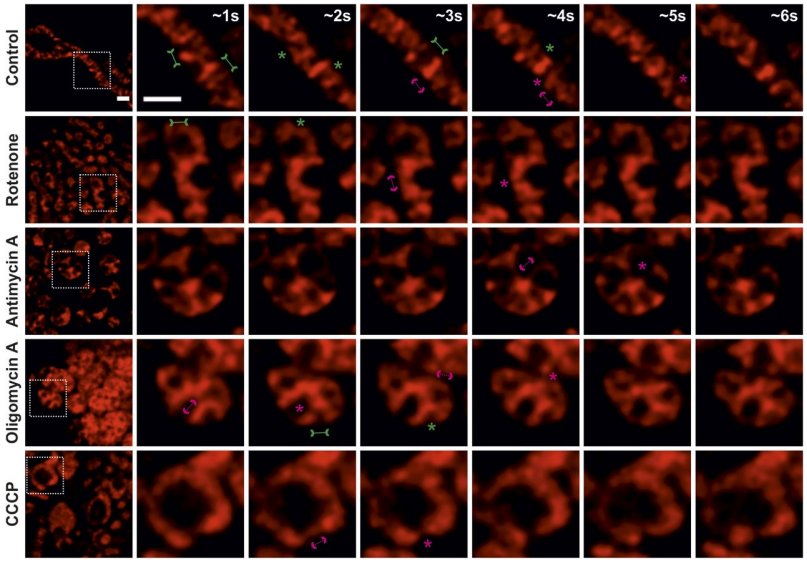

Figure S5. Fragmentation of mitochondria along with swelling is observed 4 h after treatment with mitochondrial toxins. HeLa cells expressing ATP5I-SNAP were treated with silicon–rhodamine for imaging cristae while being treated with mitochondrial toxins for 4 h. Mitochondrial morphology was highly fragmented accompanied by enlargement. Cristae morphology revealed highly interconnected cristae with reduced cristae dynamics as opposed to untreated HeLa cells.

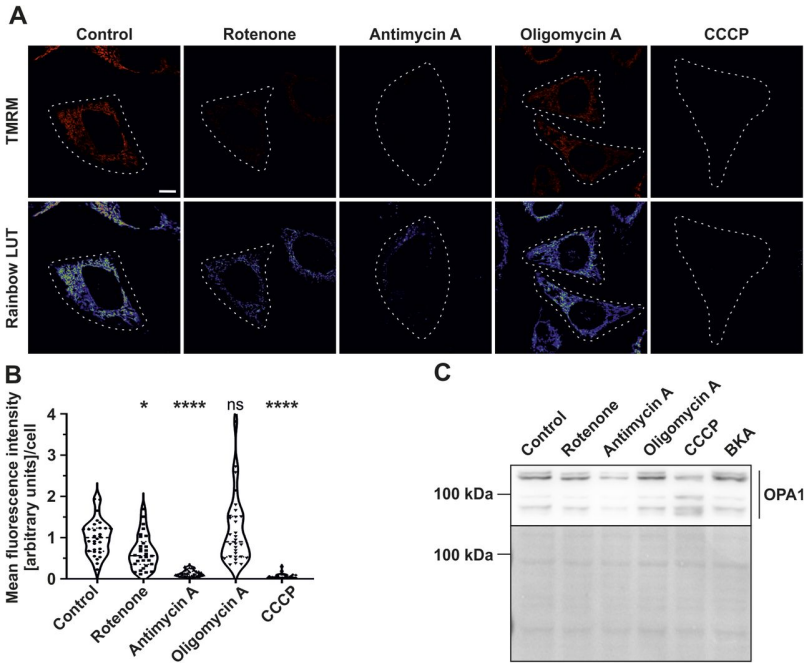

Figure S6. Mitochondrial membrane potential is depleted upon treatment with rotenone, antimycin A, and CCCP but not oligomycin A. (A) Representative confocal images of HeLa cells (indicated by white dotted line) stained with TMRM either untreated or treated with rotenone, antimycin A, oligomycin A, and CCCP (top row). Corresponding pseudocolour rainbow LUT intensities of respective TMRM signal is shown in the bottom row. Scale bar represents 10 µm. **(B)** Quantification of $\Delta\Psi_m$ based on mean TMRM fluorescence intensity measurements of individual HeLa cells either treated without or with various mitochondrial toxins mentioned. Results are shown as violin plots, with all individual data points. Data are obtained from three independent experiments (52–65 cells). Statistical comparisons were drawn between the untreated control group and the toxin-treated conditions. (ns = nonsignificant *P*-value > 0.05, **P*-value ≤ 0.05, *****P*-value ≤ 0.0001). One-way ANOVA was used for statistical analysis. **(C)** Western blots showing L-OPA1 and S-OPA1 forms in HeLa cells treated with or without mitochondrial toxins. Only CCCP treatment shows enhanced S-OPA1 forms. Lower panel depicts Ponceau S staining of the membrane as loading control.

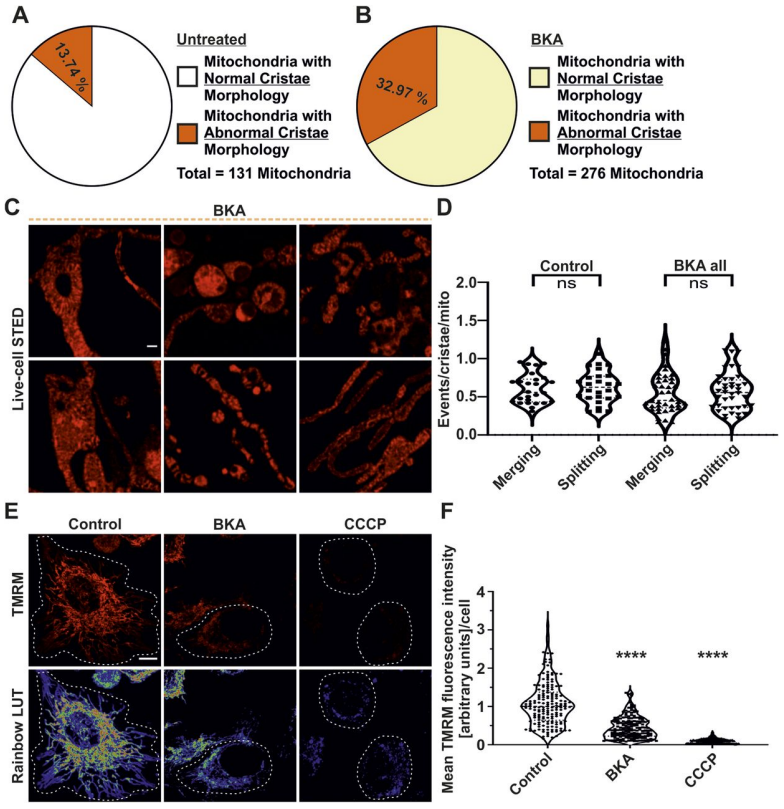

Figure S7. Inhibition of ANT perturbs cristae morphology and reduces $\Delta\Psi_m$ without influencing the balance of merging and splitting events. (A, B) Pie charts showing percentage mitochondria with normal and abnormal cristae morphology in (A) untreated and (B) BKA-treated HeLa cells. 131 and 276 mitochondria from 54 and 95 STED SR images were considered, respectively. **(C)** Representative STED SR images of HeLa cells expressing ATP5I-SNAP, stained with silicon–rhodamine, display perturbed crista morphology in BKA-treated cells. Scale bar represents 500 nm. **(D)** Blind quantification of cristae merging and splitting events per mitochondrion when HeLa cells were treated with BKA or not. Pooled data from five separate experiments with 26–40 mitochondria are shown as violin plots with individual data points. Each symbol represents one mitochondrion. **(E)** Representative confocal images of control HeLa cells and cells treated with BKA or CCCP which were stained with TMRM are shown in the top panel. Corresponding pseudocolor rainbow LUT intensities are shown in the bottom panel. Scale bar represents 10 µm. **(F)** Quantification of $\Delta\Psi_m$ based on TMRM mean fluorescence intensity measurements of individual HeLa cells that were not treated or treated with BKA or CCCP. Results are shown as violin plots including all individual data points. Data are obtained from three independent experiments, with each condition having 170–191 cells. Statistical comparisons were drawn between the untreated control group and the toxin-treated conditions. (ns = nonsignificant *P*-value > 0.05, ****P-value ≤ 0.0001). One-way ANOVA was used for statistical analysis.

3.2. MIC26 and MIC27 cooperate to regulate cardiolipin levels and the landscape of OXPHOS complexes

Research Article

TRANSPARENT PROCESS OPEN ACCESS Life Science Alliance

MIC26 and MIC27 cooperate to regulate cardiolipin levels and the landscape of OXPHOS complexes

Ruchika Anand[1], Arun Kumar Kondadi[1], Jana Meisterknecht[2,3,4], Mathias Golombek[1], Oliver Nortmann[1], Julia Riedel[1], Leon Peifer-Weiß[1], Nahal Brocke-Ahmadinejad[1], David Schlütermann[5], Björn Stork[5], Thomas O Eichmann[6,7], Ilka Wittig[2,3,4], Andreas S Reichert[1]

Homologous apolipoproteins of MICOS complex, MIC26 and MIC27, show an antagonistic regulation of their protein levels, making it difficult to deduce their individual functions using a single gene deletion. We obtained single and double knockout (DKO) human cells of *MIC26* and *MIC27* and found that DKO show more concentric onion-like cristae with loss of CJs than any single deletion indicating overlapping roles in formation of CJs. Using a combination of complexome profiling, STED nanoscopy, and blue-native gel electrophoresis, we found that MIC26 and MIC27 are dispensable for the stability and integration of the remaining MICOS subunits into the complex suggesting that they assemble late into the MICOS complex. MIC26 and MIC27 are cooperatively required for the integrity of respiratory chain (super) complexes (RCs/SC) and the F_1F_o–ATP synthase complex and integration of F_1 subunits into the monomeric F_1F_o–ATP synthase. While cardiolipin was reduced in DKO cells, overexpression of cardiolipin synthase in DKO restores the stability of RCs/SC. Overall, we propose that MIC26 and MIC27 are cooperatively required for global integrity and stability of multimeric OXPHOS complexes by modulating cardiolipin levels.

DOI 10.26508/lsa.202000711 | Received 20 March 2020 | Revised 20 July 2020 | Accepted 21 July 2020 | Published online 11 August 2020

Introduction

Mitochondria are vital cellular organelles that perform several important functions involving energy conversion, cellular metabolism, reactive oxygen species (ROS) production, heme synthesis, calcium homeostasis, and apoptosis. Mitochondrial shape is highly variable and changes constantly depending on energy demands and mitochondrial functions. Mitochondria are enclosed by a double membrane where the inner membrane (IM) folds inward to form the cristae membrane. Cristae host respiratory chain complexes and therefore are the major sites of energy conversion (Vogel et al, 2006; Wurm & Jakobs, 2006). Cristae are compositionally and functionally distinct from the rest of the IM, called inner boundary membrane (IBM) (Vogel et al, 2006; Wurm & Jakobs, 2006), presumably due to the presence of crista junctions (CJs) which are small, pore-, or slit-like openings present at the neck of a crista (Perkins et al, 1997; Mannella et al, 2001). CJs with diameter of 12–40 nm are proposed to act as diffusion barrier for ions and metabolites and therefore divide mitochondria to various sub-compartments which help streamline mitochondrial functions (Mannella, 2008; Zick et al, 2009; Mannella et al, 2013). For example, cytochrome *c* is normally trapped in the intracristal space and is released into cytosol during apoptosis after widening of CJs (Scorrano et al, 2002; Frezza et al, 2006). Recently, it was shown that CJs provide electric insulation between cristae that can display different membrane potential (Wolf et al, 2019). Cristae shape varies considerably depending on the bioenergetic demands during physiological changes and stress, including hypoxia, nutrient starvation, ROS, or induction of apoptosis (Mannella, 2006; Gomes et al, 2011; Cogliati et al, 2016; Pernas & Scorrano, 2016; Plecita-Hlavata et al, 2016; Baker et al, 2019; Dlaskova et al, 2019). The shape of cristae was suggested to govern the assembly and the stability of the respiratory chain complexes (RCs) and supercomplexes (SCs) (Cogliati et al, 2013). Aberrant cristae are present in a variety of human diseases but whether cristae ultrastructural manifestations are a cause or consequences of the pathology is often unclear. Using live-cell stimulated emission depletion (STED) super-resolution nanoscopy, we recently showed that CJs and cristae undergo dynamic remodelling in a balanced and reversible manner that is MICOS complex-dependent (Kondadi et al, 2020).

The molecular mechanisms for shaping cristae are beginning to be understood, yet an interplay of three major protein complexes, namely, OPA1, F_1F_o–ATP synthase, and the MICOS complex, is known to be required for formation and maintenance of cristae and CJs in

[1]Institute of Biochemistry and Molecular Biology I, Heinrich Heine University Düsseldorf, Medical Faculty, Düsseldorf, Germany [2]Functional Proteomics, Sonderforschungsbereich (SFB) 815 Core Unit, Faculty of Medicine, Goethe-University, Frankfurt am Main, Germany [3]Cluster of Excellence "Macromolecular Complexes", Goethe University, Frankfurt am Main, Germany [4]German Center of Cardiovascular Research (DZHK), Partner Site RheinMain, Frankfurt, Germany [5]Institute of Molecular Medicine I, Heinrich Heine University Düsseldorf, Medical Faculty, Düsseldorf, Germany [6]Center for Explorative Lipidomics, BioTechMed-Graz, Graz, Austria [7]Institute of Molecular Biosciences, University of Graz, Graz, Austria

Correspondence: anand@hhu.de; reichert@hhu.de

eukaryotic cells (Kondadi et al, 2019). OPA1 is a large dynamin-like GTPase present in the IM and has dual functions in managing mitochondrial fusion and cristae morphology (Cipolat et al, 2004). Loss of OPA1 causes severe fragmentation of mitochondria combined with reduced number of cristae that are swollen (Duvezin-Caubet et al, 2006; Song et al, 2007; Anand et al, 2013; MacVicar & Langer, 2016; Lee et al, 2017). The F_1F_o–ATP synthase complex well known for its classical role in converting ATP from ADP and P_i using the electrochemical gradient energy across the IM also plays an important role in cristae formation (Paumard et al, 2002). The loss of the dimeric-specific subunits of F_1F_o–ATP synthase (Su e or Su g) leads to aberrant cristae structure with loss of the cristae rims and an arrangement of cristae as onion slices (Paumard et al, 2002). Long ribbon-like rows of F_1F_o–ATP synthase dimers are present at the cristae rims (Davies et al, 2011; Blum et al, 2019). An important breakthrough in understanding the mechanisms of cristae and CJs formation comes from the identification of several subunits of the MICOS ("mitochondrial contact site and cristae organizing system") complex (Rabl et al, 2009; Harner et al, 2011; Hoppins et al, 2011; von der Malsburg et al, 2011). MICOS is a large oligomeric complex required for the formation of contact sites between outer membrane and IM and formation of CJs. MICOS is highly conserved with seven bona fide subunits identified till now in mammalian system: MIC10/Minos1, MIC13/Qil1, MIC19/CHCHD3, MIC25/CHCHD6, MIC26/APOO, MIC27/APOOL, and MIC60/Mitofilin (Rampelt et al, 2017b; Quintana-Cabrera et al, 2018a). MIC10 and MIC60 are the core components of the MICOS complex because deletion of either of them causes virtually complete loss of CJs and cristae featuring as onion slices (Harner et al, 2011; Hoppins et al, 2011; von der Malsburg et al, 2011; Callegari et al, 2019; Kondadi et al, 2020). Mutations in bona fide subunits of MICOS, *MIC60*, *MIC13*, and *MIC26* are found in human diseases such as Parkinson's (Tsai et al, 2018), mitochondrial encephalopathy with liver dysfunction (Guarani et al, 2016; Zeharia et al, 2016) and mitochondrial myopathy with lactic acidosis, cognitive impairment, and autistic features (Beninca et al, 2020), respectively.

Most of the research about cristae-shaping molecules, particularly the MICOS complex, are performed in baker's yeast. There is a lack of comprehensive studies addressing the individual role of mammalian MICOS subunits in managing cristae structure and mitochondrial function. We have earlier identified novel MICOS subunits in mammals, namely, MIC13, MIC26 and MIC27 using complexome profiling (Weber et al, 2013; Koob et al, 2015; Anand et al, 2016). In this study, we focus on determining the molecular role of the homologous subunits of MICOS, MIC26 and MIC27, in regulating cristae structure. MIC26/Apolipoprotein O and MIC27/Apolipoprotein O-like belong to family of apolipoproteins. Normally, apolipoproteins bind to lipids and transport them within the lymphatic and circulatory system. MIC26 was identified at elevated levels in the heart transcriptome of a diabetic model in dogs (Lamant et al, 2006) and its glycosylated (secreted) form is present at higher amounts in blood plasma of human patients of acute coronary syndrome (ACS) (Yu et al, 2012), indicating its significance to human health. We found that next to this secreted glycosylated form (55 kD), a non-glycosylated form of MIC26/APOO (22 kD) resides in the IM representing a bona fide subunit of MICOS complex (Koob et al, 2015). Only a mitochondrial form of MIC27 is observed so far. MIC26 and MIC27 are part of the subcomplex of MICOS, MIC13-MIC10-MIC26-MIC27 where MIC27 was shown to bind to cardiolipin (CL) (Weber et al, 2013; Friedman et al, 2015), and levels of MIC26 and MIC27 are positively correlated with tafazzin, an enzyme required for cardiolipin remodelling in mitochondria (Koob et al, 2015). Both Mic26 and Mic27 are considered noncore components of the MICOS complex in yeast because their individual deletion does not lead to drastic cristae alterations (Harner et al, 2011; Hoppins et al, 2011; von der Malsburg et al, 2011; Zerbes et al, 2016; Eydt et al, 2017). In yeast, Mic26-Mic27 antagonism and cardiolipin are required for assembly of Mic10 oligomers (Rampelt et al, 2018). Partial knockdown of *MIC26* and *MIC27* in mammalian cells also causes only moderate cristae defects (Weber et al, 2013; Koob et al, 2015). Intriguingly, Western blots revealed that steady-state levels of MIC26 and MIC27 are reciprocally regulated as depletion or overexpression of one of them is always accompanied with increase or decrease in protein level of the second protein, respectively, showing an antagonistic regulation (Koob et al, 2015; Rampelt et al, 2018). This antagonistic regulation makes it difficult to infer their individual role using only single deletion mutants. This could mean that the moderate defects observed in cristae structure upon single depletion of MIC26 or MIC27 might occur because of their partial overlapping function and compensation by the second protein. Therefore, to determine the individual as well as overlapping functions of MIC26 and MIC27, we decided to knockout *MIC26* and *MIC27* individually and in combination in mammalian cell lines. We found that double knockout (DKO) cell lines lacking *MIC26* and *MIC27* show accumulation of aberrant cristae and reduced F_1F_o–ATP synthase activity and cellular respiration. This was accompanied by decreased steady-state levels of OXPHOS complexes with reduced cardiolipin levels, and complexome profiling showed a partial dissociation of F_1 subunits from the F_1F_o monomer in the DKO of *MIC26* and *MIC27*. Overall, we suggest that MIC26 and MIC27 act in cooperation to regulate cristae structure and the global integrity of respiratory chain complexes and supercomplexes (RCs and SCs) and F_1F_O–ATP synthase complex.

Results

MIC26 and MIC27 are reciprocally regulated at the posttranscriptional level

To determine the molecular role of MIC26 and MIC27 in maintaining cristae structure, we obtained single as well as double knockout (DKO) cells for *MIC26* and *MIC27*. These cells were generated in haploid cell lines, HAP1 cells. Single knockouts (SKOs) were prepared using non-homologous end joining CRISPR-Cas method, yielding a 1-bp insertion and an 8-bp deletion in exon 3 of *MIC26* and *MIC27*, respectively. These insertions or deletions yielded frame shift and missense mutations causing premature termination of transcription and complete loss of proteins determined by Western blot analysis using antibodies against endogenous MIC26 or MIC27 (Fig 1A). The DKO cells lacking MIC26 and MIC27 were obtained by targeting *MIC27* using CRISPR-Cas that causes a 160-bp deletion in exon 3 of *MIC27* in *MIC26* KO cells. DKO cells lack the full-length

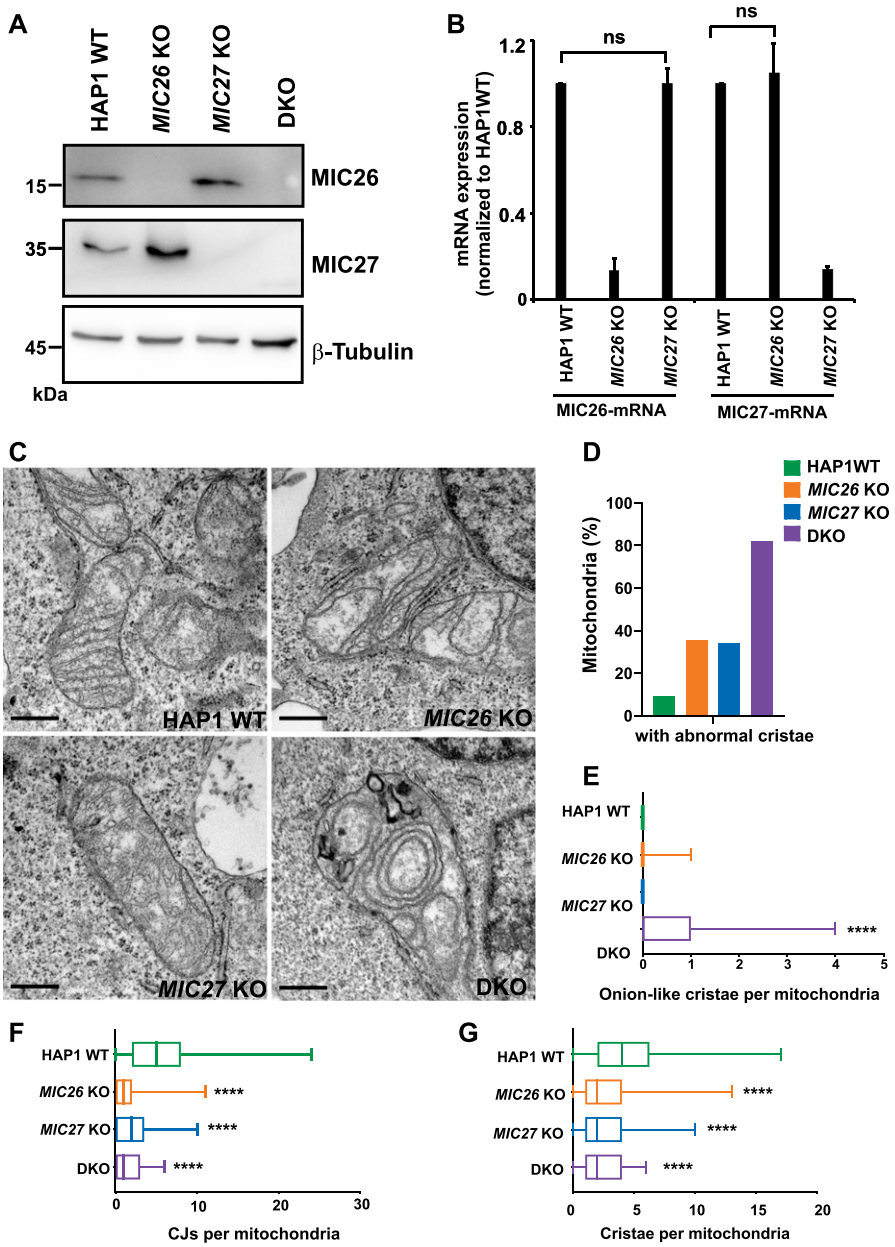

Figure 1. MIC26 and MIC27 cooperatively determine cristae morphology and are required for formation of crista junctions (CJs).
(A) Western blots from total cell lysates from HAP1 WT, *MIC26* KO, *MIC27* KO or double knockout (DKO) cells show loss of respective protein and increased level of the respective other protein (reciprocal regulation). DKO cells lacking *MIC26* and *MIC27* show virtually a complete loss of both full-length proteins. **(B)** Quantification from qRT-PCR using HAP1 WT, *MIC26* KO or *MIC27* KO cells and probed for the mRNA levels of MIC26 or MIC27 using specific primers. The house-keeping genes HPRT1 and GAPDH were used as controls. Data from three independent experiments represented as mean ± SEM. *P*-values calculated using *t* test show no significant differences (ns). **(C)** Representative images from electron microscopy in HAP1 WT, *MIC26* KO, *MIC27* KO, or DKO cells show accumulation of concentric cristae in DKO cells and loss of CJs in single knockouts (SKOs) and DKO cells. Scale bar 0.5 μm. **(D)** Bar graph show the percentage of mitochondria that have abnormal cristae in respective cell lines. Data from total of 60–90 mitochondrial sections of two independent experiments are represented. **(E)** Box plot showing the number of concentric onion-like cristae per mitochondrial section. DKO cells show high accumulation of concentric cristae. Data from total of 60–90 mitochondrial section of two independent experiments. ****P-value ≤ 0.0001 indicated in the plot shows comparison between WT and DKO. *t* test was used for statistical analysis. **(F)** Box plot showing the number of CJs per mitochondrial section in respective cell lines. SKOs and DKO cells have significant reduction in CJs per mitochondrial section. Data from total of 60–90 mitochondrial section of two independent experiments. ****P-value ≤ 0.0001. *P*-value indicated in the graph show comparison between WT and respective cell lines. Comparisons between *MIC26* KO and *MIC27* KO as well as DKO with *MIC26* KO were not significantly different (*P*-value > 0.5). Comparison between *MIC27* KO and DKO show slightly significant difference (*P*-value = 0.04). *t* test was used for statistical analysis. **(G)** Box plot showing the number of cristae per mitochondrial section in respective cell lines. SKOs and DKO cells have significant reduction in cristae per mitochondrial section. Data from total of 60–90 mitochondrial sections of two independent experiments. ****P-value ≤ 0.0001. *P*-value indicated in the graph show comparison between WT and respective cell lines. Comparisons between *MIC26* KO and *MIC27* KO as well as DKO with *MIC26* KO or *MIC27* KO were not significantly different (*P*-value > 0.5). *t* test was used for statistical analysis.

MIC27 protein, although occasionally we observe a very faint band at lower molecular weight, which likely occurs because of alternative splicing and skipping the deleted exon. The steady-state levels of MIC26 and MIC27 were increased in *MIC27* and *MIC26* KO cells, respectively, corroborating the reciprocal and antagonist regulation reported earlier (Koob et al, 2015) (Figs 1A and 3C). To check whether this regulation at steady-state levels is determined by a transcriptional regulation, we performed quantitative real time PCR (qRT-PCR) using primers specific to mRNA of MIC26 and MIC27 and compared them with the house-keeping genes, HPRT1 and GAPDH in *MIC26* and *MIC27* SKOs. We found that the mRNA levels of MIC26 and MIC27 are not significantly altered in *MIC27* and *MIC26* KO cell lines, respectively (Fig 1B), implying that this change in the protein levels of MIC26 or MIC27 occurs at a posttranscriptional level.

MIC26 and MIC27 are cooperatively required to maintain mitochondrial cristae ultrastructure

Depletion of MIC26 or MIC27 was reported to show moderate defects in cristae structure accounting for these subunits to be considered as noncore subunits of the MICOS complex (Weber et al, 2013; Koob et al, 2015). However, as stated above, steady-state levels of MIC26 or MIC27 are reciprocally maintained, and deletion of one of these subunits is always accompanied by concomitant increase in the respective other protein (Fig 1A). Therefore, it is possible that cristae

defects observed because of the deletion of single subunit is masked or caused by simultaneous up-regulation of the other homologous subunit. This could also point to a partial or complete redundant function of MIC26 and MIC27 in regulating cristae morphology. Hence, to determine the combined molecular role of MIC26 and MIC27 in regulating cristae architecture, we analyzed the ultrastructure of mitochondria using electron microscopy in SKOs and DKO cells of *MIC26* and *MIC27*. Control HAP1 cells show typical lamellar cristae that are arranged parallel to each other and connected to the IBM via CJs (Fig 1C). At a first glance, only cristae from DKO cells show the presence of characteristic MICOS-specific cristae defects where cristae are arranged as onion stacks in the mitochondria (Fig 1C). We determine the percentage of mitochondria that contain abnormal cristae in all the cell lines and found that while SKOs show accumulation of aberrant cristae, much higher percentage of mitochondria show abnormal cristae in DKO cells (Fig 1D). In addition, the appearance of aberrant onion-like cristae structures was significantly increased only in DKO cells compared with control or SKOs (Fig 1E). Longitudinal and vesicular cristae were more prevalent in *MIC26* KO and *MIC27* KO, respectively (Fig 1C). We performed a detailed analysis for various parameters using the electron micrographs from all cell lines. We observed that both SKOs and DKO cells show significantly reduced CJs per mitochondrial section compared with the controls (Fig 1F). In addition, the number of cristae per mitochondrial section was significantly reduced in all the KO cells compared with control, with a slightly more pronounced reduction in DKO cells compared with SKOs (Fig 1G). Since MIC26 and MIC27 only partially complement each other regarding cristae defects in their respective SKOs and as the most pronounced effects are seen in DKO cells (Fig 1C–G), we can conclude that both MIC26 and MIC27 are functionally overlapping, yet not fully redundant.

Simultaneous deletion of MIC26 and MIC27 causes reduced respiration and mitochondrial fragmentation

Next, we asked how cristae defects associated with SKOs and DKO cells lacking *MIC26* and/or *MIC27* affect mitochondrial function. First, we analyzed oxygen consumption rates to determine the

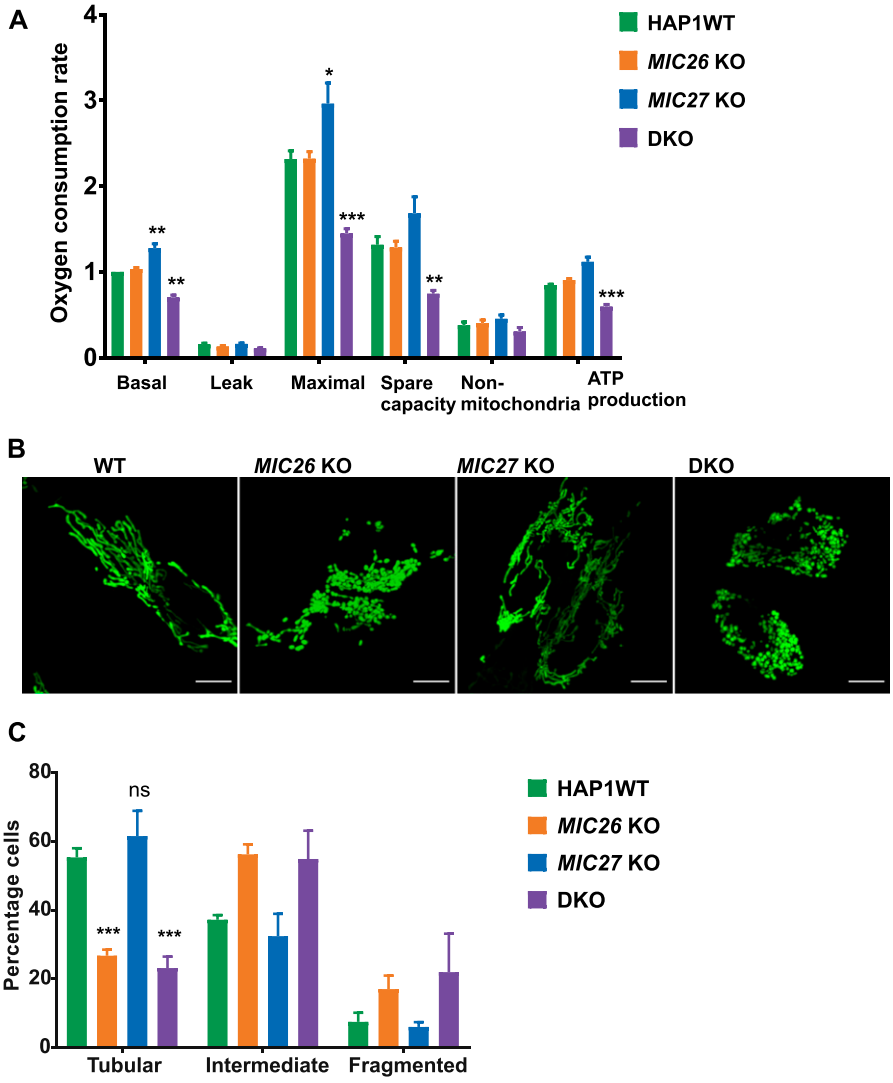

Figure 2. Mitochondrial respiration is impaired and mitochondria show fragmentation in double knockout (DKO) cells lacking *MIC26* and *MIC27*.
(A) Oxygen consumption rates (pmol O_2/s, normalized for cell numbers by Hoechst staining), including basal respiration (Basal), proton leak, maximal respiration (Maximal) after uncoupling by FCCP, spare respiratory capacity (Spare capacity), non-mitochondrial respiration (Non-mitochondrial), and ATP production is shown for HAP1 WT, *MIC26* KO, *MIC27* KO, or DKO cells. Data are normalized to basal respiration from HAP1 WT and the mean ± SEM from four independent experiments is shown. DKO cells lacking *MIC26* and *MIC27* show reduced respiration, whereas *MIC27* KO show slight but significant increase compared with HAP1 WT. **P*-value ≤ 0.05, ***P*-value ≤ 0.01, ****P*-value ≤ 0.001 (*t* test). For comparison of basal respiration, one sample *t* test was performed. **(B)** Representative confocal images of mitochondria from HAP1 WT, *MIC26* KO, *MIC27* KO, or DKO cells show mitochondrial fragmentation in *MIC26* KO and DKO cells. **(C)** Quantification of percentage of cells having tubular, intermediate, or fragmented mitochondrial morphology in HAP1 WT, *MIC26* KO, *MIC27* KO, or DKO cells. Data show mean ± SEM from three independent experiments. *t* test was used for comparison of percentage of cells having tubular mitochondria in *MIC26* KO, *MIC27* KO, or DKO cells with HAP1 WT. ****P*-value ≤ 0.001.

cellular respiration in SKOs and DKO cells. We found that basal and maximal mitochondrial respiration in DKO cells are significantly reduced compared with control cells (Fig 2A). Although respiration in *MIC26* KO cells was not grossly altered despite the ultrastructural defects, we observed a slight but significant increase in basal and maximal respiration of *MIC27* KO compared with controls (Fig 2A). This indicates that in these cell lines, only the simultaneous deletion of MIC26 and MIC27 can sufficiently affect the mitochondrial respiration, whereas the respiration in SKOs can be compensated (or even enhanced) due to concomitant overexpression of the second protein. To check for the specificity of respiration defects in DKO cells, we stably reintroduced MIC26 and/or MIC27 in these cell lines (Fig S1A) and found that overexpression of both MIC26 and MIC27 could significantly restore the oxygen consumption rates of DKO (Fig S1B). Mitochondrial morphology is another determinant of cellular or mitochondrial dysfunction (Duvezin-Caubet et al, 2006). Thus, we checked the mitochondrial morphology in SKOs and DKO cells of *MIC26* and *MIC27* and found that *MIC26* KO and DKO cells show a similar increase in the extent of mitochondrial fragmentation (Fig 2B and C), whereas *MIC27* KO cells show normal mitochondria which were comparable to control cells (Fig 2B and C). This indicates a role of MIC26 in regulating mitochondrial morphology that cannot be compensated by MIC27 and is therefore independent of MIC27 function.

MIC26 and MIC27 are dispensable for the incorporation of other MICOS subunits into MICOS complex

To determine the molecular basis for the reduction in the amount of CJs that we observed in SKOs and DKO cells of *MIC26* and *MIC27* (Fig 1F), we asked whether MIC26 and MIC27 influence the MICOS complex and/or the assembly of the F_1F_o–ATP synthase, two important players determining cristae morphogenesis in baker's yeast (Rabl et al, 2009; Eydt et al, 2017; Rampelt et al, 2017a). We characterized the immunostaining pattern of MIC26 and MIC27 using STED super-resolution nanoscopy. It was shown that MIC10 or MIC60, the core MICOS subunits, show an equally spaced rail-like arrangement of punctae across the mitochondrial length (Jans et al, 2013; Stoldt et al, 2019; Kondadi et al, 2020). The staining pattern of MIC26 and MIC27 resembles the MICOS-specific punctae and appeared similar to that of MIC60 and MIC10 indicating that MIC26 and MIC27 assembled in a regular rail-like fashion characteristic of the MICOS complex (Figs 3A and 4A). Next, we asked how the loss of MIC26 and/or MIC27 affects the stability or integrity of the MICOS complex. First, we determined the steady-state levels of other MICOS subunits in SKOs and DKO cells. We did not observe any significant and consistent change in steady-state levels of other MICOS subunits in SKOs or DKO cells apart from increase in levels of MIC26 and MIC27 in *MIC27* and *MIC26* KO cells (reciprocal regulation) (Fig 3B and C). Only a minor increase in the amount of MIC25 was seen in DKO cells (Fig 3C). We conclude that MIC26 and MIC27 are not required for the stability of other MICOS subunits. Second, we checked how the loss of MIC26 and/or MIC27 affects the localization or arrangement of core components of MICOS complex, namely, MIC60 or MIC10 in the mitochondria using STED super-resolution nanoscopy. Consistent with earlier reports (Jans et al, 2013; Stoldt et al, 2019; Kondadi et al, 2020), MIC60 and MIC10 showed a MICOS-specific pattern of regularly arranged punctae across the mitochondrial length in WT HAP1 cells (Fig 4A). This staining pattern was indistinguishable in SKOs or DKO cells lacking *MIC26* and/or *MIC27* indicating that MIC26 and MIC27 are dispensable for the formation of the MICOS scaffold in the IBM of mitochondria (Fig 4A). Third, to determine the composition or the integrity of the whole MICOS in our KO cell lines, we performed complexome profiling. Upon carefully comparing the complexome profiles of mitochondria isolated from SKOs and DKO cells with the controls, we found that MIC26 or MIC27 can assemble into high molecular weight complexes independent of each other, and none of them is required for incorporation of other MICOS subunits into these higher molecular weight complexes (Figs 4B and S2). In DKO mitochondria, the remaining MICOS subunits were shifted to a lower molecular weight complex than control cells (Figs 4B and S2), which is also seen consistently in blue-native (BN)–PAGE (Fig 4C). The observation that the amount of the high molecular weight MICOS complex, but not that of the lower molecular weight MICOS complex, is slightly reduced in *MIC26* KO and DKO cells can be attributed to the loss of the respective subunits (Figs 4B and S2). However, we cannot exclude

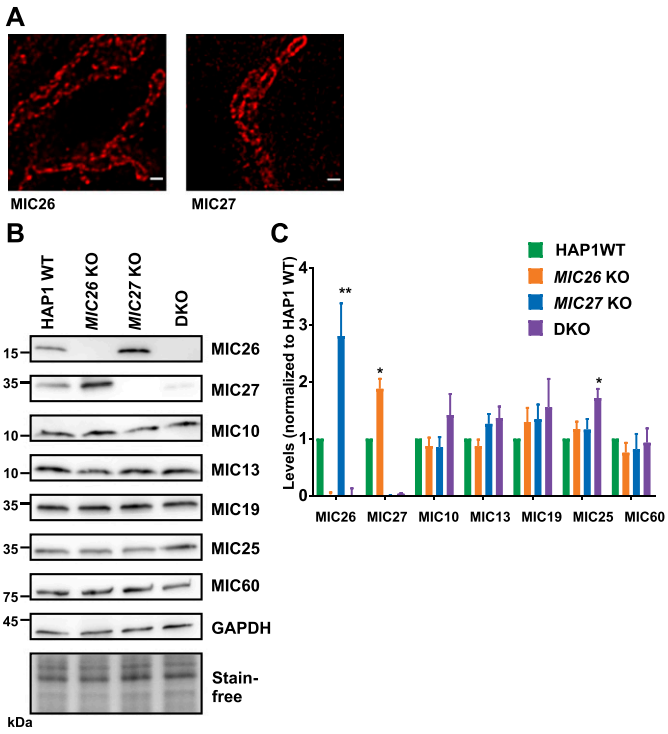

Figure 3. MIC26 and MIC27 are not required for the stability of other MICOS subunits.
(A) Representative STED super-resolution images of MIC26 or MIC27 in control cells show the punctae rail-like arrangement within mitochondria that resemble the staining from MIC60 or MIC10 (see also Fig 4A). Scale bar 0.5 μm. **(B)** Western blots of total cell lysates from HAP1 WT, *MIC26* KO, *MIC27* KO, or double knockout (DKO) cells probed for various subunits of the MICOS complex. **(C)** Densitometric quantification of Western blots from four independent experiments (mean ± SEM) in HAP1 WT, *MIC26* KO, *MIC27* KO, or DKO cells that are normalized to levels of each MICOS subunits to the HAP1 WT. Except MIC26 or MIC27 levels (showing reciprocal change), steady-state levels of other MICOS subunits were not drastically reduced in single knockouts or DKO cells of *MIC26* and *MIC27*. One sample *t* test was used for comparison. Marginal increase in MIC25 was found in DKO cells. **P*-value ≤ 0.05. ***P*-value ≤ 0.01.

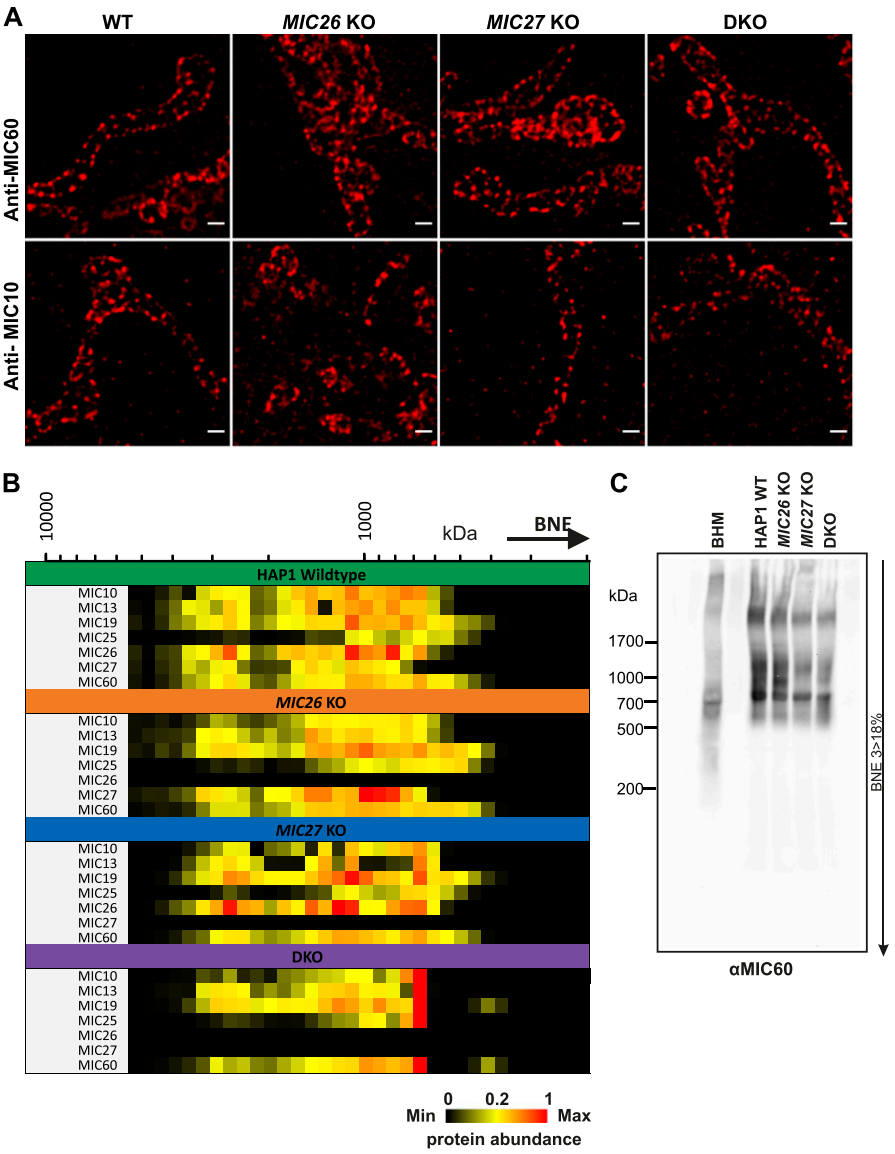

Figure 4. MIC26 and MIC27 are dispensable for the spatial arrangement of MIC10 and MIC60 in mitochondria and the incorporation of other MICOS subunits into the complex.
(A) Representative images of endogenous staining of MIC60 or MIC10 in HAP1 WT, *MIC26* KO, *MIC27* KO, or double knockout (DKO) cells using STED super-resolution nanoscopy show that the rail-like punctae arrangement of MIC60 or MIC10 remain unaltered in single knockouts or DKO cells. **(B)** Complexome profiling data representing the heat map of abundance of occurrence of MICOS subunits in isolated mitochondria from HAP1 WT, *MIC26* KO, *MIC27* KO, or DKO cells show that cluster of MICOS complex shifts to a lower molecular weight in DKO mitochondria but the remaining subunits remain associated to this complex. **(C)** Blue-native gel electrophoresis blotted for anti-MIC60 show MICOS complex in single knockouts or DKO cells lacking *MIC26* and/or *MIC27*. BHM, bovine heart mitochondria.

that MIC26 and MIC27 play a role in the integrity of the high molecular weight MICOS complex. Yet, as the stability of MICOS subunits and their incorporation in MICOS is not grossly perturbed, we conclude that MIC26 and MIC27 do not play a role in bridging the two subcomplexes, MIC19-25-60 and MIC13-10-26-27, of the MICOS complex as was reported for MIC13 (Guarani et al, 2015; Anand et al, 2016). This would be consistent with MIC26 and MIC27 assembling into the MICOS complex at a rather late stage and fits to the observation that the steady-state levels of all other MICOS subunits are not reduced upon loss of MIC26 and/or MIC27.

MIC26 and MIC27 are required for the assembly and stability of the monomeric F_1F_o–ATP synthase

The oligomerization of the F_1F_o–ATP synthase is associated with proper formation of cristae, in particular by inducing a positive curvature at the rim of a crista (Strauss et al, 2008; Rabl et al, 2009). To further determine whether loss of MIC26 and MIC27 affect the oligomerization and stability of the F_1F_o–ATP synthase and thus contribute to the cristae defect observed earlier, we checked the activity and oligomerization of F_1F_o–ATP synthase in SKOs and DKO cells. For this, we performed in-gel ATP hydrolysis activity assays after native gel electrophoresis to reveal F_1F_o–ATP synthase oligomers, dimers, monomers, or active F_1 subcomplexes. In this assay, we found a striking reduction of the overall intensity of F_1F_o–ATP synthase activity in DKO cells compared with SKOs and control cells (Fig 5A, left panel). This was not due to unequal loading as confirmed by Western blot analysis and Ponceau S staining (Fig 5A, right panel). The relative amounts of F_1F_o–ATP synthase complex found as oligomers, dimers, or monomers were not significantly altered in DKO cells compared with the SKOs or control cells (Fig 5B), indicating no obvious defect in the oligomerization of monomeric

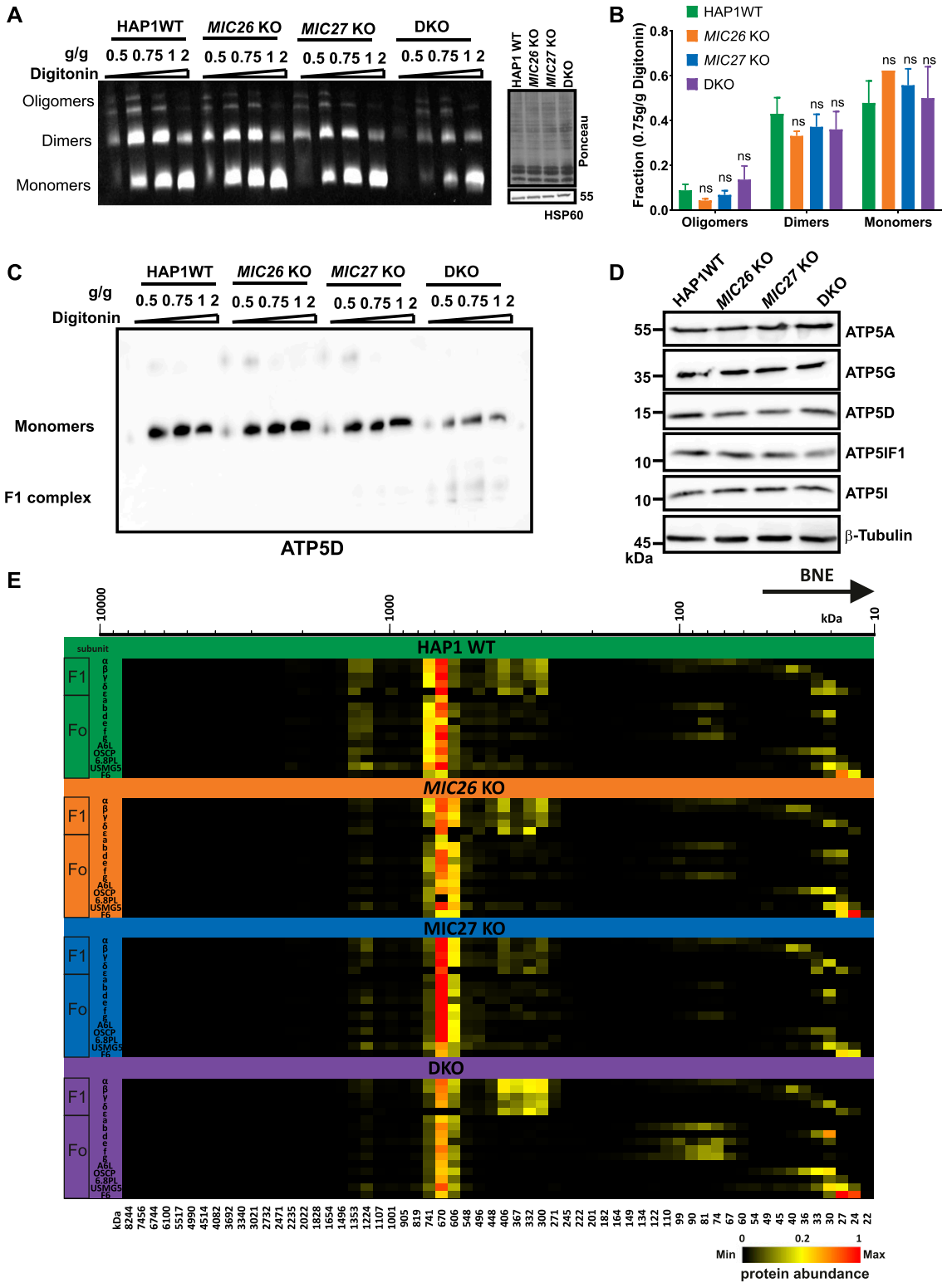

Figure 5. MIC26 and MIC27 are cooperatively required for the stability and assembly of the F_1F_o–ATP synthase complex.
(A) Blot showing the in-gel activity of F_1F_o–ATP synthase using isolated mitochondria of HAP1 WT, *MIC26* KO, *MIC27* KO, or double knockout (DKO) cells that were solubilized with increasing concentration of digitonin (g/g). The blot show oligomers, dimers, and monomers forms of F_1F_o–ATP synthase. The intensity (or activity) was reduced in DKO cells. The same mitochondrial lysate was blotted on SDS–PAGE to probe for equal loading among the samples. **(B)** The quantification of ratio of oligomers or dimers or monomers of F_1F_o–ATP synthase to the total intensity in the lane specific for 0.75 g/g digitonin was calculated from three independent experiments (mean ± SEM) show no significant difference among them in single knockouts or DKO cells lacking *MIC26* and/or *MIC27* compared with HAP1 WT. ns = *P*-value > 0.05 (nonsignificant).

F_1F_o–ATP synthase complexes despite the reduced overall activity (Fig 5A). This result is distinct to data from baker's yeast, where loss of Mic26 showed reduced oligomerization of the F_1F_o–ATP synthase (Eydt et al, 2017) pointing to a difference in regulation of F_1F_o–ATP synthase oligomerization in mammals as compared with fungi. The reduced staining in the in-gel activity assay could be attributed to either the loss of the functionality or reduced amounts of the F_1F_o–ATP synthase complex. To check this, we performed BN–PAGE and probed with an antibody specific for F_1F_o–ATP synthase complex, ATP5D, using mitochondrial lysates from SKOs and DKO cells lacking *MIC26* and *MIC27* and control cells (Fig 5C). In BN–PAGE, we found a considerable decrease in the amount of the monomeric F_1F_o–ATP synthase in the DKO as compared with SKOs and control cells (Fig 5C). This indicates that the reduced activity of F_1 in the F_1F_o–ATP synthase complex in DKO cells is due to reduced amount of the F_1F_o–ATP synthase complex. Moreover, we observed an accumulation of a low molecular weight band specifically in mitochondria derived from DKO cells which we attribute to a detached/non-assembled F_1 subcomplex. We also checked the steady-state levels of several subunits of F_o- or F_1-moieties in knockout cell lines and found no drastic or significant change in either of the subunits tested (Fig 5D), showing that the reduced amount of the F_1F_o–ATP synthase complex does not arise because of decrease in the supply of the subunits that we tested. To check this in more detail and test whether the assembly of the F_1F_o–ATP synthase complex is impaired, we analyzed our mitochondrial complexome profiling data from all the knockout cell lines. A comparison between the heat map for the F_1F_o–ATP synthase complexes in our control and knockout cell lines showed a drastic decrease in the amount of the F_1F_o–ATP synthase complex in DKO mitochondria (Figs 5E and S3), whereas *MIC27* KO mitochondria appeared to have even slightly higher levels of this complex. In WT mitochondria, the subunits of the monomeric F_1F_o–ATP synthase cluster at expected size of around 600 kD (Figs 5E and S3). In DKO mitochondria, apart from this complex, we find that F_1 subunits were accumulating at a lower molecular weight (Figs 5E and S3). This indicates an impaired assembly of the monomeric F_1F_o–ATP synthase complex or a partial disassembly of F_1 subunits upon solubilization from this complex in DKO cells consistent with the BN–PAGE data described above (Fig 5C). Overall, we conclude that in mammalian cells, MIC26 and MIC27 are dispensable for the oligomerization of the F_1F_o–ATP synthase complex but are rather specifically required for the integration of F_1 subunits into the monomeric F_1F_o–ATP synthase which stabilize the F_1F_o–ATP synthase complex.

MIC26 and MIC27 regulate the stability of respiratory chain complexes and supercomplexes

Mitochondrial cristae shape mediated by OPA1 was suggested to regulate the assembly of respiratory chain supercomplexes (SCs) and respiratory capacity (Cogliati et al, 2013). To further decipher the basis for the impaired respiration observed earlier (Fig 2A) and to test whether there is a link between MIC26/MIC27 and respiratory chain complexes (RCs) and SCs formation, we performed BN–PAGE from mitochondria isolated from control cells, SKOs, and DKO cells lacking *MIC26* and/or *MIC27* and probed with the antibodies specific for complexes I, III, and IV. We find that the individual complexes and their higher associations into SCs were drastically reduced in the DKO compared with the controls or the SKOs (Fig 6A, left panel). This was not due to reduced loading among the cell lines (Fig 6A, right panel). To further substantiate the role of MIC26 and MIC27 in RCs and SCs formation, we analyzed our complexome profiling data and found that there was a clear and drastic reduction in RCs and SCs in DKO cells (Figs 6B and S4), consistent with the BN–PAGE (Fig 6A). *MIC27* KO cells show slight increase in RCs and SCs that could be attributed to increased respiration in these cells (Fig 2A). Moreover, we observed certain changes that are specific to individual SKOs of *MIC26* and *MIC27*, for example, a higher molecular weight distribution of complex II in *MIC27* KO but not in other cell lines (Figs 6B and S4). We then examined the steady-state levels of marker proteins from the various RCs using Western blot analysis and found that their levels were not significantly reduced in the DKO cells (Fig S5A and B), indicating that the decrease in the levels of RCs or SCs is not due to an overall reduction in the subunits of the RCs. However, we cannot rule out that some key assembly factors causing destabilization of RCs or SCs are specifically affected in these knockout cell lines. Overall, we provide several lines of evidence that cristae defects caused by deletion of *MIC26* and *MIC27* are associated with reduced steady-state levels of fully assembled RCs and SCs. As OPA1 levels were shown to determine the assembly of SCs and respiration (Cogliati et al, 2013), we wanted to check the levels of the distinct OPA1 forms (long or short-OPA1) in the KO cells to determine whether a change in OPA1 levels could be a cause of reduced levels of SCs (or RCs). Typically, five prominent forms of OPA1 (two long forms, a/b, and three short form, c/d/e) are observed in cultured mammalian cells arising from various splice variants and two proteolytic cleavage sites (for OMA1 or YME1L) (Duvezin-Caubet et al, 2006, 2007; Anand et al, 2013; MacVicar & Langer, 2016), contributing to a complex regulation. We did not observe any consistent or drastic change in the amount or the prevalence of OPA1 forms (long or short forms) in any of our knockout cells compared with control cells (Fig S6A and B), indicating no obvious difference in OPA1 levels in cells deleted for *MIC26* or *MIC27*. From this, we conclude that the reduced levels of RCs or SCs in the knockout of *MIC26* or *MIC27* occurs independent of OPA1 regulation.

Cardiolipin levels are reduced upon double deletion of MIC26 and MIC27

MIC26 and MIC27 are apolipoproteins that normally bind lipids and MIC27 was shown to bind to cardiolipin (CL) in vitro (Weber et al,

t test was used for statistical analysis. **(C)** Blue-native gel electrophoresis of isolated mitochondria from HAP1 WT, *MIC26* KO, *MIC27* KO, or DKO cells that were solubilized with increasing concentration of digitonin (g/g) is blotted and probed for F_1F_o–ATP synthase subunit, ATP5D show reduced staining in DKO cells lacking MIC26 and MIC27 with concomitant appearance of lower molecular weight complex (F_1). **(D)** Western blot from the lysate of HAP1 WT, *MIC26* KO, *MIC27* KO, or DKO cells were probed with antibodies specific to various subunits of F_1F_o–ATP synthase complex, do not show any consistent change in either of them in single knockouts or DKO cells. **(E)** Complexome profiling of isolated mitochondria from HAP1 WT, *MIC26* KO, *MIC27* KO, or DKO cells for the F_1F_o–ATP synthase complex showing the heat map of occurrence of subunits of F_1F_o–ATP synthase. F_1F_o–ATP synthase complex is reduced and subunits of the F1 part are partially dissociated from the complex in DKO cells lacking *MIC26* and *MIC27*.

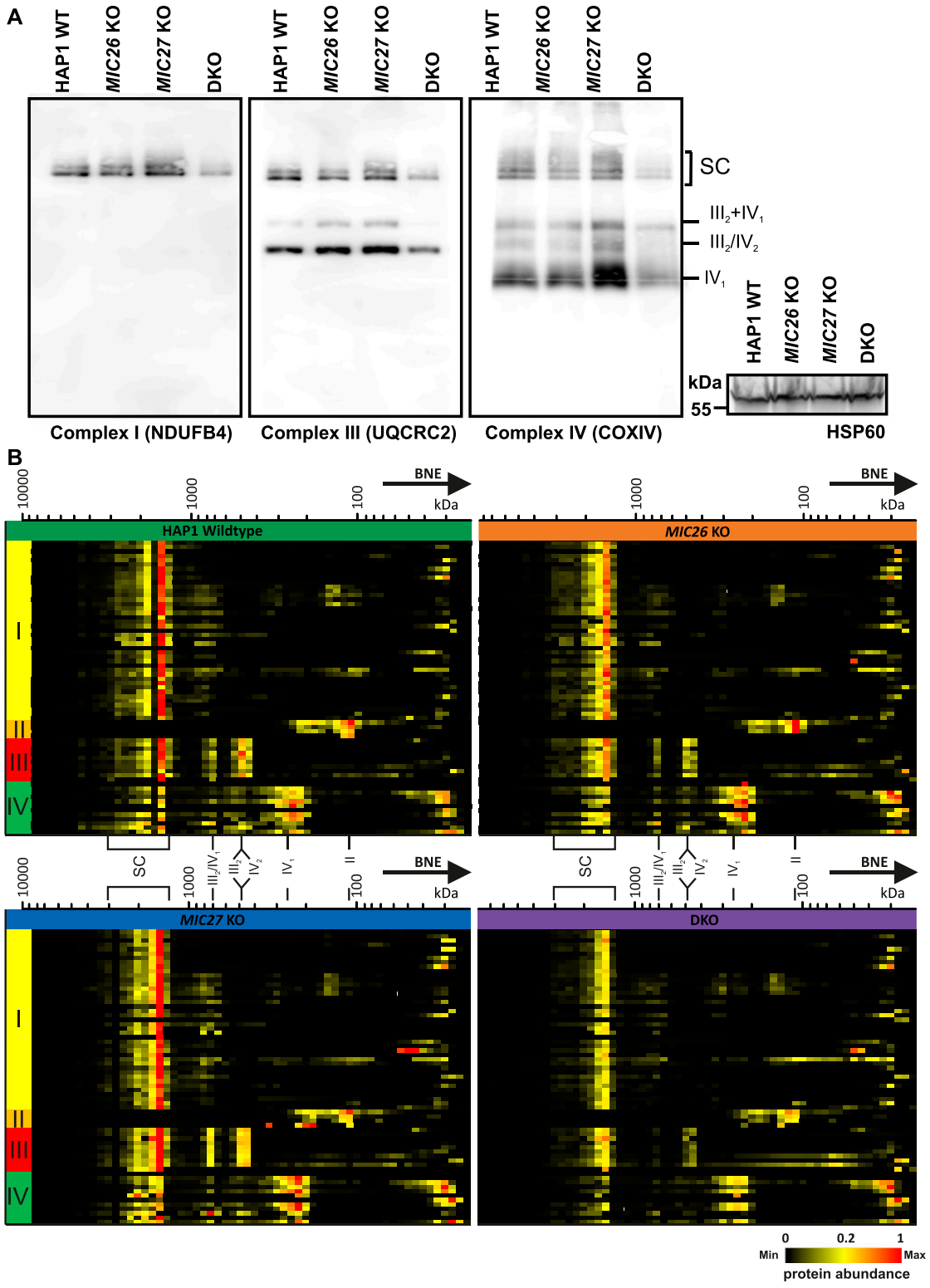

Figure 6. MIC26 and MIC27 are required for the stability of respiratory chain (super) complexes.
(A) Blue-native gel electrophoresis for isolated mitochondria from HAP1 WT, *MIC26* KO, *MIC27* KO, or double knockout (DKO) cells that were solubilized and blotted for antibodies specific for complex I (NDUFB4), complex III (UQCRC2), or complex IV (COX1V) show reduced staining of respiratory chain complexes (RCs) and their higher assemblies (supercomplexes). The same mitochondrial lysate was blotted on SDS–PAGE to probe for equal loading among the samples. **(B)** Complexome profiling of isolated mitochondria from HAP1 WT, *MIC26* KO, *MIC27* KO, or DKO cells for respiratory chain complexes (RCs)/supercomplexes (SCs) showing the heat map of occurrence of subunits of respiratory chain complexes which were reduced in DKO cells lacking *MIC26* and *MIC27*.

2013). Cardiolipin is required for the formation and stabilization of RCs and SCs (Zhang et al, 2002; Pfeiffer et al, 2003; Bottinger et al, 2012). We hypothesize that the deletion of *MIC26* and *MIC27* (or MICOS) possibly alters the cardiolipin composition of the lipid bilayer of mitochondria and thereby affects the integrity of RCs and/or SCs. Therefore, we determined the levels of cardiolipin in SKOs and DKO cells of *MIC26* and *MIC27* using mass spectrometry. We found significantly reduced levels of cardiolipin in DKO and *MIC26* KO cells, whereas they remain normal in *MIC27* KO cells (Fig 7A). This overall reduction of CL in DKO and *MIC26* KO cells was not due to specific cardiolipin species being affected predominantly (Fig 7B) but rather appeared to occur for all CL species, indicating no major defect in cardiolipin remodelling. To determine whether the reduced levels of cardiolipin affect the stability of the RCs and SCs in DKO cells, we stably overexpressed cardiolipin synthase (CRLS1) in DKO cells and analyzed RCs and SCs using BN-PAGE. As a control, we stably overexpressed MIC26 or/and MIC27 in DKO cells (Fig S1A) and found that overexpression of both MIC26 and MIC27 rescued the levels of RCs and SCs in DKO cells comparable to the control conditions (Fig 7C). Stable overexpression of CRLS1 in DKO cells could restore the stability of the RCs and SCs compared with the DKO cells with empty vector. In addition, we wanted to analyze whether overexpression of CRLS1 that restored the stability of RCs and SCs could then rescue the reduced respiration of DKO cells. Indeed, we found a significant increase in maximal respiration and ATP production upon overexpression of CRLS1 in DKO cells compared to DKO cells with empty vector (Fig S1B) showing that reduced cardiolipin in DKO cells directly affect the stability of RCs and SCs as well as respiration of DKO cells. Overall, we propose a model that the homologous subunits of MICOS, MIC26 and MIC27, are cooperatively required to modulate the levels of cardiolipin in mitochondria and influence the general stability and integrity of the respiratory chain (super) complexes and F_1F_o–ATP synthase complex (Fig 7D).

Discussion

MIC26 and MIC27 are homologous proteins of the MICOS complex whose steady-state protein levels are reciprocally regulated. Here, we found that SKOs of *MIC26* and *MIC27* show moderate cristae defects when compared with DKO cells that show a clear increase in extent of cristae defects with accumulation of onion-like cristae. Therefore, MIC26 or MIC27 can partially complement each other, yet also fulfil functional roles that cannot be fully compensated by the respective other subunit. This shows that the coordinated function of MIC26 and MIC27 is required for the proper formation of CJs and indicates cooperation between MIC26 and MIC27 to regulate cristae structure. How do MIC26 and MIC27 affect MICOS complex function and thereby CJ formation? Unlike the loss of MIC60, MIC10, or MIC13 that led to destabilization of either the whole or part of the MICOS subcomplex, MIC26 and MIC27 were not required for the stability of the known remaining subunits of the MICOS complex and their incorporation into higher molecular weight complexes. STED super-resolution nanoscopy showed no change in the pattern of localization of MIC60 or MIC10 in the DKO cells lacking *MIC26* and *MIC27*, reiterating that they do not grossly perturb the spatial organization of the MICOS complex within mitochondria and perhaps assemble later than MIC10 or MIC60 during the formation of MICOS complex. This is also consistent with our recent finding that the staining pattern of MIC60 remains unperturbed in *MIC10* KO cells that have virtually complete loss of CJs (Kondadi et al, 2020) and imply that MIC60 acts as a priming factor for the formation of CJs and remain associated at sites or hotspots of the CJ formation (Friedman et al, 2015; Stoldt et al, 2019; Kondadi et al, 2020). Mitochondrial morphology is a result of opposing cycles of fusion and fission (Pernas & Scorrano, 2016). *MIC26* KO and DKO cells show a comparable extent of mitochondrial fragmentation, whereas *MIC27* KO show normal mitochondrial morphology indicating that perhaps mitochondrial defect of *MIC26* KO cannot be compensated by MIC27 and rather MIC26 acts independent of MIC27 in regulating mitochondrial morphology. Neither OPA1 levels nor the abundance of different forms were altered, indicating that mitochondrial fusion is normal in these cells. Further experiments are required to understand why and how MIC26 specifically regulates mitochondrial dynamics. On the other hand, we found that only DKO cells show reduced respiration, whereas *MIC26* KO cells show no change, and *MIC27* KO cells even show slight increase in respiration that could be attributed to compensation (or even enhancement) of the respiration defect by each other in SKOs of *MIC26* and *MIC27*.

The levels of respiratory chain complexes (RCs) or supercomplexes (SCs) were drastically reduced in DKO cells lacking *MIC26* and *MIC27*. The major respiratory chain complexes I, III, and IV are organized into supramolecular assemblies called supercomplexes (SCs) (Schägger & Pfeiffer, 2000). Although individual, isolated complexes are functional, formation of SCs is proposed to promote the stability of single complexes that enhances electron flow among them while reducing formation of ROS (Lapuente-Brun et al, 2013; Milenkovic et al, 2017). Experiments using mutants of tBid and acute ablation of OPA1 show that the cristae shape determines the stability and assembly of SCs (Cogliati et al, 2013). Here, we found that loss of CJs in *MIC26* and *MIC27* DKO cells determine the stability of the RCs or SCs. However, in this scenario, levels of OPA1 remain unaltered suggesting that these changes are independent of OPA1 regulation. CL is thought to act as a glue holding the respiratory chain (super) complex with several components of RCs which harbour CL-binding sites. Mutations in tafazzin (TAZ) that is required of remodelling of CL has been associated with Barth syndrome (Brady et al, 2006) and other mitochondrial deficiencies, whereas decreased amounts of cardiolipin are found in many human diseases, including diabetic cardiomyopathy. Deletion of *cardiolipin synthase* in *Drosophila* flight muscle causes aberrant cristae (Acehan et al, 2011). Barth syndrome patients' cells have altered cristae structure accompanied by destabilized RCs (McKenzie et al, 2006; Acehan et al, 2007), providing a molecular link between cristae structure and RCs formation. We found that overexpression of cardiolipin synthase (CRLS1) restored the stability of RCs and SCs and respiration in DKO cells showing that the reduced levels of cardiolipin in DKO cells directly affect the stability and integrity of RCs or SCs. However, the question remains how loss of CJs in conjunction with cristae defects affects the levels of CL or vice versa. Either the MICOS subunits (MIC26 and MIC27) directly influence the biosynthesis of cardiolipin or indirectly affect cardiolipin levels due to change in

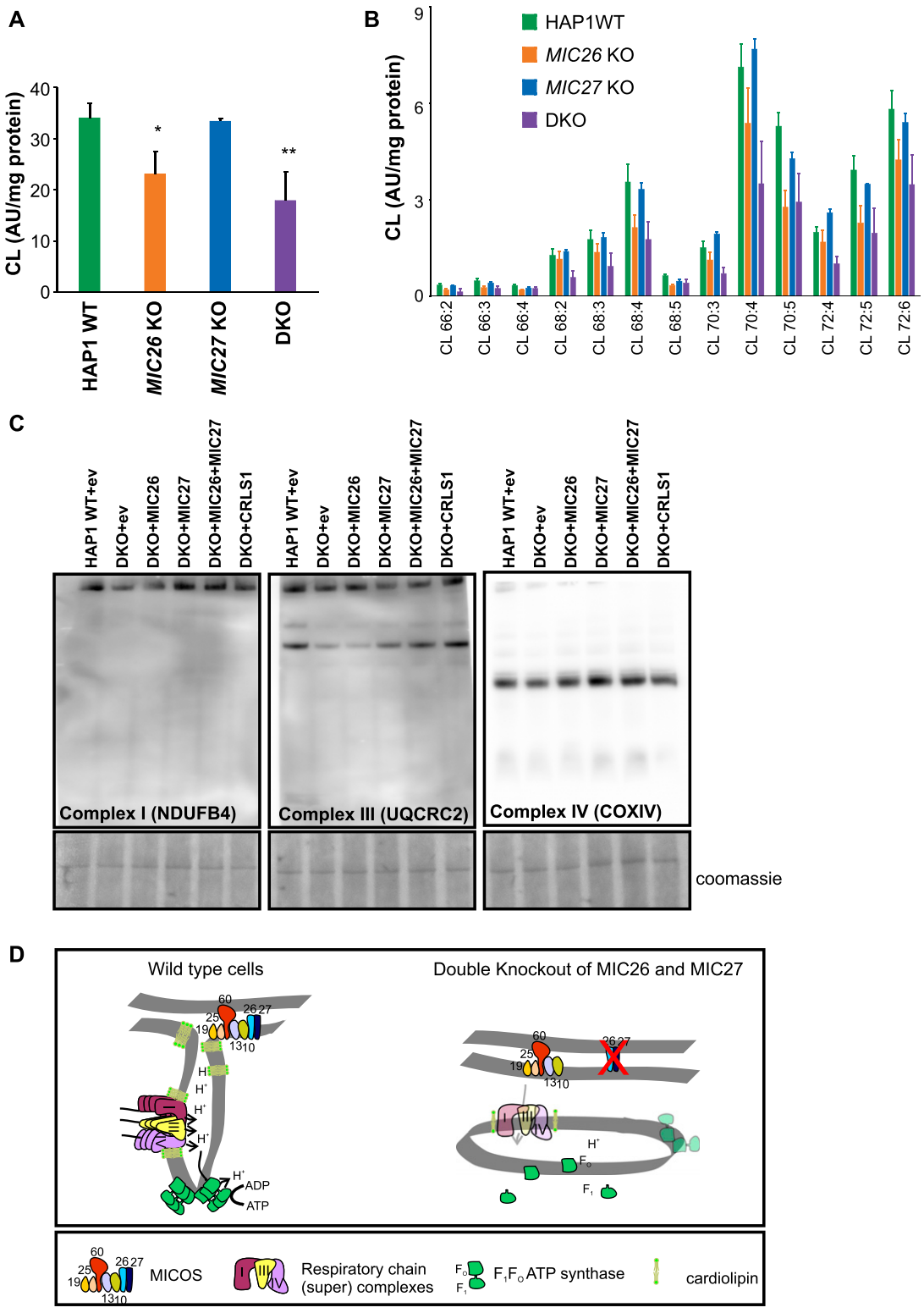

Figure 7. MIC26 and MIC27 maintain cardiolipin levels that are required for stability of respiratory chain (super) complexes.
(A) Graph representing the levels of cardiolipin shown as arbitrary units normalized to mg of protein in each cell types show significant reduction in MIC26 KO and double knockout (DKO) cells. *P-value ≤ 0.05, **P-value ≤ 0.01. t test was used for statistical analysis. **(B)** Graph showing the distribution of various cardiolipin species (arbitrary units normalized to mg of protein) in HAP1 WT, *MIC26* KO, *MIC27* KO, and DKO cells. **(C)** Blue-native gel electrophoresis for isolated mitochondria from HAP1 WT expressing empty vector (ev) and DKO cell lines that are stably expressing ev or MIC26 or MIC27 or MIC26 and MIC27 together or CRLS1 (cardiolipin synthase) were solubilized and blotted for antibodies specific for complex I (NDUFB4), complex III (UQCRC2), or complex IV (COX1V). The restoration of staining of respiratory chain (super)

cristae/CJs organization which might disrupt the membranes or supply of precursors required for cardiolipin synthesis. A large cardiolipin-synthesizing scaffold is present in mitochondria that interacts with MIC60 or MIC19 (Serricchio et al, 2018), and MICOS influences phospholipid synthesis (Harner et al, 2014; Aaltonen et al, 2016). In addition, intramitochondrial phospholipid transport in conjugation with MICOS is required for the formation of tubular cristae (Kojima et al, 2019). In our study, we propose that MIC26 and MIC27 being lipid-binding proteins of the MICOS provide the crucial interface between phospholipids such as CL and other scaffolding proteins to mediate formation of CJs and confer stability to RCs and SCs (Fig 7D).

A complex interplay between several cristae-shaping protein complexes is thought to sculpt the intricate cristae structures (Kondadi et al, 2019). While MICOS is required for the formation of highly curved CJs, rows of dimers of F_1F_o–ATP synthase complex are required for the formation of positive curvature at the rim of a crista. In yeast, Mic60/Fcj1 functions antagonistic to F_1F_o–ATP synthase for the formation of CJs and crista rims, respectively (Rabl et al, 2009). Mic10 binds to dimeric F_1F_o–ATP synthase, whereas Mic27 also binds to Su e (the yeast homolog of ATP5I), both promoting the oligomerization of F_1F_o–ATP synthase (Eydt et al, 2017; Rampelt et al, 2017a). In mammalian cells, OPA1 functionally interacts with F_1F_o–ATP synthase and favours its oligomerization (Patten et al, 2014; Quintana-Cabrera et al, 2018b). This prompted us to check the status of F_1F_o–ATP synthase oligomerization in our DKO cells lacking *MIC26* and *MIC27*. There was no obvious defect in oligomerization of the F_1F_o–ATP synthase, but the overall amount of the whole complex (monomers and oligomers) was reduced, demonstrating a reduced stability or integrity of the F_1F_O–ATP synthase complex upon simultaneous deletion of *MIC26* and *MIC27*. Our complexome data show a specific partial dissociation of subunits belonging specifically to the F_1 part of the complex from the monomeric complex in DKO cells, perhaps causing the instability and loss of the monomeric (F_1F_o) complex. This is different to baker's yeast where Mic27 rather influences the assembly and stability of the dimeric/oligomeric F_1F_o–ATP synthase complex (Eydt et al, 2017; Rampelt et al, 2017a), indicating an evolutionary divergence in regulation of the assembly of the F_1F_o–ATP synthase. Despite common evolutionary routes, the auxiliary factors required for assembly and regulation of F_1F_o–ATP synthase are not conserved among different organisms (Ruhle & Leister, 2015). INAC complex (comprising Ina22 and Ina17) helps in promoting the linkage between F_1 and F_o in yeast, whereas its mammalian homolog is not yet identified (Lytovchenko et al, 2014; Naumenko et al, 2017).

The regulation of these apolipoproteins is highly complex because of the presence of a 55-kDa glycosylated form of MIC26 ($MIC26_{55kDa}$), which is usually secreted and found in blood plasma. $MIC26_{55kD}$ is elevated in the heart transcriptome of an animal model of diabetes (Lamant et al, 2006). Human patients of ACS have increased levels of $MIC26_{55kDa}$ in the plasma that correlated with an independent inflammatory marker for ACS (Yu et al, 2012). Although $MIC26_{55kD}$ is present in high density lipoproteins, its in vivo function is not clear as it does not apparently influence any of the high density lipoproteins function tested. Although overexpression of Mic26 in a mouse heart caused ROS production and cardiac lipotoxicity (Turkieh et al, 2014), it leads to aggravated liver steatosis and accumulation of triglycerides in liver (Tian et al, 2017). It is possible that the effects observed upon the overexpression of Mic26 in mouse model or cardiomyopathic conditions could occur as a consequence of impaired mitochondrial respiratory machinery as we observed earlier (Koob et al, 2015) and here.

In summary, we find that apolipoproteins of the MICOS complex, MIC26 and MIC27, act cooperatively to regulate the formation of CJs and manage the stability and assembly of the RCs/SCs and F_1F_o–ATP synthase perhaps by modulating the cardiolipin levels. With a comprehensive functional analysis of cells after simultaneous deletion of *MIC26* and *MIC27* including a complexome approach, we revealed a novel cooperative function of these two proteins in determining the stability and integrity of the landscape of OXPHOS complexes. Further experiments are needed to provide mechanistic insights about how MIC26 and MIC27 affect OXPHOS complex biogenesis and cardiolipin levels and how this is linked to the pathophysiological role of these proteins in human diseases such as diabetic cardiomyopathy and mitochondrial myopathy (Beninca et al, 2020).

Materials and Methods

Cell culture

HAP1 WT, *MIC26* KO, *MIC27* KO, and DKO cells were obtained and custom-made by Horizon (UK) using the CRISPR-Cas method. The following guided RNA sequences were selected—for *MIC26*, TGAGGGTCAATCGAAGTATG in exon 3 and for *MIC27*, ACAACCAGTTGCAGTGCGGA in exon 3. *MIC26* KO cells contain a 1-bp insertion in exon 3, whereas *MIC27* KO cells contain an 8-bp deletion in exon 3. Later, *MIC26* KO cells were used to target *MIC27* with the same guided RNA that this time yielded a 160-bp deletion in the exon 3 of *MIC27*. The HAP1 cells were cultured using IMDM media supplemented with 20% fetal bovine serum and 1% penicillin and streptomycin. The cells were grown in an incubator at 37° C supplemented with 5% CO_2.

Generation of stable cell lines using retroviral transduction

MIC26, MIC27, and CRLS1 were cloned into pMSCVpuro (PT3303-5; Clontech) using GIBSON cloning (E2611L; New England Biolabs). CRLS1 ORF was obtained from Sino Biological (HG20234-U). ORFs of MIC26 and MIC27 were taken from pcDNA3.1-Myc-MIC26 (Koob et al,

complexes compared with DKO (with ev) was found upon expression of MIC26 and MIC27 as well as CRLS1 in DKO cell lines. The part of the BN–PAGE stained with Coomassie is shown to represent the loading among the cell lines. **(D)** The scheme summarizing the phenotype occurring due to loss of *MIC26* and *MIC27* that show MIC26 and MIC27 are cooperatively required for the formation of crista junctions, maintenance of cardiolipin levels, and stability of respiratory chain (super) complexes and F_1F_O–ATP synthase. In addition, MIC26 and MIC27 are required for the assembly of F_1F_o–ATP synthase by facilitating the association of F_1 and F_o part. Loss of *MIC26* and *MIC27* leads to impaired respiration.

2015) and pcDNA3.1-MIC27-FLAG (Weber et al, 2013). For retroviral transduction, Plat-E cells (kindly provided by Toshio Kitamura, Institute of Medical Science, University of Tokyo, Japan [Morita et al, 2000]) were plated in a 6-cm dish overnight and transfected with the respective plasmids (pMSCVpuro (ev), pMSCVpuro-MIC26, pMSCVpuro-MIC27, both pMSCVpuro-MIC26 and pMSCVpuro-MIC27 together, and pMSCVpuro-CRLS1) using FuGENE transfection reagent (Promega). After 48 h, the recombinant vesicular stomatitis virus-G pseudotyped retroviruses were recovered from the supernatant of Plat-E cells after centrifugation and transferred to the target cells (HAP1 WT and DKO of *MIC26* and *MIC27*). After 72 h, the target cells were subjected to selection in puromycin (2 μg/ml) containing media to select the cells that stably express the transgene that confer puromycin resistance. The cell lines were confirmed by Western blots (MIC26 and MIC27) or sequencing (CRLS1).

Electron microscopy

HAP1 WT, *MIC26* KO, *MIC27* KO, and DKO cells were grown on a petri dish and processed for electron microscopy as described earlier (Anand et al, 2016). Briefly, the cells were fixed using 3% glutaraldehyde in 0.1M sodium cacodylate buffer, pH 7.2, and subsequently pelleted. The cell pellets were embedded in agarose and stained with 1% osmium tetroxide for 50 min and 1% uranyl acetate/1% phosphotungstic acid for 1 h. The ultrathin sections were prepared using microtome, and imaging was performed on transmission electron microscope (H600; Hitachi) at 75 V equipped with Bioscan model 792 camera (Gatan) and analyzed with ImageJ software.

SDS electrophoresis and Western blotting

For preparing the samples of Western blotting, the cells were collected in a small tube and proteins were extracted using RIPA lysis buffer. The amount of the solubilized proteins in each sample was estimated using the Lowry method (Bio-Rad). 15% SDS electrophoresis gel was used for running the protein samples. The proteins were subsequently blotted onto nitrocellulose membrane and probed with antibodies listed here, MIC13 (custom-made by Pineda; against human MIC13 peptide CKAREYSKEGWEYVKARTK), MIC27 (HPA000612; Atlas Antibodies), MIC26 (MA5-15493; Thermo Fisher Scientific), MIC60 (custom-made, Pineda; against human MIC60 using the peptide CTDHPEIGEGKPTPALSEEAS), MIC10 (ab84969; Abcam), MIC25 (20639-1-AP; Proteintech), β-tubulin (Cell Signaling Technology), and MIC19 (25625-1-AP; Proteintech). ATP5A (ab14748; Abcam), ATP5G (Abcam), ATP5D (ab97491; Abcam), ATP5IF1 (ab110277; Abcam), ATP5I (16483-1-AP; Proteintech), NDUFB4 (ab110243; Abcam), SDHB (ab14714; Abcam), UQCRC2 (ab14745; Abcam), COXIV (ab16056; Abcam), and OPA1 (custom-made, Pineda against human OPA1 using peptide CDLKKVREIQEKLDAFIEALHQEK, [Barrera et al, 2016]). The chemiluminescent signals were captured using VILBER LOURMAT Fusion SL (Peqlab). LI-COR Image studio software was used for quantification and image analysis.

Respiration measurements

All the respiration measurements were performed using Seahorse XFe96 Analyzer (Agilent). The HAP1 cells were seeded in Seahorse XF96 cell culture plate (Agilent) at a density of 3×10^4 to 3.3×10^4 cells per well overnight. On the subsequent day, cells were washed and incubated in basic DMEM media (D5030; Sigma-Aldrich) supplemented with glucose, glutamine, and pyruvate at 37°C in non-CO_2 incubator 1 h before the assay. Mitochondrial respiration function was measured using Seahorse XF Cell Mito Stress Test kit (Agilent) according to the manufacturer's instructions. Briefly, the delivery chambers of the sensor cartridge were loaded with Oligomycin (F_1F_o–ATPase synthase inhibitor) or FCCP (uncoupler) or Rotenone and Antimycin (Complex I and Complex III inhibitor, respectively) to measure basal, proton leak, maximal, and residual respiration in XFe96 Analyzer. Cell number was normalized after the run using Hoechst staining. Data were analyzed using wave software (Agilent).

Mitochondrial morphology imaging and quantification

HAP1 cells expressing matrix-targeted GFP were used to study the mitochondrial morphology on a PerkinElmer spinning disc confocal microscope equipped with a 60× oil objective (NA = 1.49) and a chamber maintaining 37°C and 5% CO_2. Images were acquired with a Hamamatsu C9100 camera having dimensions of 1,000 × 1,000 pixels after excitation at 488 nm. The cells were classified as tubular, intermediate, and fragmented depending on the majority of mitochondria present in a cell belonging to a particular class. Cells classified as intermediate class contained a mixture of predominantly short pieces, few tubular or fragmented mitochondria, whereas cells classified as tubular and fragmented contained mostly long tubular and very short fragments of mitochondria, respectively.

Immunofluorescence staining

HAP1 and HeLa cells were fixed with 3.7% pre-warmed (37°C) paraformaldehyde for 20 min, washed thrice with PBS, permeabilized with 0.15% Triton X-100 and blocked using 10% goat serum for 15 min each. After blocking, the cells were incubated with respective primary antibodies overnight at 4°C and washed thrice. Secondary antibody incubation was performed at room temperature for 1 h followed by three washes with PBS. The samples were then used for STED imaging.

STED super-resolution nanoscopy

Images were acquired using a 100× oil (NA = 1.4) or 93× glycerol (NA = 1.3) objective to acquire a field of 9.7 × 9.7 μm area (12× zoom for 100× and 12.9× zoom for 93× objectives, respectively) on Leica SP8 microscope fitted with a STED module. For HAP1 cells, primary antibodies were used against MIC10 (84969; Abcam), MIC60 (custom-made; Pineda), and MIC27 (HPA000612; Atlas Antibodies) after which goat antirabbit Abberior STAR 635P (Abberior) was used as the secondary antibody. Using a hybrid detector (HyD), images of HAP1 cells immunostained for MIC10, MIC60, and MIC27 were acquired at an emission range from 640 to 735 nm, whereas the signal was depleted using a pulsed STED depletion laser active at 775 nm. To increase the specificity of the signal, gating STED was active from 1 ns onward, where the images acquired had a pixel size of 17 nm. HeLa cells expressing MIC26-GFP were used as samples for staining

MIC26. Mouse Anti-GFP antibody (11814460001; Merck) and goat antimouse Alexa Fluor 488 (Thermo Fisher Scientific) were used as primary and secondary antibodies, respectively. Images were acquired from 495 to 585 emission range, whereas the signal was depleted using a continuous wave STED depletion laser active at 592 nm. Gating STED was used from 1.5 ns onward, whereas the images acquired had a pixel size of 21 nm. Images were processed as described earlier (Kondadi et al, 2020).

Complexome analysis

Sample preparation, mass spectrometry, data analysis, and raw mass spectrometry data of complexome analysis have been deposited to the ProteomeXchange Consortium via the PRIDE partner repository (Perez-Riverol et al, 2019) with the dataset identifier PXD016733 and PXD016732. Averaged subunit quantification values were used for complex reference profiles. Reference profiles were normalized to maximum appearance between samples.

Mitochondrial isolation and BN gel electrophoresis

For mitochondrial isolation, cells were pelleted at 600*g* for 5 min and resuspended in an isotonic buffer containing 220 mM mannitol, 70 mM sucrose, 20 nM Hepes (pH 7.5, KOH), 1 mM EDTA and 1× protease inhibitor cocktail (Roche). The cells were mechanically ruptured by repeatedly passing through a syringe needle of 26 G cannula for 20 times. Debris or nuclei were separated by centrifugation at 1,000*g* for 5 min. The supernatant was then centrifuged at 8,000*g* for 10 min to collect the mitochondrial pellet. The protein estimation was performed using the Lowry method (Bio-Rad). Mitochondria were solubilized using 2 g/g of digitonin to protein ratio and equal amounts of mitochondria from each cell lines were loaded on a gradient gel (3–18%) and proceeded according to the method described earlier (Anand et al, 2016).

In-gel activity of F_1F_o–ATP synthase

Isolated mitochondria were solubilized with increasing concentration of digitonin to protein ratio (in g/g) and were loaded on a 4–13% gradient gel to separate the macromolecular complexes. The gel slice was incubated in ATP synthase activity buffer (35 mM Tris, 270 mM glycine, 14 mM $MgSO_4$, 0.2% wt/vol $Pb(NO_3)_2$, and 8 mM ATP pH 8.3) at 25°C for 4 h and fixed using 50% methanol and transferred to water for imaging.

qRT-PCR

For RNA isolation, 1 × 10^6 cells from each cell line were collected and homogenized using QIAshredder (QIAGEN), and RNA was extracted using RNeasy kit (QIAGEN) according to the manufacturer protocol. 1 μg of RNA was converted into cDNA using QuantiNova Reverse Transcription kit (QIAGEN). 15 ng of cDNA from each cell lines (HAP1 WT, *MIC26* KO, and *MIC27* KO) was used to perform qRT-PCR reaction using QuantiNova SYBR Green PCR kit (QIAGEN) with the following primers: MIC26 (forward: 5′-CCGTGAAGGTTGATGAGCTT reverse: 5′-GGAGCTGTGAGATGCTTTCTT), MIC27 (forward: 5′-ATGCAGCCAAACAAGAGGAA reverse: 5′-GGAGCGGTGGTGCAGTAT), GAPDH (forward: 5′-CCCCGGTTTCTATAAATTGAGC reverse: 5′-CGAACAGGAGGAGCAGAGAG), and HPRT1 (forward: 5′-CCTGGCGTCGTGATTAGTG reverse: 5′-TGAGGAATAAACACCCTTTCCA) in qRT-PCR Rotorgene 6000 (Corbett Research/QIAGEN). The analysis was performed using the Rotor-Gene Q 2.3.4 software for calculating $2_T^{-\Delta\Delta C}$ (Livak & Schmittgen, 2001).

Lipid analysis

Cell pellets containing 2 × 10^6 cells were extracted according to Matyash et al (2008). In brief, samples were homogenized using two beads (stainless steel, 6 mm) on a Mixer Mill (GER; 2 × 10 s, frequency 30/s; Retsch) in 700 μl methyl-tert-butyl ether/methanol (3/1, vol/vol) containing 500 pmol butylated hydroxytoluene, 1% acetic acid, and 150 pmol internal standard (IS; 18:3/18:3/18:3 triacylglycerol; Larodan). Total lipid extraction was performed under constant shaking for 30 min at room temperature. After addition of 140 μl dH_2O and further incubation for 30 min at room temperature, the samples were centrifuged at 1,000*g* for 15 min. 500 μl of the upper, organic phase was collected and dried under a stream of nitrogen. Lipids were resolved in 500 μl 2-propanol/methanol/dH_2O (7/2.5/1, vol/vol/v) for UHPLC–Q-TOF analysis. The extracted cell proteins were dried and solubilized in 0.3 N NaOH at 65°C for 4 h and the protein content was determined using Pierce BCA reagent (Thermo Fisher Scientific) and BSA as standard.

Chromatographic separation was performed on a 1290 Infinity II LC system (Agilent) equipped with a Zorbax Extend-C18 rapid resolution HT column (2.1 × 50 mm, 1.8 μm; Agilent) running a 16-min linear gradient from 60% solvent A (H_2O; 10 mM ammonium acetate, 0.1% formic acid, 8 μM phosphoric acid) to 100% solvent B (2-propanol; 10 mM ammonium acetate, 0.1% formic acid, 8 μM phosphoric acid). The column compartment was kept on 50°C. A 6560 Ion Mobility Q-TOF mass spectrometer (Agilent) equipped with Dual AJS ESI source was used for detection of lipids in positive Q-TOF mode. Data acquisition was done by MassHunter Data Acquisition software (B.09; Agilent). Lipids were manually identified, and lipid data were processed using MassHunter Quantitative Analysis (B.09; Agilent). Data were normalized for recovery, extraction-, and ionization efficacy by calculating analyte/IS ratios (AU) and expressed as AU/mg protein.

Statistics

t test was used for comparison. In case of comparison between the values that were normalized to 1, one sample *t* test was used. GraphPad prism software was used for statistical analysis and preparation of figures.

Data Availability

The complexome profiling data from this publication has been deposited to ProteomeXchange Consortium via the PRIDE partner repository (Perez-Riverol et al, 2019) with the dataset identifier PXD016733 and PXD016732. The dataset is publicly available.

Supplementary Information

Supplementary Information is available at https://doi.org/10.26508/lsa.202000711.

Acknowledgements

We thank Andrea Borchardt for excellent technical assistance in electron microscopy experiments and help in cell culture work. Experiments with STED were performed at the Centre for Advanced Imaging facility, Düsseldorf. This research is supported by research funding from the Research Committee of the Medical faculty of Heinrich Heine University Düsseldorf Foko-02/2015 (R Anand and AS Reichert) and FoKo-37/2015 (AK Kondadi) and Deutsche Forschungsgemeinschaft (DFG) grant RE 1575/2-1 (AS Reichert). Data were partly compiled within the Collaborative Research Center 1208: Identity and dynamics of membrane systems–from molecules to cellular functions funded by the DFG (German Research Foundation) – Project-ID 267205415 – Collaborative Research Center 1208 – project B12 (AS Reichert). I Wittig is supported by the DFG: Collaborative Research Center 815/Z1, EXC2026: Cardio Pulmonary Institute and by the Bundesministerium für Bildung und Forschung (BMBF) mitoNET—German Network for Mitochondrial Disorders 01GM1906D.

Author Contributions

R Anand: conceptualization, data curation, formal analysis, supervision, investigation, visualization, methodology, project administration, and writing—original draft, review, and editing.
AK Kondadi: data curation, formal analysis, supervision, validation, investigation, visualization, and methodology.
J Meisterknecht: investigation and methodology.
M Golombek: investigation and methodology.
O Nortmann: investigation and methodology.
J Riedel: investigation and methodology.
L Peifer-Weiß: investigation and methodology.
N Brocke-Ahmadinejad: formal analysis, validation, investigation, visualization, and methodology.
D Schlütermann: investigation and methodology.
B Stork: supervision, investigation, and methodology.
TO Eichmann: resources, data curation, formal analysis, validation, investigation, visualization, and methodology.
I Wittig: resources, data curation, formal analysis, supervision, validation, investigation, visualization, and methodology.
AS Reichert: conceptualization, data curation, supervision, funding acquisition, investigation, project administration, and writing—original draft, review, and editing.

Conflict of Interest Statement

The authors declare that they have no conflict of interest.

References

Aaltonen MJ, Friedman JR, Osman C, Salin B, di Rago JP, Nunnari J, Langer T, Tatsuta T (2016) MICOS and phospholipid transfer by Ups2-Mdm35 organize membrane lipid synthesis in mitochondria. *J Cell Biol* 213: 525–534. doi:10.1083/jcb.201602007

Acehan D, Malhotra A, Xu Y, Ren M, Stokes DL, Schlame M (2011) Cardiolipin affects the supramolecular organization of ATP synthase in mitochondria. *Biophys J* 100: 2184–2192. doi:10.1016/j.bpj.2011.03.031

Acehan D, Xu Y, Stokes DL, Schlame M (2007) Comparison of lymphoblast mitochondria from normal subjects and patients with Barth syndrome using electron microscopic tomography. *Lab Invest* 87: 40–48. doi:10.1038/labinvest.3700480

Anand R, Langer T, Baker MJ (2013) Proteolytic control of mitochondrial function and morphogenesis. *Biochim Biophys Acta* 1833: 195–204. doi:10.1016/j.bbamcr.2012.06.025

Anand R, Strecker V, Urbach J, Wittig I, Reichert AS (2016) Mic13 is essential for formation of crista junctions in mammalian cells. *PLoS One* 11: e0160258. doi:10.1371/journal.pone.0160258

Baker N, Patel J, Khacho M (2019) Linking mitochondrial dynamics, cristae remodeling and supercomplex formation: How mitochondrial structure can regulate bioenergetics. *Mitochondrion* 49: 259–268. doi:10.1016/j.mito.2019.06.003

Barrera M, Koob S, Dikov D, Vogel F, Reichert AS (2016) OPA1 functionally interacts with MIC60 but is dispensable for crista junction formation. *FEBS Lett* 590: 3309–3322. doi:10.1002/1873-3468.12384

Beninca C, Zanette V, Brischigliaro M, Johnson M, Reyes A, do Valle DA, Robinson AJ, Degiorgi A, Yeates A, Telles BA, et al (2020) Mutation in the MICOS subunit gene APOO (MIC26) associated with an X-linked recessive mitochondrial myopathy, lactic acidosis, cognitive impairment and autistic features. *J Med Genet*. doi:10.1136/jmedgenet-2020-106861

Blum TB, Hahn A, Meier T, Davies KM, Kuhlbrandt W (2019) Dimers of mitochondrial ATP synthase induce membrane curvature and self-assemble into rows. *Proc Natl Acad Sci U S A* 116: 4250–4255. doi:10.1073/pnas.1816556116

Bottinger L, Horvath SE, Kleinschroth T, Hunte C, Daum G, Pfanner N, Becker T (2012) Phosphatidylethanolamine and cardiolipin differentially affect the stability of mitochondrial respiratory chain supercomplexes. *J Mol Biol* 423: 677–686. doi:10.1016/j.jmb.2012.09.001

Brady AN, Shehata BM, Fernhoff PM (2006) X-linked fetal cardiomyopathy caused by a novel mutation in the TAZ gene. *Prenat Diagn* 26: 462–465. doi:10.1002/pd.1438

Callegari S, Muller T, Schulz C, Lenz C, Jans DC, Wissel M, Opazo F, Rizzoli SO, Jakobs S, Urlaub H, et al (2019) A MICOS-TIM22 association promotes carrier import into human mitochondria. *J Mol Biol* 431: 2835–2851. doi:10.1016/j.jmb.2019.05.015

Cipolat S, Martins de Brito O, Dal Zilio B, Scorrano L (2004) OPA1 requires mitofusin 1 to promote mitochondrial fusion. *Proc Natl Acad Sci U S A* 101: 15927–15932. doi:10.1073/pnas.0407043101

Cogliati S, Enriquez JA, Scorrano L (2016) Mitochondrial cristae: Where beauty meets functionality. *Trends Biochem Sci* 41: 261–273. doi:10.1016/j.tibs.2016.01.001

Cogliati S, Frezza C, Soriano ME, Varanita T, Quintana-Cabrera R, Corrado M, Cipolat S, Costa V, Casarin A, Gomes LC, et al (2013) Mitochondrial cristae shape determines respiratory chain supercomplexes assembly and respiratory efficiency. *Cell* 155: 160–171. doi:10.1016/j.cell.2013.08.032

Davies KM, Strauss M, Daum B, Kief JH, Osiewacz HD, Rycovska A, Zickermann V, Kuhlbrandt W (2011) Macromolecular organization of ATP synthase and complex I in whole mitochondria. *Proc Natl Acad Sci U S A* 108: 14121–14126. doi:10.1073/pnas.1103621108

Dlaskova A, Spacek T, Engstova H, Spackova J, Schrofel A, Holendova B, Smolkova K, Plecita-Hlavata L, Jezek P (2019) Mitochondrial cristae narrowing upon higher 2-oxoglutarate load. *Biochim Biophys Acta Bioenerg* 1860: 659–678. doi:10.1016/j.bbabio.2019.06.015

Duvezin-Caubet S, Jagasia R, Wagener J, Hofmann S, Trifunovic A, Hansson A, Chomyn A, Bauer MF, Attardi G, Larsson NG, et al (2006) Proteolytic processing of OPA1 links mitochondrial dysfunction to alterations in mitochondrial morphology. *J Biol Chem* 281: 37972–37979. doi:10.1074/jbc.m606059200

Duvezin-Caubet S, Koppen M, Wagener J, Zick M, Israel L, Bernacchia A, Jagasia R, Rugarli EI, Imhof A, Neupert W, et al (2007) OPA1 processing reconstituted in yeast depends on the subunit composition of the m-

AAA protease in mitochondria. *Mol Biol Cell* 18: 3582–3590. doi:10.1091/mbc.e07-02-0164

Eydt K, Davies KM, Behrendt C, Wittig I, Reichert AS (2017) Cristae architecture is determined by an interplay of the MICOS complex and the F1FO ATP synthase via Mic27 and Mic10. *Microb Cell* 4: 259–272. doi:10.15698/mic2017.08.585

Frezza C, Cipolat S, Martins de Brito O, Micaroni M, Beznoussenko GV, Rudka T, Bartoli D, Polishuck RS, Danial NN, De Strooper B, et al (2006) OPA1 controls apoptotic cristae remodeling independently from mitochondrial fusion. *Cell* 126: 177–189. doi:10.1016/j.cell.2006.06.025

Friedman JR, Mourier A, Yamada J, McCaffery JM, Nunnari J (2015) MICOS coordinates with respiratory complexes and lipids to establish mitochondrial inner membrane architecture. *Elife* 4: e07739. doi:10.7554/elife.07739

Gomes LC, Di Benedetto G, Scorrano L (2011) During autophagy mitochondria elongate, are spared from degradation and sustain cell viability. *Nat Cell Biol* 13: 589–598. doi:10.1038/ncb2220

Guarani V, Jardel C, Chretien D, Lombes A, Benit P, Labasse C, Lacene E, Bourillon A, Imbard A, Benoist JF, et al (2016) QIL1 mutation causes MICOS disassembly and early onset fatal mitochondrial encephalopathy with liver disease. *Elife* 5: e17163. doi:10.7554/elife.17163

Guarani V, McNeill EM, Paulo JA, Huttlin EL, Frohlich F, Gygi SP, Van Vactor D, Harper JW (2015) QIL1 is a novel mitochondrial protein required for MICOS complex stability and cristae morphology. *Elife* 4: e06265. doi:10.7554/elife.06265

Harner M, Körner C, Walther D, Mokranjac D, Kaesmacher J, Welsch U, Griffith J, Mann M, Reggiori F, Neupert W (2011) The mitochondrial contact site complex, a determinant of mitochondrial architecture. *EMBO J* 30: 4356–4370. doi:10.1038/emboj.2011.379

Harner ME, Unger AK, Izawa T, Walther DM, Ozbalci C, Geimer S, Reggiori F, Brugger B, Mann M, Westermann B, et al (2014) Aim24 and MICOS modulate respiratory function, tafazzin-related cardiolipin modification and mitochondrial architecture. *Elife* 3: e01684. doi:10.7554/elife.01684

Hoppins S, Collins SR, Cassidy-Stone A, Hummel E, Devay RM, Lackner LL, Westermann B, Schuldiner M, Weissman JS, Nunnari J (2011) A mitochondrial-focused genetic interaction map reveals a scaffold-like complex required for inner membrane organization in mitochondria. *J Cell Biol* 195: 323–340. doi:10.1083/jcb.201107053

Jans DC, Wurm CA, Riedel D, Wenzel D, Stagge F, Deckers M, Rehling P, Jakobs S (2013) STED super-resolution microscopy reveals an array of MINOS clusters along human mitochondria. *Proc Natl Acad Sci U S A* 110: 8936–8941. doi:10.1073/pnas.1301820110

Kojima R, Kakimoto Y, Furuta S, Itoh K, Sesaki H, Endo T, Tamura Y (2019) Maintenance of cardiolipin and crista structure requires cooperative functions of mitochondrial dynamics and phospholipid transport. *Cell Rep* 26: 518–528.e6. doi:10.1016/j.celrep.2018.12.070

Kondadi AK, Anand R, Hansch S, Urbach J, Zobel T, Wolf DM, Segawa M, Liesa M, Shirihai OS, Weidtkamp-Peters S, et al (2020) Cristae undergo continuous cycles of membrane remodelling in a MICOS-dependent manner. *EMBO Rep* 21: e49776. doi:10.15252/embr.201949776

Kondadi AK, Anand R, Reichert AS (2019) Functional interplay between cristae biogenesis, mitochondrial dynamics and mitochondrial DNA integrity. *Int J Mol Sci* 20: 4311. doi:10.3390/ijms20174311

Koob S, Barrera M, Anand R, Reichert AS (2015) The non-glycosylated isoform of MIC26 is a constituent of the mammalian MICOS complex and promotes formation of crista junctions. *Biochim Biophys Acta* 1853: 1551–1563. doi:10.1016/j.bbamcr.2015.03.004

Lamant M, Smih F, Harmancey R, Philip-Couderc P, Pathak A, Roncalli J, Galinier M, Collet X, Massabuau P, Senard JM, et al (2006) ApoO, a novel apolipoprotein, is an original glycoprotein up-regulated by diabetes in human heart. *J Biol Chem* 281: 36289–36302. doi:10.1074/jbc.m510861200

Lapuente-Brun E, Moreno-Loshuertos R, Acin-Perez R, Latorre-Pellicer A, Colas C, Balsa E, Perales-Clemente E, Quiros PM, Calvo E, Rodriguez-Hernandez MA, et al (2013) Supercomplex assembly determines electron flux in the mitochondrial electron transport chain. *Science* 340: 1567–1570. doi:10.1126/science.1230381

Lee H, Smith SB, Yoon Y (2017) The short variant of the mitochondrial dynamin OPA1 maintains mitochondrial energetics and cristae structure. *J Biol Chem* 292: 7115–7130. doi:10.1074/jbc.m116.762567

Livak KJ, Schmittgen TD (2001) Analysis of relative gene expression data using real-time quantitative PCR and the 2(-Delta Delta C(T)) method. *Methods* 25: 402–408. doi:10.1006/meth.2001.1262

Lytovchenko O, Naumenko N, Oeljeklaus S, Schmidt B, von der Malsburg K, Deckers M, Warscheid B, van der Laan M, Rehling P (2014) The INA complex facilitates assembly of the peripheral stalk of the mitochondrial F1Fo-ATP synthase. *EMBO J* 33: 1624–1638. doi:10.15252/embj.201488076

MacVicar T, Langer T (2016) OPA1 processing in cell death and disease: The long and short of it. *J Cell Sci* 129: 2297–2306. doi:10.1242/jcs.159186

Mannella CA (2006) The relevance of mitochondrial membrane topology to mitochondrial function. *Biochim Biophys Acta* 1762: 140–147. doi:10.1016/j.bbadis.2005.07.001

Mannella CA (2008) Structural diversity of mitochondria: Functional implications. *Ann N Y Acad Sci* 1147: 171–179. doi:10.1196/annals.1427.020

Mannella CA, Lederer WJ, Jafri MS (2013) The connection between inner membrane topology and mitochondrial function. *J Mol Cell Cardiol* 62: 51–57. doi:10.1016/j.yjmcc.2013.05.001

Mannella CA, Pfeiffer DR, Bradshaw PC, Moraru II, Slepchenko B, Loew LM, Hsieh CE, Buttle K, Marko M (2001) Topology of the mitochondrial inner membrane: Dynamics and bioenergetic implications. *IUBMB Life* 52: 93–100. doi:10.1080/15216540152845885

Matyash V, Liebisch G, Kurzchalia TV, Shevchenko A, Schwudke D (2008) Lipid extraction by methyl-tert-butyl ether for high-throughput lipidomics. *J Lipid Res* 49: 1137–1146. doi:10.1194/jlr.d700041-jlr200

McKenzie M, Lazarou M, Thorburn DR, Ryan MT (2006) Mitochondrial respiratory chain supercomplexes are destabilized in Barth Syndrome patients. *J Mol Biol* 361: 462–469. doi:10.1016/j.jmb.2006.06.057

Milenkovic D, Blaza JN, Larsson NG, Hirst J (2017) The enigma of the respiratory chain supercomplex. *Cell Metab* 25: 765–776. doi:10.1016/j.cmet.2017.03.009

Morita S, Kojima T, Kitamura T (2000) Plat-E: An efficient and stable system for transient packaging of retroviruses. *Gene Ther* 7: 1063–1066. doi:10.1038/sj.gt.3301206

Naumenko N, Morgenstern M, Rucktaschel R, Warscheid B, Rehling P (2017) INA complex liaises the F1Fo-ATP synthase membrane motor modules. *Nat Commun* 8: 1237. doi:10.1038/s41467-017-01437-z

Patten DA, Wong J, Khacho M, Soubannier V, Mailloux RJ, Pilon-Larose K, MacLaurin JG, Park DS, McBride HM, Trinkle-Mulcahy L, et al (2014) OPA1-dependent cristae modulation is essential for cellular adaptation to metabolic demand. *EMBO J* 33: 2676–2691. doi:10.15252/embj.201488349

Paumard P, Vaillier J, Coulary B, Schaeffer J, Soubannier V, Mueller DM, Brethes D, di Rago JP, Velours J (2002) The ATP synthase is involved in generating mitochondrial cristae morphology. *EMBO J* 21: 221–230. doi:10.1093/emboj/21.3.221

Perez-Riverol Y, Csordas A, Bai J, Bernal-Llinares M, Hewapathirana S, Kundu DJ, Inuganti A, Griss J, Mayer G, Eisenacher M, et al (2019) The PRIDE database and related tools and resources in 2019: Improving support

for quantification data. *Nucleic Acids Res* 47: D442–D450. doi:10.1093/nar/gky1106

Perkins G, Renken C, Martone ME, Young SJ, Ellisman M, Frey T (1997) Electron tomography of neuronal mitochondria: Three-dimensional structure and organization of cristae and membrane contacts. *J Struct Biol* 119: 260–272. doi:10.1006/jsbi.1997.3885

Pernas L, Scorrano L (2016) Mito-Morphosis: Mitochondrial fusion, fission, and cristae remodeling as key mediators of cellular function. *Annu Rev Physiol* 78: 505–531. doi:10.1146/annurev-physiol-021115-105011

Pfeiffer K, Gohil V, Stuart RA, Hunte C, Brandt U, Greenberg ML, Schagger H (2003) Cardiolipin stabilizes respiratory chain supercomplexes. *J Biol Chem* 278: 52873–52880. doi:10.1074/jbc.m308366200

Plecita-Hlavata L, Engstova H, Alan L, Spacek T, Dlaskova A, Smolkova K, Spackova J, Tauber J, Stradalova V, Malinsky J, et al (2016) Hypoxic HepG2 cell adaptation decreases ATP synthase dimers and ATP production in inflated cristae by mitofilin down-regulation concomitant to MICOS clustering. *FASEB J* 30: 1941–1957. doi:10.1096/fj.201500176

Quintana-Cabrera R, Mehrotra A, Rigoni G, Soriano ME (2018a) Who and how in the regulation of mitochondrial cristae shape and function. *Biochem Biophys Res Commun* 500: 94–101. doi:10.1016/j.bbrc.2017.04.088

Quintana-Cabrera R, Quirin C, Glytsou C, Corrado M, Urbani A, Pellattiero A, Calvo E, Vazquez J, Enriquez JA, Gerle C, et al (2018b) The cristae modulator Optic atrophy 1 requires mitochondrial ATP synthase oligomers to safeguard mitochondrial function. *Nat Commun* 9: 3399. doi:10.1038/s41467-018-05655-x

Rabl R, Soubannier V, Scholz R, Vogel F, Mendl N, Vasiljev-Neumeyer A, Körner C, Jagasia R, Keil T, Baumeister W, et al (2009) Formation of cristae and crista junctions in mitochondria depends on antagonism between Fcj1 and Su e/g. *J Cell Biol* 185: 1047–1063. doi:10.1083/jcb.200811099

Rampelt H, Bohnert M, Zerbes RM, Horvath SE, Warscheid B, Pfanner N, van der Laan M (2017a) Mic10, a core subunit of the mitochondrial contact site and cristae organizing system, interacts with the dimeric F1Fo-ATP synthase. *J Mol Biol* 429: 1162–1170. doi:10.1016/j.jmb.2017.03.006

Rampelt H, Wollweber F, Gerke C, de Boer R, van der Klei IJ, Bohnert M, Pfanner N, van der Laan M (2018) Assembly of the mitochondrial cristae organizer Mic10 is regulated by Mic26-Mic27 antagonism and cardiolipin. *J Mol Biol* 430: 1883–1890. doi:10.1016/j.jmb.2018.04.037

Rampelt H, Zerbes RM, van der Laan M, Pfanner N (2017b) Role of the mitochondrial contact site and cristae organizing system in membrane architecture and dynamics. *Biochim Biophys Acta Mol Cell Res* 1864: 737–746. doi:10.1016/j.bbamcr.2016.05.020

Ruhle T, Leister D (2015) Assembly of F1F0-ATP synthases. *Biochim Biophys Acta* 1847: 849–860. doi:10.1016/j.bbabio.2015.02.005

Schägger H, Pfeiffer K (2000) Supercomplexes in the respiratory chains of yeast and mammalian mitochondria. *EMBO J* 19: 1777–1783. doi:10.1093/emboj/19.8.1777

Scorrano L, Ashiya M, Buttle K, Weiler S, Oakes SA, Mannella CA, Korsmeyer SJ (2002) A distinct pathway remodels mitochondrial cristae and mobilizes cytochrome c during apoptosis. *Dev Cell* 2: 55–67. doi:10.1016/s1534-5807(01)00116-2

Serricchio M, Vissa A, Kim PK, Yip CM, McQuibban GA (2018) Cardiolipin synthesizing enzymes form a complex that interacts with cardiolipin-dependent membrane organizing proteins. *Biochim Biophys Acta Mol Cell Biol Lipids* 1863: 447–457. doi:10.1016/j.bbalip.2018.01.007

Song Z, Chen H, Fiket M, Alexander C, Chan DC (2007) OPA1 processing controls mitochondrial fusion and is regulated by mRNA splicing, membrane potential, and Yme1L. *J Cell Biol* 178: 749–755. doi:10.1083/jcb.200704110

Stoldt S, Stephan T, Jans DC, Bruser C, Lange F, Keller-Findeisen J, Riedel D, Hell SW, Jakobs S (2019) Mic60 exhibits a coordinated clustered distribution along and across yeast and mammalian mitochondria. *Proc Natl Acad Sci U S A* 116: 9853–9858. doi:10.1073/pnas.1820364116

Strauss M, Hofhaus G, Schroder RR, Kuhlbrandt W (2008) Dimer ribbons of ATP synthase shape the inner mitochondrial membrane. *EMBO J* 27: 1154–1160. doi:10.1038/emboj.2008.35

Tian F, Wu CL, Yu BL, Liu L, Hu JR (2017) Apolipoprotein O expression in mouse liver enhances hepatic lipid accumulation by impairing mitochondrial function. *Biochem Biophys Res Commun* 491: 8–14. doi:10.1016/j.bbrc.2017.06.128

Tsai PI, Lin CH, Hsieh CH, Papakyrikos AM, Kim MJ, Napolioni V, Schoor C, Couthouis J, Wu RM, Wszolek ZK, et al (2018) PINK1 phosphorylates MIC60/mitofilin to control structural plasticity of mitochondrial crista junctions. *Mol Cell* 69: 744–756.e6. doi:10.1016/j.molcel.2018.01.026

Turkieh A, Caubere C, Barutaut M, Desmoulin F, Harmancey R, Galinier M, Berry M, Dambrin C, Polidori C, Casteilla L, et al (2014) Apolipoprotein O is mitochondrial and promotes lipotoxicity in heart. *J Clin Invest* 124: 2277–2286. doi:10.1172/jci74668

Vogel F, Bornhövd C, Neupert W, Reichert AS (2006) Dynamic subcompartmentalization of the mitochondrial inner membrane. *J Cell Biol* 175: 237–247. doi:10.1083/jcb.200605138

von der Malsburg K, Muller JM, Bohnert M, Oeljeklaus S, Kwiatkowska P, Becker T, Loniewska-Lwowska A, Wiese S, Rao S, Milenkovic D, et al (2011) Dual role of mitofilin in mitochondrial membrane organization and protein biogenesis. *Dev Cell* 21: 694–707. doi:10.1016/j.devcel.2011.08.026

Weber TA, Koob S, Heide H, Wittig I, Head B, van der Bliek A, Brandt U, Mittelbronn M, Reichert AS (2013) APOOL is a cardiolipin-binding constituent of the Mitofilin/MINOS protein complex determining cristae morphology in mammalian mitochondria. *PLoS One* 8: e63683. doi:10.1371/journal.pone.0063683

Wolf DM, Segawa M, Kondadi AK, Anand R, Bailey ST, Reichert AS, van der Bliek AM, Shackelford DB, Liesa M, Shirihai OS (2019) Individual cristae within the same mitochondrion display different membrane potentials and are functionally independent. *EMBO J* 38: e101056. doi:10.15252/embj.2018101056

Wurm CA, Jakobs S (2006) Differential protein distributions define two sub-compartments of the mitochondrial inner membrane in yeast. *FEBS Lett* 580: 5628–5634. doi:10.1016/j.febslet.2006.09.012

Yu BL, Wu CL, Zhao SP (2012) Plasma apolipoprotein O level increased in the patients with acute coronary syndrome. *J Lipid Res* 53: 1952–1957. doi:10.1194/jlr.p023028

Zeharia A, Friedman JR, Tobar A, Saada A, Konen O, Fellig Y, Shaag A, Nunnari J, Elpeleg O (2016) Mitochondrial hepato-encephalopathy due to deficiency of QIL1/MIC13 (C19orf70), a MICOS complex subunit. *Eur J Hum Genet* 24: 1778–1782. doi:10.1038/ejhg.2016.83

Zerbes RM, Hoss P, Pfanner N, van der Laan M, Bohnert M (2016) Distinct roles of Mic12 and Mic27 in the mitochondrial contact site and cristae organizing system. *J Mol Biol* 428: 1485–1492. doi:10.1016/j.jmb.2016.02.031

Zhang M, Mileykovskaya E, Dowhan W (2002) Gluing the respiratory chain together. Cardiolipin is required for supercomplex formation in the inner mitochondrial membrane. *J Biol Chem* 277: 43553–43556. doi:10.1074/jbc.c200551200

Zick M, Rabl R, Reichert AS (2009) Cristae formation-linking ultrastructure and function of mitochondria. *Biochim Biophys Acta* 1793: 5–19. doi:10.1016/j.bbamcr.2008.06.013

3.3. Involvement of necroptosis in the selective toxicity of the natural compound (±) gossypol on squamous skin cancer cells in vitro

Archives of Toxicology (2023) 97:1997–2014
https://doi.org/10.1007/s00204-023-03516-1

GENOTOXICITY AND CARCINOGENICITY

Involvement of necroptosis in the selective toxicity of the natural compound (±) gossypol on squamous skin cancer cells in vitro

Lisa Haasler[1] · Claudia von Montfort[1] · Arun Kumar Kondadi[1] · Mathias Golombek[1] · Lara Ebbert[1] · Chantal-Kristin Wenzel[1] · Wilhelm Stahl[1] · Andreas S. Reichert[1] · Peter Brenneisen[1]

Received: 21 December 2022 / Accepted: 8 May 2023 / Published online: 21 May 2023

Abstract

Cutaneous basal and squamous cell carcinoma reflect the first and second most common type of non-melanoma skin cancer, respectively. Especially cutaneous squamous cell carcinoma has the tendency to metastasize, finally resulting in a rather poor prognosis. Therapeutic options comprise surgery, radiation therapy, and a systemic or targeted chemotherapy. There are some good treatment results, but overall, the response rate of newly developed drugs is still modest. Drug repurposing represents an alternative approach where already available and clinically approved substances are used, which originally intended for other clinical benefits. In this context, we tested the effect of the naturally occurring polyphenolic aldehyde (±) gossypol with concentrations between 1 and 5 µM on the invasive squamous cell carcinoma cell line SCL-1 and normal human epidermal keratinocytes. Gossypol treatment up to 96 h resulted in a selective cytotoxicity of SCL-1 cells (IC_{50}: 1.7 µM, 96 h) compared with normal keratinocytes (IC_{50}: ≥ 5.4 µM, 96 h) which is mediated by mitochondrial dysfunction and finally leading to necroptotic cell death. Taken together, gossypol shows a high potential as an alternative anticancer drug for the treatment of cutaneous squamous cell carcinoma.

Keywords Cutaneous squamous cell carcinoma · Gossypol · Mitochondrial dysfunction · Necroptosis · Keratinocytes

Introduction

Skin cancer, mainly the out-of-control growth of specific cells in the epidermis, roughly comprises cutaneous melanoma (CM) and non-melanoma skin cancer (NMSC). NMSC are subdivided in the two keratinocyte skin cancers (KSC) named basal cell carcinoma (BCC) and cutaneous squamous cell carcinoma (cSCC), reflecting the first and second most common types of skin cancer (Dubas and Ingraffea 2013; Fania et al. 2021). Non-melanoma skin cancer has been demonstrated to associate with significant morbidity, mortality, and economic burden (Cakir et al. 2012; Nehal and Bichakjian 2018). The Global Burden of Disease Study (GBDS 2019) (Fitzmaurice et al. 2019) pointed out NMSC is the topmost of the global top ten cancers in 2017 with 7.7 million new cases of NMSC of which roughly 25% represent squamous cell carcinomas. While both BCC and cSCC are normally described to exhibit a benign clinical behavior, about 5% of cSCC cases will become locally advanced, recur or metastasize (Ribero et al. 2017; Varra et al. 2018). Among other risk factors, UVB irradiation (280–320 nm) is associated with the highest risk for the development of BCC and cSCC (Watson et al. 2016; Laikova et al. 2019). Options of treatment against cSCC comprise surgery, radiation therapy, and a systemic or targeted chemotherapy, either each of those alone or in a combination (Burton et al. 2016; Dessinioti and Stratigos 2022). Patients with advanced unresectable or metastatic cSCC have access to a systemic treatment with platinum compounds, 5-fluorouracil, methotrexate, taxanes, and anthracyclines (Nakamura et al. 2013; Ribero et al. 2017) or a more targeted treatment with small molecule drugs or monoclonal antibodies targeting specific proteins (Corchado-Cobos et al. 2020; García-Foncillas et al. 2022). In a number of clinical trials, it has become evident that the overall response rate is rather modest and accompanied by resistances (Wheeler et al. 2008) as well as side effects from skin reactions to anaphylaxis (Hu et al. 2007; Marti et al. 2016; Agirgol et al. 2020). An alternative to the

✉ Peter Brenneisen
peter.brenneisen@hhu.de

[1] Institute of Biochemistry and Molecular Biology I, Medical Faculty, Heinrich-Heine University Düsseldorf, 40225 Düsseldorf, Germany

high expenditure of time and exorbitant rising costs for the development of novel drugs is the modified use of already available and clinically approved substances, which originally intended for other clinical benefit (drug repurposing) (Gupta et al. 2013; Zhang et al. 2020). As an example, the chlorinated 4-aminoquinoline derivative chloroquine originally developed for prophylaxis and treatment of malaria was repurposed as inhibitor of autophagy and anticancer agent (Vlahopoulos et al. 2014). Further on, (±) gossypol (GP), a naturally occurring polyphenolic aldehyde from cottonseed (Adams et al. 1960) and originally being tested as a male contraceptive (Coutinho 2002), is now in the focus as an anticancer drug (Zeng et al. 2019; Liu et al. 2022). As a BH3 mimetic agent, it was shown that GP inhibited the anti-apoptotic proteins BCL-2, BCL-xL, and MCL-1 (Opydo-Chanek et al. 2017; Melo et al. 2022). Recently, it was described that GP acetate at high concentrations led to an autophagic block in the human non-small-cell lung cancer cell line A549 (Cai et al. 2022). Previously, we demonstrated that GP exhibited a selective toxicity on A375 melanoma cells via mitochondrial dysfunction finally resulting in apoptotic cell death (Haasler et al. 2021). In this in vitro study, we focused on the effect of GP on the NMSC cell line SCL-1 which is a model of cSCC showing malignant growth characteristics and an invasive capacity in vivo (Boukamp et al. 1982). GP caused a selective toxicity in the tumor cells compared to normal keratinocytes which was mediated by mitochondrial changes and finally resulted in necroptotic cell death.

Materials and methods

Materials

The used chemicals and Dulbecco's modified Eagle's medium (DMEM) were purchased from Sigma-Aldrich (Taufkirchen, Germany) or Merck (Darmstadt, Germany), if not otherwise stated. ABT-199/venetoclax (CAS 1257044-40-) and (±) gossypol (GP, CAS 303-45-7) were obtained from Abcam (Cambrigde, UK). Fetal bovine serum (FBS) was from Pan-Biotech (Aidenbach, Germany). Penicillin/Streptomycin was purchased from Biochrom (Berlin, Germany) and Glutamax from Gibco (Darmstadt, Germany). The keratinocyte basal (C-20211) and growth medium including SupplementMix (C-20011) were obtained from PromoCell (Heidelberg, Germany). The pan-caspase inhibitor Z-VAD(OMe)-FMK (zVAD) was purchased from Santa Cruz Biotechnology (Heidelberg, Germany). Tetramethylrhodamine methylester (TMRM) and Molecular Probes MitoTRACKER™ Green FM were obtained from Thermo Fisher Scientific (Waltham, Massachusetts, USA). The Seahorse XF Cell Mito Stress Test Kit (Cat. 103015-100) was obtained from Agilent Technologies (Waldbronn, Germany). The ProLong Gold Antifade Reagent with DAPI (Cat. 8961) was ordered from Cell Signaling Technology (Danvers, Massachusetts, USA). Caspase 3/7 (Cat. 22795), Caspase 8 (Cat. 22812), and Caspase 9 (Cat. 22813) Activity Apoptosis Assays were purchased from AAT Bioquest (Biomol, Hamburg, Germany). The lactate dehydrogenase (LDH) ELISA kit (Cat. ab183367) was from Abcam and the DC™ protein assay kit was purchased from Bio-Rad (Feldkirchen, Germany).

The following primary antibodies were used: polyclonal anti-PARP (Cat. 9542), the monoclonals anti-Bax (Cat. 5023), anti-BcL-xL (Cat. 2764), anti-phospho-RIP3 (Ser227; Cat. 93654), and anti-ß-Tubulin (Cat. 2128) from Cell Signaling Technology; monoclonal anti-Bcl-2 (Cat. Ab32124) from Abcam; monoclonal anti-RIP3 (Cat. sc-374639) from Santa Cruz Biotechnology. As secondary antibodies, the horseradish peroxidase (HRP)-conjugated goat anti-rabbit IgG (Cat. 111-035-144) from Dianova (Hamburg, Germany) and Alexa Fluor 568 goat anti-mouse IgG (red; Cat. A-11004) from Thermo Fisher were used.

Cell culture

The human cutaneous squamous carcinoma cell line SCL-1 was a gift from Prof. Dr. Norbert Fusenig from the German Cancer Research Center (DKFZ, Heidelberg, Germany) (Boukamp et al. 1982). The human melanoma cell line A375 (ATCC CRL-1619) was obtained from the American Type Culture Collection (ATCC, Virginia, USA). Normal human epidermal keratinocytes (NHEK, C-12001) were ordered from PromoCell (Heidelberg, Germany). SCL-1 and A375 tumor cells were cultured in Dulbecco's modified Eagle's medium (DMEM, low glucose), supplemented with 10% fetal bovine serum (FBS), streptomycin (100 µg/ml), penicillin (100 U/ml), and GlutaMAX™ (2 mM) at 37 °C in 5% CO_2. NHEK were cultured in keratinocyte growth medium (C-20011, PromoCell) including SupplementMix (C-39016), streptomycin (100 µg/ml) and penicillin (100 U/ml) at 37 °C in 5% CO_2. Subconfluent cells (70–80% confluence) were used for all experiments, if not otherwise stated. For treatment, SCL-1 and A375 were incubated in high glucose (4500 mg/L) DMEM without FBS, while NHEK were grown in keratinocyte basal medium (C-20211, PromoCell). Gossypol and other substances such as ABT-199, inhibitors, and fluorescent dyes were directly added to the cells at the appropriate concentrations.

Cell viability assay

The cell viability was either measured by the MTT (3-(4,5-dimethylthiazol-2-yl)-2,5-diphenyltetrazolium bromide) or sulforhodamine B (SRB) assay which are based

on the activity of mitochondrial dehydrogenases (Mosmann 1983) and on the pH-dependent staining of total proteins, respectively (Maydt et al. 2013). For MTT assay, the enzyme catalyzes the conversion from MTT to a purple formazan dye. Subconfluent cells were treated with different concentrations of GP or mock-treated in 24-well plates. After washing with PBS, MTT solution (0.5 mg/ml) was directly added to the cells and incubated between 0.5 and 2 h depending on the cell type. After removal of MTT, the cells were washed with PBS and 500 µl DMSO per well was added for formazan extraction. Absorbance was measured at 570 nm with a plate reader (FLUOstar OPTIMA, BMG Labtech, Ortenberg, Germany). The mock-treated control was set at 100%. The SRB assay was performed with subconfluent cells in four-well plates. Cells were treated with different concentration of GP or mock treated. Subsequently, cells were washed with PBS and fixed with 10% (w/v) cold trichloroacetic acid solution (500 µl/well) for 1 h at 4 °C. After washing several times with dH_2O, cells were dried at RT. For the staining, cells were incubated with SRB solution (0.4% (w/v) in 1% acetic acid, 300 µl/well) for 15 min at RT, washed with 1% acetic acid and dried at RT. For extraction of SRB, 400 µl TRIS-Base (10 mmol/l) was added per well and the plate was gently rotated for 5 min. The absorbance was measured at 492 nm minus background values at 620 nm using a microplate reader (Tecan M200 pro, Männedorf, Switzerland). Cell viability of mock-treated cells was set at 100%.

Intracellular measurement of GP (HPLC)

Cellular uptake of GP was determined by high performance liquid chromatography (HPLC) after treatment of cells with 5 µM GP. Tumor and normal cells were grown to subconfluence in Ø 10 cm culture dishes. After incubation with GP for different time periods and washing with PBS, cells were harvested in 2 ml PBS. Samples were centrifuged at 500×g for 8 min at 4 °C, washed with PBS, and centrifuged at 5.000xg for 6 min at 4 °C. Cell pellets were resuspended in 150 µl acetonitrile (AcN), mixed thoroughly, and centrifuged at 20.000xg for 5 min at 4 °C. For analysis, 50 µl of the AcN extract was injected, and the GP concentration was quantified using a standard curve. HPLC was performed on a Supelco pKb 100 (250 × 4.6 mm) column with a mobile phase consisting of AcN/water/trifluoroacetic acid (90/10/0.1, v/v/v) at a flow rate of 1.0 ml/min (0–10 min) and UV detection at 367 nm. Retention time of GP was around 5 min (Haasler et al. 2021). Only intracellular GP and not its metabolites were measured. For protein quantification, the solvent residue was evaporated and the cell pellet was solved in 1% SDS lysis buffer containing 0.1% protease inhibitor cocktail and sonicated. For quantification of the intracellular GP content, the concentration of GP was set in relation to the protein amount, which was calculated using the DC™ Protein Assay Kit.

Mitochondrial membrane potential (ΔΨm)

To study changes in ΔΨm, SCL-1 tumor cells and NHEK were seeded on glass bottom dishes (Ø 3.5 cm, MatTek, Son, Netherlands) and incubated with 2.5 µM GP or mock treated (DMSO) for 2 and 4 h, respectively, or with 10 µM carbonyl cyanide m-chlorophenyl hydrazone (CCCP), an oxidative phosphorylation uncoupler (Mahalaxmi et al. 2022), for 2 h as positive control. After incubation, cells were washed with PBS and loaded with 100 nM of the mitochondrial membrane potential sensitive dye tetramethylrhodamine methyl ester (TMRM) (Creed and McKenzie 2019) and 100 nM of MitoTRACKER™ Green for 0.5 h at 37 °C. After washing with PBS, fresh medium was added to the cells. Cells were analyzed with an Ultraview spinning disc confocal microscope (PerkinElmer Corporation, Waltham, Massachusetts, USA). At least 20 image stacks per sample were evaluated. The ΔΨm was calculated by the quotient TMRM to MitoTRACKER™ Green. The mock-treated controls were set at 100%.

Mitochondrial fragmentation

To test for mitochondrial fragmentation as a parameter of mitochondrial dysfunction, the squamous tumor cells and normal keratinocytes were treated as described above for ΔΨm. MitoTRACKER™ Green images were used to evaluate mitochondrial morphology and the quantification was performed as described before (Duvezin-Caubet et al. 2006; Aplak et al. 2020): tubular, at least one mitochondrial tubule of 5 µm or more; intermediate, at least one tubule between 0.5 and 5 µm; fragmented, no tubules of more than 0.5 µm in length. At least 30 cells per sample were analyzed.

Cell characterization and Mito Stress Test

To assess mitochondrial function in cells, the Seahorse XF Cell Mito Stress Test was performed according to the manufacturer's protocol based on the measurement of the oxygen consumption rate (OCR) (Gu et al. 2021) including parameters such as basal and maximal respiration, spare respiratory capacity (SRC), ATP production, and proton leak. A characterization of each cell type was performed to determine the most suitable conditions for the experiments. For that, different cell numbers for each cell type were seeded in a Seahorse 96-well plate (80 µl/well). Different concentrations of the inhibitor oligomycin (Oligo), the protonophore carbonyl cyanide p-trifluoromethoxyphenyl hydrazone (FCCP), and the inhibitors rotenone plus antimycin A (Rot/AA) were tested according to

manufacturer's manual. For subsequent Mito Stress Test, optimal cell numbers and FCCP concentrations were used based on the previously carried out cell characterization. The appropriate cell numbers (SCL-1: 15,000, NHEK: 20,000) were seeded in a Seahorse 96-well plate and the sensor was equilibrated in Seahorse equilibration buffer in a CO_2-free incubator overnight. All cells were washed and mock treated or treated with different concentrations of GP in Seahorse medium (eight replicates/conditions) and were incubated for 1 h in a CO_2-free incubator at 37 °C. Meanwhile, the cartridge was loaded with appropriate concentrations of Oligo [Port A; SCL-1: 2 µM (final conc.), NHEK: 2 µM (final conc.)], FCCP [Port B; SCL-1: 0.5 µM (final conc.), NHEK: 2 µM (final conc.)], and Rot/AA [Port C; SCL-1: 0.5 µM (final conc.), NHEK: 0.5 µM (final conc.)]. After equilibration of the sensor, the assay was performed as described above. For data analysis, the Agilent Seahorse Wave Desktop software was used. The raw data were normalized to the corresponding Hoechst staining. The program calculated the parameters based on the OCR, including basal, maximal and non-mitochondrial respiration, SRC, proton leak, and ATP production. The percentage of each parameter was referred to mock-treated cells.

Caspase activity assay

Caspase activity assays were performed according to the manufacturer's specification. In principle, a selective substrate for the used caspase was added to the cells, which can be cleaved by active caspases. The formation of the fluorescent product was measured and an increase in fluorescence correlated with the activation of caspases upon stimulation of apoptosis. Caspase 8 activity representing the extrinsic pathway and caspase 9 activity representing the intrinsic pathway as well as the activity of the executioner caspases 3/7 were analyzed. Cells were grown to subconfluence in 96-well plates and incubated with different concentrations of GP or mock treated for 6 and 24 h, respectively. Staurosporine (Sts) at a concentration of 20 µM served as positive control. The substrate caspase working solution (3/7, 8, or 9) was prepared and added for 1 h. The inhibitor zVAD-(OMe)-FMK (zVAD) was added 10 min prior to the end of the incubation time to prevent further cleavage of the substrate. Cell-free wells served as background control. Subsequently, the fluorescence was measured using a microplate reader under different emission (Em) and excitations (Ex) wavelengths dependent on the caspase (caspase 3/7: Ex 360 nm, Em 470 nm; caspase 8: Ex 370 nm, Em 450 nm; caspase 9: Ex 375, Em 435 nm). For quantification, the background values were subtracted, the mock-treated control was set at 1.0, and the GP treatment was calculated in relation to the control.

SDS-PAGE and western blot analysis

For sodium dodecyl sulfate polyacrylamide gel electrophoresis (SDS) and western blotting (Laemmli 1970), GP and mock-treated cells were lysed in 1% SDS (Roth, Karlsruhe, Germany) with 0.1% diluted protease inhibitor cocktail and sonicated. Protein concentration was determined using the DC™ Protein Assay Kit. For each sample, 20 µg protein was mixed with 4xSDS-PAGE sample buffer (40% glycerol, 20% β-mercaptoethanol, 12% SDS, 0.4% bromophenol blue) and heated at 95 °C for 10 min. Subsequently, the samples were subjected to 12% or 15% (w/v), SDS-polyacrylamide gels, respectively. After blotting the proteins onto polyvinylidene difluoride (PVDF) membranes (GE Healthcare, Solingen, Germany) and blocking (5% (w/v) milk powder), incubation with the primary (1:1000) and secondary antibody (1:15,000) was performed, the blot developed using the ECL-system (Cell Signaling Technology), and monitored by the Fusion SL Advance gel documentation device (Peqlab, Erlangen, Germany). Quantification of proteins was done using the FusionCapt Advance software.

Immunostaining

Immunofluorescence experiments were performed to visualize the protein of interest. Cells were grown until a confluence of 50–70% in six-well plates containing coverslips and, then, mock treated or treated with GP. After incubation and washing with PBS, cells were fixed with preheated (37 °C) 4% paraformaldehyde (PFA) for 20 min at RT. After washing with PBS, 1 ml Triton-X-100 (0.15% in PBS) was added for 15 min to permeabilize the cells. Subsequently, the cells were blocked in 10% normal goat serum (NGS) in PBS for further 15 min. The adequate primary antibody was diluted 1:100 in 1% NGS in PBS and 100 µl added to each sample. After incubation at 4 °C overnight and washing with PBS, the secondary antibody (100 µl/sample) at a concentration of 0.1% in 1% NGS in PBS was added and incubated for 1 h in the dark. After discarding the antibody solution and three washing steps with PBS for 10 min in the dark, the coverslips were fixed on microscopic slides using ProLong™ Gold Antifade Reagent with DAPI. The immunofluorescence of pRIP3 and RIP3 after GP treatment was recorded using an Ultraview spinning disc confocal microscope (PerkinElmer Corporation). The intensity of the signals was calculated using Image J software (Wayne

Rasband, NIH). At least ten pictures of each condition were quantified. The ratio of pRIP3 to RIP3 was determined and mock-treated control was set at 1.0.

Trypan blue staining

For determination of the cell membrane integrity, the trypan blue exclusion method was performed (Tran et al. 2011). Here, cells were grown in six-well plates to subconfluence. The cells were mock treated or treated with different concentrations of GP alone or in combination with necrostatin-1 (Nec1), an inhibitor of necroptosis. The detergent Triton-X-100 (500 ppm) was used as positive control. After incubation, cells were washed with PBS and incubated with 200 µl of trypsin for 5 min in a humidified atmosphere (37 °C, 5% CO_2) to detach the cells, which were collected in an Eppendorf tube. The reaction was stopped by adding 800 µl growth medium. After mixing, 10 µl of the cell suspension was mixed with 10 µl of a 0.4% trypan blue solution and 10 µl of this was used to determine the number of unstained and blue colored cells by means of a Neubauer counting chamber. For evaluation, the total cell number was calculated and the percentage of cells with an intact and permeabilized cell membrane was determined.

Extracellular LDH measurement

Rupture of the cell membrane is a marker of necrotic and necroptotic cell death (Zhang et al. 2018). To measure this, the occurrence of extracellular amounts of the cytosolic lactate dehydrogenase can be measured using a LDH ELISA kit. Subconfluent cells were mock treated or treated with GP for 6, 24, and 48 h. After incubation, the supernatant was collected and centrifuged at 2000×g for 10 min at RT. The supernatant (50 µl/well) was used for the LDH ELISA. The assay was performed in accordance with the manufacturer's protocol. For quantification, the cell number was determined using a Neubauer counting chamber. A standard curve was included in each experiment. The absorbance was measured at 450 nm and the amount of extracellular LDH was derived from the standard curve. The mock-treated control was set at 1.0 and all other conditions were normalized to it.

Statistics

Means were calculated from at least three independent experiments ($n \geq 3$), unless otherwise stated. Error bars represent the standard error of mean (SEM). Statistical analysis was performed by one-way ANOVA with post hoc test (Dunnett or Bonferroni) or student's *t* test using GraphPad Prism 5 software; $*p \leq 0.05$, $**p \leq 0.01$ and $***p \leq 0.001$ were chosen as levels of significance.

Results

High expression of anti-apoptotic BCL-2 proteins in tumor cells

An evasion of cell death is described for several tumor types due to the disruption of the intrinsic pathway of apoptosis and/or an imbalance of the expression of pro- and anti-apoptotic proteins toward an increase in the amount of anti-apoptotic BCL-2 proteins (Adams and Cory 2007; Hanahan and Weinberg 2011; Sharma et al. 2019). To find out whether the skin tumor cell line SCL-1 exhibits a higher amount of anti-apoptotic proteins, the basal amount of BCL-2 and BCL-xL as well as the amount of the pro-apoptotic protein BAX was determined by western blots and compared with normal human epidermal keratinocytes (NHEK) (Fig. 1). The densitometric analysis of three independent experiments resulted in a significant increase in the amount of BCL-2 in SCL-1 cells compared with NHEK (Fig. 1A). Furthermore, the BCL-xL protein level was also moderately elevated in the tumor cells compared with NHEK (Fig. 1B). The expression of BAX was virtually similar in SCL-1 cells and normal keratinocytes (Fig. 1C).

ABT-199 lowered cell viability in both cell types while GP showed selective toxicity

As epidemiological studies also showed that the expression of anti-apoptotic BCL-2 can be higher than the expression of BCL-xL and MCL-1 in skin cancer cells (D'Aguanno and del Bufalo 2020), BH3 mimetic substances are in the focus of research and clinical trials (Kehr and Vogler 2021). ABT-199/venetoclax (Fig. 2A) is a selective and the first FDA-approved BH3 mimetic binding to the BH3 binding groove of BCL-2 with high affinity and being described to be active in numerous cancer types (Vaillant et al. 2013; Bose et al. 2017; Hafezi and Rahmani 2021). The effect of ABT-199 on cell viability was determined in both tumor and normal cells. For that, the cells were treated with varying concentrations of the compound for 96 h and cell viability was measured. ABT-199 decreased cell viability in a dose-dependent manner in SCL-1 carcinoma cells (Fig. 2B) and NHEK (Fig. 2C). However, ABT-199 showed a similar effect on normal as well as on tumor cells, which is reflected in the calculated IC_{50} values (via non-linear curve fit analysis) of 1.8 µM for SCL-1 and of 0.7 µM for the normal keratinocytes. In context of a minimization of toxic effects on normal cells being responsible for numerous side effects in patients, ABT-199 was not used for further in vitro experiments as normal keratinocytes responded even more sensitive to this compound than the tumor cells (Fig. 2C).

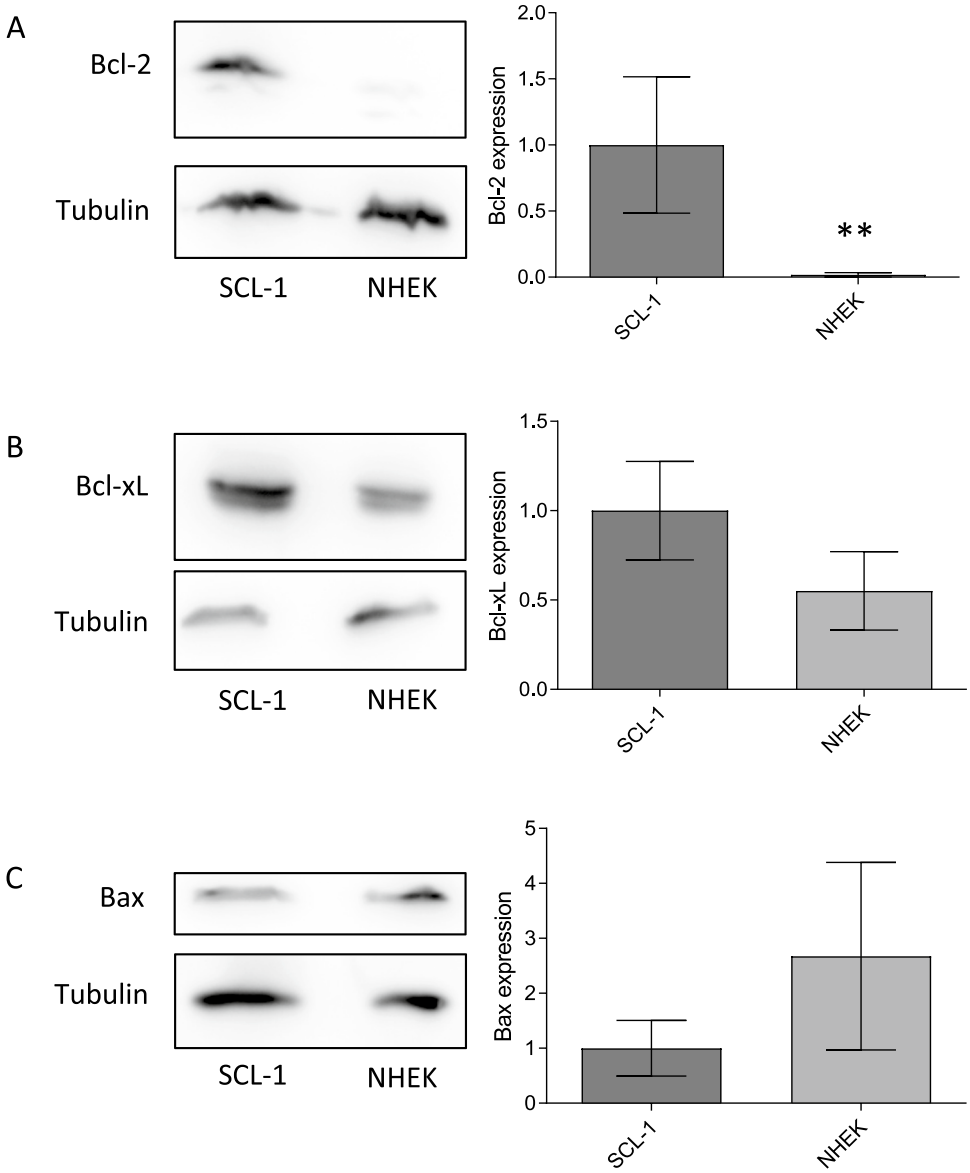

Fig. 1 Expression of anti-apoptotic and pro-apoptotic proteins. Basal protein expression of anti-apoptotic (BCL-2, BCl-xL) and pro-apoptotic (BAX) proteins in SCL-1 carcinoma cells and normal keratinocytes was determined by western blot. Representative blots were depicted. Tubulin served as loading control. **A–C** Densitometric analysis of the western blots was performed. The protein amount was set in relation to the respective loading control and the protein level of SCL-1 cells was set at 1.0. Data represent means ± SEM of three independent experiment ($n = 3$). Student's t test was used for the determination of statistical significance; $^{**}p < 0.01$

The natural compound gossypol (GP, Fig. 3A) consists of (+) and (−) enantiomers and acts as pan-Bcl-2 inhibitor (Liu et al. 2022). We could show earlier (Haasler et al. 2021), that GP exerted a selective toxicity on melanoma cells, but had no toxic effect on normal (healthy) cells such as melanocytes. Therefore, the effect of GP on cell viability of squamous SCL-1 and normal keratinocytes was tested. After 96 h, cell viability of SCL-1 carcinoma cells and NHEK was measured by MTT (Fig. 3B) and SRB assay (Fig. 3C). GP lowered cell viability of the tumor cell line in a dose-dependent manner compared to the mock-treated controls. A significant loss of cell viability was determined in the higher concentration range between 2 and 5 µM GP. In contrast to that, only the highest concentration of 5 µM lowered cell viability of NHEK (Fig. 3C, SRB assay). Nevertheless, the viability of NHEK was still significantly higher than for SCL-1 cells. The calculated SCL-1 IC_{50} values of MTT (Fig. 3D) and SRB data (Fig. 3E) were almost identical, 1.7 µM versus 1.74 µM. As GP exerted a selective toxicity on the studied cell types, the pan-BCL-2 inhibitor GP was used for further studies at a concentration of 2.5 µM in most cases, and in some experimental approaches, a concentration of 5 µM GP was included as well.

Similar uptake of GP in tumor and normal cells

The experiments regarding cytotoxicity of GP showed a selective effect of this compound. To examine whether that effect is due to differences in uptake, the concentration of GP within the cells was determined by HPLC. Therefore, SCL-1 carcinoma cells and NHEK were incubated with 5 µM GP for 0.25, 1, and 2 h. The results are shown in

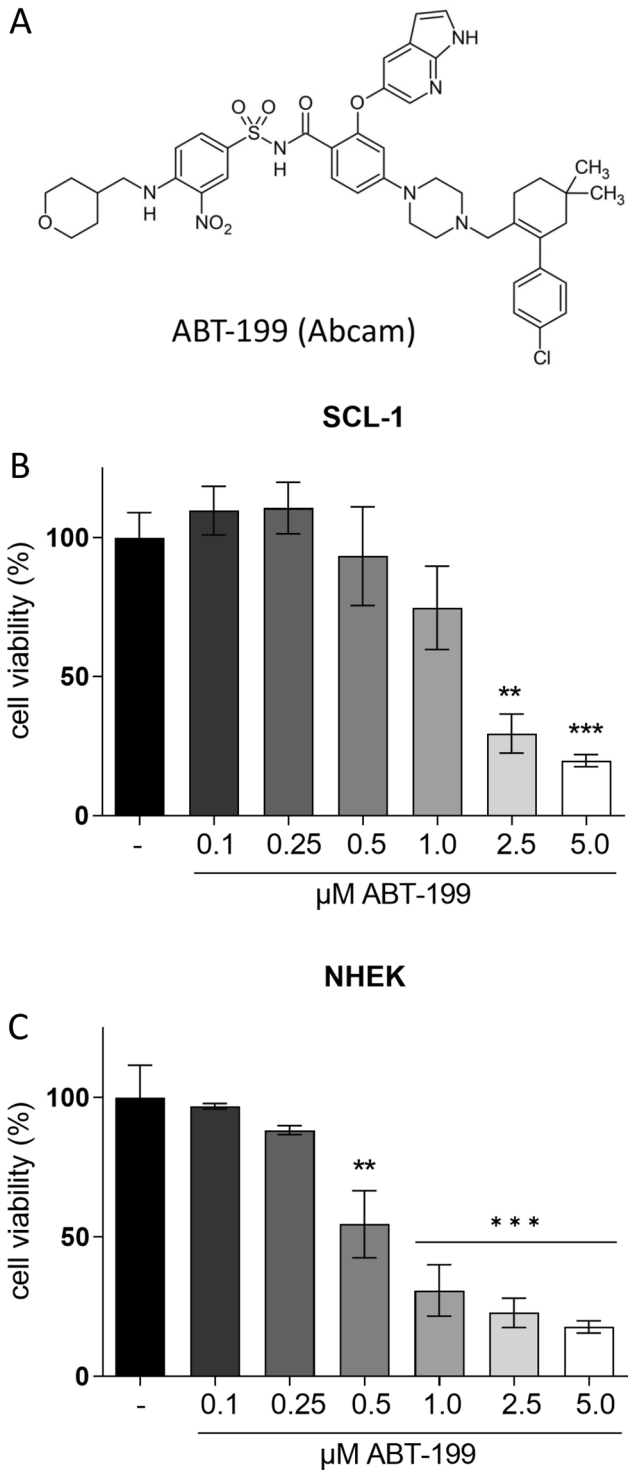

Fig. 2 Effect of ABT-199 on cell viability of SCL-1 and NHEK. **A** Chemical structure of ABT-199/venetoclax. To determine the effect of ABT-199 on cell viability, SCL-1 carcinoma cells **(B)** and keratinocytes (NHEK) **(C)** were treated with different concentrations of ABT-199 for 96 h. Cell viability was measured by MTT assay. Mock-treated control was set at 100%. Data represent means ± SEM of at least three independent experiments ($n \geq 3$). One-way ANOVA with Dunnett's multiple comparison test was used for the determination of statistical significance compared to mock-treated control; $^{**}p < 0.01$, $^{***}p < 0.001$

Fig. 4. The average of intracellular concentrations of GP was about 10–12 µg GP per mg protein. The detectable amount of GP (t = 0.25 h) within the cells related to the amount of GP applied was on the average of 15%. There was no difference in the absorbed GP amount between tumor and normal cells, which was identical to the earlier published data on melanoma cells and melanocytes (Haasler et al. 2021).

Decreased mitochondrial membrane potential and increased fragmentation by GP

Changes in mitochondrial membrane potential ($\Delta\psi_m$) and/or mitochondrial membrane permeability (MMP) often correlate with mitochondrial dysfunction (e.g., fragmentation), changes in oxidative phosphorylation (OXPHOS), and activation of cell death mechanisms (Landes and Martinou 2011; Bock and Tait 2020). As BH3 mimetic substances have been shown to affect the mitochondrial membrane potential ($\Delta\psi_m$) (Henz et al. 2019), a GP-mediated modulation of $\Delta\psi_m$ and mitochondrial dysfunction was investigated (Fig. 5). GP significantly diminished $\Delta\psi_m$ in SCL-1 cells after a 4 h treatment at a concentration of 2.5 µM GP (Fig. 5A, B) compared to mock-treated cells. In contrast, no decrease of $\Delta\psi_m$ was observed in NHEK (Fig. 5D, E). In tendency, $\Delta\psi_m$ slightly increased in the normal (healthy) cells after 4 h. With regard to a reported correlation between a drop in $\Delta\psi_m$ and a change in mitochondrial fragmentation being a measure for mitochondrial dysfunction (Tang et al. 2018), the mitochondrial morphology was assessed after GP treatment of SCL-1 and NHEK. GP induced a fragmentation in about 80% of SCL-1 cells (Fig. 5C) after 2 h which was further increased over 95% after 4 h. This finding was similar to the OXPHOS uncoupler carbonyl cyanide m-chlorophenyl hydrazone (CCCP)-treated cells, which served as positive control. As opposed to the tumor cells, no change in mitochondrial morphology after GP treatment was determined in NHEK (Fig. 5F) compared to the mock-treated cells. On the contrary, CCCP treatment also resulted in an increased mitochondrial fragmentation in NHEK.

GP decreases OXPHOS in squamous skin cancer cells

As the energy production by OXPHOS requires an intact $\Delta\psi_m$ (Zorova et al. 2018), the effect of GP on mitochondrial respiration was determined using Seahorse XF Analyzer. As the drop in $\Delta\psi_m$ occurred rapidly after GP was added to the SCL-1 cells and the IC_{50} value of the GP-treated SCL-1 cells was calculated to be 2.8 µM at 24 h post-treatment, concentrations < 2.8 µM GP for oxygen consumption rate (OCR) measurements were used. The tumor cells and normal keratinocytes were pre-incubated for 1 h with 1.0 and 2.5 µM GP before the Mito Stress Tests were performed (Gu et al. 2021). The assay provides information about oxygen

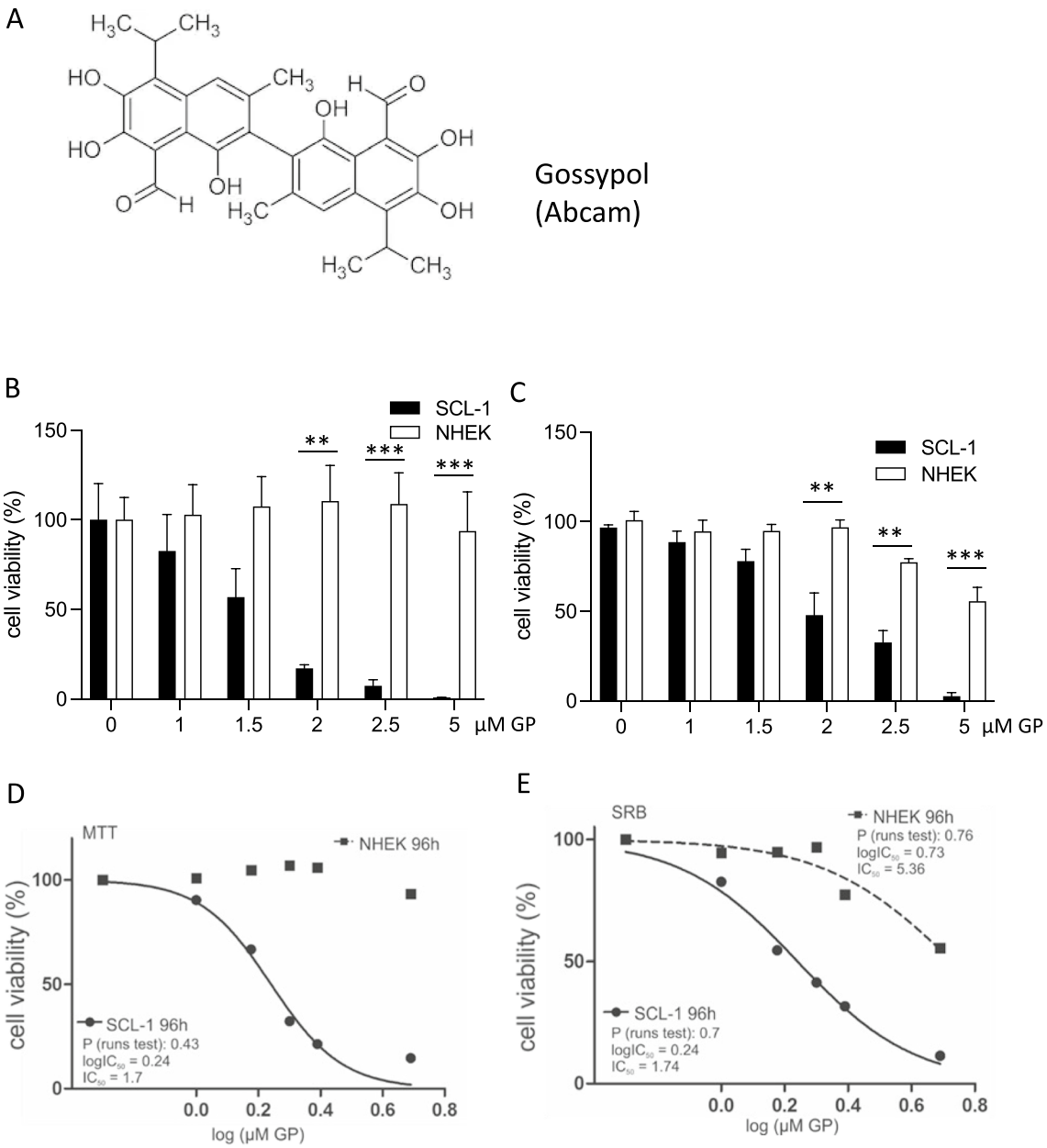

Fig. 3 Selective effect of GP on cell viability of skin cells. **A** Chemical structure of gossypol (GP). To examine the effect of GP on cell viability, SCL-1 carcinoma cells and keratinocytes (NHEK) were treated with different concentrations of GP for 96 h or mock treated (0) and cell viability was measured by MTT **(B)** and SRB **(C)** assay. Mock-treated controls were set at 100%. Data represent means ± SEM of at least three independent experiments ($n \geq 3$). Student's t test was used for the determination of statistical significance; $^{**}p < 0.01$, $^{***}p < 0.001$. **D, E** IC_{50} values were calculated by non-linear curve fit analysis (GraphPad Prism 5) based on MTT **(D)** and SRB assay **(E)**

consumption rate (OCR) after the addition of different mitochondrial stressors including oligomycin (Oligo), the uncoupler FCCP, and rotenone/antimycin A (Rot/AA), from which the bioenergetic parameters (Figs. 6, 7) can be calculated such as basal respiration, ATP production, spare respiratory capacity (SRC; a measure of the cell's ability to respond to energetic demand), and proton leak, meaning that some protons "leak" back across the mitochondrial inner membrane due to damaged mitochondria and/or to maintain the activity of the respiratory chain (Divakaruni et al. 2014; Darcy et al. 2020; Marchetti et al. 2020).

The basal respiration rather tended to increase to 1.7-fold and twofold in SCL-1 carcinoma cells after application of 1.0 and 2.5 µM GP compared to mock treated controls (Fig. 6A). At a concentration of 2.5 µM GP, the ATP production was lowered to 50% compared to control level (Fig. 6B),

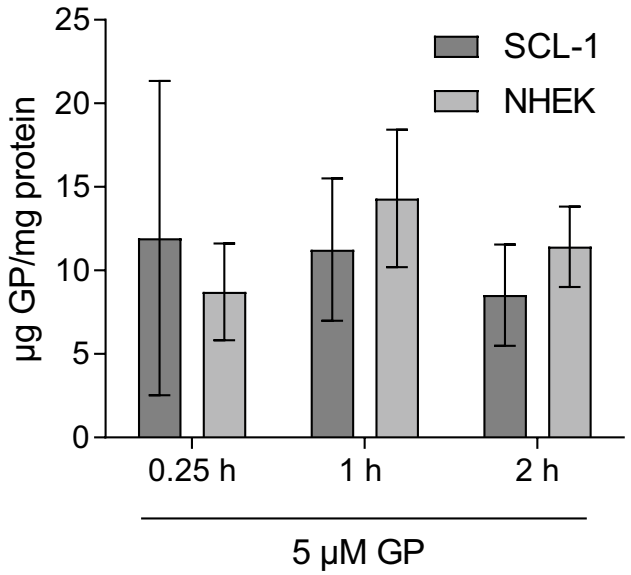

Fig. 4 Intracellular amount of GP in SCL-1 cells and keratinocytes (NHEK). Cells were harvested after treatment with 5 µM GP for 0.25, 1, and 2 h and analyzed by HPLC. The amount of intracellular GP was related to the respective protein level. Experiments were performed in triplicate ($n = 3$)

the spare respiratory capacity was completely lost (Fig. 6C), and the proton leak significantly increased (Fig. 6D). Unlike the effect of GP on respiration in tumor cells, only minor effects were observed in normal (healthy) keratinocytes. Even though the highest GP concentration of 2.5 µM also increased the basal respiration of NHEK (Fig. 7A), the ATP production was unaffected after GP treatment at the studied concentrations (Fig. 7B). In addition, the SRC was lowered after treatment with 2.5 µM GP, but this effect was not significant compared to mock treated cells (Fig. 7C). At the highest concentration of 2.5 µM, the proton leak significantly raised similar to the rate in the squamous tumor cells. Interestingly, the proton leak of NHEK was about half of the value of the SCL-1 cells after treatment with 1 µM GP (Fig. 7D). In summary, treatment of the SCL-1 carcinoma cells with GP resulted in a decrease of both ATP production and SRC and an increase in the proton leak.

GP does not initiate apoptosis in SCL-1 tumor cells

As described above, changes in mitochondrial membrane potential may result in apoptotic cell death. In earlier studies, we could show that GP resulted in apoptotic cell death of A375 melanoma cells (Haasler et al. 2021). In that context and due to the potential of GP inducing a cytotoxic effect on SCL-1 carcinoma cells and not on NHEK, apoptosis markers such as the activity of the initiator caspases 8 and 9, the executioner caspases 3 and 7, and poly (ADP-ribose) polymerase (PARP) cleavage were studied after treating the tumor cells with 2.5 and 5 µM GP or 20 µM staurosporine (Sts) as positive control (Fig. 8). The activity of the initiator caspases was measured after 6 h and the activity of the executioner caspases 24 h after treatment, based on earlier published data with melanoma cells (Haasler et al. 2021). In contrast to melanoma cells, GP neither activated the initiator caspases 8 or 9 nor the executioner caspases 3 and 7. Conversely, Sts significantly increased the activity of caspase 8 and 9, but only a slight increase of caspase 3/7 activity was measured (Fig. 8A). To verify these data, the expression level of the apoptosis relevant protein PARP was determined by western blot analysis. For this purpose, SCL-1 carcinoma cells were treated with 2.5 and 5 µM GP up to 48 h to measure the protein level of full length and cleaved PARP. At 48 h post-treatment, the time course analysis indicated a significant loss of cell viability ($\leq 50\%$) at the used concentrations (data not shown). In contrast to the Sts control, the cleaved PARP level in GP-treated cells did not exceed the protein level of the mock-treated cells (Fig. 8B). To finally demonstrate a GP-initiated caspase and PARP-independent cell death of SCL-1 carcinoma cells, the cells were incubated with GP combined with the pan-caspase inhibitor zVAD(OMe)-FMK. In contrast to melanoma cells (Haasler et al. 2021), the induced cytotoxic effect of GP on SCL-1 tumor cells did not change in the presence of zVAD indicating that the cell death occurred independent of apoptosis (Fig. 8C).

GP initiates necroptosis in SCL-1 tumor cells

None of the above tested apoptotic markers could be detected in SCL-1 cells. There is increasing evidence that necroptosis is a back-up cell death pathway to kill tumor cells efficiently (Chen et al. 2016). The molecular mechanisms are based on a signal cascade mediated by receptor-interacting serine/threonine protein kinase (RIP) 1 and RIP3, finally resulting in an increase in membrane permeability and release of lactate dehydrogenase (Gong et al. 2019; Kim et al. 2021). To figure out whether the necroptotic pathway was activated after GP treatment in SCL-1 carcinoma cells, necrostatin-1 (Nec1), a cell-permeable and selective inhibitor of the RIP1 kinase and downstream phosphorylation of RIP3 was tested, which finally interrupts the mechanisms required for necroptotic cell death (Cao and Mu 2021). SCL-1 carcinoma cells were pre-treated with Nec1 prior to the GP treatment. The GP-induced decrease in cell viability was significantly diminished in the presence of Nec1, indicating that necroptosis could be involved (Fig. 9B). However, no complete recovery was seen with Nec-1, suggesting that GP might stimulate additional mechanisms resulting in cell death. As proof of principle, Nec1 was also tested in A375 melanoma cells. Nec1 had no impact on A375 cell viability (Fig. 9A), which can be killed by GP-mediated apoptosis (Haasler et al. 2021). To determine whether

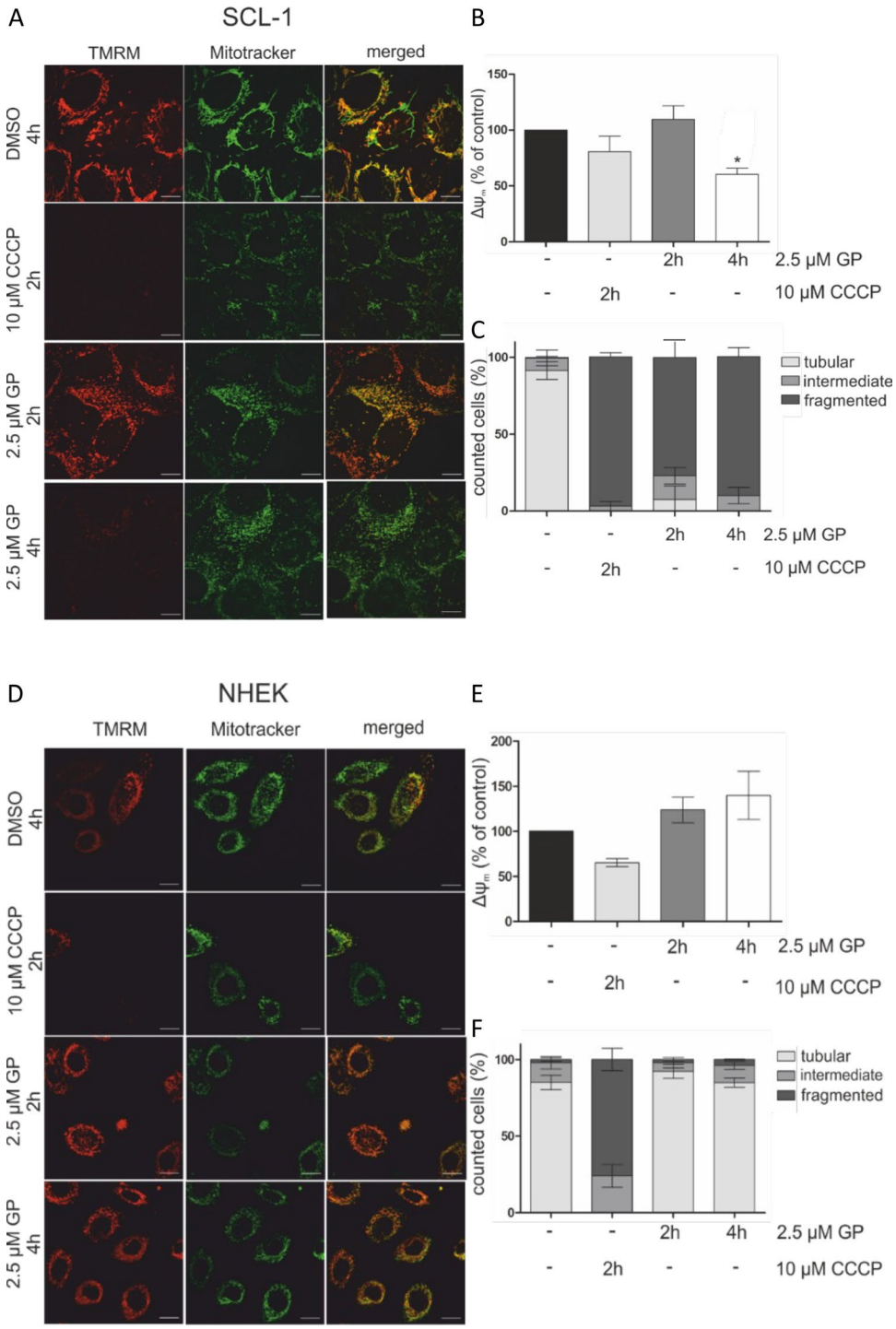

Fig. 5 Effect of GP on mitochondrial membrane potential ($\Delta\psi_m$) and mitochondrial fragmentation in SCL-1 cells and NHEK. Subconfluent SCL-1 cells **(A)** and NHEK **(B)** were mock treated (−) or treated with 2.5 µM GP for 2 or 4 h. CCCP at a concentration of 10 µM (2 h) served as positive control. Subsequently, cells were incubated with 100 nM TMRM and 100 nM MitoTRACKER™ Green for 30 min and analyzed by confocal microscopy. The scale bar is 20 µm. **A, D** Representative pictures are shown. **B, E** Calculation of the intensity of TMRM to MitoTRACKER™ Green was performed using Image J. The mock-treated control was set at 100%. One-way ANOVA with Dunnett's multiple comparison test was used for the determination of statistical significance; $*p < 0.05$. **C, F** For quantification of mitochondrial morphology/fragmentation (Duvezin-Caubet et al. 2006), at least 30 cells of each condition were counted. Data represent means ± SEM of three independent experiments ($n = 3$)

GP has an impact on the permeabilization of the cellular membrane, trypan blue staining was performed in SCL-1 carcinoma cells. The treatment with Triton-X-100 resulted in 100% trypan blue positive cells (data not shown). At a concentration of 2.5 µM GP, around 30% of the counted cells had permeabilized cell membranes after 24 h, which further increased up to 50% after 48 h. The higher doses of 5 µM GP enhanced this effect resulting in nearly 90% of tumor cells with permeabilized cell membranes after 48 h (Fig. 9C). To demonstrate that this effect was due to necroptosis, a combination treatment with Nec1 was performed. Nec1 diminished the extent of damaged cells by GP after 24 and 48 h indicating that necroptosis was involved in the cytotoxic effect of GP on SCL-1 carcinoma cells (Fig. 9C). As a consequence of the permeabilized membranes, cellular contents, such as lactate dehydrogenase (LDH), can be

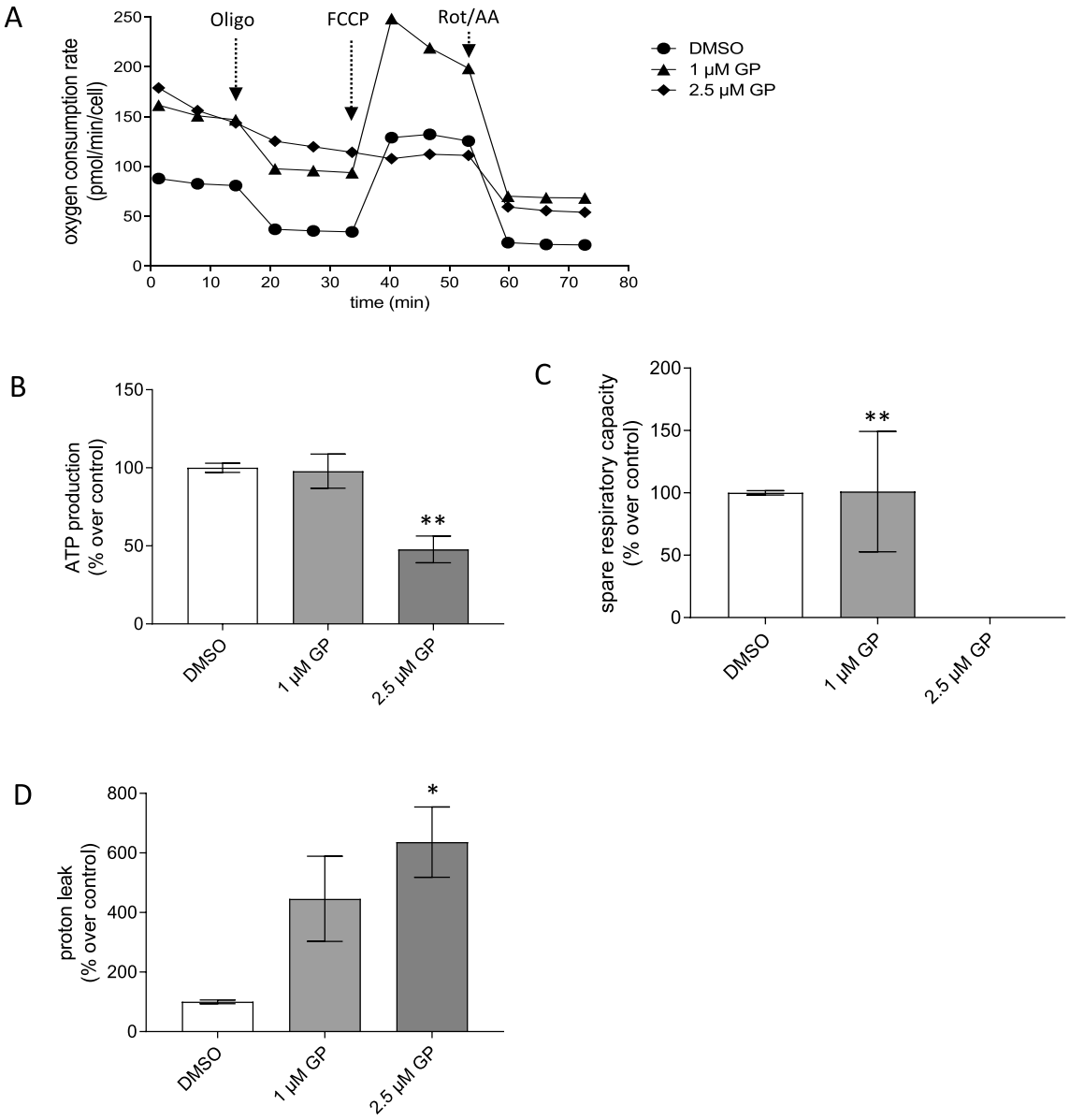

Fig. 6 Mitochondrial respiration of GP-treated SCL-1 carcinoma cells. **A** After treatment with different concentrations of GP for 1 h or mock treated (DMSO), the oxygen consumption rate (OCR) was measured after successive injection of oligomycin (Oligo), FCCP, and rotenone/antiymcin A (Rot/AA) by Seahorse XF Analyzer. Representative curves were depicted. **B–D** Based on the OCR in response to these mitochondrial stressors, ATP production **(B)**, spare respiratory capacity **(C),** and proton leak **(D)** were calculated. The values of mock treated cells were set at 100%. Data represent means ± SEM of three independent experiments ($n = 3$). One-way ANOVA with Dunnett's multiple comparison test was used for the determination of statistical significance between mock treated and GP-treated cells; $^{*}p < 0.05$, and $^{**}p < 0.01$

released. Therefore, the extracellular amount of LDH was measured after GP treatment for 6, 24, and 48 h in SCL-1 carcinoma cells. In fact, the LDH amount increased after the treatment of 2.5 µM GP at the studied time points, which was further enhanced using 5 µM GP (Fig. 9D). As both the increase in membrane permeability and LDH release are late markers of necroptosis, an early key event had to be examined as well. In this context, RIP kinases play a crucial role. After dissociation of RIP1 from a complex including inactive caspase 8, the protein recruits RIP3 followed by phosphorylation of RIP3 (Gong et al. 2019). For this reason, the phosphorylation of RIP3 was determined in GP-treated SCL-1 carcinoma cells. GP at a concentration of 2.5 µM significantly elevated the phosphorylation of RIP3 in relation

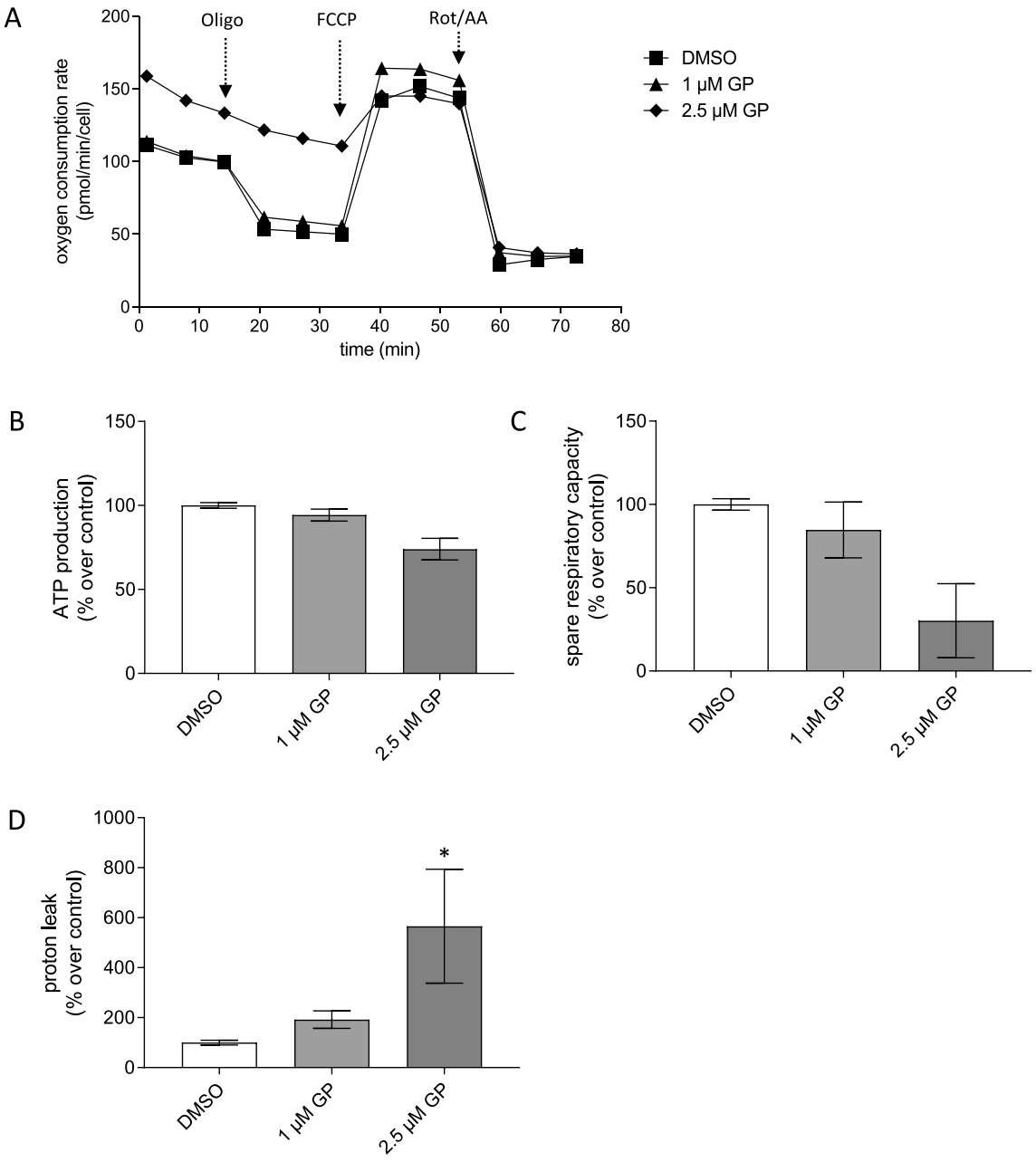

Fig. 7 Mitochondrial respiration of GP-treated normal keratinocytes (NHEK). **A** After treatment with different concentrations of GP or mock treated for 1 h, the oxygen consumption rate (OCR) was measured after successive injection of oligomycin (Oligo), FCCP, and rotenone/antiymcin A (Rot/AA) by Seahorse XF Analyzer. Representative curves are depicted. **B–D** Based on the OCR in response to these mitochondrial stressors, ATP production **(B)**, spare respiratory capacity **(C),** and proton leak **(D)** were calculated. The values of untreated cells were set at 100%. Data represent means ± SEM of three independent experiments ($n = 3$). One-way ANOVA with Dunnett's multiple comparison test was used for the determination of statistical significance between mock treated and GP-treated cells; $^{*}p < 0.01$

to unphosphorylated RIP3 after 24 h (Fig. 9E). Moreover, the localization of unphosphorylated RIP3 changed after GP treatment. Under basal conditions, RIP3 was predominantly located around the nucleus, whereas it was uniformly distributed in the presence of GP (Fig. 9E). In summary, the data indicate that treatment of SCL-1 carcinoma cells with GP resulted at least in part in a necroptotic cell death.

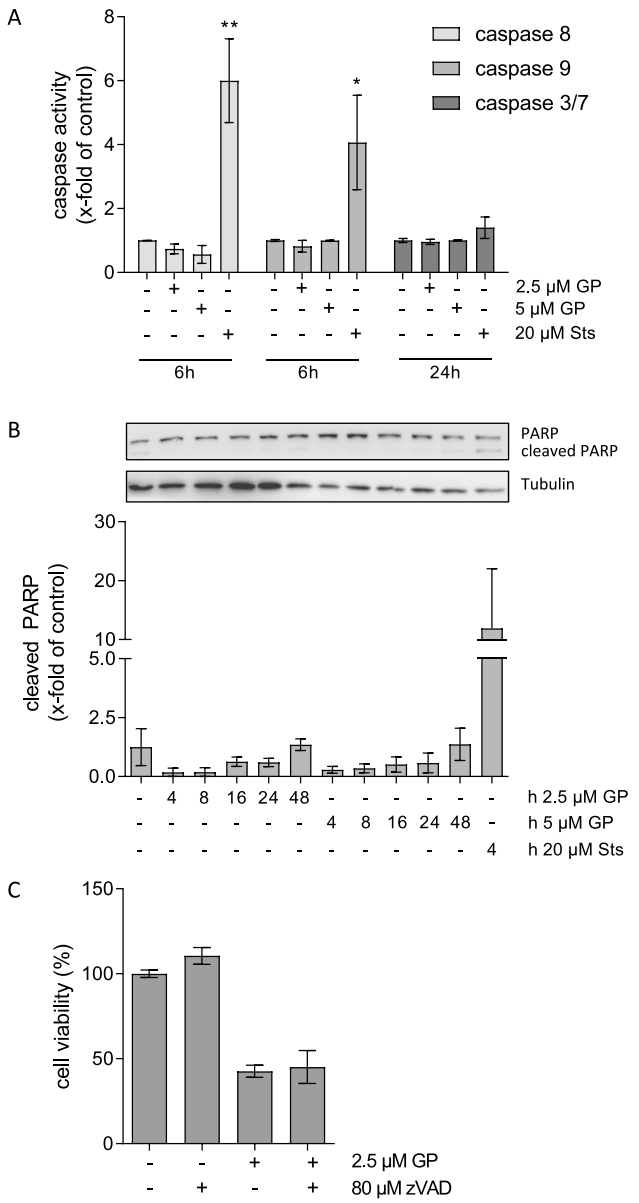

Fig. 8 Effect of GP on apoptosis in SCL-1 carcinoma cells. **A** After treatment with 2.5 or 5 µM GP or mock treated (-) for 6 or 24 h, caspase activity was measured. Staurosporine (Sts, 20 µM) served as positive control. Mock treated control was set at 1.0. Data represent means ± SEM of three independent experiments ($n = 3$). One-way ANOVA with Dunnett's multiple comparison test was used for the determination of statistical significance; $*p < 0.05$, $**p < 0.01$. **B** Subconfluent cells were treated with 2.5 or 5 µM GP for 4, 8, 16, 24, and 48 h. Mock treated cells were used as negative control, 20 µM staurosporine (Sts) served as positive control. Protein expression of full length and cleaved PARP was determined by western blot. Beta-tubulin was used as loading control. A representative blot of three independent experiments was depicted ($n = 3$). Quantification of the protein amount was calculated compared to the mock-treated control. Mock treated control was set at 1.0. **C** For rescue experiment, subconfluent cells were pre-treated for 4 h with 80 µM of the pan-caspase inhibitor zVAD, followed by GP (2.5 µM) treatment for further 24 h. Cell viability was measured by MTT assay. Mock treated control was set at 100%. Data represent means ± SEM of three independent experiments ($n = 3$)

Discussion

In context of cutaneous squamous cell carcinoma, a systemic and/or targeted therapy is the treatment of choice in the majority of cases of advanced unresectable or metastatic cSCC (Ribero et al. 2017; Corchado-Cobos et al. 2020). However, the response rate is rather modest in context of resistance, recurrence, and severe side effects (Marti et al. 2016; Agirgol et al. 2020). An interesting alternative is the use of BH3 mimetics to antagonize overexpressed anti-apoptotic BCL-2 proteins to release pro-apoptotic proteins (Vogler 2014; Townsend et al. 2021). In our study, BCL-xL was overexpressed in SCL-1 cells compared to normal (healthy) cells, which is in line with data of patients with cutaneous squamous cell carcinoma (cSCC) having elevated BCL-xL levels as well (Vasiljević et al. 2009). Numerous validated and putative BH3 mimetics are described to be in use for in vitro studies and clinical trials, but most of them deal with melanoma and head and neck squamous cell carcinoma (Swiecicki et al. 2016; Melo et al. 2022). Currently, very little is known about the effect of BCL-2 inhibitors on squamous cell carcinoma of the skin. Only one publication reported that cSCC cells are more sensitive to the BCL-2 inhibitor ABT-737, if the BCL-2 family member MCL-1 was suppressed in these cells (Geserick et al. 2015). For our studies on squamous skin carcinoma, the FDA-approved drug ABT-199/venetoclax and the natural compound (±) gossypol (GP) have been tested. ABT-199 was described to be effective in the treatment of specific types of leukemia (Cang et al. 2015; Thol and Ganser 2020). However, side effects such as skin rash, vitiligo, cytopenia, and tumor lysis syndrome were described as well (Abdeen et al. 2022). Our in vitro data showed that ABT-199 also has a toxic effect on normal skin cells in contrast to GP showing a selective toxicity on the studied squamous skin carcinoma cells. These data are in line with earlier published data on the effect of GP on melanoma cells (Haasler et al. 2021).

Decades ago, it was already described that gossypol has a modulatory effect on the mitochondrial membrane potential (Martínez 1992; Barhoumi 1996). This effect seemed to fall into oblivion for some time, even though changes in the mitochondrial membrane potential or permeability affect mitochondrial dynamics, result in mitochondrial dysfunction, and trigger cell death pathways (Landes and Martinou 2011; Bock and Tait 2020). As BH3 mimetics, AT-101 and GP initiated mitochondrial dysfunction and different types of cell death such as mitophagic or autophagic cell death as well as apoptosis in glioma and colon cancer cells (Lu et al. 2017; Meyer et al. 2018), GP was tested on modulation of the mitochondrial membrane potential ($\Delta\psi_m$) of the cSCC cell

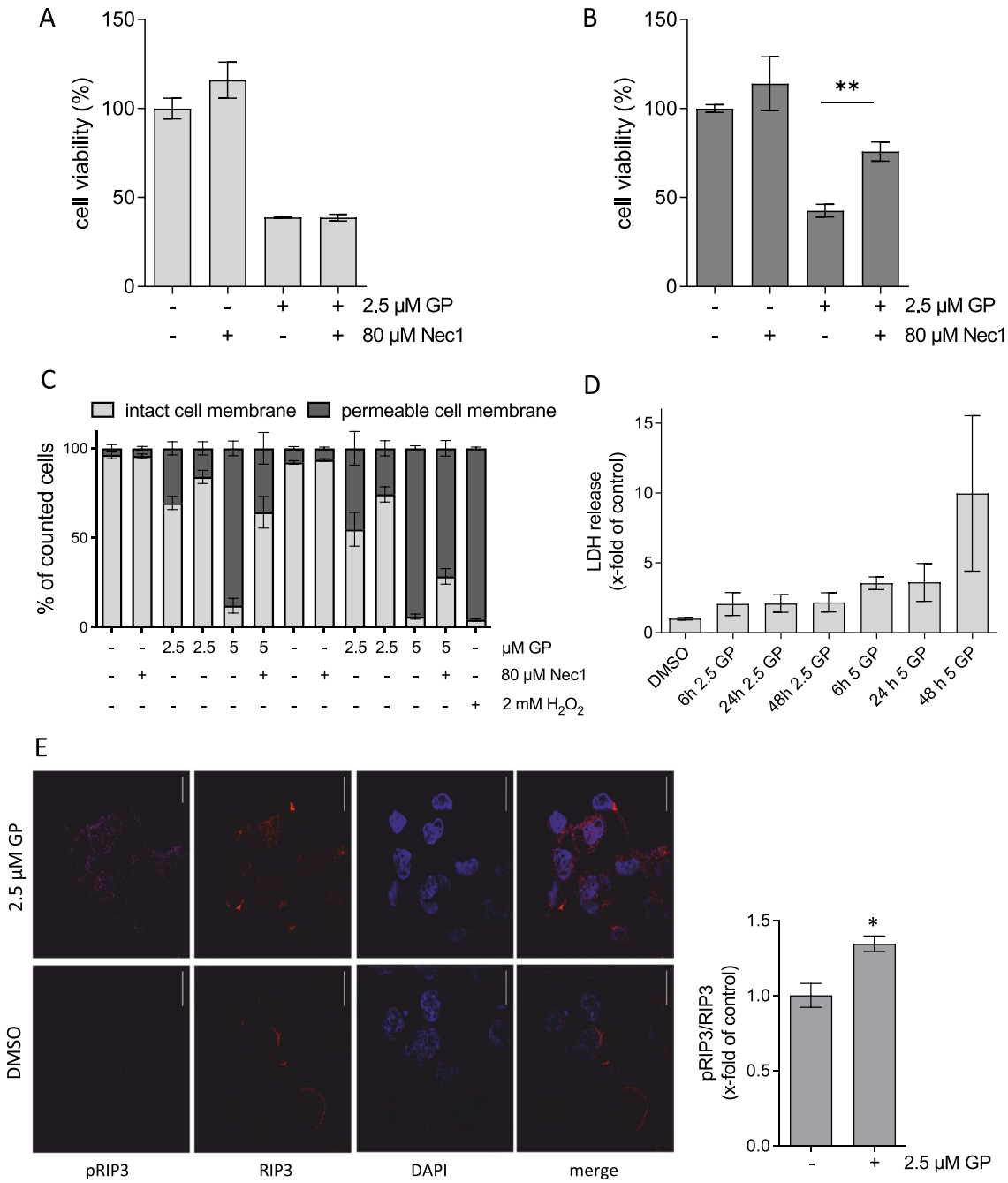

Fig. 9 Effect of GP on necroptosis in SCL-1 carcinoma cells. **A, B** After pre-incubation with 80 µM of the necroptosis inhibitor necrostatin-1 (Nec1) for 4 h, cells were mock treated (-) or 2.5 µM GP was added to A375 melanoma (**A**) and SCL-1 carcinoma cells (**B**) for further 24 h. Cell viability was measured by MTT assay. Mock treated cells were set at 100%. Data represent means ± SEM of three independent experiments ($n = 3$). Student's t test was used for determination of statistical significance; $^{**}p < 0.01$. Subconfluent cells were mock treated (−) or pre-treated with 80 µM Nec1 for 4 h, followed by treatment with 2.5 and 5 µM GP for further 24 and 48 h. H_2O_2 (2 mM) was used as positive control. Subsequently, the number of cells was counted using trypan blue staining. Blue colored cells were defined as having a permeable membrane. The total cell number of each condition was set at 100% and the percentage of cells with an intact versus a permeable membrane is shown. **D** After treatment of subconfluent cells with 2.5 and 5 µM GP for 6, 24, and 48 h, the LDH content in the supernatant was measured. Data represent x-fold increase of extracellular LDH compared to mock treated control (DMSO), which was set at 1.0. One-way ANOVA with Dunnett's multiple comparison test was used for the determination of statistical significance ($n = 4$). **E** After incubation without (DMSO) and with 2.5 µM GP for 24 h, immunostaining against phosphorylated RIP3 (pRIP3) and unphosphorylated RIP3 (RIP3) was performed. DAPI was used for nucleus staining. Representative pictures are shown. Scale bars represent 20 µm. For quantification, the fluorescence intensity of pRIP3 was set in relation to RIP3. Mock treated control (-, represents DMSO) was set at 1. Data represent means ± SEM of three independent experiments ($n = 3$). Student's t test was used for the determination of statistical significance; $^{*}p < 0.05$

line SCL-1 and normal keratinocytes. $\Delta\psi_m$ was significantly lowered and the number of fragmented mitochondria increased by GP in the tumor cells in contrast to the normal cells. In this regard, ABT-199, S63845 (MCL-1 inhibitor), and A-1331852 (BCL-xL inhibitor) have been described to affect $\Delta\psi_m$ in hematological malignancies accompanied by swollen mitochondria, rupture of the mitochondrial outer membrane as well as loss of cristae structure (Henz et al. 2019). As dysfunctional mitochondria may result in a drop of energy production (Auger et al. 2015), we checked the effect of GP on ATP production and loss of spare respiratory capacity (SRC, also called mitochondrial reserve capacity) being a sign for mitochondrial dysfunction (Marchetti et al. 2020). ATP production was significantly decreased in squamous SCL-1 cells compared to normal keratinocytes. Additionally, tumor cells showed no spare respiratory capacity (SRC) after 2.5 µM GP treatment in contrast to NHEK. In addition, we measured a higher proton leak in SCL-1 cells at a concentration of 1 µM GP compared to NHEK. This is in line with earlier published data indicating that gossypol has an uncoupling effect on rat liver mitochondria (Abou-Donia and Dieckert 1974) and TM4 cells originally derived from mouse testicular cells (Reyes et al. 1986).

In contrast to the finding in A375 melanoma cells (Haasler et al. 2021), SCL-1 carcinoma cells showed a different mechanism of cell death upon GP treatment. Although drastic effects on mitochondria were observed in SCL-1 cells, no apoptotic markers were found. Here, the necroptosis inhibitor necrostatin-1 resulted in a partial rescue of GP-induced cytotoxicity of the tumor cells, suggesting that necroptosis (Gong et al. 2019) might be involved. In that context, the BH3 mimetic drug obatoclax (GX15-070) also induced necroptosis in human oral squamous cell carcinoma (Sulkshane and Teni 2017). In addition, the necroptotic pathway shares morphological features of necrosis, including plasma membrane permeabilization/rupture and release of intracellular content such as lactate dehydrogenase (Gong et al. 2019), which we also found in this study. In the study of Maeda and coworkers, plasma membrane rupture was observed after mitochondrial fragmentation in the immortalized T lymphocyte cell line Jurkat (Maeda and Fadeel 2014) suggesting an interplay between mitochondrial effects and necroptosis. The switch from apoptosis to necroptosis usually depends on the activation status of caspase 8. Functional caspase 8 induces the extrinsic pathway of apoptotic cell death, whereas the inhibition of caspase 8 triggers the formation of necrosome and, thus, promotes necroptotic cell death (Fritsch et al. 2019). In line with this, no caspase 8 activity was observed in SCL-1 carcinoma cells suggesting that non-functional caspase 8 might be responsible for the switch of the cell death pathway. Recently, it was published that an interplay exists between autophagy and necroptosis, but the role of autophagy in necroptosis is still controversially discussed with regard to prevention or promotion of necroptosis (Zhang et al. 2022). As we do not see a full rescue from GP-initiated cytotoxic effect with the inhibitor necrostatin-1, we may speculate that autophagic processes might play a role in the GP-mediated cell death of the studied squamous carcinoma cells. Interestingly, it was demonstrated that (−) gossypol treatment resulted in an increased cytotoxicity on the lung carcinoma cell line A549 which is mediated by an upregulation of autophagic processes (Cai et al. 2022). Future studies will focus on that aspect.

In conclusion, our study showed for the first time, that, in addition to its main function as an inducer of apoptosis, (±) gossypol also promotes a necroptotic cell death in squamous skin cancer cells. The selectivity of the substance within a concentration range may also offer the possibility to use it for the effective treatment of squamous skin carcinoma in vivo without affecting normal (healthy) cells and, thus, alleviate harmful effects.

Acknowledgements The authors thank Claudia Wyrich for excellent technical assistance.

Author contributions LH planned/performed the experiments and partially analyzed the data. CvM planned experiments and analyzed/discussed the data. AKK and MG performed immunofluorescence microscopy. LE and CKW established methods and corrected the manuscript. WS and ASR critically reviewed and corrected the manuscript. PB designed the study, acquired funding for the project, analyzed the data, and wrote the manuscript. All the authors have read and approved the final version of this manuscript.

Funding Open Access funding enabled and organized by Projekt DEAL. This study was supported by P.B. grant BR1551/7-1 DFG—Deutsche Forschungsgemeinschaft (https://www.dfg.de/). The funders had no role in study design, data collection and analysis, decision to publish, or preparation of the manuscript.

Availability of data and materials The datasets generated during and/or analyzed during the current study are available from the corresponding author on reasonable request.

Declarations

Conflict of interest The authors declare that they have no conflict of interest.

Ethics approval The manuscript does not contain clinical studies or patient data.

Consent to participate Not applicable.

Consent for publication Not applicable.

Code availability Not applicable.

References

Abdeen M, Vusqa UT, Asawa P et al (2022) Venetoclax-induced vitiligo in a patient with chronic lymphocytic leukemia. Anticancer Drugs 33:1167–1170. https://doi.org/10.1097/CAD.0000000000001350

Abou-Donia MB, Dieckert JW (1974) Gossypol: Uncoupling of respiratory chain and oxidative phosphorylation. Life Sci 14:1955–1963. https://doi.org/10.1016/0024-3205(74)90412-3

Adams JM, Cory S (2007) The Bcl-2 apoptotic switch in cancer development and therapy. Oncogene 26:1324–1337. https://doi.org/10.1038/sj.onc.1210220

Adams R, Geissman TA, Edwards JD (1960) Gossypol, a pigment of cottonseed. Chem Rev 60:555–574. https://doi.org/10.1021/cr60208a002

Agirgol S, Çaytemel C, Pilanci KN (2020) Dermatological side effects of targeted antineoplastic therapies: a prospective study. Cutan Ocul Toxicol 39:380–384. https://doi.org/10.1080/15569527.2020.1833028

Aplak E, von Montfort C, Haasler L et al (2020) CNP mediated selective toxicity on melanoma cells is accompanied by mitochondrial dysfunction. PLoS ONE 15:e0227926. https://doi.org/10.1371/journal.pone.0227926

Auger C, Alhasawi A, Contavadoo M, Appanna VD (2015) Dysfunctional mitochondrial bioenergetics and the pathogenesis of hepatic disorders. Front Cell Dev Biol. https://doi.org/10.3389/fcell.2015.00040

Barhoumi R (1996) Kinetic analysis of the chronology of patulin- and gossypol-induced cytotoxicity in vitro. Fundam Appl Toxicol 30:290–297. https://doi.org/10.1006/faat.1996.0067

Bock FJ, Tait SWG (2020) Mitochondria as multifaceted regulators of cell death. Nat Rev Mol Cell Biol 21:85–100. https://doi.org/10.1038/s41580-019-0173-8

Bose P, Gandhi V, Konopleva M (2017) Pathways and mechanisms of venetoclax resistance. Leuk Lymphoma 58:2026–2039. https://doi.org/10.1080/10428194.2017.1283032

Boukamp P, Tilgen W, Dzarlieva RT et al (1982) Phenotypic and genotypic characteristics of a cell line from a squamous cell carcinoma of human skin. J Natl Cancer Inst 68:415–427

Burton KA, Ashack KA, Khachemoune A (2016) Cutaneous squamous cell carcinoma: a review of high-risk and metastatic disease. Am J Clin Dermatol 17:491–508. https://doi.org/10.1007/s40257-016-0207-3

Cai B, Gong L, Zhu Y et al (2022) Identification of gossypol acetate as an autophagy modulator with potent anti-tumor effect against cancer cells. J Agric Food Chem 70:2589–2599. https://doi.org/10.1021/acs.jafc.1c06399

Cakir BÖ, Adamson P, Cingi C (2012) Epidemiology and economic burden of nonmelanoma skin cancer. Facial Plast Surg Clin North Am 20:419–422. https://doi.org/10.1016/j.fsc.2012.07.004

Cang S, Iragavarapu C, Savooji J et al (2015) ABT-199 (venetoclax) and BCL-2 inhibitors in clinical development. J Hematol Oncol 8:129. https://doi.org/10.1186/s13045-015-0224-3

Cao L, Mu W (2021) Necrostatin-1 and necroptosis inhibition: pathophysiology and therapeutic implications. Pharmacol Res 163:105297. https://doi.org/10.1016/j.phrs.2020.105297

Chen D, Yu J, Zhang L (2016) Necroptosis: an alternative cell death program defending against cancer. Biochimica Et Biophysica Acta (BBA) Rev Cancer 1865:228–236. https://doi.org/10.1016/j.bbcan.2016.03.003

Corchado-Cobos R, García-Sancha N, González-Sarmiento R et al (2020) Cutaneous squamous cell carcinoma: from biology to therapy. Int J Mol Sci 21:2956. https://doi.org/10.3390/ijms21082956

Coutinho EM (2002) Gossypol: a contraceptive for men. Contraception 65:259–263. https://doi.org/10.1016/S0010-7824(02)00294-9

Creed S, McKenzie M (2019) Measurement of mitochondrial membrane potential with the fluorescent dye tetramethylrhodamine methyl ester (TMRM). In: Methods in Molecular Biology. pp 69–76

D'Aguanno S, del Bufalo D (2020) Inhibition of anti-apoptotic Bcl-2 proteins in preclinical and clinical studies: current overview in cancer. Cells 9:1287. https://doi.org/10.3390/cells9051287

Darcy J, Wang C-H, Tseng Y-H (2020) Analyzing mitochondrial function in brown adipocytes with a bioenergetic analyzer. In: Methods in Molecular Biology. pp 289–296

Dessinioti C, Stratigos AJ (2022) Recent advances in the diagnosis and management of high-risk cutaneous squamous cell carcinoma. Cancers (basel) 14:3556. https://doi.org/10.3390/cancers14143556

Divakaruni AS, Paradyse A, Ferrick DA, et al (2014) Analysis and interpretation of microplate-based oxygen consumption and pH data. In: Methods in Enzymology. pp 309–354

Dubas LE, Ingraffea A (2013) Nonmelanoma skin cancer. Facial Plast Surg Clin North Am 21:43–53. https://doi.org/10.1016/j.fsc.2012.10.003

Duvezin-Caubet S, Jagasia R, Wagener J et al (2006) Proteolytic processing of OPA1 links mitochondrial dysfunction to alterations in mitochondrial morphology. J Biol Chem 281:37972–37979. https://doi.org/10.1074/jbc.M606059200

Fania L, Didona D, di Pietro FR et al (2021) Cutaneous squamous cell carcinoma: from pathophysiology to novel therapeutic approaches. Biomedicines 9:171. https://doi.org/10.3390/biomedicines9020171

Fitzmaurice C, Abate D, Abbasi N et al (2019) Global, regional, and national cancer incidence, mortality, years of life lost, years lived with disability, and disability-adjusted life-years for 29 cancer groups, 1990 to 2017. JAMA Oncol 5:1749. https://doi.org/10.1001/jamaoncol.2019.2996

Fritsch M, Günther SD, Schwarzer R et al (2019) Caspase-8 is the molecular switch for apoptosis, necroptosis and pyroptosis. Nature 575:683–687. https://doi.org/10.1038/s41586-019-1770-6

García-Foncillas J, Tejera-Vaquerizo A, Sanmartín O et al (2022) Update on management recommendations for advanced cutaneous squamous cell carcinoma. Cancers (basel) 14:629. https://doi.org/10.3390/cancers14030629

Geserick P, Wang J, Feoktistova M, Leverkus M (2015) Erratum: the ratio of Mcl-1 and Noxa determines ABT737 resistance in squamous cell carcinoma of the skin. Cell Death Dis 6:e1673–e1673. https://doi.org/10.1038/cddis.2015.55

Gong Y, Fan Z, Luo G et al (2019) The role of necroptosis in cancer biology and therapy. Mol Cancer 18:100. https://doi.org/10.1186/s12943-019-1029-8

Gu X, Ma Y, Liu Y, Wan Q (2021) Measurement of mitochondrial respiration in adherent cells by Seahorse XF96 cell mito stress

test. STAR Protoc 2:100245. https://doi.org/10.1016/j.xpro.2020.100245
Gupta SC, Sung B, Prasad S et al (2013) Cancer drug discovery by repurposing: teaching new tricks to old dogs. Trends Pharmacol Sci 34:508–517
Haasler L, Kondadi AK, Tsigaras T et al (2021) The BH3 mimetic (±) gossypol induces ROS-independent apoptosis and mitochondrial dysfunction in human A375 melanoma cells in vitro. Arch Toxicol 95:1349–1365. https://doi.org/10.1007/s00204-021-02987-4
Hafezi S, Rahmani M (2021) Targeting BCL-2 in cancer: advances, challenges, and perspectives. Cancers (basel) 13:1292. https://doi.org/10.3390/cancers13061292
Hanahan D, Weinberg RA (2011) Hallmarks of cancer: the next generation. Cell 144:646–674. https://doi.org/10.1016/j.cell.2011.02.013
Henz K, Al-Zebeeby A, Basoglu M et al (2019) Selective BH3-mimetics targeting BCL-2, BCL-XL or MCL-1 induce severe mitochondrial perturbations. Biol Chem 400:181–185. https://doi.org/10.1515/hsz-2018-0233
Hu JC, Sadeghi P, Pinter-Brown LC et al (2007) Cutaneous side effects of epidermal growth factor receptor inhibitors: clinical presentation, pathogenesis, and management. J Am Acad Dermatol 56:317–326. https://doi.org/10.1016/j.jaad.2006.09.005
Kehr S, Vogler M (2021) It's time to die: BH3 mimetics in solid tumors. Biochimica Et Biophysica Acta (BBA) Mol Cell Res 1868:118987. https://doi.org/10.1016/j.bbamcr.2021.118987
Kim S, Lee H, Lim J, Kim H (2021) Astaxanthin induces NADPH oxidase activation and receptor-interacting protein kinase 1-mediated necroptosis in gastric cancer AGS cells. Mol Med Rep 24:837. https://doi.org/10.3892/mmr.2021.12477
Laemmli U (1970) Cleavage of structural proteins during the assembly of the head of bacteriophage T4. Nature 227:680–685. https://doi.org/10.1038/227680a0
Laikova, Oberemok, Krasnodubets, et al (2019) Advances in the understanding of skin cancer: ultraviolet radiation, mutations, and antisense oligonucleotides as anticancer drugs. Molecules 24:1516. https://doi.org/10.3390/molecules24081516
Landes T, Martinou J-C (2011) Mitochondrial outer membrane permeabilization during apoptosis: the role of mitochondrial fission. Biochimica Et Biophysica Acta (BBA) Mol Cell Res 1813:540–545. https://doi.org/10.1016/j.bbamcr.2011.01.021
Liu Y, Wang L, Zhao L, Zhang Y (2022) Structure, properties of gossypol and its derivatives—from physiological activities to drug discovery and drug design. Nat Prod Rep 39:1282–1304. https://doi.org/10.1039/D1NP00080B
Lu M-D, Li L-Y, Li P-H et al (2017) Gossypol induces cell death by activating apoptosis and autophagy in HT-29 cells. Mol Med Rep 16:2128–2132. https://doi.org/10.3892/mmr.2017.6804
Maeda A, Fadeel B (2014) Mitochondria released by cells undergoing TNF-α-induced necroptosis act as danger signals. Cell Death Dis 5:e1312–e1312. https://doi.org/10.1038/cddis.2014.277
Mahalaxmi G, Ashok S, Arun G, Srinivas G (2022) Albumin binds to uncoupler CCCP to diminish depolarization of mitochondria. Toxicol Vitro 80:105325. https://doi.org/10.1016/j.tiv.2022.105325
Marchetti P, Fovez Q, Germain N et al (2020) Mitochondrial spare respiratory capacity: mechanisms, regulation, and significance in non-transformed and cancer cells. FASEB J 34:13106–13124. https://doi.org/10.1096/fj.202000767R
Marti A, Fauconneau A, Ouhabrache N et al (2016) Complete remission of squamous cell carcinoma after treatment with panitumumab in a patient with cetuximab-induced anaphylaxis. JAMA Dermatol 152:343. https://doi.org/10.1001/jamadermatol.2015.4134
Martínez F (1992) The antifertility agent, gossypol, changes several mitochondrial functions in the presence of Mg2+. Comp Biochem Physiol Part C Comp Pharmacol 103:87–90. https://doi.org/10.1016/0742-8413(92)90232-V
Maydt D, de Spirt S, Muschelknautz C et al (2013) Chemical reactivity and biological activity of chalcones and other α, β-unsaturated carbonyl compounds. Xenobiotica 43:711–718. https://doi.org/10.3109/00498254.2012.754112
Melo G, Silva CAB, Hague A et al (2022) Anticancer effects of putative and validated BH3-mimetic drugs in head and neck squamous cell carcinomas: an overview of current knowledge. Oral Oncol 132:105979. https://doi.org/10.1016/j.oraloncology.2022.105979
Meyer N, Zielke S, Michaelis JB et al (2018) AT 101 induces early mitochondrial dysfunction and HMOX1 (heme oxygenase 1) to trigger mitophagic cell death in glioma cells. Autophagy 14:1693–1709. https://doi.org/10.1080/15548627.2018.1476812
Mosmann T (1983) Rapid colorimetric assay for cellular growth and survival: application to proliferation and cytotoxicity assays. J Immunol Methods 65:55–63. https://doi.org/10.1016/0022-1759(83)90303-4
Nakamura K, Okuyama R, Saida T, Uhara H (2013) Platinum and anthracycline therapy for advanced cutaneous squamous cell carcinoma. Int J Clin Oncol 18:506–509. https://doi.org/10.1007/s10147-012-0411-y
Nehal KS, Bichakjian CK (2018) Update on keratinocyte carcinomas. N Engl J Med 379:363–374. https://doi.org/10.1056/NEJMra1708701
Opydo-Chanek M, Gonzalo O, Marzo I (2017) Multifaceted anticancer activity of BH3 mimetics: current evidence and future prospects. Biochem Pharmacol 136:12–23. https://doi.org/10.1016/j.bcp.2017.03.006
Reyes J, Borriero L, Tanphaichitr N et al (1986) Energy metabolism of cultured TM4 cells and the action of gossypol1. Biol Reprod 34:809–819. https://doi.org/10.1095/biolreprod34.5.809
Ribero S, Stucci LS, Daniels GA, Borradori L (2017) Drug therapy of advanced cutaneous squamous cell carcinoma: is there any evidence? Curr Opin Oncol 29:129–135. https://doi.org/10.1097/CCO.0000000000000359
Sharma A, Boise L, Shanmugam M (2019) Cancer metabolism and the evasion of apoptotic cell death. Cancers (basel) 11:1144. https://doi.org/10.3390/cancers11081144
Sulkshane P, Teni T (2017) BH3 mimetic Obatoclax (GX15–070) mediates mitochondrial stress predominantly via MCL-1 inhibition and induces autophagy-dependent necroptosis in human oral cancer cells. Oncotarget 8:60060–60079. https://doi.org/10.18632/oncotarget.11085
Swiecicki PL, Bellile E, Sacco AG et al (2016) A phase II trial of the BCL-2 homolog domain 3 mimetic AT-101 in combination with docetaxel for recurrent, locally advanced, or metastatic head and neck cancer. Invest New Drugs 34:481–489. https://doi.org/10.1007/s10637-016-0364-5
Tang Q, Liu W, Zhang Q et al (2018) Dynamin-related protein 1-mediated mitochondrial fission contributes to IR-783-induced apoptosis in human breast cancer cells. J Cell Mol Med 22:4474–4485. https://doi.org/10.1111/jcmm.13749
Thol F, Ganser A (2020) Treatment of relapsed acute myeloid leukemia. Curr Treat Options Oncol 21:66. https://doi.org/10.1007/s11864-020-00765-5
Townsend PA, Kozhevnikova MV, Cexus ONF et al (2021) BH3-mimetics: recent developments in cancer therapy. J Exp Clin Cancer Res 40:355. https://doi.org/10.1186/s13046-021-02157-5
Tran S-L, Puhar A, Ngo-Camus M, Ramarao N (2011) Trypan blue dye enters viable cells incubated with the pore-forming toxin HlyII of Bacillus cereus. PLoS ONE 6:e22876. https://doi.org/10.1371/journal.pone.0022876
Vaillant F, Merino D, Lee L et al (2013) Targeting BCL-2 with the BH3 mimetic ABT-199 in estrogen receptor-positive breast cancer. Cancer Cell 24:120–129. https://doi.org/10.1016/j.ccr.2013.06.002

Varra V, Woody NM, Reddy C et al (2018) Suboptimal outcomes in cutaneous squamous cell cancer of the head and neck with nodal metastases. Anticancer Res 38:5825–5830. https://doi.org/10.21873/anticanres.12923

Vasiljevic N, Andersson K, Bjelkenkrantz K et al (2009) The Bcl-xL inhibitor of apoptosis is preferentially expressed in cutaneous squamous cell carcinoma compared with that in keratoacanthoma. Int J Cancer 124:2361–2366. https://doi.org/10.1002/ijc.24197

Vlahopoulos S, Critselis E, Voutsas I et al (2014) New use for old drugs? Prospective targets of chloroquines in cancer therapy. Curr Drug Targets. https://doi.org/10.2174/1389450115666140714121514

Vogler M (2014) Targeting BCL2-proteins for the treatment of solid tumours. Adv Med 2014:1–14. https://doi.org/10.1155/2014/943648

Watson M, Holman DM, Maguire-Eisen M (2016) Ultraviolet radiation exposure and its impact on skin cancer risk. Semin Oncol Nurs 32:241–254. https://doi.org/10.1016/j.soncn.2016.05.005

Wheeler DL, Huang S, Kruser TJ et al (2008) Mechanisms of acquired resistance to cetuximab: role of HER (ErbB) family members. Oncogene 27:3944–3956. https://doi.org/10.1038/onc.2008.19

Zeng Y, Ma J, Xu L, Wu D (2019) Natural product gossypol and its derivatives in precision cancer medicine. Curr Med Chem 26:1849–1873. https://doi.org/10.2174/0929867324666170523123655

Zhang Y, Chen X, Gueydan C, Han J (2018) Plasma membrane changes during programmed cell deaths. Cell Res 28:9–21. https://doi.org/10.1038/cr.2017.133

Zhang Z, Zhou L, Xie N et al (2020) Overcoming cancer therapeutic bottleneck by drug repurposing. Signal Transduct Target Ther 5:113. https://doi.org/10.1038/s41392-020-00213-8

Zhang L, Cui T, Wang X (2022) The interplay between autophagy and regulated necrosis. Antioxid Redox Signal. https://doi.org/10.1089/ars.2022.0110

Zorova L, Popkov V, Plotnikov E et al (2018) Mitochondrial membrane potential. Anal Biochem 552:50–59

4. Discussion

The notion of static cristae membranes has not drastically changed in the first ~130 years of mitochondrial research. Although different sources described a remodelling of the IMM, for example during alteration of ADP to ATP ratio or induction of apoptosis and cytochrome *c* release, this view did not change [73, 214, 215]. Over time several proteins were identified to be involved in crista and crista junction architecture, such as OPA1 or MICU1 [219, 241-244]. However, remodelling of the IMM on the level of individual crista has not been reported. Live-cell STED imaging allowed observation of individual cristae membrane fission and fusion events for the first-time. These events took place in a MICOS-dependent manner in the time scale of less than a single second [166, 206]. Although the paradigm of static cristae membranes has been challenged and changed by establishing the cristae fission and fusion model (CriFF) (**Figure 7**), the underlying mechanism and overall role of IMM remodelling is not fully understood to date [70]. Few things are known about the (physiological) role of MICOS-dependent cristae remodelling and many open questions remain. What are the chemical and bioenergetic requirements to maintain IMM remodelling? Which proteins are directly involved in regulation of cristae membrane dynamics and do they regulate each other? Is there an active regulation of cristae dynamics or is it just a passive process? Within the scope of this doctoral thesis, I tried to answer some of these interesting questions and provide new inside into mitochondrial IMM dynamics.

During the course of this doctoral thesis, I could prove that mitochondrial IMM remodelling takes place in a balanced manner in bioenergetically compromised mitochondria, even if their morphonology and cristae architecture was altered (**Figure 8**). This thesis shows that crista merging and splitting events occur in the time scale of less than one second and independent of changes in the mitochondrial ATP levels or the mitochondrial membrane potential $\Delta\Psi_m$. In addition to these findings, the adenine nucleotide translocators (ANTs) were identified as novel possible regulators of cristae dynamics, as live-cell STED nanoscopy experiments showed that inhibition of ANTs with bongkrekic acid (BKA) reduced the IMM remodelling rates in mitochondria with altered crista structure (**Figure 8**).

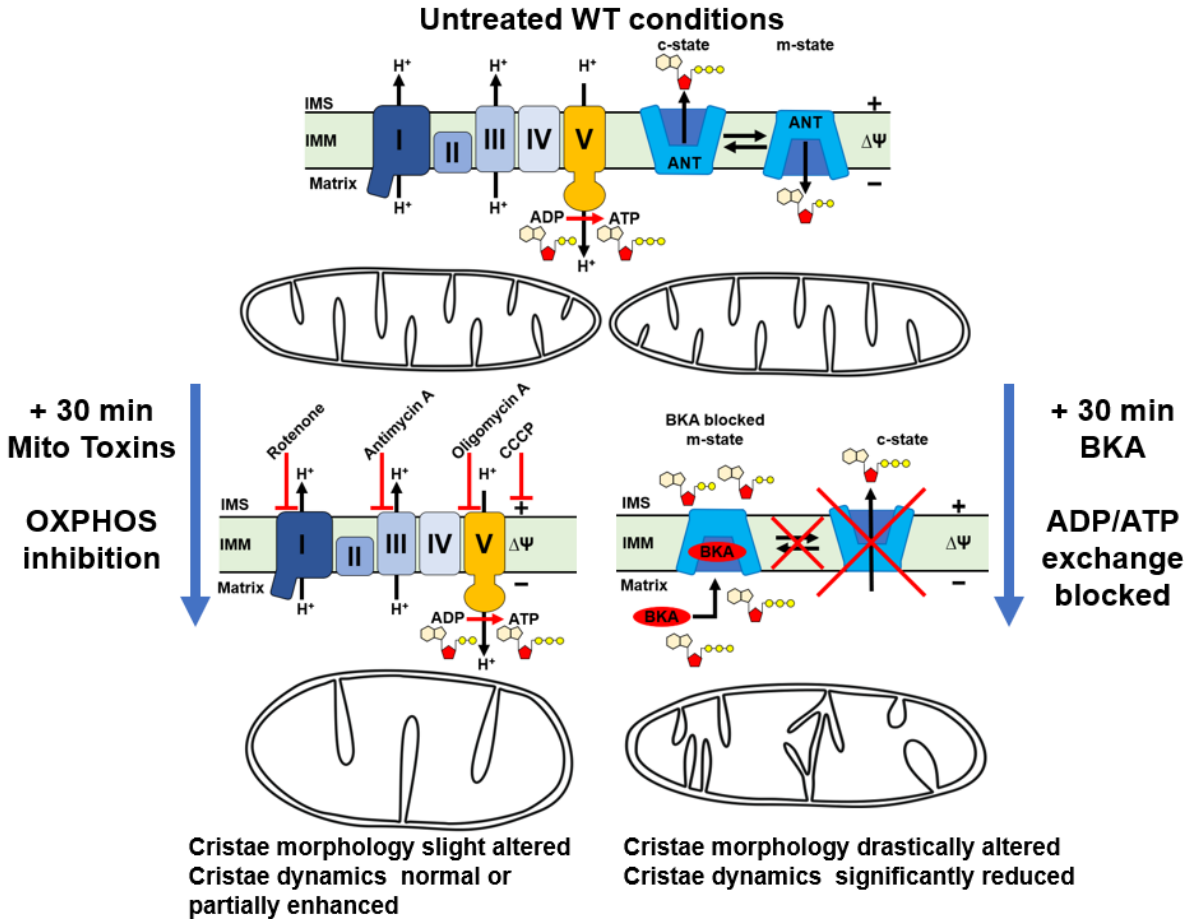

Figure 8. Effects of OXPHOS and ANT inhibition. Inhibition of CI with rotenone, CIII with antimycin A and CV with oligomycin A as well as depletion of $\Delta\Psi_m$ by CCCP effects mitochondrial morphology and crista distribution across the organelle. The treatments cause mitochondrial swelling and a reduction of crista number per area of mitochondrion. IMM remodelling still occurred in these conditions and in some cases even enhanced. Under normal conditions ANTs exchange ATP from the mitochondrial matrix to the IMS and ADP from the IMS to the matrix. This process requires a conformational change of the carrier from the c-state to the m-state. This transition between states and thereby the exchange of ATP and ADP can be efficiently blocked by within 30 min by a dose of 50 µM BKA, locking the carrier in the m-state. BKA treatment induces aberrancies in cristae morphology (clustering of crista, enhanced interconnection or swelling) with reduced cristae dynamics [206, 229].

Furthermore, I participated in answering the questions how the two apolipoproteins MIC26 and MIC27 effect regulation of cardiolipin levels and assembly of OXPHOS complexes and supercomplexes. Loss of the individual proteins does not have drastic effects on other MICOS proteins, crista morphology or cellular function. This drastically changes upon combinational deletion of both genes. When both proteins are lost, the mitochondrial ultrastructure is affected to a similar extend as upon loss of one of the MICOS core subunits like MIC60 or MIC10. Cardiolipin levels and cellular respiration are significantly reduced and the assembly of OXPHOS complexes

hindered. These phenotypes could be rescued upon stable expression of both apolipoproteins in the double knockout background as well as by stable expression of cardiolipin synthase (CRLS1).

The third and final project of my doctoral thesis focused less on IMM remodelling and MICOS but on the role of mitochondria in skin cancer and respective therapy, as I helped to elucidate the mechanism of action of the naturally occurring compound gossypol in cancer cell toxicity. Gossypol was shown to be selectively toxic for SCL-1 cells as it induced by mitochondrial dysfunction and necroptotic cell death.

4.1. Bioenergetic and "chemical" requirements for cristae remodelling

Mitochondria are essential for their role in energy metabolism. OXPHOS is one of the key mechanisms for ATP production, however it is unclear if the ongoing remodelling of crista may represent a passive process that is taking place without hydrolysis of ATP. To bring some light in this we asked a simple question if mitochondrial ATP levels and cristae dynamics correlate or if they are independent from one another. To start investigating this question, we used classical inhibitors of the ETC and the ATP-synthase and analysed the effects on crista morphology and dynamics. Surprisingly after the treatment, we observed continuous merging and splitting events occurring in all treatment conditions without a drastic observable reduction in merging and splitting rates. Indeed, the treated conditions displayed a tendency for increased cristae dynamics in the rotenone, antimycin A and oligomycin A treated groups with CCCP treated mitochondria displaying a significant increase in merging and splitting events. In the test conditions, mitochondria showed an altered morphology consisting of enlarged diameter, reduction of cristae density and increased inter-cristae distance (**Figure 8**).

To correlate the dynamic behaviour of cristae with the mitochondrial ATP levels upon toxin treatment we used FRET sensor mitGO-ATeam2 [245, 246]. This sensor consists of a green fluorescence protein (GFP) and an orange fluorescence protein (OPF) connected by a linker derived from the subunit e of the ANT synthase. In the presence of ATP, the linker undergoes a conformational change, bringing the fluorophores in close proximity of each other to allow an energy transfer from the FRET-donor (GFP) to the FRET-acceptor (OFP). A ratiometric quantification of the individual fluorescence channels allows detailed comparisons of mitochondrial ATP

levels upon toxin treatment. Our initial observations show a drastic reduction of mitochondrial ATP levels upon treatment with rotenone, antimycin A and oligomycin A. This reduction was uniform among these three groups and equally severe in the enlargement of mitochondrial diameter to untreated mitochondria width. In the similar experiments, CCCP showed an aberrant behaviour, where the mitochondrial ATP levels did not change when compared to control. In conclusion, the enhanced merging and splitting rates in the context of mitochondrial dysfunction by chemical inhibitors may function as a compensatory mechanism to maintain ATP production on a functional level. To fully understand the mechanical basis of this phenomenon, further experiment would be needed.

To support this conclusion, it would be an interesting approach correlate the dynamics of a single mitochondria to its specific ATP levels. This is only possible with a sequential imaging setup to first view mitochondrial ATP levels followed by STED imaging of respective mitochondria. Although such setup is highly challenging, it could provide valuable insights into a possible regulation of mitochondrial ATP levels by cristae dynamics. At the moment, it is clear that although the mitochondrial ATP levels varied upon toxin treatment, cristae dynamics still takes place. This hints to an independent relation of ATP levels and cristae dynamics.

Ion homeostasis is essential for mitochondrial function. How are ions balanced in mitochondria? Mitochondria feature a number of ion transporters and channels specifically K^+, Ca^{2+} or Cl^-. These channels are found in the OMM and IMM and can be regulated by pH, voltage, ROS or ATP [247]. Some mitochondrial ion carries are like the ATP-sensitive potassium channel of mitochondria ($mitoK_{ATP}$) are highly specific in their function and not associated with other processes despite ion exchange [248]. Other ion carriers like the mitochondrial calcium uniporter (MCU) are reported not only to exchange and balance charges, but to be relevant for crista junction stabilization, cytochrome *c* release and $\Delta\Psi_m$ maintenance [219, 249]. Mitochondria are known to play a vital role in cellular Ca^{2+} buffering and signalling [14]. Especial the regulation of the mitochondrial Ca^{2+} household across the CJs was lately associated with bioenergetics and the local maintenance of the membrane potential [221, 250]. In our study we found that inhibition of OXPHOS for about 30 min caused significant swelling of mitochondrial (**Figure 8**). The most prominent reason for this is the induction of an osmotic imbalance. This imbalance most notably causes swelling of the matrix due to

influx of water and thereby changes the morphology. Osmotic imbalance could be triggered by changes in the ion or Ca^{2+} environment and after a certain threshold enhanced by opening of the mitochondrial permeability transition pore (MPTP). Opening of this pore allows free influx of solutes with a molecular mass of up to 1.5 kDa through the IMM. This could potentially cause quick changes in the viscosity of the mitochondrial matrix due to enhanced influx of water combined with overall more space for crista to expand could be a physiological catalyser of membrane remodelling. These proposed changes in matrix viscosity could occur very rapidly as only small volumes of water are required to affect the matrix composition of a mitochondrion with a width of a few hundred nm. Although several fluorescent probes were developed in recent years to detect changes in mitochondrial matrix viscosity for *in vitro* and *in vivo* applications, these experiments require extensive standardization to be setup for detection of rapid and minimal changes in matrix viscosity [251, 252].

Another key factor that is essential for correct and efficient mitochondrial function is the mitochondrial membrane potential $\Delta\Psi_m$. As previously explained, it is established by the protein complexes of the ETC, especially Complex I and Complex III. The proton gradient formation is then utilized by the ATP-Synthase to continuously produce ATP. Furthermore, it is associated with the regulation of the configuration of the mitochondrial matrix and the release of cytochrome *c* during apoptosis [253]. For determination of the $\Delta\Psi_m$, the charge-dependent dye TMRM was used. This dye carries a negative charge and localizes at the inner leaflet of the IMM. Quantification of the respective fluorescence intensities are a direct readout of the membrane potential. In our studies we found altering levels of $\Delta\Psi_m$ depending on the respective toxin. As expected, an inhibition of function of the two main proton pumps of the ETC (Complex I by rotenone and Complex III by antimycin A) caused a significant reduction of the potential, with antimycin A having a more drastic effect compared to rotenone. Surprisingly inhibition of the ATP synthase by oligomycin A did not alter the $\Delta\Psi_m$ drastically. However, considering the usage of $\Delta\Psi_m$ by the ATP-Synthase one would not expect a reduction of the gradient upon the activity of ATP synthase. CCCP on the other hand completely depletes the $\Delta\Psi_m$ as expected. Previous studies could show, that CCCP treatment causes a decrease of cristae density [254].

Consistent with our previous data, that a drastic depletion of $\Delta\Psi_m$ had no negative effects on cristae remodelling. The strongest reduction of the $\Delta\Psi_m$ was found

in antimycin A and CCCP treated cells. Upon inhibition of Complex III the rates of merging and splitting displayed a strong but not significant tendency towards an increase. For CCCP merging and splitting events were significantly enhanced. Interestingly, it provides evidence that the regulation of cristae dynamics is not affected by a key factor for mitochondrial function and fitness, the $\Delta\Psi_m$.

4.2. Molecular players involved in cristae remodelling

In 2020 MICOS was determined as the first essential protein complex to be required for ongoing cristae dynamics [166]. Loss of individual MICOS subunits including MIC13, MIC10, MIC19 and MIC60 caused reduction in IMM merging and splitting [166, 218]. MICOS being one of the key elements of crista junction stabilization, recently other proteins including OPA1 were also shown to be involved in regulation of the cristae dynamics [218]. Previous studies could show that balanced levels of L-OPA1 and S-OPA1 are required for the establishment of tightened CJs [244]. In our treatment conditions, we did not observe drastic changes in OPA1 cleavage, except after the treatment with CCCP. Here an increased amount of S-OPA1 was observed, whereas the steady state levels in the other treatment conditions remained the same. One could correlate this enhanced cleavage to the increased rates of merging and splitting events observed in the enlarged mitochondria. The effect of OPA1 depletion on cristae dynamics and on cristae morphology were investigated. Studies could provide evidence that upon loss of OPA1 cristae dynamics is reduced [218] similar to a reduced and disorganized morphology [243]. Although OPA1 is not necessarily required for maintenance of CJs, OPA1 was shown to be involved regulation of cristae remodelling [244, 255]. OPA1 helps to adjust the width of CJs as it can form higher oligomers with a unidirectional orientation of the individual OPA1 molecules. These oligomers can form either right- or left-handed helical pattern. It was reported that a left-handed helical pattern of OPA1 results in a widening of a lipid tube, while a right-handed orientation of OPA1 can tighten a CJ [256]. An overall reduction of cristae number can directly result in a reduced number of merging and splitting events, this could only be explained if the rates are significantly increased. In our study we did not deplete OPA1 but shifted the balance of L-OPA1 and S-OPA1. Under cellular stress conditions OPA1 can be processed by OMA1 causing a shift in L-OPA1 and S-OPA1 ratio, causing mitochondrial fragmentation and even loss of CJ [52, 257].

Such a drastic shift in OPA1-L to OPA1-S was not observed upon mitochondrial toxin treatment for 30 min. Only in CCCP conditions a stronger shift between the two OPA1-forms was observed and an increase of cristae dynamics, too [206]. This observed increase in dynamics could be a compensatory mechanism, to regain an even distribution of OPA1-forms across several crista or a passive effect prior to a loss of crista junctions by a shift of the OPA1 ratio towards OPA1-S. The protease YME1L that cleaves OPA1 together with OMA1 has been reported to effect IMM remodelling, too, as loss of YME1L causes detachment of cristae membranes. Detailed studies of mammalian cell lines that are deficient for OPA1, YME1L and OMA1 could help to elucidate how these three proteins might interact to regulate IMM remodelling. Besides MICOS and OPA1 other molecules were identified as possible regulators of IMM remodelling. Similar to loss the of MICOS complexes loss of SAMM50 was reported to reduce cristae dynamics [218]. A factor that places a role in IMM remodelling, too, is the ATPase family AAA domain containing 3A (ATADA3). ATADA3 deficient cell lines were shown to display increased cristae dynamics [218]. How these factors contribute to the regulation of IMM or might influence each other expression levels the induce or hinder cristae remodelling is not understood to this day.

In our study we could clearly show that inhibition of ANTs by bongkrekic acid (BKA) can have drastic effects on cristae as well as mitochondrial morphology (**Figure 8**). Blockage of ANTs in the m-state causes several effects ranging from mitochondrial swelling to fragmentation. These alterations in mitochondrial morphology were often accompanied by changes in cristae morphology. The extent of mitochondria with altered cristae morphology was shown to be increased to about 33% of the total population. While some mitochondria kept their natural IMM structure, the alterations in the affected mitochondria were drastic. Ranging from static cristae, to heavily interconnected or honey comb like cristae, to areas void of cristae. In some extreme cases it appeared that even large cristae vesicles are formed, detaching on one side of the IMM and be transported across the matrix to be reattached on the other side of the IMM. In the group with these highly effected mitochondria merging and splitting events were significantly reduced. These observations suggest that the ANT carrier family might be another molecular player, which is not only involved in cristae formation but also in the regulation of cristae dynamics. However, to fully support this statement further studies will be needed, though. It is essential to exclude that these drastic changes in mitochondrial and cristae morphology are not specific to the use of BKA or

the trapping of ANTs in the m-state. To exclude a BKA-exclusive effect, observations of the dynamic behaviour upon treatment with different inhibitors is crucial.

Further blockage of ANTs by carboxyatractyloside (CATR) in the c-state is also interesting. Unfortunately, we found that this CATR is not capable of passing the cell membrane without artificial membrane permeabilization (unpublished data from Yulia Schaumkessel). Studies of effects of a cell permeable compound that can trap the ANTs in their c-state on cristae dynamics could help to understand the underlying mechanism of ANT involvement and to rule out any BKA- or m-state specific off target effects. An essential model to fully understand the role of ANTs in the background of cristae remodelling are ANT deficient cell lines. Here especially ANT2 and ANT3 are interesting, as in humans ANT2 is expressed in many tissues but enriched in highly proliferating cells, while ANT3 is expressed to low levels in virtually all tissues. ANT1 is mostly expressed in tissues with high metabolic activities like heart and skeletal muscle, while ANT4 is mainly expressed in the brain, liver and testis [225]. To fully study the involvement of ANTs, a combined KO of both genes is helpful as the regulation of expression of these carrier family is not fully understood to date. For instance, a possible depletion of ANT2 could be compensated by increased levels of ANT3 or vice versa. These kinds of reciprocal expression to maintain cellular or mitochondrial function, is not uncommon as it has been reported for several examples of same family of proteins or complex like MIC26 and MIC27 [132]. In this regard, a wide screen of gene and protein expression levels in several MICOS and ANT mutants could provide valuable insights in a possible interaction and combined role in regulation of cristae dynamics.

Deficiencies of the MICOS complex core proteins MIC10, MIC13 or MIC60 are known to reduce cristae dynamics as they cause disruption of the MICOS complex as a whole and thereby destabilize the formation of CJs in the first place [15, 151, 166, 258]. But do they effect the expression levels of ANTs or their distribution across the IMM, and if so, to which extend or vice versa? Answering these questions could help to unravel the complex interaction patterns of molecular players, involved in regulation of cristae dynamics.

4.3. Possible roles of cristae remodelling

For long time the inner mitochondrial membrane was considered to be a static entity. Although some early hints about changes in morphology were already collected in the 1960s proof for higher dynamics was missing [214]. It was not until newly developed imaging techniques combined with highly photostable dyes allowed imaging of individual cristae merging and splitting event in the time scale of second. The first identification of this phenomenon was followed by characterizations of few molecular players involved in its regulation. MICOS being one of the most important molecular regulators of cristae dynamics, as it does not only establish formation of CJs but was shown to cause a drastic loss of merging and splitting event frequency upon deletion of individual MICOS subunits e.g., MIC13 [166]. As previously discussed, there are certain key protein complexes that are essential for stabilization of the mitochondrial ultrastructure, MICOS, ATP-synthase, OPA1, MICU1, YME1, SLC25A46 and others, yet, it is unknown how the changes in crista morphology might affect their dynamic behaviour, making it is difficult to pinpoint to the exact role of cristae dynamics.

In our studies, we analysed the effect of various mitochondrial toxins on cristae dynamics and overall structure of mitochondria. Overall, we did not find a treatment condition that completely blocked these dynamics. The different types of cristae fission and fusion events were characterized in previous work. Depending on motion of the CJs or the CM itself the most common form of events were transvers, X-type and Y-type of events, summed up in the CriFF model (**Figure 7**) [69, 70, 166]. In some rare cases, a full separation for the CM from the CJ followed by fusion at the opposing side of the matrix were observed, hinting towards transient formation of cristae vesicles. In theory these vesicles provide an ideal solution for proton trapping (**Figure 9**). Unlike CJs that always have a small pore or slit with a width of few nm towards the intermembrane space, a cristae vesicle is completely sealed by a membrane allowing for optimal maintenance of the proton gradient across it´s membrane and thereby enhanced synthesis of ATP. These vesicles could be transiently formed within malfunctioning mitochondria to provide short term elevation of ATP production and maintenance of cellular fitness as a mechanism to compensate a cellular stress. But if these transient vesicles can help to boost ATP synthesis, why are they not formed in high numbers? A vesicle allows nearly perfect proton trapping and thereby can potentially establish a high proton gradient across the CM and a high proton motive force to boost ATP production. A drawback of these vesicles is that metabolite

exchange between IBM and CM is harder and occurs with lower rates as there the direct connection between these two membrane compartments is missing. Damaged ETC complexes cannot be exchanged or new ones imported and assembled to mature complexes. Another limiting factor for longer presence of these vesicles is the amount of ADP that is available for synthesis of ATP. A high proton gradient across the CM could not be utilized if the substrates for ATP synthesis are not available. Due to reduced metabolite exchange this imbalance between ADP and ATP could potentially increase over time [259]. The idea of individual crista switching to a proton trapping mode for a short duration of time is not deceptive, as previous studies proved that individual crista can be viewed as separate bioenergetic units [217]. Individual crista were shown to exhibit different membrane potentials when compared to their neighbouring crista and act functionally independent from one another [217]. The dynamic tap and flux (DynaTrux) – model was proposed recently and describes the possible benefits and drawbacks of a transient cristae vesicle when compared to a cristae membrane that is connected to the IBM via the MICOS complex [259]. Crista vesicles were described but the mechanism of induction for release of vesicle from the IBM are not clear yet. Combining the idea that crista can function independent from one another it would be interesting to investigate if transient formation of crista vesicles can be promoted under condition of high energy demand in combination with high metabolite accessibility. One could imagine that crista “load” with metabolites via the CJ, form a vesicle, generate a high proton gradient and utilize it produce an increased amount of ATP before refusing with the IBM and repeating this process until the high metabolic demand has vanished. Depending on the time required for such a “loading” phase the proton gradient might stay high during this process before repeating another cycle. The dynamic behaviour of membrane bound crista and free vesicles makes it tempting to speculate about a protein machinery that is able to pinch off cristae membranes entirely and detect them to reattach the vesicle with the IBM. MICOS is certainly the most interesting candidate for such a mechanism, as it is essential for formation of CJs in the first place [15]. Evidence that MICOS is able to reattach cristae membranes back to the IBM on its own still needs to be provided.

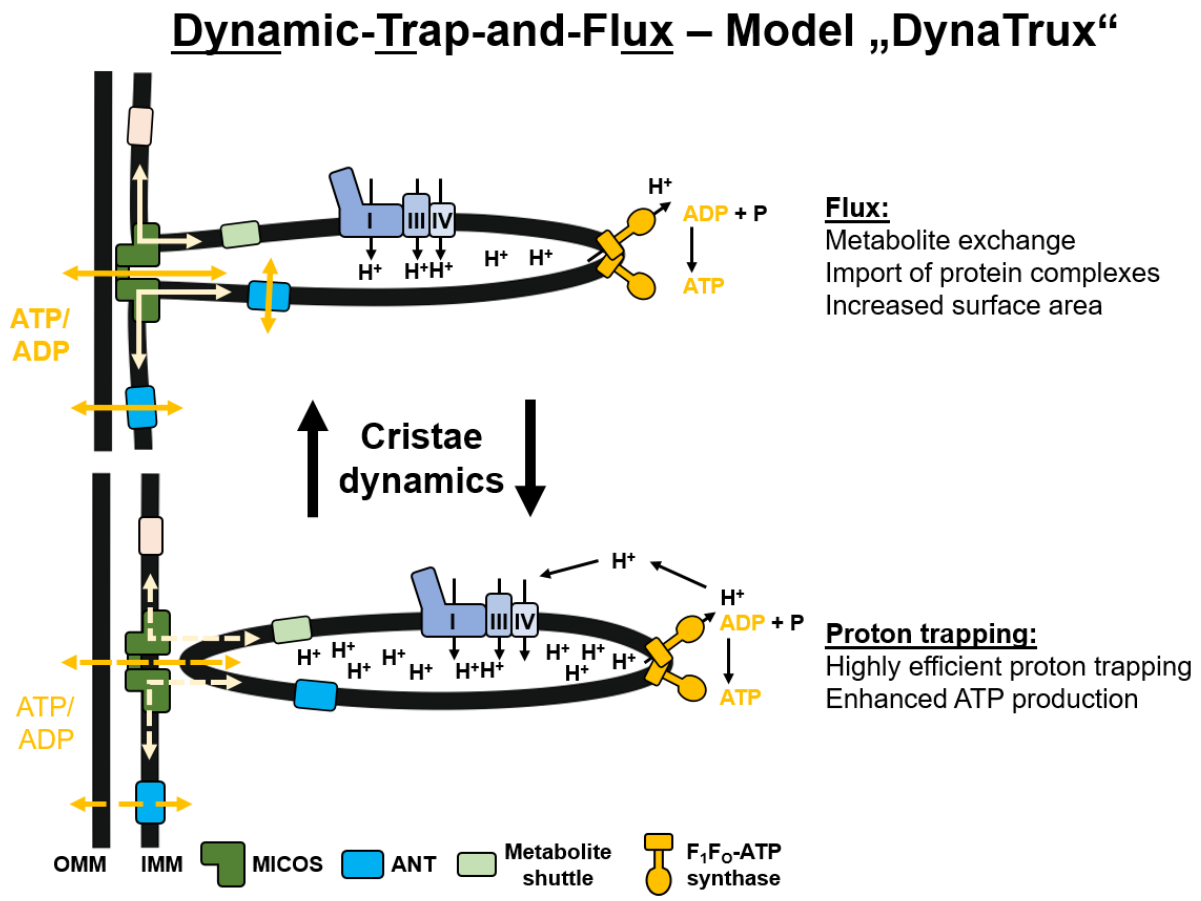

Figure 9. The dynamic trap and flux – model (DynaTrux) describes the switch of CMs between a mode favouring metabolite exchange and one promoting proton trapping [259]. During the continues cycles of CM fission and fusion a transient formation of cristae vesicles was reported. When a CM is attached to the IBM via the MICOS complex, exchange of metabolites as well as relocalization of OXPHOS complexes, metabolite exchangers like ANTs or metabolite shuttles is possible. Formation of a transient crista vesicle does not allow these exchanges, but can help to establish a high proton gradient across the CM as a vesicle improves proton trapping and ATP synthesis. Model and scheme adapted from [259].

Our studies displayed a variety of morphological parameters that were altered upon toxin treatment. We found changes in crista distribution across mitochondria upon increase in mitochondrial diameter, represented by reduced number of crista per mitochondrial area as well as a greater distance between individual crista. In the CCCP treated conditions these two parameters were accompanied with significant increase in both merging and splitting rates. One could try and correlate these two findings by speculating, that the larger distances from one cristae to another could be bridged by higher movement of the CJ or that the created space created by the void if crista gives more room for X- and Y-shaped crista merging and splitting events. Opposing to this hypothesis, in some cases individual mitochondria showed a high interconnection of

crista combined with an increase in width after treatment with mitochondrial toxins. In some instances, these “honey comb” like crista networks displayed higher rates of merging and splitting without drastic changes in motion of the CJs. One could speculate that these morphological alterations might be a result of higher fission rates or an imbalanced remodelling behaviour. Our detailed quantification on the levels of individual splitting events did not support this hypothesis, but rather displayed an equally balanced merging and splitting rates once the respective treatment groups were compared.

As previously discussed, the full understanding of the overall mechanism and it´s requirements are not available to date, making direct functions highly speculative. Our data suggest that the maintenance and partial enhancement of crista merging and splitting rates might be a short-term compensatory mechanism to cope for the inhibition of individual OXPHOS complexes. One might speculate that these dynamics might be kept high, as the mitochondrion tries to sort out some of the already inhibited proteins of the ETC to maintain its function. This might occur due to a directed transport of inhibited proteins to a “pole” of one mitochondrion before a mitochondrial fission event removes the inefficiently working part of the mitochondrion or to maintain the mitochondrial function across larger regions with several crista. Processes like these not only require a short contact of two cristae membranes in a “kiss and run” manner but a full membrane fusion, followed by content mixing, an exchange of membrane proteins and fission. In some these fusion events combined with content mixing have already been reported. For instance, as the membrane potential of individual cristae was altered during fusion events or are light induced GFP activation spread across different crista during fusion events [166, 217]. From a technical point of view these experiments are highly challenging to setup. Moreover, finding these respective events with high resolution without bleaching the dye or other disturbances to provide reliable results requires a high sample throughput. To achieve such results a high-throughput screen combined with an automated imaging analysis pipeline would be an ideal tool. At the moment, such approaches are limited by several factors like resolution, photobleaching, frame rate and exposure time and especially image quality, as image processing is prone to introduce artefacts if not performed cautiously. In near future further developments of fluorescent dyes, microscopes and artificial intelligence or machine learning can make screening of these datasets more user-friendly. Considering the fact that more and more diseases are associated with aberrant crista

morphology, an expanded analysis of dynamics in these illnesses could provide more insights in the role IMM remodelling.

4.4. Conclusions

This doctoral study aimed to determine the role of MICOS in cristae remodelling and to answer the question whether inhibition of individual ETC complexes and the elimination of the mitochondrial membrane potential by classical mitochondrial toxins. It was shown that merging and splitting events continuously took place in bioenergetically compromised mitochondria in a balanced manner with a time resolution of below one second. Although the treatment with rotenone, antimycin A, oligomycin A and CCCP caused significant changes in the mitochondrial morphology and crista morphology, remodelling still took place. Astonishingly even significant alterations of mitochondria, the ATP levels and irregular changes of the $\Delta\Psi_m$ throughout the various treatment conditions did not uniformly change the cristae dynamics. For example, in the CCCP treated group, the uncoupling agent displayed a significant increase in merging and splitting events while the mitochondrial ATP levels were not altered and the membrane potential was completely lost. These observations make it tempting to speculate that enhanced cristae dynamics can act as a compensatory mechanism to counteract reduced ATP production. To prove this hypothesis, further experiments are required. On a molecular level CCCP is an interesting candidate, as it was the only condition to display a slight change in OPA1 cleavage.

Analysis of role of mitochondrial ADP/ATP nucleotide translocator provided interesting insights. Upon blockade of the adenine nucleotide translocator (ANT) by treatment with bongkrekic acid (BKA) we observed an increased number of mitochondria with perturbed crista structure. The initial analysis of the dynamic behaviour of mitochondria from the BKA treated group did not provide changes in crista merging and splitting rates. Once the data sets were separated into mitochondria with normal and altered crista morphology, we observed a significant decrease in these rates. This outcome hints towards a strict connection between form and function on cristae membranes and to ANTs as a possible new regulator of cristae dynamics. Overall, we utilized state-of-the-art imaging techniques combined with specialized image analysis to provide new insights into the role of MICOS-dependent cristae

remodelling. To fully understand the underlying mechanism and role of this process further studies are necessary.

As the mechanism of regulation of cristae remodelling still needs to investigated further it could be an interesting target for alternative cancer therapy, too. Screening of established anticancer drugs or natural occurring compounds could lead to discovery of substances that inhibit IMM remodelling. This would hinder content mixing within the mitochondrion and perturb its function. Other coupons induce extensive formation of crista vesicles without refusion to the IBM. This could potentially cause a shortage of ADP and other metabolites due to reduced exchange and further downstream to less efficiently functioning mitochondria and cell death.

MICOS has been established as a key regulator of IMM remodelling. Some results from this thesis link MICOS subunits to regulation of cardiolipin levels and OXPHOS complex assembly. It would be intriguing to study these three aspects in combination. Answering the question of a possible mutual regulation of cardiolipin synthesis and regulation of crista fission and fusion rates could provide valuable insights into the role IMM remodelling in destitution of OXPHOS complexes among individual crista.

5. Summary

Over the past decades the representation of mitochondria in many textbooks has changed from being presented as a small bean-shaped organelle with the main function to provide energy in the form of ATP to an organelle that form a vast and highly dynamic network throughout the cell and is involved in numerous metabolic and regulatory processes. More recently, several working groups could show that the inside of the organelle is even more in motion than the overall network. If the fine ultra-structure of the IMM is correctly established, cristae membranes undergo continues cycles of membrane merging and splitting in a time scale of less than a single second. MICOS has been established as a key player for cristae dynamics, as the initial formation of crista is required for their fission and fusion. Different types of IMM fission and fusion are described in the crista fission and fusion (CriFF) model. Despite some proposed functions of CriFF like a regulatory role of intramitochondrial quality control, the direct functions of IMM remodelling remain unknown. Several questions remain unanswered, as it is unknown what molecular players are involved in the maintenance of cristae dynamics or what bioenergetically requirements must be fulfilled to keep the membranes in motion. It is not known if this process is of a passive nature or an active process that requires a continuous hydrolysis of ATP. This thesis aimed to answer some of these open questions by inhibition of some key proteins of mitochondrial energy production and associated features of functional mitochondria. We utilized state-of-the-art super-resolution live-cell imaging with a highly detailed image analysis. Our studies provided reliable data showing that inhibition of individual OXPHOS complexes and a depletion of the mitochondrial membrane potential ($\Delta\Psi_m$) did not inhibit IMM merging and splitting, while altering the mitochondrial ultrastructure. Furthermore, we could show that cristae remodelling can occur despite heavily reduced mitochondrial ATP levels and provide prove that maintenance of the $\Delta\Psi_m$ is not required for IMM remodelling.

Additionally, we examined the role of adenine nucleotide translocator (ANT) in the context of cristae remodelling. In doing so we used the ANT inhibitor bongkrekic acid (BKA). This compound locks the ANTs in the m-state and prevents any further exchange of ADP and ATP. With the applied concentration of about 50 µM we observed a drastic reduction in respiration of HeLa WT cells after 30 min. With live-cell STED super-resolution imaging we observed a strong increase of mitochondria with aberrant in crista structure compared to the control group and confirmed these

observations with electron microscopy. Treatment with 50 µM BKA over a period also revealed a significant reduction of $\Delta\Psi_m$, less drastic than a total membrane uncoupling with CCCP, though. Of high interest are the results of ANT inhibition in the background of cristae dynamics. The ADP/ATP translocases have not been associated with cristae dynamics so far, we on the other hand could demonstrate that rates of crista merging and splitting events are significantly reduced upon BKA treatment in a subset of mitochondria with aberrant crista structure.

Furthermore, some results obtained in this doctoral thesis linked the regulatory role of the apolipoproteins MIC26 and MIC27 to formation of OXPHOS complexes via regulation of cardiolipin levels. It was shown that loss of both apolipoproteins results in drastic changes of mitochondrial morphology, reduced respiration, changes in cardiolipin levels and perturbed OXPHOS complex assembly. These drastic reductions were rescued by stable expression of the MIC26 and MIC27 in combination and by expression of CRLS1.

Although the main focus of this doctoral thesis is the investigation of the physiological role, relevance and regulation of MICOS-dependent cristae remodelling I contributed to a project that focused a therapeutic treatment of the invasive squamous cell carcinoma cell line SCL-1 with the naturally occurring polyphenolic aldehyde (±) gossypol. Gossypol has a selective cytotoxicity on SCL-1 cells. This toxicity is induced by mitochondrial dysfunction, causing necroptotic cell death. These results indicate a high potential for gossypol as an alternative anticancer drug for the treatment of cutaneous squamous cell carcinoma.

In summary, we showed that IMM remodelling takes place in metabolically compromised mitochondria, even after significant reduction of mitochondrial ATP levels or depletion of $\Delta\Psi_m$ and proposing ANTs as a possible regulator of IMM architecture and dynamics. Furthermore, proposing a connection between membrane architecture and function, with as mitochondria with highly perturbed IMM morphology featured a reduction in membrane merging and splitting.

6. References

1. Gray MW., G.B., B. Franz Lang, *Mitochondrial Evolution.* 1999.
2. L., S., *On the Origin of Mitosing Cdls.* 1967.
3. Gray, M.W., *Mitochondrial evolution.* Cold Spring Harb Perspect Biol, 2012. **4**(9): p. a011403.
4. Embley, T.M. and W. Martin, *Eukaryotic evolution, changes and challenges.* Nature, 2006. **440**(7084): p. 623-30.
5. Garrido, C., et al., *Mechanisms of cytochrome c release from mitochondria.* Cell Death Differ, 2006. **13**(9): p. 1423-33.
6. Reichert, A.S. and W. Neupert, *Mitochondriomics or what makes us breathe.* Trends Genet, 2004. **20**(11): p. 555-62.
7. Lill, R., *Function and biogenesis of iron-sulphur proteins.* Nature, 2009. **460**(7257): p. 831-8.
8. van der Sluis, E.O., et al., *Parallel Structural Evolution of Mitochondrial Ribosomes and OXPHOS Complexes.* Genome Biol Evol, 2015. **7**(5): p. 1235-51.
9. Falkenberg, M., N.G. Larsson, and C.M. Gustafsson, *DNA replication and transcription in mammalian mitochondria.* Annu Rev Biochem, 2007. **76**: p. 679-99.
10. Hallberg, B.M. and N.G. Larsson, *Making proteins in the powerhouse.* Cell Metab, 2014. **20**(2): p. 226-40.
11. Kondadi, A.K. and A.S. Reichert, *Mitochondrial Dynamics at Different Levels: From Cristae Dynamics to Interorganellar Cross Talk.* Annu Rev Biophys, 2024.
12. Pfanner, N., B. Warscheid, and N. Wiedemann, *Mitochondrial proteins: from biogenesis to functional networks.* Nat Rev Mol Cell Biol, 2019. **20**(5): p. 267-284.
13. Wiedemann, N. and N. Pfanner, *Mitochondrial Machineries for Protein Import and Assembly.* Annu Rev Biochem, 2017. **86**: p. 685-714.
14. Santo-Domingo, J. and N. Demaurex, *Calcium uptake mechanisms of mitochondria.* Biochim Biophys Acta, 2010. **1797**(6-7): p. 907-12.
15. Rabl, R., et al., *Formation of cristae and crista junctions in mitochondria depends on antagonism between Fcj1 and Su e/g.* J Cell Biol, 2009. **185**(6): p. 1047-63.
16. Zick, M., R. Rabl, and A.S. Reichert, *Cristae formation-linking ultrastructure and function of mitochondria.* Biochim Biophys Acta, 2009. **1793**(1): p. 5-19.
17. Kölliker, A., *Einige Bemerkungen über die Endigungen der Hautnerven und den Bau der Muskeln.* Zeitschr f wissensch Zool, 1857. **8**: p. 311-325.
18. Ernster, L.S., G., *Mitochondria: A Historical Review.* J Cell Biol, 1981. **91**(3): p. 227-255.
19. Altmann, R., *Die Elementarorganismen und ihre Beziehungen zu den Zellen*. 1894: de Gruyter.
20. Benda, C., *Ueber die spermatogenese der vertebraten und höherer evertebraten, II. Theil: Die histiogenese der spermien.* Arch. Anat. Physiol, 1898. **73**: p. 393-398.
21. Yuan, Y., et al., *Comprehensive molecular characterization of mitochondrial genomes in human cancers.* Nat Genet, 2020. **52**(3): p. 342-352.
22. Wallace, D.C., *Mitochondrial genetic medicine.* Nat Genet, 2018. **50**(12): p. 1642-1649.
23. Burke, P.J., *Mitochondria, Bioenergetics and Apoptosis in Cancer.* Trends Cancer, 2017. **3**(12): p. 857-870.
24. Vyas, S., E. Zaganjor, and M.C. Haigis, *Mitochondria and Cancer.* Cell, 2016. **166**(3): p. 555-566.
25. Coskun, P., et al., *A mitochondrial etiology of Alzheimer and Parkinson disease.* Biochim Biophys Acta, 2012. **1820**(5): p. 553-64.
26. Colina-Tenorio, L., et al., *Shaping the mitochondrial inner membrane in health and disease.* J Intern Med, 2020.
27. Siegmund, S.E., et al., *Three-Dimensional Analysis of Mitochondrial Crista Ultrastructure in a Patient with Leigh Syndrome by In Situ Cryoelectron Tomography.* iScience, 2018. **6**: p. 83-91.
28. Xu, Y., et al., *Cardiolipin remodeling enables protein crowding in the inner mitochondrial membrane.* EMBO J, 2021. **40**(23): p. e108428.
29. Cojocaru, K.A., et al., *Mitochondrial Dysfunction, Oxidative Stress, and Therapeutic Strategies in Diabetes, Obesity, and Cardiovascular Disease.* Antioxidants (Basel), 2023. **12**(3).

30. Khan, M., Y. Baussan, and E. Hebert-Chatelain, *Connecting Dots between Mitochondrial Dysfunction and Depression.* Biomolecules, 2023. **13**(4).
31. Riley, J.S. and S.W. Tait, *Mitochondrial DNA in inflammation and immunity.* EMBO Rep, 2020: p. e49799.
32. He, B., et al., *Mitochondrial cristae architecture protects against mtDNA release and inflammation.* Cell Rep, 2022. **41**(10): p. 111774.
33. Haasler, L., et al., *Involvement of necroptosis in the selective toxicity of the natural compound (+/-) gossypol on squamous skin cancer cells in vitro.* Arch Toxicol, 2023. **97**(7): p. 1997-2014.
34. Vasan, K., M. Werner, and N.S. Chandel, *Mitochondrial Metabolism as a Target for Cancer Therapy.* Cell Metab, 2020. **32**(3): p. 341-352.
35. Wallace, D.C., *Mitochondria and cancer.* Nat Rev Cancer, 2012. **12**(10): p. 685-98.
36. Brandon, M., P. Baldi, and D.C. Wallace, *Mitochondrial mutations in cancer.* Oncogene, 2006. **25**(34): p. 4647-62.
37. Ng, Y.S. and D.M. Turnbull, *Mitochondrial disease: genetics and management.* J Neurol, 2016. **263**(1): p. 179-91.
38. Thompson, K., et al., *Recurrent De Novo Dominant Mutations in SLC25A4 Cause Severe Early-Onset Mitochondrial Disease and Loss of Mitochondrial DNA Copy Number.* Am J Hum Genet, 2016. **99**(4): p. 860-876.
39. Shimomura, O., F.H. Johnson, and Y. Saiga, *Extraction and Properties of Halistaurin, a Bioluminescent Protein from the Hydromedusan Halistaura.* J Cell Comp Physiol, 1963. **62**: p. 9-15.
40. Morise, H., et al., *Intermolecular energy transfer in the bioluminescent system of Aequorea.* Biochemistry, 1974. **13**(12): p. 2656-62.
41. Twig, G., et al., *Tagging and tracking individual networks within a complex mitochondrial web with photoactivatable GFP.* Am J Physiol Cell Physiol, 2006. **291**(1): p. C176-84.
42. Bereiter-Hahn, J. and M. Vöth, *Dynamics of mitochondria in living cells: shape changes, dislocations, fusion, and fission of mitochondria.* Microsc Res Tech, 1994. **27**(3): p. 198-219.
43. Twig, G., et al., *Fission and selective fusion govern mitochondrial segregation and elimination by autophagy.* EMBO J, 2008. **27**(2): p. 433-46.
44. Twig, G. and O.S. Shirihai, *The interplay between mitochondrial dynamics and mitophagy.* Antioxid Redox Signal, 2011. **14**(10): p. 1939-51.
45. Liu, X., et al., *Mitochondrial 'kiss-and-run': interplay between mitochondrial motility and fusion-fission dynamics.* EMBO J, 2009. **28**(20): p. 3074-89.
46. Archer, S.L., *Mitochondrial dynamics--mitochondrial fission and fusion in human diseases.* N Engl J Med, 2013. **369**(23): p. 2236-51.
47. Chen, H., et al., *Mitofusins Mfn1 and Mfn2 coordinately regulate mitochondrial fusion and are essential for embryonic development.* J Cell Biol, 2003. **160**(2): p. 189-200.
48. Koshiba, T., et al., *Structural Basis of Mitochondrial Tethering by Mitofusin Complexes.* Science, 2004. **305**: p. 858-862.
49. Rojo, M., et al., *Membrane topology and mitochondrial targeting of mitofusins, ubiquitous mammalian homologs of the transmembrane GTPase Fzo.* J Cell Sci, 2002. **115**: p. 1663-1674.
50. Bach, D., et al., *Mitofusin-2 determines mitochondrial network architecture and mitochondrial metabolism. A novel regulatory mechanism altered in obesity.* J Biol Chem, 2003. **278**(19): p. 17190-7.
51. de Brito, O.M. and L. Scorrano, *Mitofusin 2 tethers endoplasmic reticulum to mitochondria.* Nature, 2008. **456**(7222): p. 605-10.
52. Duvezin-Caubet, S., et al., *Proteolytic processing of OPA1 links mitochondrial dysfunction to alterations in mitochondrial morphology.* J Biol Chem, 2006. **281**(49): p. 37972-9.
53. Chen, H., et al., *Mitochondrial fusion is required for mtDNA stability in skeletal muscle and tolerance of mtDNA mutations.* Cell, 2010. **141**(2): p. 280-9.
54. Yapa, N.M.B., et al., *Mitochondrial dynamics in health and disease.* FEBS Lett, 2021. **595**(8): p. 1184-1204.

55. Chan, D.C., *Mitochondrial Dynamics and Its Involvement in Disease.* Annu Rev Pathol, 2020. **15**: p. 235-259.
56. Loson, O.C., et al., *Fis1, Mff, MiD49, and MiD51 mediate Drp1 recruitment in mitochondrial fission.* Mol Biol Cell, 2013. **24**(5): p. 659-67.
57. Lee, J.E., et al., *Multiple dynamin family members collaborate to drive mitochondrial division.* Nature, 2016. **540**(7631): p. 139-143.
58. Abrisch, R.G., et al., *Fission and fusion machineries converge at ER contact sites to regulate mitochondrial morphology.* J Cell Biol, 2020. **219**(4).
59. Kleele, T., et al., *Distinct fission signatures predict mitochondrial degradation or biogenesis.* Nature, 2021. **593**(7859): p. 435-439.
60. Lewis, M.R. and W.H. Lewis, *Mitochondria (and other cytoplasmic structures) in tissue cultures.* American Journal of Anatomy, 1915. **17**(3): p. 339-401.
61. Scott, S.V. and D.J. Klionsky, *Delivery of proteins and organelles to the vacuole from the cytoplasm.* **Current Opinion in Cell Biology**, 1998. **10**: p. 523-529.
62. Zimmermann, M. and A.S. Reichert, *How to get rid of mitochondria: crosstalk and regulation of multiple mitophagy pathways.* Biol Chem, 2017. **399**(1): p. 29-45.
63. Youle, R.J. and D.P. Narendra, *Mechanisms of mitophagy.* Nat Rev Mol Cell Biol, 2011. **12**(1): p. 9-14.
64. Novak, I., et al., *Nix is a selective autophagy receptor for mitochondrial clearance.* EMBO Rep, 2010. **11**(1): p. 45-51.
65. Marinkovic, M. and I. Novak, *A brief overview of BNIP3L/NIX receptor-mediated mitophagy.* FEBS Open Bio, 2021. **11**(12): p. 3230-3236.
66. Vo, M.T., et al., *Activation of NIX-mediated mitophagy by an interferon regulatory factor homologue of human herpesvirus.* Nat Commun, 2019. **10**(1): p. 3203.
67. PALADE, G.E., *THE FINE STRUCTURE OF MITOCHONDRIA.* 1952.
68. Kunji, E.R.S., et al., *The SLC25 Carrier Family: Important Transport Proteins in Mitochondrial Physiology and Pathology.* Physiology (Bethesda), 2020. **35**(5): p. 302-327.
69. Anand, R., A.S. Reichert, and A.K. Kondadi, *Emerging Roles of the MICOS Complex in Cristae Dynamics and Biogenesis.* Biology (Basel), 2021. **10**(7).
70. Kondadi, A.K., R. Anand, and A.S. Reichert, *Cristae Membrane Dynamics - A Paradigm Change.* Trends Cell Biol, 2020. **30**(12): p. 923-936.
71. Sjöstrand, F.S., *ELECTRON MICROSCOPY OF MITOCHONDRIA AND CYTOPLASMIC DOUBLE MEMBRANES.* Nature, 1953. **171**: p. 30-31.
72. Daems, W.T. and E. Wisse, *Shape and Attachment of the Cristae Mitochondriales in Mouse Hepatic Cell Mitochondria.* J. Ultrastructure Research, 1966. **16**: p. 123-140.
73. Mannella, C.A., *Structure and dynamics of the mitochondrial inner membrane cristae.* Biochim Biophys Acta, 2006. **1763**(5-6): p. 542-8.
74. Mannella, C.A., *Structural diversity of mitochondria: functional implications.* Ann N Y Acad Sci, 2008. **1147**: p. 171-9.
75. Frey, T.G. and C.A. Mannella, *The internal structure of mitochondria.* Trends Biochem Sci, 2000. **25**: p. 319-324.
76. Koob, S. and A.S. Reichert, *Novel intracellular functions of apolipoproteins: the ApoO protein family as constituents of the Mitofilin/MINOS complex determines cristae morphology in mitochondria.* Biol Chem, 2014. **395**(3): p. 285-96.
77. Gustafsson, C.M., M. Falkenberg, and N.G. Larsson, *Maintenance and Expression of Mammalian Mitochondrial DNA.* Annu Rev Biochem, 2016. **85**: p. 133-60.
78. K, N.M.M., *Mitochondrial DNA.* 1969.
79. K., N.M., *Mitochondrial DNA: Advances, Problems, and Goals.* 1969.
80. M M NASS, S.N., B A AFZELIUS, *The general occurrence of mitochondrial DNA.* 1965.
81. M.K., N., *Reversible Generation of Circular Dimer and Higher Multiple Forms of Mitochondrial DNA.* 1969.

82. Anderson S., A.T.B., B. G. Barrell, M. H. L. de Bruijn, A. R. Coulson, J. Drouin*, I. C. Eperon, D. P. Nierlich*, B. A. Roe*, F. Sanger, P. H. Schreier*, A. J. H. Smith, R. Staden & I. G. Young, *Sequence and organization of the human mitochondrial genome.* 1981.
83. Bruser, C., J. Keller-Findeisen, and S. Jakobs, *The TFAM-to-mtDNA ratio defines inner-cellular nucleoid populations with distinct activity levels.* Cell Rep, 2021. **37**(8): p. 110000.
84. Kukat, C., et al., *Cross-strand binding of TFAM to a single mtDNA molecule forms the mitochondrial nucleoid.* Proc Natl Acad Sci U S A, 2015. **112**(36): p. 11288-93.
85. Kukat, C. and N.G. Larsson, *mtDNA makes a U-turn for the mitochondrial nucleoid.* Trends Cell Biol, 2013. **23**(9): p. 457-63.
86. Kukat, C., et al., *Super-resolution microscopy reveals that mammalian mitochondrial nucleoids have a uniform size and frequently contain a single copy of mtDNA.* Proc Natl Acad Sci U S A, 2011. **108**(33): p. 13534-9.
87. Kaufman, B.A., et al., *The mitochondrial transcription factor TFAM coordinates the assembly of multiple DNA molecules into nucleoid-like structures.* Mol Biol Cell, 2007. **18**(9): p. 3225-36.
88. Milenkovic, D., et al., *TWINKLE is an essential mitochondrial helicase required for synthesis of nascent D-loop strands and complete mtDNA replication.* Hum Mol Genet, 2013. **22**(10): p. 1983-93.
89. Tyynismaa, H., et al., *Twinkle helicase is essential for mtDNA maintenance and regulates mtDNA copy number.* Hum Mol Genet, 2004. **13**(24): p. 3219-27.
90. Carrodeguas, J.A., K.G. Pinz, and D.F. Bogenhagen, *DNA binding properties of human pol gammaB.* J Biol Chem, 2002. **277**(51): p. 50008-14.
91. Iborra FJ, H.K.a.P.R.C., *The functional organization of mitochondrial genomes in human cells.* BMC Biology, 2004.
92. Garrido, N., et al., *Composition and dynamics of human mitochondrial nucleoids.* Mol Biol Cell, 2003. **14**(4): p. 1583-96.
93. Falkenberg, M., *Mitochondrial DNA replication in mammalian cells: overview of the pathway.* Essays Biochem, 2018. **62**(3): p. 287-296.
94. Wang, Y. and D.F. Bogenhagen, *Human mitochondrial DNA nucleoids are linked to protein folding machinery and metabolic enzymes at the mitochondrial inner membrane.* J Biol Chem, 2006. **281**(35): p. 25791-802.
95. Kopek, B.G., et al., *Correlative 3D superresolution fluorescence and electron microscopy reveal the relationship of mitochondrial nucleoids to membranes.* Proc Natl Acad Sci U S A, 2012. **109**(16): p. 6136-41.
96. Brown, T.A., et al., *Superresolution fluorescence imaging of mitochondrial nucleoids reveals their spatial range, limits, and membrane interaction.* Mol Cell Biol, 2011. **31**(24): p. 4994-5010.
97. Zorkau, M., et al., *High-resolution imaging reveals compartmentalization of mitochondrial protein synthesis in cultured human cells.* Proc Natl Acad Sci U S A, 2021. **118**(6).
98. Ojala, J.M.G.A., *tRNA punctuation model of RNA processing in human mitochondria.* 1981.
99. Rossmanith, W., *Of P and Z: mitochondrial tRNA processing enzymes.* Biochim Biophys Acta, 2012. **1819**(9-10): p. 1017-26.
100. Rey, T., et al., *Mitochondrial RNA granules are fluid condensates, positioned by membrane dynamics.* 2019.
101. Amunts, A., et al., *Structure of the yeast mitochondrial large ribosomal subunit.* Science, 2014. **343**(6178): p. 1485-1489.
102. Kaushal, P.S., et al., *Cryo-EM structure of the small subunit of the mammalian mitochondrial ribosome.* Proc Natl Acad Sci U S A, 2014. **111**(20): p. 7284-9.
103. Antonicka, H. and E.A. Shoubridge, *Mitochondrial RNA Granules Are Centers for Posttranscriptional RNA Processing and Ribosome Biogenesis.* Cell Rep, 2015.
104. Tu, Y.T. and A. Barrientos, *The Human Mitochondrial DEAD-Box Protein DDX28 Resides in RNA Granules and Functions in Mitoribosome Assembly.* Cell Rep, 2015. **10**(6): p. 854-864.

105. Pearce, S.F., et al., *Regulation of Mammalian Mitochondrial Gene Expression: Recent Advances.* Trends Biochem Sci, 2017. **42**(8): p. 625-639.
106. Goto, Y., I. Nonaka, and S. Horai, *A mutation in the tRNALeu(UUR) gene associated with the MELAS subgroup of mitochondrial encephalomyopathies.* Nature, 1990. **348**: p. 651-653.
107. Pek, N.M.Q., et al., *Mitochondrial 3243A > G mutation confers pro-atherogenic and pro-inflammatory properties in MELAS iPS derived endothelial cells.* Cell Death Dis, 2019. **10**(11): p. 802.
108. Yoo, D.H., et al., *Identification of FASTKD2 compound heterozygous mutations as the underlying cause of autosomal recessive MELAS-like syndrome.* Mitochondrion, 2017. **35**: p. 54-58.
109. Mourier, A., et al., *Loss of LRPPRC causes ATP synthase deficiency.* Hum Mol Genet, 2014. **23**(10): p. 2580-92.
110. Ruzzenente, B., et al., *LRPPRC is necessary for polyadenylation and coordination of translation of mitochondrial mRNAs.* EMBO J, 2012. **31**(2): p. 443-56.
111. Sasarman, F., et al., *Tissue-specific responses to the LRPPRC founder mutation in French Canadian Leigh Syndrome.* Hum Mol Genet, 2015. **24**(2): p. 480-91.
112. Bennett, C.F., P. Latorre-Muro, and P. Puigserver, *Mechanisms of mitochondrial respiratory adaptation.* Nat Rev Mol Cell Biol, 2022.
113. Tseng, W.W. and A.C. Wei, *Kinetic Mathematical Modeling of Oxidative Phosphorylation in Cardiomyocyte Mitochondria.* Cells, 2022. **11**(24).
114. Martinez-Reyes, I. and N.S. Chandel, *Mitochondrial TCA cycle metabolites control physiology and disease.* Nat Commun, 2020. **11**(1): p. 102.
115. Green, D.E. and A. Tzagoloff, *The mitochondrial electron transfer chain.* Archives of Biochemistry and Biophysics, 1966. **116**: p. 293-304.
116. Xu, J., et al., *Recent Advancements in Mitochondria-Targeted Nanoparticle Drug Delivery for Cancer Therapy.* Nanomaterials (Basel), 2022. **12**(5).
117. Zhu, J., K.R. Vinothkumar, and J. Hirst, *Structure of mammalian respiratory complex I.* Nature, 2016. **536**(7616): p. 354-358.
118. Fiedorczuk, K., et al., *Atomic structure of the entire mammalian mitochondrial complex I.* Nature, 2016. **538**(7625): p. 406-410.
119. Sazanov, L.A. and P. Hinchliffe, *Structure of the Hydrophilic Domain of Respiratory Complex I from Thermus thermophilus.* Science, 2006. **311**: p. 1430-1436.
120. Sherer, T.B., et al., *Mechanism of Toxicity in Rotenone Models of Parkinson's Disease.* The Journal of Neuroscience, 2003. **23**(34): p. 10756 –10764.
121. Rasheed, M. and G. Tarjan, *Succinate Dehydrogenase Complex: An Updated Review.* Arch Pathol Lab Med, 2018. **142**(12): p. 1564-1570.
122. Xia, D., et al., *Structural analysis of cytochrome bc1 complexes: implications to the mechanism of function.* Biochim Biophys Acta, 2013. **1827**(11-12): p. 1278-94.
123. Kim, H., et al., *Structure of Antimycin A1, a Specific Electron Transfer Inhibitor of Ubiquinol-Cytochrome c Oxidoreductase.* J. Am. Chem. Soc., 1999. **121**: p. 4902-4903.
124. Yoshikawa, S. and A. Shimada, *Reaction mechanism of cytochrome c oxidase.* Chem Rev, 2015. **115**(4): p. 1936-89.
125. Stoldt, S., et al., *Spatial orchestration of mitochondrial translation and OXPHOS complex assembly.* Nat Cell Biol, 2018. **20**(5): p. 528-534.
126. Needs, H.I., et al., *Interplay between Mitochondrial Protein Import and Respiratory Complexes Assembly in Neuronal Health and Degeneration.* Life (Basel), 2021. **11**(5).
127. Schägger, H. and K. Pfeiffer, *Supercomplexes in the respiratory chains of yeast and mammalian mitochondria.* EMBO J, 2000. **19**: p. 1777±1783.
128. Letts, J.A. and L.A. Sazanov, *Clarifying the supercomplex: the higher-order organization of the mitochondrial electron transport chain.* Nat Struct Mol Biol, 2017. **24**(10): p. 800-808.
129. Vercellino, I. and L.A. Sazanov, *The assembly, regulation and function of the mitochondrial respiratory chain.* Nat Rev Mol Cell Biol, 2022. **23**(2): p. 141-161.

130. Lobo-Jarne, T. and C. Ugalde, *Respiratory chain supercomplexes: Structures, function and biogenesis.* Semin Cell Dev Biol, 2018. **76**: p. 179-190.
131. Guo, R., et al., *Structure and mechanism of mitochondrial electron transport chain.* Biomed J, 2018. **41**(1): p. 9-20.
132. Anand, R., et al., *MIC26 and MIC27 cooperate to regulate cardiolipin levels and the landscape of OXPHOS complexes.* Life Sci Alliance, 2020. **3**(10).
133. Mitchell, P., *Coupling of Phosphorylation to Electron and Hydrogen Transfer by a Chemi-Osmotic type of Mechanism.* Nature, 1961. **191**: p. 144-148.
134. Spikes, T.E., M.G. Montgomery, and J.E. Walker, *Structure of the dimeric ATP synthase from bovine mitochondria.* Proc Natl Acad Sci U S A, 2020. **117**(38): p. 23519-23526.
135. Blum, T.B., et al., *Dimers of mitochondrial ATP synthase induce membrane curvature and self-assemble into rows.* Proc Natl Acad Sci U S A, 2019. **116**(10): p. 4250-4255.
136. Muhleip, A., et al., *ATP synthase hexamer assemblies shape cristae of Toxoplasma mitochondria.* Nat Commun, 2021. **12**(1): p. 120.
137. Kuhlbrandt, W., *Structure and Mechanisms of F-Type ATP Synthases.* Annu Rev Biochem, 2019. **88**: p. 515-549.
138. Abbas, Y.M., et al., *Structure of V-ATPase from the mammalian brain.* Science, 2020. **367**: p. 1240–1246.
139. Acin-Perez, R., et al., *Inhibition of ATP synthase reverse activity restores energy homeostasis in mitochondrial pathologies.* EMBO J, 2023. **42**(10): p. e111699.
140. Guerrieri, F., et al., *On the Mechanism of Action of Oligomycin and Acidic Uncouplers on Proton Translocation and Energy Transfer in "Sonic" Submitochondrial Particles.* J Bioenerg Biomembr, 1976. **8**: p. 131-142.
141. Pfanner, N., et al., *Uniform nomenclature for the mitochondrial contact site and cristae organizing system.* J Cell Biol, 2014. **204**(7): p. 1083-6.
142. Huynen, M.A., et al., *Evolution and structural organization of the mitochondrial contact site (MICOS) complex and the mitochondrial intermembrane space bridging (MIB) complex.* Biochim Biophys Acta, 2016. **1863**(1): p. 91-101.
143. Munoz-Gomez, S.A., et al., *The evolution of MICOS: Ancestral and derived functions and interactions.* Commun Integr Biol, 2015. **8**(6): p. e1094593.
144. Munoz-Gomez, S.A., et al., *Ancient homology of the mitochondrial contact site and cristae organizing system points to an endosymbiotic origin of mitochondrial cristae.* Curr Biol, 2015. **25**(11): p. 1489-95.
145. Hoppins, S., et al., *A mitochondrial-focused genetic interaction map reveals a scaffold-like complex required for inner membrane organization in mitochondria.* J Cell Biol, 2011. **195**(2): p. 323-40.
146. Harner, M., et al., *The mitochondrial contact site complex, a determinant of mitochondrial architecture.* EMBO J, 2011. **30**(21): p. 4356-70.
147. von der Malsburg, K., et al., *Dual role of mitofilin in mitochondrial membrane organization and protein biogenesis.* Dev Cell, 2011. **21**(4): p. 694-707.
148. Xie, J., et al., *The mitochondrial inner membrane protein mitofilin exists as a complex with SAM50, metaxins 1 and 2, coiled-coil-helix coiled-coil-helix domain-containing protein 3 and 6 and DnaJC11.* FEBS Lett, 2007. **581**(18): p. 3545-9.
149. Ott, C., et al., *Detailed analysis of the human mitochondrial contact site complex indicate a hierarchy of subunits.* PLoS One, 2015. **10**(3): p. e0120213.
150. Dietz, J.V., et al., *Mitochondrial contact site and cristae organizing system (MICOS) machinery supports heme biosynthesis by enabling optimal performance of ferrochelatase.* Redox Biol, 2021. **46**: p. 102125.
151. Anand, R., et al., *Mic13 Is Essential for Formation of Crista Junctions in Mammalian Cells.* PLoS One, 2016. **11**(8): p. e0160258.
152. John, G.B., et al., *The mitochondrial inner membrane protein mitofilin controls cristae morphology.* Mol Biol Cell, 2005. **16**(3): p. 1543-54.

153. Stoldt, S., et al., *Mic60 exhibits a coordinated clustered distribution along and across yeast and mammalian mitochondria.* Proc Natl Acad Sci U S A, 2019. **116**(20): p. 9853-9858.
154. Tarasenko, D., et al., *The MICOS component Mic60 displays a conserved membrane-bending activity that is necessary for normal cristae morphology.* J Cell Biol, 2017. **216**(4): p. 889-899.
155. Korner, C., et al., *The C-terminal domain of Fcj1 is required for formation of crista junctions and interacts with the TOB/SAM complex in mitochondria.* Mol Biol Cell, 2012. **23**(11): p. 2143-55.
156. Michaud, M., et al., *AtMic60 Is Involved in Plant Mitochondria Lipid Trafficking and Is Part of a Large Complex.* Curr Biol, 2016. **26**(5): p. 627-39.
157. Ding, C., et al., *Mitofilin and CHCHD6 physically interact with Sam50 to sustain cristae structure.* Sci Rep, 2015. **5**: p. 16064.
158. Tang, J., et al., *Sam50-Mic19-Mic60 axis determines mitochondrial cristae architecture by mediating mitochondrial outer and inner membrane contact.* Cell Death Differ, 2020. **27**(1): p. 146-160.
159. Bock-Bierbaum, T., et al., *Structural insights into crista junction formation by the Mic60-Mic19 complex.* Sci Adv, 2022. **8**(35): p. eabo4946.
160. Bohnert, M., et al., *Central role of Mic10 in the mitochondrial contact site and cristae organizing system.* Cell Metab, 2015. **21**(5): p. 747-55.
161. Milenkovic, D. and N.G. Larsson, *Mic10 Oligomerization Pinches off Mitochondrial Cristae.* Cell Metab, 2015. **21**(5): p. 660-1.
162. Barbot, M., et al., *Mic10 oligomerizes to bend mitochondrial inner membranes at cristae junctions.* Cell Metab, 2015. **21**(5): p. 756-63.
163. Rampelt, H., et al., *Mic10, a Core Subunit of the Mitochondrial Contact Site and Cristae Organizing System, Interacts with the Dimeric F1Fo-ATP Synthase.* J Mol Biol, 2017. **429**(8): p. 1162-1170.
164. Guarani, V., et al., *QIL1 is a novel mitochondrial protein required for MICOS complex stability and cristae morphology.* Elife, 2015. **4**.
165. Urbach, J., et al., *Conserved GxxxG and WN motifs of MIC13 are essential for bridging two MICOS subcomplexes.* Biochim Biophys Acta Biomembr, 2021. **1863**(12): p. 183683.
166. Kondadi, A.K., et al., *Cristae undergo continuous cycles of membrane remodelling in a MICOS -dependent manner.* EMBO reports, 2020.
167. Weber, T.A., et al., *APOOL is a cardiolipin-binding constituent of the Mitofilin/MINOS protein complex determining cristae morphology in mammalian mitochondria.* PLoS One, 2013. **8**(5): p. e63683.
168. Feng, Y., et al., *Mitofilin Heterozygote Mice Display an Increase in Myocardial Injury and Inflammation after Ischemia/Reperfusion.* Antioxidants (Basel), 2023. **12**(4).
169. Marco-Hernandez, A.V., et al., *Mitochondrial developmental encephalopathy with bilateral optic neuropathy related to homozygous variants in IMMT gene.* Clin Genet, 2022. **101**(2): p. 233-241.
170. Tsai, P.I., et al., *PINK1 Phosphorylates MIC60/Mitofilin to Control Structural Plasticity of Mitochondrial Crista Junctions.* Mol Cell, 2018. **69**(5): p. 744-756 e6.
171. Zeharia, A., et al., *Mitochondrial hepato-encephalopathy due to deficiency of QIL1/MIC13 (C19orf70), a MICOS complex subunit.* Eur J Hum Genet, 2016. **24**(12): p. 1778-1782.
172. Kishita, Y., et al., *A novel homozygous variant in MICOS13/QIL1 causes hepato-encephalopathy with mitochondrial DNA depletion syndrome.* Mol Genet Genomic Med, 2020. **8**(10): p. e1427.
173. Russell, B.E., et al., *Expanding and Underscoring the Hepato-Encephalopathic Phenotype of QIL1/MIC13.* Hepatology, 2019. **70**(3): p. 1066-1070.
174. Guarani, V., et al., *QIL1 mutation causes MICOS disassembly and early onset fatal mitochondrial encephalopathy with liver disease.* Elife, 2016. **5**.
175. Meurs, K.M., et al., *A QIL1 Variant Associated with Ventricular Arrhythmias and Sudden Cardiac Death in the Juvenile Rhodesian Ridgeback Dog.* Genes (Basel), 2019. **10**(2).

176. Beninca, C., et al., *Mutation in the MICOS subunit gene APOO (MIC26) associated with an X-linked recessive mitochondrial myopathy, lactic acidosis, cognitive impairment and autistic features.* J Med Genet, 2021. **58**(3): p. 155-167.
177. Peifer-Weiss, L., et al., *A X-linked nonsense APOO/MIC26 variant causes a lethal mitochondrial disease with progeria-like phenotypes.* Clin Genet, 2023. **104**(6): p. 659-668.
178. Kimura, T., et al., *Plasmalogen loss caused by remodeling deficiency in mitochondria.* Life Sci Alliance, 2019. **2**(4).
179. Ye, C., Z. Shen, and M.L. Greenberg, *Cardiolipin remodeling: a regulatory hub for modulating cardiolipin metabolism and function.* J Bioenerg Biomembr, 2016. **48**(2): p. 113-23.
180. Chowdhury, A., et al., *Defective Mitochondrial Cardiolipin Remodeling Dampens HIF-1alpha Expression in Hypoxia.* Cell Rep, 2018. **25**(3): p. 561-570 e6.
181. Mukherjee, I., M. Ghosh, and M. Meinecke, *MICOS and the mitochondrial inner membrane morphology - when things get out of shape.* FEBS Lett, 2021. **595**(8): p. 1159-1183.
182. Vogel, F., et al., *Dynamic subcompartmentalization of the mitochondrial inner membrane.* J Cell Biol, 2006. **175**(2): p. 237-47.
183. Rath, S., et al., *MitoCarta3.0: an updated mitochondrial proteome now with sub-organelle localization and pathway annotations.* Nucleic Acids Res, 2021. **49**(D1): p. D1541-D1547.
184. Qiu, J., et al., *Coupling of mitochondrial import and export translocases by receptor-mediated supercomplex formation.* Cell, 2013. **154**(3): p. 596-608.
185. Schmidt, O., et al., *Regulation of mitochondrial protein import by cytosolic kinases.* Cell, 2011. **144**(2): p. 227-39.
186. Shiota, T., et al., *Molecular architecture of the active mitochondrial protein gate.* Science, 2015. **349**(6255).
187. Bausewein, T., et al., *Cryo-EM Structure of the TOM Core Complex from Neurospora crassa.* Cell, 2017. **170**(4): p. 693-700 e7.
188. Backes, S., et al., *Tom70 enhances mitochondrial preprotein import efficiency by binding to internal targeting sequences.* J Cell Biol, 2018. **217**(4): p. 1369-1382.
189. Hohr, A.I.C., et al., *Membrane protein insertion through a mitochondrial beta-barrel gate.* Science, 2018. **359**(6373).
190. Chacinska, A., et al., *Essential role of Mia40 in import and assembly of mitochondrial intermembrane space proteins.* Embo J, 2004. **23**(19): p. 3735-46.
191. Sideris, D.P., et al., *A novel intermembrane space-targeting signal docks cysteines onto Mia40 during mitochondrial oxidative folding.* J Cell Biol, 2009. **187**(7): p. 1007-22.
192. Sirrenberg, C., et al., *Import of carrier proteins into the mitochondrial inner membrane mediated by Tim22.* Nature, 1996. **384**.
193. Kerscher, O., et al., *The Tim54p–Tim22p Complex Mediates Insertion of Proteins into the Mitochondrial Inner Membrane.* J Cell Biol, 1997. **139**: p. 1663–1675.
194. Koehler, C.M., et al., *Tim9p, an essential partner subunit of Tim10p for the import of mitochondrial carrier proteins.* The EMBO Journal, 1998. **17**: p. 6477–6486.
195. Vial, S., et al., *Assembly of Tim9 and Tim10 into a functional chaperone.* J Biol Chem, 2002. **277**(39): p. 36100-8.
196. Lohret, T.A., R.E. Jensen, and K.W. Kinnally, *Tim23, a Protein Import Component of the Mitochondrial Inner Membrane, Is Required for Normal Activity of the Multiple Conductance Channel, MCC.* J Cell Biol, 1997. **137**: p. 377–386.
197. Kang, P.J., et al., *Requirement for hsp70 in the mitochondrial matrix for translocation and folding of precursor proteins.* Nature, 1990. **348**: p. 137-143.
198. Huff, J., *The Airyscan detector from ZEISS: confocal imaging with improved signal-to-noise ratio and super-resolution.* Nature Methods, 2015. **12**(12): p. i-ii.
199. Wilson, T., *Resolution and optical sectioning in the confocal microscope.* J Microsc, 2011. **244**(2): p. 113-21.
200. Loriette, V., et al., *Dynamics of mitochondrial membranes under photo-oxidative stress with high spatiotemporal resolution.* Front Cell Dev Biol, 2023. **11**: p. 1307502.

201. Betzig E, P.G., Sougrat R, Lindwasser, O.S. OW, Bonifacino JS, Davidson MW,, and H.H. Lippincott-Schwartz J, *Imaging Intracellular Fluorescent Proteins at Nanometer Resolution.* Science, 2006. **VOL 313**.
202. Willig, K.I., et al., *Nanoscale resolution in GFP-based microscopy.* Nat Methods, 2006. **3**(9): p. 721-3.
203. Rust, M.J., M. Bates, and X. Zhuang, *Sub-diffraction-limit imaging by stochastic optical reconstruction microscopy (STORM).* Nat Methods, 2006. **3**(10): p. 793-5.
204. Bottanelli, F., et al., *Two-colour live-cell nanoscale imaging of intracellular targets.* Nat Commun, 2016. **7**: p. 10778.
205. Los G., Lance P. Encell†, Mark G. McDougall‡, Danette D. Hartzell†, Natasha Karassina†, Chad Zimprich†, Monika G. Wood†, Randy Learish†, Rachel Friedman Ohana†, Marjeta Urh†, Dan Simpson†, Jacqui Mendez†, Kris Zimmerman†, Paul Otto†, Gediminas Vidugiris†,JiZhu‡, Aldis Darzins†,§, Dieter H. Klaubert‡, Robert F. Bulleit†, and Keith V. Wood†, *HaloTag: A Novel Protein Labeling Technology for Cell Imaging and Protein Analysis.* 2008.
206. Golombek, M., et al., *Cristae dynamics is modulated in bioenergetically compromised mitochondria.* Life Sci Alliance, 2024. **7**(2).
207. Weber, M., et al., *MINSTED fluorescence localization and nanoscopy.* Nat Photonics, 2021. **15**(5): p. 361-366.
208. Eilers, Y., et al., *MINFLUX monitors rapid molecular jumps with superior spatiotemporal resolution.* Proc Natl Acad Sci U S A, 2018. **115**(24): p. 6117-6122.
209. Pape, J.K., et al., *Multicolor 3D MINFLUX nanoscopy of mitochondrial MICOS proteins.* Proc Natl Acad Sci U S A, 2020. **117**(34): p. 20607-20614.
210. Bates, M., et al., *Optimal precision and accuracy in 4Pi-STORM using dynamic spline PSF models.* Nat Methods, 2022. **19**(5): p. 603-612.
211. Perry, S.W., et al., *Mitochondrial membrane potential probes and the proton gradient: a practical usage guide.* Biotechniques, 2011. **50**(2): p. 98-115.
212. Wang, C., et al., *A photostable fluorescent marker for the superresolution live imaging of the dynamic structure of the mitochondrial cristae.* Proc Natl Acad Sci U S A, 2019. **116**(32): p. 15817-15822.
213. Mannella, C.A., et al., *Topology of the mitochondrial inner membrane: dynamics and bioenergetic implications.* IUBMB Life, 2001. **52**(3-5): p. 93-100.
214. Hackenbrock, C.R., *Ultrastructural bases for metabolically linked mechanical activity in mitochondria: I. Reversible ultrastructural changes with change in metabolic steady state in isolated liver mitochondria.* The Journal of cell biology, 1966. **30**(2): p. 269-297.
215. Luca Scorrano, M.A., 1 Karolyn Buttle,2 Solly Weiler,1 Scott A. Oakes,1 Carmen A. Mannella,2 and a.S.J. Korsmeyer, *A Distinct Pathway Remodels Mitochondrial Cristae and Mobilizes Cytochrome c during Apoptosis.* 2002.
216. Stephan, T., et al., *Live-cell STED nanoscopy of mitochondrial cristae.* Sci Rep, 2019. **9**(1): p. 12419.
217. Wolf, D.M., et al., *Individual cristae within the same mitochondrion display different membrane potentials and are functionally independent.* The EMBO Journal, 2019.
218. Hu, C., et al., *OPA1 and MICOS Regulate mitochondrial crista dynamics and formation.* Cell Death Dis, 2020. **11**(10): p. 940.
219. Gottschalk, B., et al., *MICU1 controls cristae junction and spatially anchors mitochondrial Ca(2+) uniporter complex.* Nat Commun, 2019. **10**(1): p. 3732.
220. Gottschalk, B., et al., *Intracellular Ca(2+) release decelerates mitochondrial cristae dynamics within the junctions to the endoplasmic reticulum.* Pflugers Arch, 2018. **470**(8): p. 1193-1203.
221. Gottschalk, B., C.T. Madreiter-Sokolowski, and W.F. Graier, *Cristae junction as a fundamental switchboard for mitochondrial ion signaling and bioenergetics.* Cell Calcium, 2022. **101**: p. 102517.
222. Ruprecht, J.J. and E.R.S. Kunji, *The SLC25 Mitochondrial Carrier Family: Structure and Mechanism.* Trends Biochem Sci, 2020. **45**(3): p. 244-258.

223. Janer, A., et al., *SLC25A46 is required for mitochondrial lipid homeostasis and cristae maintenance and is responsible for Leigh syndrome.* EMBO Mol Med, 2016. **8**(9): p. 1019-38.
224. Brandolin, G., Y. Dupont, and P.V. Vignais, *Substrate-Induced Modifications of the Intrinsic Fluorescence of the Isolated Adenine Nucleotide Carrier Protein: Demonstration of Distinct Conformational States.* Biochemistry, 1985. **24**: p. 1991-1997.
225. Dolce, V., et al., *A fourth ADP/ATP carrier isoform in man: identification, bacterial expression, functional characterization and tissue distribution.* FEBS Lett, 2005. **579**(3): p. 633-7.
226. Bround, M.J., D.M. Bers, and J.D. Molkentin, *A 20/20 view of ANT function in mitochondrial biology and necrotic cell death.* J Mol Cell Cardiol, 2020. **144**: p. A3-A13.
227. Ruprecht, J.J. and E.R.S. Kunji, *Structural Mechanism of Transport of Mitochondrial Carriers.* Annu Rev Biochem, 2021. **90**: p. 535-558.
228. King, M.S., et al., *Expanding the phenotype of de novo SLC25A4-linked mitochondrial disease to include mild myopathy.* Neurol Genet, 2018. **4**(4): p. e256.
229. Ruprecht, J.J., et al., *The Molecular Mechanism of Transport by the Mitochondrial ADP/ATP Carrier.* Cell, 2019. **176**(3): p. 435-447 e15.
230. Anwar, M., et al., *Bongkrekic Acid-a Review of a Lesser-Known Mitochondrial Toxin.* J Med Toxicol, 2017. **13**(2): p. 173-179.
231. SIRAK, C.D.S.a.H.D., *ADENINE NUCLEOTIDE-INDUCED CONTRACTION OF THE INNER MITOCHONDRIAL MEMBRANE.* 1973.
232. Steffen, J., et al., *Rapid degradation of mutant SLC25A46 by the ubiquitin-proteasome system results in MFN1/2-mediated hyperfusion of mitochondria.* Mol Biol Cell, 2017. **28**(5): p. 600-612.
233. Bitetto, G., et al., *SLC25A46 mutations in patients with Parkinson's Disease and optic atrophy.* Parkinsonism Relat Disord, 2020. **74**: p. 1-5.
234. Palmieri, F., P. Scarcia, and M. Monne, *Diseases Caused by Mutations in Mitochondrial Carrier Genes SLC25: A Review.* Biomolecules, 2020. **10**(4).
235. Brenner, C., et al., *Adenine nucleotide translocase family: four isoforms for apoptosis modulation in cancer.* Oncogene, 2011. **30**(8): p. 883-95.
236. Kaukonen, J., et al., *Role of Adenine Nucleotide Translocator 1 in mtDNA Maintenance.* Science, 2000. **289**.
237. Palmieri, L., et al., *Complete loss-of-function of the heart/muscle-specific adenine nucleotide translocator is associated with mitochondrial myopathy and cardiomyopathy.* Hum Mol Genet, 2005. **14**(20): p. 3079-88.
238. Echaniz-Laguna, A., et al., *Complete loss of expression of the ANT1 gene causing cardiomyopathy and myopathy.* J Med Genet, 2012. **49**(2): p. 146-50.
239. Ogunbona, O.B., M.G. Baile, and S.M. Claypool, *Cardiomyopathy-associated mutation in the ADP/ATP carrier reveals translation-dependent regulation of cytochrome c oxidase activity.* Mol Biol Cell, 2018. **29**(12): p. 1449-1464.
240. Hoshino, A., et al., *The ADP/ATP translocase drives mitophagy independent of nucleotide exchange.* Nature, 2019.
241. Glytsou, C., et al., *Optic Atrophy 1 Is Epistatic to the Core MICOS Component MIC60 in Mitochondrial Cristae Shape Control.* Cell Rep, 2016. **17**(11): p. 3024-3034.
242. Lee, H., S.B. Smith, and Y. Yoon, *The short variant of the mitochondrial dynamin OPA1 maintains mitochondrial energetics and cristae structure.* J Biol Chem, 2017. **292**(17): p. 7115-7130.
243. Olichon, A., et al., *Loss of OPA1 perturbates the mitochondrial inner membrane structure and integrity, leading to cytochrome c release and apoptosis.* J Biol Chem, 2003. **278**(10): p. 7743-6.
244. Frezza, C., et al., *OPA1 controls apoptotic cristae remodeling independently from mitochondrial fusion.* Cell, 2006. **126**(1): p. 177-89.

245. Imamuraa, H., et al., *Visualization of ATP levels inside single living cells with fluorescence resonance energy transfer-based genetically encoded indicators.* Proc Natl Acad Sci U S A, 2009. **106**(37): p. 15651–15656.
246. Nakano, M., et al., *Ca(2)(+) regulation of mitochondrial ATP synthesis visualized at the single cell level.* ACS Chem Biol, 2011. **6**(7): p. 709-15.
247. Szabo, I. and A. Szewczyk, *Mitochondrial Ion Channels.* Annu Rev Biophys, 2023. **52**: p. 229-254.
248. Paggio, A., et al., *Identification of an ATP-sensitive potassium channel in mitochondria.* Nature, 2019. **572**(7771): p. 609-613.
249. Tomar, D., et al., *MICU1 regulates mitochondrial cristae structure and function independently of the mitochondrial Ca2+ uniporter channel.* Sci. Signal., 2023. **16**: p. 1-13.
250. Gottschalk, B., et al., *MICU1 controls spatial membrane potential gradients and guides Ca(2+) fluxes within mitochondrial substructures.* Commun Biol, 2022. **5**(1): p. 649.
251. Peng, M., J. Yin, and W. Lin, *Tracking mitochondrial viscosity in living systems based on a two-photon and near red probe.* New Journal of Chemistry, 2019. **43**(43): p. 16945-16949.
252. Zhang, Y., et al., *Real-time imaging mitochondrial viscosity dynamic during mitophagy mediated by photodynamic therapy.* Anal Chim Acta, 2021. **1178**: p. 338847.
253. Gottlieb, E., et al., *Mitochondrial membrane potential regulates matrix configuration and cytochrome c release during apoptosis.* Cell Death Differ, 2003. **10**(6): p. 709-17.
254. Segawa, M., et al., *Quantification of cristae architecture reveals time-dependent characteristics of individual mitochondria.* Life Sci Alliance, 2020. **3**(7).
255. Barrera, M., et al., *OPA1 functionally interacts with MIC60 but is dispensable for crista junction formation.* FEBS Lett, 2016. **590**(19): p. 3309-3322.
256. Faelber, K., et al., *Structure and assembly of the mitochondrial membrane remodelling GTPase Mgm1.* Nature, 2019. **571**(7765): p. 429-433.
257. Gilkerson, R., P. De La Torre, and S. St Vallier, *Mitochondrial OMA1 and OPA1 as Gatekeepers of Organellar Structure/Function and Cellular Stress Response.* Front Cell Dev Biol, 2021. **9**: p. 626117.
258. Stephan, T., et al., *MICOS assembly controls mitochondrial inner membrane remodeling and crista junction redistribution to mediate cristae formation.* EMBO J, 2020. **39**(14): p. e104105.
259. Reichert, A.S.E., *The Dynamic Nature of Mitochondria: from Ultrastructure to Health and Disease.* CRC Press, 2024. **1**.

7. Publications

1. Cristae dynamics is modulated in bioenergetically compromised mitochondria. Life Sci Alliance. 2023 Nov 13. doi: 10.26508/lsa.202302386

Mathias Golombek, Thanos Tsigaras, Yulia Schaumkessel, Sebastian Hänsch, Stefanie Weidtkamp-Peters, Ruchika Anand, Andreas S. Reichert, Arun Kumar Kondadi.

Contributions of Mathias Golombek to the manuscript:

Data curation (except EM, STED and IF with AKK, Seahorse by YS, crista morphology with TT), software, formal analysis, validation, investigation, visualization, methodology, represented in all figures except

Writing—review and editing with AKK

2. MIC26 and MIC27 cooperate to regulate cardiolipin levels and the landscape of OXPHOS complexes. Life Sci Alliance. 2020 Aug 11;3(10):e202000711. doi: 10.26508/lsa.202000711

Ruchika Anand, Arun Kumar Kondadi, Jana Meisterknecht, **Mathias Golombek**, Oliver Nortmann, Julia Riedel, Leon Peifer-Weiß, Nahal Brocke-Ahmadinejad, David Schlütermann, Björn Stork, Thomas O Eichmann, Ilka Wittig, Andreas S Reichert.

Contributions of Mathias Golombek to the manuscript:

Investigation and methodology, shown in Figure 7 C (generation of stable cell lines, expressing ev or MIC26 or MIC27 or MIC26 and MIC27 together or CRLS1 (cardiolipin synthase, followed by isolation of mitochondria and blue-native gel electrophoresis.

3. Involvement of necroptosis in the selective toxicity of the natural compound (±) gossypol on squamous skin cancer cells in vitro. Arch Toxicol. 2023 Jul;97(7):1997-2014. doi: 10.1007/s00204-023-03516-1

Lisa Haasler, Claudia von Montfort, Arun Kumar Kondadi, **Mathias Golombek**, Lara Ebbert, Chantal-Kristin Wenzel, Wilhelm Stahl, Andreas S Reichert, Peter Brenneisen.

Contributions of Mathias Golombek to the manuscript:

Immunofluorescence microscopy featured in figure 9 E.

8. Acknowledgments

Although this is my doctoral thesis, many people contributed to this project either directly or indirectly and I would like to recognize and acknowledge these efforts. First of all, I want to thank Prof. Dr. Andreas Reichert for giving me the outstanding opportunity to work on my doctoral thesis in his institute. I am really thankful for his trust and support throughout the years. Without his support I would not have been able to live through the endeavour of a PhD.

Furthermore, I want to thank my mentor Prof. Dr. Andreas Weber for his support in proceeding with my scientific career. I am thankful for his valuable inputs and discussions we had during our project meetings.

Another very important person, whom I want to thank is Dr. Arun Kumar Kondadi. I am thankful for his supervision thought the years, starting back in 2019 with my Master thesis. He taught me a lot. I did not only learn about mitochondria and imaging, but also a lot about critical thinking, pursuing ideas and the world of science.

I also want to thank Prof. Dr. Peter Brenneisen for the chance to collaborate with him on our gossypol project and for our numerous discussion we had during our meetings and retreats. I always liked his questions a lot, as they came from a different perspective and helped me a lot developing new ideas.

Furthermore, I want to thank Prof. Dr. Stefanie Weidtkamp-Peters and Dr. Sebastian Hänsch from The Center for Advanced Imaging at HHU. They introduced me to the wonders of microscopy, several years back during my Master courses and were always there for help and support. For me it always has been a huge privilege and lots of fun to use their microscopes (especially the Leica SP8).

I want to thank our technicians, Andrea Borchardt, Tanja Protugall, Gisela Pansegrau and Sandra Schmidt for their excellent technical assistance. I want to thank Sandra for a the work she puts into organizing the Lab and supporting us scientists, I want to thank Tanja for her great support at my initial start in the Institute, teaching me cell culture and supporting me with all different kinds sample preparations, I want to thank Andrea for all the amazing EM images she took for my projects and the help with changing the CO_2 bottles and last but by no means least I want to thank Gisela for her motivational

and friendly words in the morning, there is no better way to start the week off with a Lab Meeting and a nice and honest greeting from Gisela.

Over the years in the Institute for biochemistry and molecular biology I, I had the pleasure to work with many unique people. Without the support of so many outstanding characters this doctoral thesis would have been much harder to finish. Overtime many great stories took place in and out of the institute. I am very glad that I had the opportunity to share so many unique memories with my great colleagues.

Finally, I would like to thank my family and friends for their support. It is great to share stories of success and adventures from the Lab with people who can relate and are happy for one's achievements. But it is even more important to know whom to talk to if there is a rocky read ahead. Times are not always easy and there are many ups and down in life. I am extremely blessed with people who back me up whenever I stumble.

Thank you.

Eidesstattliche Erklärung

Ich versichere an Eides Statt, dass die vorliegende Dissertation von mir selbständig und ohne unzulässige fremde Hilfe unter Beachtung der Grundsätze zur Sicherung guter wissenschaftlicher Praxis an der Heinrich-Heine-Universität Düsseldorf erstellt worden ist. Die aus fremden Quellen übernommenen Gedanken sind als solche kenntlich gemacht. Die Dissertation wurde in der vorgelegten oder in ähnlicher Form noch bei keiner anderen Institution eingereicht. Ich habe bisher keine erfolglosen Promotionsversuche unternommen.

Düsseldorf, den 07.03.2024 Mathias Golombek